Multimodal analysis of neurovascular coupling in the newborn

Mina Nourhashemi

▶ **To cite this version:**

Mina Nourhashemi. Multimodal analysis of neurovascular coupling in the newborn. Agricultural sciences. Université de Picardie Jules Verne, 2018. English. NNT : 2018AMIE0059 . tel-03648471

HAL Id: tel-03648471
https://theses.hal.science/tel-03648471

Submitted on 21 Apr 2022

HAL is a multi-disciplinary open access archive for the deposit and dissemination of scientific research documents, whether they are published or not. The documents may come from teaching and research institutions in France or abroad, or from public or private research centers.

L'archive ouverte pluridisciplinaire **HAL**, est destinée au dépôt et à la diffusion de documents scientifiques de niveau recherche, publiés ou non, émanant des établissements d'enseignement et de recherche français ou étrangers, des laboratoires publics ou privés.

Thèse de Doctorat

Mention Biologie Santé
Spécialité Neurosciences-traitement de signal

présentée à l'Ecole Doctorale en Sciences Technologie et Santé (ED 585)

de l'Université de Picardie Jules Verne

Par

Mina Nourhashemi

Pour obtenir le grade de Docteur de l'Université de Picardie Jules Verne

Analyse multimodale du couplage neurovasculaire chez le nouveau-né

Soutenue le 20/ 3/2018, après avis des rapporteurs, devant le jury d'examen :

M. E. Saliba, MD-PhD, Professeur	**Rapporteur**
M^me^ N. Bednarek, Professeur	**Rapporteur**
M^me^ A. Planat-Chrétien, Professeur	**Examinateur**
M. G. Kongolo, MD-PhD	**Examinateur**
M. F. Wallois, MD-PhD, Professeur	**Directeur de Thèse**

GRAMFC

Groupe de Recherche sur l'Analyse Multimodale de la Fonction Cérébrale
INSERM U1105

Multimodal analysis of neurovascular coupling in the newborn

Neurovascular coupling (NVC) has become the key aspect for understanding brain function. A multimodal exploration would aim to identify the early NVC biomarkers and determine their predictive character. **Paper (1):** In this chapter, the photothermal interaction of NIR laser on human tissues were modelled in silico. The results demonstrated the safety of the noninvasive optical evaluation of the brain function and the maximum temperature increase was higher in the neonatal brain than in the adult brain. **Paper (2 & 3):** The main purpose of this thesis was to provide a multimodal view of the NVC and cerebrovascular regulation in the neonatal premature brain. **Paper (2):** Key findings included that rCBV and rCMRO2 have a predominant driving influence on rCBF at the resting-state in the preterm neonatal brain. **Paper (3):** The bursts of electroencephalographic activity in neonates in resting state were found to be coupled to a transient hemodynamic response involving different types of hemodynamic response including: (a) positive stereotyped hemodynamic responses (increases in HbO, decreases in HbR together with increases in CBF and CMRO2), (b) negative hemodynamic responses (increases in HbR, decreases in HbO together with decreases in CBF and CMRO2), (c) Increases and decreases in both HbO-HbR and CMRO2 together with no changes in CBF. The establishment of neurovascular coupling system was observed as a function of age. High coherence was observed between the cerebral hemodynamic (vascular) and electrical (neuronal) oscillations which was less in the non-encephalopathic newborns than in the two pathological groups.

Analyse multimodale de couplage neurovasculaire chez le nouveau-né

Une exploration multimodale permettrait d'identifier les biomarqueurs précoces du CNV permettrait de déterminer leur caractère prédictif. Chapitre (3): Dans ce chapitre, les résultats présentés montrent que l'augmentation maximale de la température était plus élevée dans le cerveau néonatal que dans le cerveau adulte. Chapitre (4 et 5): Le but principal de cette thèse était de fournir une approche multimodale du CNV et de la régulation neurovasculaire dans le cerveau du nouveau-né prématuré. Chapitre (4): Les résultats montrent que le volume sanguin cérébral régional (rCBV) et le rCMRO2 (Cerebral metabolic rate of oxygen) exercent une influence prédominante sur le débit sanguin cérébral régional (rCBF) à l'état de repos chez le prématuré. Chapitre (5): Les bouffées d'activité électroencéphalographique caractéristiques chez les nouveau-nés au repos se sont révélés couplées à une réponse hémodynamique transitoire complexes avec différents types de réponses incluant: (a) des réponses hémodynamiques stéréotypées positives (augmentations de HbO, CBF et CMRO2, diminution de HbR), (b) des réponses hémodynamiques négatives (augmentations de HbR, diminutions de HbO avec des diminutions de CBF et CMRO2), (c) des augmentations et des diminutions à la fois de HbO -HbR et de CMRO2 sans modification du CBF. Malgré des profils de réponse hémodynamique différents qui reflètent l'immaturité et la complexité des systèmes vasculaires et des réseaux neuronaux, l'établissement d'un couplage neurovasculaire a été caractérisé avec une évolution en fonction de l'âge.

Contents

ACKNOWLEDGEMENTS

There are many people to whom I am indebted to in helping me to complete this thesis. First of all, I would like to express my deepest and sincerest thanks to my supervisor, *Prof. Dr. Fabrice Wallois*, for giving me the opportunity to work on this thesis in his laboratory. I am grateful for all his constant support, excellent guidance, critical comments, creating an energetic atmosphere with his warmth and humor, and encouragement throughout my studies without which I would not have been able to produce this piece of work. I am especially appreciative of his patience in reviewing my thesis. I owe a huge debt of gratitude to *Dr. Guy Kongolo* for his support, patience, excellent guidance and advice. It has been my privilege to work closely with *Dr. Fabrice Wallois* and *Dr. Guy Kongolo*, I have enjoyed the opportunity to watch and learn from their knowledge and experience.

I would like to thank *Dr. Mahdi Mahmoudzadeh*, for his thoughtful supervision, for taking my hand and guiding me in this path and for all what he taught me.

I also wish to thank *Dr. Sabrina Goudjil*, for help during the recruitment and clinical data collection phases in NICU of the South hospital of Amiens, France.

This project was generously funded by the "*Conseil Régional de Picardie"*, France. I am grateful for their financial support.

I am indebted to all my friends who have supported me over the last few years. I have enjoyed entertaining discussions with my friends in Inserm_U1105 laboratory and most kind people imaginable in CHU 's clinical team.

Above all, I want to thank my family, my father & mother, my sisters & brother: Mitra, Ghazal & Mohamad, for their support and encouragement. Finally, huge thanks, love and appreciation go to Mahdi, for his grace, generosity and presence in my life.

GLOSSARY

BOLD blood oxygenation level dependent

CBF cerebral blood flow

CBV cerebral blood volume

CSF cerebrospinal fluid

CW Continuous wave

CPP Cerebral perfusion pressure

DCS Diffuse correlation spectroscopy

DPF differential pathlength factor

EEG electroencephalogram

fMRI functional magnetic resonance imaging

fNIRS functional near-infrared spectroscopy

Hb deoxy-haemoglobin

Hb haemoglobin

HbO oxy-haemoglobin

ICP Intracranial pressure

IVH Intra-ventricular hemorrhage

MBLL modified Beer-Lambert law

MBP arterial mean blood pressure

NIR near infrared

rCBF relative Cerebral Blood Flow

rCBV relative Cerebral Blood Volume

$rCMRO_2$ relative Cerebral Metabolic Rate of Oxygen

SNR signal-to-noise ratio

SPECT single photon emission computed tomography

TE Transfer Entropy

tHb total hemoglobin

TOI tissue oxygenation index

StO_2 tissue hemoglobin oxygen saturation

Δ**Hb** changes in deoxy-hemoglobin concentration

Δ**HbO** changes in oxy-hemoglobin concentration

List of publications and presentations

Journal papers

*• Nourhashemi M, Mahmoudzadeh M, Wallois F. "**Thermal impact of near-infrared laser in advanced noninvasive optical brain imaging. Neurophotonics".** 2016 Jan;3(1):015001. doi: 10.1117/1.NPh.3.1.015001. Epub 2016 Jan 14.*

*• Mina Nourhashemi, Guy Kongolo, Mahdi Mahmoudzadeh, Sabrina Goudjil, Fabrice Wallois. **"Relationship between relative cerebral blood flow, relative cerebral blood volume, and relative cerebral metabolic rate of oxygen in the preterm neonatal brain. Neurophotonics".** 2017 Apr;4(2):021104. doi: 10.1117/1.NPh.4.2.021104. Epub 2017 Apr 18.*

*• Mina Nourhashemi, Mahdi Mahmoudzadeh, Guy Kongolo, Sabrina Goudjil, Fabrice Wallois. "**Neurovascular Coupling in the Developing Neonatal Brain in Resting State", submitted in PNAS.***

Posters

- ***"Thermal Impact of Functional Near Infrared Optical Brain Imaging"** 2014, SNCLF Congrès de la Société de Neurophysiologie Clinique de Langue Française 25 – 27 Juin 2014 ANGERS.*
- ***"Thermal Impact of Functional Near Infrared Optical Brain Imaging"** 2014, FNIRS congress, 10-12 October Montreal.*
- ***"Multimodal Imaging of Neurovascular Coupling Relationship Between Spontaneous EEG, CMRO2 And Hemodynamic Responses In preterm Infants",**ISCBFM congress, 27-30 June Vancouver, Canada.*
- ***"rCBF - rCMRO2 Interrelation of Neonatal Premature Brain, A simultaneous NIRS – DCS analysis",** OHBM congress, 26 - 30 June 2016 Geneva, Switzerland.*
- ***"rCBF - rCMRO2 Interrelation of Neonatal Premature Brain",** FNIRS congress, 10-12 October 2016 Paris, France.*
- ***"rCBF - rCMRO2 Interrelation of Neonatal Premature Brain",** ISCBFM congress, 1-4 April, 2017, Berlin, Germany.*

CHAPTER

1 Introduction & background

1.1 Introduction

The localized increase in blood flow to regions of elevated neuronal activity is known as the *neurovascular coupling (NVC)*. Even though many studies have been focused on this relationship in adult, the dynamic of the maturation and how much the maturation of the many compartments of this complex mechanism are unstable are still not completely understood especially in the preemies. NVC remains a key area of research due to its substantial consequences for medical diagnostics and fundamental neuroscience research. In the following sections of this chapter, at first, we will briefly describe the structure of the neuronal and vascular system and of the neurovascular unit, We will described the principle mechanisms underlying the neurovascular coupling, and some aspects of the immaturity of the neuronal, vascular and cardiovascular compartments. Finally, we will summarize the factors of immaturity of the neurovascular system that can influence the characteristics of the cerebral hemodynamic responses.

1.1.1 Structural aspects of the neuronal and vascular system

The brain consists of approximately 86 billion neurons. About 19% of the neurons constitute the cerebral cortex with the remaining 81% constitute the cerebellum (Azevedo et al., 2009), (Herculano-Houzel, 2009). Communication between neurons occurs via synaptic interaction mediated by neurotransmitter release and a combination of electrical and chemical

signals in the form of action potentials that propagate along the neuron's axons (Attwell and Laughlin, 2001). The neurons are functionally localized in a small area notably in the superficial grey matter (GM) (Mountcastle, 1997) and largely interconnected via short and long distance interconnecting fibers that built up progressively in the course of development realizing a dense network for distributed neuronal functions. Almost 50% of the brain's energy cost can be attributed to the action potentials (Attwell and Laughlin, 2001). All this energy is provided by oxygen and glucose supply related to cardiac output via an intricate network of blood vessels (Duvernoy et al., 1981).

The anterior cerebral arteries arise from the Circle of Willis, to supply the primary motor and sensory areas of the cortex. Arteries have a thicker layer of smooth muscle along the vessel walls, which makes it possible for them to maintain vessel tone in the presence of blood pressure fluctuations and to provide active vasomotion. From the cortical surface, arteries and arterioles penetrate the neuronal layers perpendicularly to the surface and supply oxygen (95-100% oxygen saturation) to the neuronal tissues. Vascular density enhances in the cortical grey matter with increasing cortical depth in layers mainly involved with information processing (Herkenham, 1980; Weber et al., 2008). Capillaries lead back to small vessels known as venules (diameter 20 μm) that flow into the larger veins (diameter 120 μm) which are oriented perpendicular to the cortical surface and drain blood from capillaries compartments towards the largesurface cortical veins. Blood then finally exits the gray matter via the pial veins (diameter: 200 μm) and larger draining veins (diameter: 1–3 mm) with approximately 60% oxygen saturation. (Duvernoy et al., 1981). In contrast to arteries, veins undergo passive changes in vessel tone and diameter that result from changes in blood flow and pressure.

1.1.2 The different structural compartments of the neurovascular unit structure

The neurovascular unit is a dynamic structure consisting of neurons, astrocytes, pericytes, vascular endothelial cells and extracellular matrix components. It plays an essential role in the maintenance of a satisfactory levels of oxygen and nutrients in the brain (Fig.1) (Kratzer et al., 2014; McAdams and Juul, 2012; Moretti et al., 2015). Astrocytes play a pivotal role in the regulation of the blood-brain barrier (BBB), as well as in neuronal synapses, to provide nutrients for neurons. The molecules are regulating astrocytic networks, and are coupling neuronal signals and metabolic activities to the cerebral vascular tones, thereby balancing oxygen and energy demands with the supply of cerebral blood flow (Winkler et al., 2011). A

unique feature of the brain vasculature is related to the endothelial vascular cells and the astrocyt endfeets, which define the blood-brain barrier (BBB). Inadequate blood supply leads to energy unbalance and reduction of ATP, followed almost by the deactivation of ion pumps, depolarization of neuronal membranes, accumulation of intracellular calcium, and cellular dysfunction (Allen and Bayraktutan, 2009). Hence, the brain relies on a complex dynamic network of vessels and regulatory mechanisms to maintain proper perfusion and prevent from the injurious effects of low levels of inadequate blood supply. The neurovascular coupling

connects cerebral blood flow (CBF) to neuronal response and affects oxygen delivery and blood volume.

Fig.1 *Detail of neurovascular unit, A) Neurons and astrocytes are in close proximity and are functionally coupled to smooth muscle cells and endothelial cells.. B) Local and propagated microvascular responses following activation (adapted from Iadecola, 2004).*

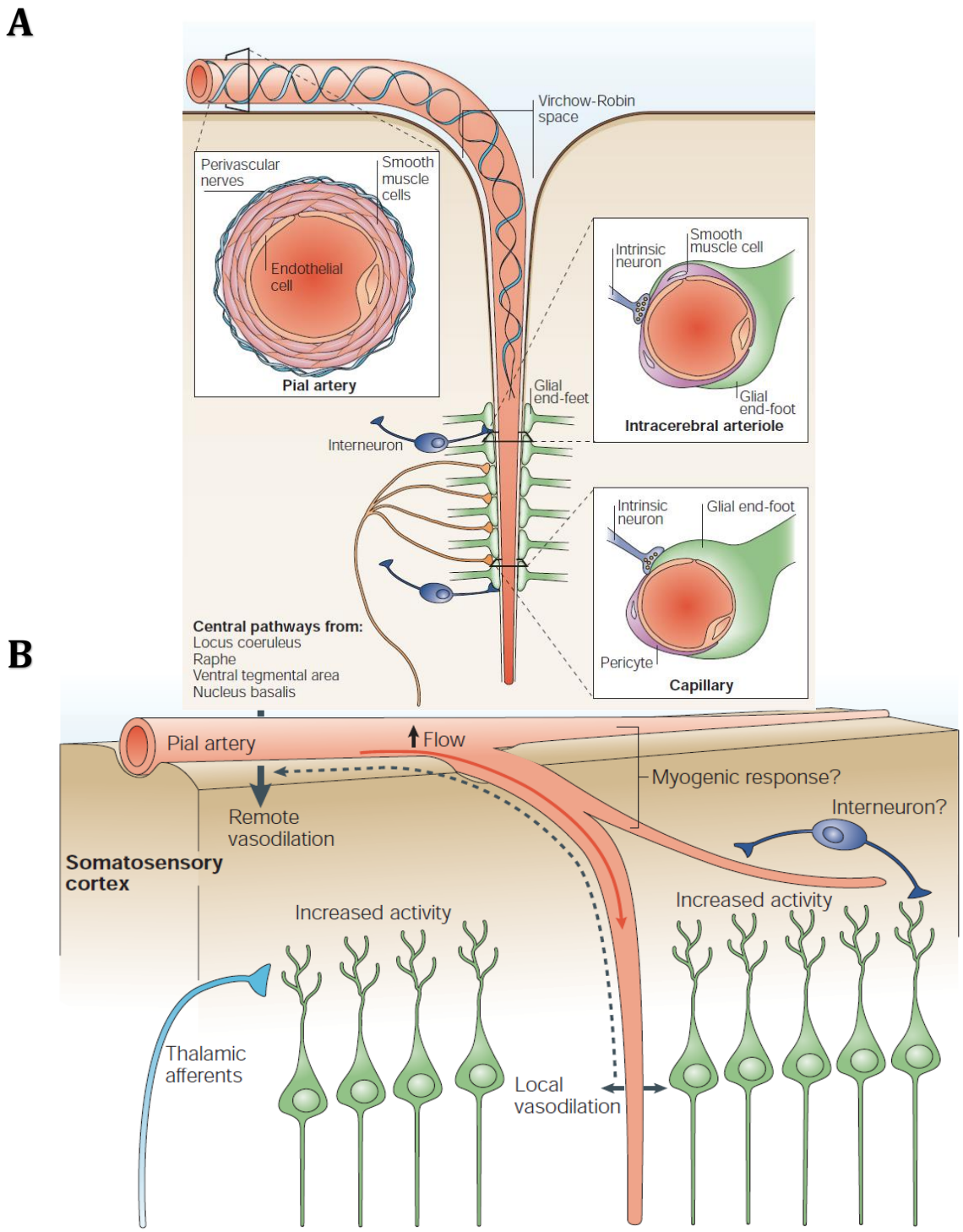

1.1.2.1 Astrocytes

Astrocytes used to be considered as passive elements and have a central position in the neurovascular coupling (Fig.2A). The astrocytes, as primary glucose-consuming cells for energy-generating, play a central role to convey neuronal signals to the blood vessels playing a crucial role in facilitating stimulus-evoked changes in cerebral blood flow (Attwell et al., 2010; Petzold and Murthy, 2011).

Synaptic activities may propel the release of components (e.g., glutamate, ATP, K+, Ca++…) that are detected by neighboring astrocytes that induced an upstream arteriolar vasodilatation effect. Calcium is an indispensable factor in the link between neural activation, inter-astrocyt communication, increased astrocyt glucose utilization, and vasodilation. ATP and glutamate also interact with receptors on astrocytes that result in an increase in the calcium waves, across many astrocytes, which ultimately reache astrocyt endfeet in contact with cerebral arterioles and finally propel vasodilation. The calcium waves provide stimulus for a variety of vasodilating pathways, such as an increase in arachidonic acid (AA) (Paulson et al., 2010). In addition the extracellular ATP can be rapidly converted to adenosine which also plays a key role in vasodilatation (Paulson et al., 2010). Another factor linked to inter-astrocytic communication and vasodilation is the changes in K+ ion flux and local production of prostanoids (Paulson et al., 2010).

Beside their general vasodilatory facilitating effect astrocytes might also elicited vasoconstriction depending on the oxygen supply (Gordon et al., 2008).

The immaturity of astrocytes is known (in size, number, branching and connectivity,) in the postnatal rat brain until postnatal day 21. In addition, the density of astrocytes does not reach the adult levels until postnatal day 50 (Seregi et al., 1987). Finally, astrocytes gap junction coupling is established only at postnatal day 11 in the rat visual cortex (Binmoller and Muller, 1992).

1.1.2.2 Pericytes

Pericytes have also been identified as essential contributors to regulate blood flow in the brain. Pericytes are related to vascular smooth muscle cells and vascular mural cells that are found on the outer surface of microvessel endothelium (Fig.2B) (capillaries, pre-capillary arterioles, and post-capillary venules) (Armulik et al., 2005). As pericytes are found at discrete locations along capillary vessels, their capability to induce localized vasoconstriction was

demonstrated (Peppiatt et al., 2006), but the functional role of pericytes in vivo may be limited (Fernandez-Klett et al., 2010). Pericytes are deeply involved in the structural patterning and the stabilization of the vasculature of the brain during angiogenesis, but the origin and function of pericytes in the human cerebral cortex are controversial (Fujimoto, 1995). The distribution of pericytes seem to decrease in adulthood, a situation that might be related to the maturation of the blood brain barrier. These developmental changes imply that pericytes might be not able to actively modulate capillary diameter during this dynamic period (Diaz-Flores et al., 1991).

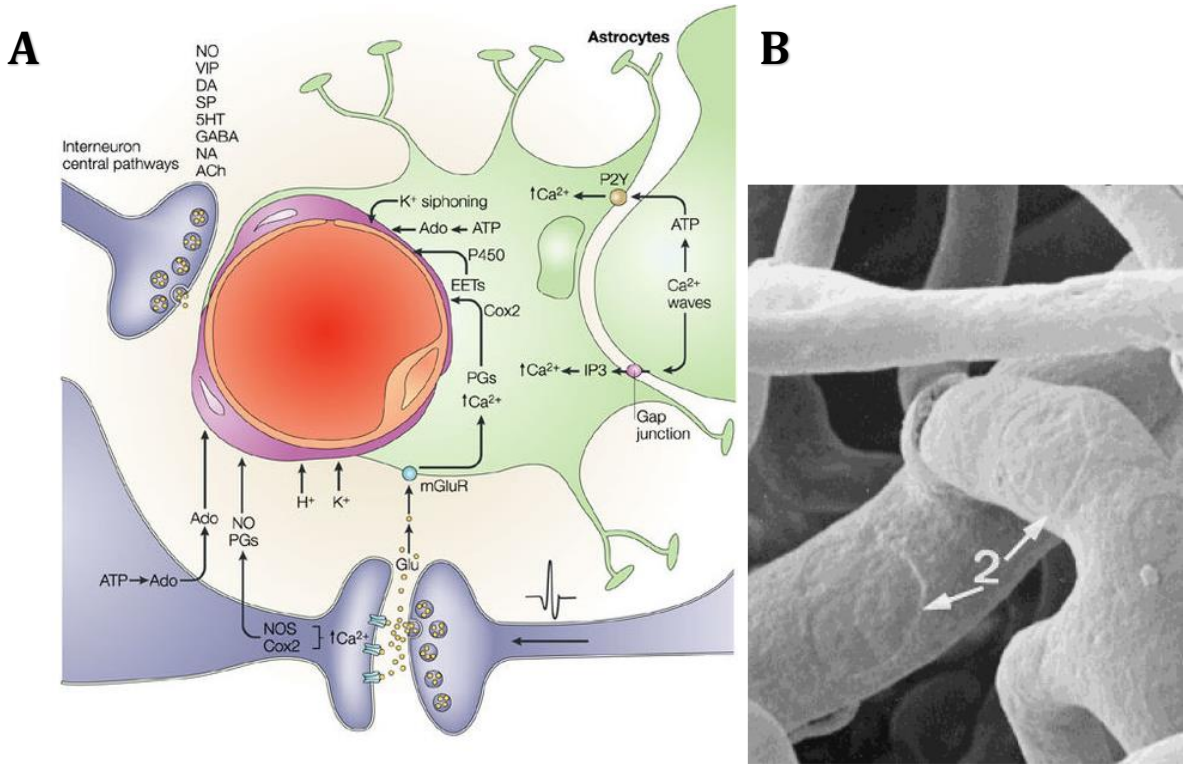

Fig.2 *A) Structural and molecular astrocytes connections within the neurovascular unit (Iadecola, 2004), B) The capillary network showed the structures around of pericytes (Reina-De La Torre et al., 1998).*

1.1.2.3 Endothelial cells

Whereas the longitudinal orientation of endothelial cells conducts signal along the length of vessels, the smooth muscle cells, are oriented perpendicularly to the endothelial cells, and are capable of actuating changes in vascular diameter by relaxing and contracting actions. Endothelial cells react to a variety of pharmacological substances such as acetylcholine (ACh) and adenosine (Ado), which cause endothelial cells to release the vasodilator nitric oxide (NO) that leads to relaxation of smooth muscle cells. Endothelium-independent vasodilator act on the biochemical pathways in smooth muscle cells instead, triggering a chain of reactions that lead to either relaxation or contraction (Ignarro et al., 1999).

1.1.2.4 Interneurons

Interneurons, which primarily use inhibitory neurotransmitters GABA and glycine, have also been demonstrated to elicit microvessel diameter changes. The large number of interneurons exhibiting complex morphology and connectivity, makes it difficult to fully understand their entire role in vascular response (Cauli et al., 2004). They might be involved in the neurogenic neurovascular coupling.

1.1.3 Mechanisms of neurovascular coupling

Neurons primarily function with high levels of aerobic mitochondrial metabolism, in addition they function via anaerobic glycolysis and net lactate extrusion. Under normal conditions, glucose and its oxidation are the main energy source producing a metabolic pathway for the brain (Siesjo, 1978). Since complete glucose oxidation has a stoichiometry of ($C_6H_{12}O_6 + 6O_2 \rightarrow 6CO_2 + 6H_2O$), the cerebral metabolic rate of oxygen consumption (CMRO2) is equal to six times the cerebral metabolic rate of glucose consumption (CMRglc). Glucose breakdown in the vicinity of oxygen releases about 36 mol of ATP per mole of glucose (in aerobic mechanisms), whereas in the absence of oxygen (in anaerobic mechanisms) glycolysis and glycogenolysis releases 1–2 mol ATP per mole of glucose. The required oxygen for the brain was carried by hemoglobin while glucose can be stored in the glia. Neuronal and glial activities have a tight correlation with their energy consumption. Since the brain's energy stock is not sizeable, CBF dynamics is essential for normal brain function by providing nutrients and removing waste. CBF helps for oxygen delivery and clearance of the products of metabolism. Cerebral tissues use about 20% of the body's oxygen via aerobic mechanisms. CBF controls the balance of metabolic demand to the oxygen supply, oxygen supply to the metabolic consumption and the metabolic consumption to product clearance.

Roy and Sherrington (1890) explained neurovascular coupling mechanism and the concept of a neurovascular unit, in this way; "the chemical products of cerebral metabolism contained in the walls of the arterioles can cause variations of the cerebral vessels: so its vascular supply can be varied locally in correspondence with local variations of functional activity." In the early 1960s, Lassen and Ingvar introduced a methodology to measure rCBF, and during the 1970s, it was more widely accepted that rCBF increases in response to cerebral activation (Lassen et al., 1978). In general, the oxygen or glucose consumption or an increase in CO2 would act as a metabolic signal which then triggered vasodilatation (Attwell et al., 2010;

Attwell and Laughlin, 2001). However, the other studies provided evidence against this hypothesis, showing that the underlying mechanisms responsible for increases in CBF upon neuronal activation are more complex (Mintun et al., 2001; Powers et al., 1996). A mismatch in CBF-metabolism coupling was reported by Fox and Raichle (Fox and Raichle, 1986), who described that, during neuronal activation, regional CBF increased without substantial increases in oxygen demand. In fact, CBF can increase in the absence of any significant variations of the cerebral metabolic rate of oxygen (CMRO2) (Fujita et al., 1999), and inversely, CMRO2 can increase with no significant increase of CBF (Okazawa and Vafaee, 2001). Whether or not a precise coupling exists between CBF and CMRO2 during neural stimulation has been the subject of numerous studies in both adults (Raichle, 1998) and preemies (Mahmoudzadeh et al., 2013b; Mahmoudzadeh et al., 2017b; Nourhashemi et al., 2017b; Nourhashemi et al., 2016c). The essential point is that although it may not be a relationship between the CBF-CMRO2 changes, there is a relationship between the CMRO2 - CMRglc changes given glucose oxidation maintained over a wide range of activity (Siesjo, 1978). With the limits of oxygen extraction, the cells switch to anaerobic metabolism. The recent evidence supports the functional attempt to accommodate the cerebral tissue's increased demand for glucose supply during neural activation with a crucial role of astrocytes in rCBF regulation (Paulson et al., 2010).

1.1.3.1 Local regulation of cerebral blood flow

A tight regulation of CBF is achieved through a complex interaction of functional brain mechanisms. In relation to Ohm's Law, pressure gradient and vascular resistance of the blood vessel are two inversely-related physiological factors affecting cerebral perfusion, (eq. 1). The pressure gradient is the difference between arterial blood pressure (ABP) and intracranial pressure (ICP) in which ICP is related to the pressure inside the skull and thus in the brain tissue and cerebrospinal fluid (CSF). Ohm's law analogy of cerebral blood flow regulation can be descriebed as follow:

$$\text{CBF} = (\text{arterial blood pressure} - \text{intracranial pressure}) / \text{vascular resistance} \quad (1)$$

Flow is assumed to be constant in this linear relationship, although flow is pulsatile in the macrovasculature, this linear relationship explains the general circulatory system (Rowell, 1993). The parameters in Equation (1) include local and systemic factors, local factors such as intracranial pressure and resistance, systemic factor such as arterial blood pressure. The arterial

blood pressure (ABP) changes are more dominant than the fluctuation in ICP (Hughson et al., 2001). Thus in the absence of cerebrovascular disease, ICP is assumed to be constant and equal to zero (Aaslid et al., 1989) and CBF changes is assumed to be more related to the changes in the vascular resistance. Poiseuille's law (Eq. 2) indicates that vascular resistance is a function of blood viscosity, vessel length, and vessel radius.

$$\text{Vascular resistance} = 8\eta \cdot L/\pi r^4 \quad (2)$$

Where η = viscosity, L = vessel length and r = vessel radius. The exponential influence of vessel radius indicates the complex local mechanisms that control vascular resistance and blood flow. The change in vascular diameters results from a combination of myogenic, neurogenic, and metabolic processes that regulate cerebrovascular resistance to maintain CBF (Paulson et al., 1990).

1.1.3.2 Myogenic regulation

The myogenic regulation relates to the apparent reflexive response of the vascular muscle of arteries to changes in blood pressure via stress sensing mechanism. This regulation is primarily due to inherent properties of the vascular smooth muscle cells to contract when they are stretched and conversely, via changing the concentration of intracellular calcium through the opening or closing of voltage-gated calcium channels (Harder et al., 2011). The regulation of vascular smooth muscle tone is complex. The vasodilatory and vasoconstricting mediators exert their effects by the level of calcium concentration (such as angiotensin II and norepinephrine result in an increase calcium, which activates myosin kinase) and/or by direct activation of the enzymes (such as arterial natriuretic peptide and nitric oxide activate myosin phosphatase and, by dephosphorylating myosin, cause vasoralaxation). Astrocytes dilate arterioles by acting on smooth muscle cells through many intermediates such as nitric oxide (NO) and/or prostaglandin (PG), epoxyeicosatrienoic acids (EET) or potassium release (Takano et al., 2006) and produce arachidonic acid (AA) that can act as a vasoconstrictor (Metea and Newman, 2006). KATP channels (adenosine triphosphate (ATP)-dependent potassium channel) are also involved in the regulation of the vascular tone (Landry and Oliver, 2001). Recent study suggest that pericytes surrounding capillaries may also participate to vasodilation even faster than SMC in response to neural activity (Hall et al., 2014).

1.1.3.3 Metabolic regulation

The metabolic regulatory mechanism refers to the relationship between local neural activity and cerebral perfusion (Park et al., 2007). The hypothesis of metabolic regulation assumes the balance between cerebral metabolism and oxygen delivery by CBF.

Action potentials associated with increased extracellular potassium levels that lead to depolarization of the neuronal membrane potentials can directly or indirectly influence vascular tone through alteration of endothelial (Filosa et al., 2006). The metabolites from dynamic processes including lactate and adenosine can directly influence vascular smooth muscle tone that seeks to balance CBF to demand (Liu et al., 2012). Metabolic regulation is a negative feedback control system that acts via a vasoactive substance.

1.1.3.4 Neurogenic regulation

The hypothesis of neurogenic regulation is about sympathetic innervation that controls the vessels resistance by the autonomic nervous system (Rowell, 1993). In contrast to both myogenic and metabolic, neurogenic regulation on CBF is likely restricted to the more extensive cerebral arteries. Larger arteries on the brain's surface are innervated by the sympathetic and the parasympathetic nervous system. Sympathetic nerves directly innervate the vascular smooth muscle through the release of norepinephrine and neuropeptide Y (Farkas and Luiten, 2001).

In addition neurogenic regulation is related to the effects of interneurons and neurons. Interneurons such as γ-Aminobutyric acid (GABA) and glutamate-mediated NVC have vasodilator effects on the microvasculature in cortical and subcortical regions (Cauli et al., 2004; Kocharyan et al., 2008), and the neurons mainly contribute to the large and rapid vasodilation during NVC (Lacroix et al., 2015).

Thus neurovascular coupling is a complex interaction between many parameters and the coupling phenomenon is not merely described as a direct relation.

1.1.3.5 Dynamic models of neurovascular coupling

Specific dynamic models are currently used for explaining empirical observations in terms of theoretical underlying mechanisms of NVC. These explanatory models are depicting the transient hemodynamic and oxygenation changes in activated cerebral areas. Since the

physiology of NVC (with a large number of unknown parameters) is not yet fully understood, it remains difficult to determine which dynamic model is actually useful for better interpretation of NVC. I explained the physiological assumptions of two common dynamic models; Balloon model and Windkessel model.

Balloon model: The balloon model incorporates the conflicting effects of dynamic changes in both blood oxygenation and blood volume in the presence of tight coupling of cerebral blood flow and oxygen metabolism throughout the activation period. In this model, it was assumed that there is no capillary recruitment and by considering the oxygen limitation, the blood volume changes occur primarily in the venous compartment. The arteriolar expansion that produces a flow increase is assumed to be a negligible change in blood volume. The vascular bed is then modelled as a dilatational venous compartment like a balloon. The volume flow rate into the tissue, as a driver of system, is defined as a function of time. The volume flow out of the system, is assumed to be dependent on the pressure in the venous compartment. As the physical picture of this model, after the arteriolar resistance is decreased, producing an increase in flow into the venous balloon, then the venous balloon swells, and the pressure increases until the flow into the balloon matches the flow out of balloon. The relationship between flow (F) and volume (V) in a compliant compartment in balloon model was defined: $\frac{dV}{dt} = F_{in}(t) - F_{out}(v)$, (Buxton et al., 1998).

Windkessel model: A physiologic model was proposed for the observed temporal mismatch between rCBF and rCBV. rCBF is determined by vasomotor control of arterioles, which produce about 70% of cerebral vascular resistance, but 80% to 85% of CBV is contained in capillaries and veins. The capillary and venous compliance was modelled in windkessel model to passively respond to pressure modulated by arteriole dilation and contraction. The relationship between flow and volume in a compliant compartment in this model was defined: $= \frac{\mathrm{V}}{\tau} + \frac{\mathrm{dV}}{\mathrm{dt}}$, where **τ** is the transit time for a volume element and dV/dt is the rate of volume change. At steady state, where dV/dt= 0, the changes in flow is equal to V/**τ** as the central volume principle. Alternatively, F and V/**τ** may represent flow into and out of an arbitrary compartment, this equation is then conservation of mass as described by the balloon model $F_{in} - F_{out} = \frac{dV}{dt}$ (Mandeville et al., 1999).

1.1.4 Cerebral autoregulation

Cerebral autoregulation (CA) (Lassen, 1959), refers to the physiological mechanisms that maintain CBF at an appropriate level during changes in ABP. It is functional for perfusion pressures between 60 and 150 mmHg (Paulson et al., 1990; van Beek et al., 2008). Autoregulation is independent of endothelial function, but is endogenous to all vascular smooth muscle cells as an intrinsic myogenic reflex. These mechanisms provide the main protection to the brain when the pressure increases or decreases (Lassen, 1985). Outside this range of pressures, a cerebral blood flow pressure-passivity occurs, results in changes in CBF that track changes in MAP. The myogenic mechanism is thought to contribute as a primary mechanism of the cerebral autoregulation process, in vitro (Harder et al., 2011) and in vivo (White et al., 2000). Other studies demonstrate the subsidiary role of surrounding tissues including the endothelium, neuronal glia and/or autonomic nervous system.

There is a linear relationship between the changes in CBF, CMRO2, and CBV under normal conditions. To assess cerebral autoregulation the correlation between cerebral perfusion pressure (CPP) and CBF should be examined, here CPP is the difference between the mean-arterial pressure (MAP) and the intracranial pressure (ICP). When cerebral perfusion pressure (CPP) decreases below the limit of autoregulation, the CBF also falls, but CMRO2 remains the same temporarily. This condition is considered as “misery perfusion” where cerebral autoregulatory capacity is exhausted, and cerebral blood supply is insufficient to meet metabolic demand. This "misery perfusion" results in a focal increase in the oxygen extraction fraction (OEF) up to the maximum value and leads to sustain brain's oxygen despite decreased CBF. Extra drops in CPP lead to ischemia and impaired neuronal function (Sette et al., 1989). Ischemic damage can be potentially reversible, or irreversible depending on CBF and CMRO2 threshold values (Baron JC, 1987). In adult, gray matter generally progresses to infarction if CMRO2 reach values below 1.3-1.5 mll.l00 g/min during more than 2-6 hours after a stroke. If CMRO2 is maintained above these values, tissue can be salvageable, consistent with the concept of potentially reversible ischemia. If oxygen supply is more than demand, a reduction of the OEF can be observed, which supposed that perfusion had been re-established (Ackerman RH, 1989; Powers et al., 1985).

When blood flow is failing, there are several lines of defensive mechanisms against oxygen insufficiency and thus tissue damage. First, when blood pressure drops, autoregulation of CBF

will decrease vascular resistance to maintain blood flow almost unchanged (in newborn, the conduit arteries are very reactive and have a more critical contribution to the vascular resistance). If the blood pressure falls toward the lower limit of autoregulation, or in impaired autoregulation due to the pathology or immaturity, CBF decrease. Then oxygen extraction increases up to 50-60% (typical oxygen extraction is about 30%). When the limits of this compensation of oxygen extraction have been reached (up to 50-60%), the cells switch to anaerobic metabolism –increase glucose consumption to produce lactate. Insufficient oxygen or decreased oxygen consumption lead to a loss of metabolic function and cellular death (Fig.3). In newborn infants, "hypoxic hypometabolism" is a mechanism that can be partially protected against hypoxic-ischemic injury (Greisen, 2012).

In autoregulation mechanism arterial smooth muscle tone is affected by different factors such as hypoxia, PCO2, changes in pH, local production of adenosine, ATP and NO, and other local neural mechanisms.

1.1.4.1 Autoregulation and hypoxia

Hypoxia induces tissue lactic acidosis and affects the entire endothelial function and the local nitric oxide (NO) production. Hypoxia decreases smooth muscle membrane potential by affecting the calcium-activated and ATP-sensitive K+ channels in the cell membrane. In the immature brain, adenosine is another factor that affects the vascular response to hypoxia. Since the membrane potential response to hypoxia is independent of the pressure, at lower pressures and in a hypotensive neonate, a superimposed hypoxic event cannot compensated this low perfusion pressure, thus leading to hypoxia-ischemia (Greisen, 2012).

1.1.4.2 Autoregulation and PCO2

Arteries and arterioles constrict with hypocapnia and dilate with hypercapnia. This reaction is mediated through changes in pH, which affect outward K+ current (in arterial smooth muscle cells) and calcium channels (Greisen, 2012).

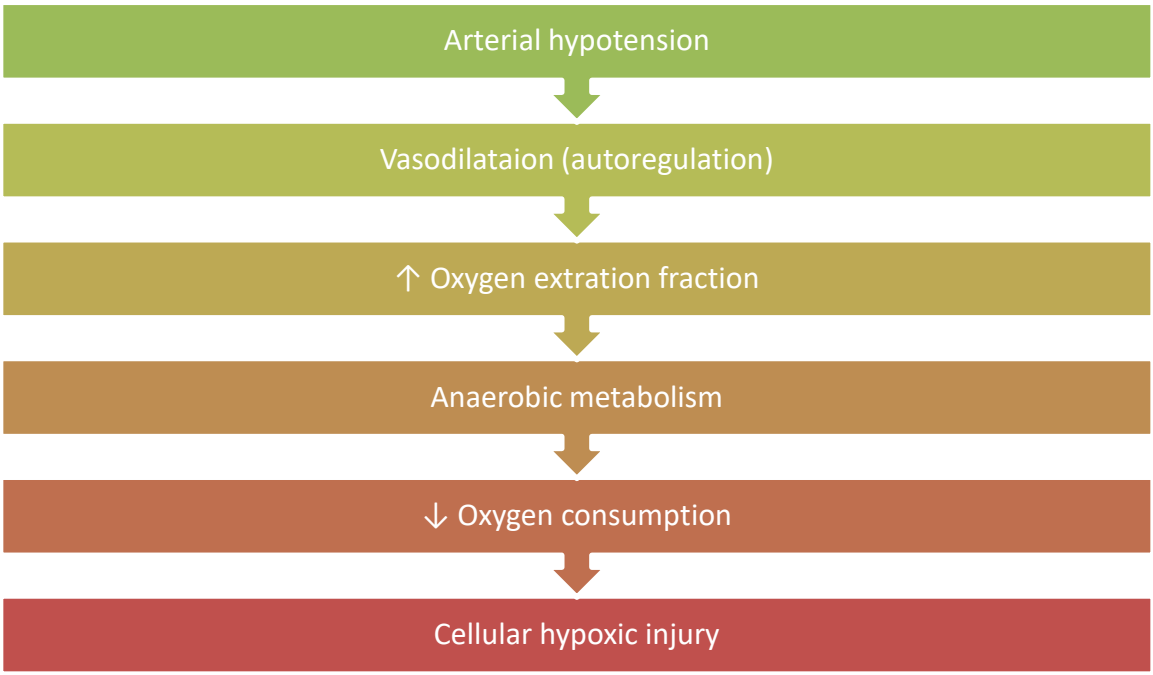

Fig.3 *The lines of defense against oxygen insufficiency, modified from: (Greisen, 2012).*

1.1.4.3 Autoregulation in the immature brain

Regulation of blood flow depends on many parameters in neonates. Recruitment of capillaries and extraction of oxygen plays a fundamental role in CBF regulation as well as other systemic factors like blood pressure, cardiac output, central venous pressure, systemic vascular resistance, partial pressure of oxygen and carbon dioxide in the arteries, postnatal and gestational age and patent ductus arteriosus (PDA).

There is less vasodilator reserve in the pressure-flow autoregulation in the immature cerebral vasculature, which restrains the efficacy of CBF autoregulation at earlier stages of development. Some studies of autoregulation in stable neonates without evidence of major brain injury suggest that autoregulation is intact (Greisen and Trojaborg, 1987). In contrast, evidence of absence autoregulation has been found under pathologic conditions such as birth asphyxia and in preterm infants with brain injury (Milligan, 1980). It was shown that the lower threshold of blood pressure for CBF autoregulation might be about 30 mmHg or below in premature neonates. Moreover, autoregulation can be assumed to be operate in most newborn infants, even the most immature. In neonates a significant blood flow can be present until the blood pressure is less than 20 mmHg (Greisen and Trojaborg, 1987).

1.1.5 Neuronal network development

In this section, a summary of the essential characteristics of the cerebral electrical activity of the premature and full-term newborn according to conceptional age (CA) will be presented.

Spontaneous electrocerebral activity in premature newborn infants –especially during the last trimester– evolves more rapidly than at any other time during human life. The rapid enlargement of the brain takes place from 28 weeks to 40 weeks CA. Its appearance changes take place before 24 weeks when the surfaces of the cerebral hemispheres are smooth, to 28 weeks when the major sulci have appeared and continue to develop. Rapid maturational changes are also apparent in the neurochemical milieu; in interneuronal connectivity, in dendritic trees and synaptogenesis; and in the myelination of axons. Despite maturational changes in anatomy, progress in brain's function is rather extensive. The premature infant of 28 weeks CA is capable of motor activity, vigorous crying, and response to syllables stimulation (Mahmoudzadeh et al., 2013b). The appearance and disappearance of specific electroencephalographic features for a given age are related to the transient activation of underlying neural networks. Such the temporal theta activities of immaturity are present before 23 weeks CA and disappear around 30 weeks CA in quiet sleep (Lamblin et al., 1999).

The cerebral activity of the premature newborn is composed of bursts containing specific patterns such as theta bursts, delta brushes, sharp frontal transients and rhythmic frontal delta activity. The characteristics of these activities are presented in the following figure (Fig.4). The delta brushes consist of a slow wave (delta) associated with fast rhythms (the brushes) which suggests the synchronization or coalescence of two generators. These elements disappear simultaneously by decreasing amplitude gradually as the premature infant approaches term. Neither the structure of these generators, nor the neural network, nor their distribution, nor the neurochemical mechanisms, nor their roles have been yet elucidated. The following figure summarizes the various EEG change as the premature infant matures to term.

Interhemispheric synchrony of cerebral bursts of activity during discontinuous portions of the EEG recording is another character of the premature neonatal brain. The degree of interhemispheric synchrony in the very young premature infant (younger than 29 weeks CA) is high around 90 to 100 percent, but it decreases to 60 to 80 percent from 30 to 35 weeks CA and gradually approaches 100 percent as the infant reaches term (Hahn, 2012).

The EEG patterns of the newborn are also dependent on the behavioral states during the recording that includes active (rapid eye movement or REM) and quiet (non-REM) sleep. EEG should be recorded in both sleep states since abnormalities may be found only in one sleep state (Hahn, 2012).

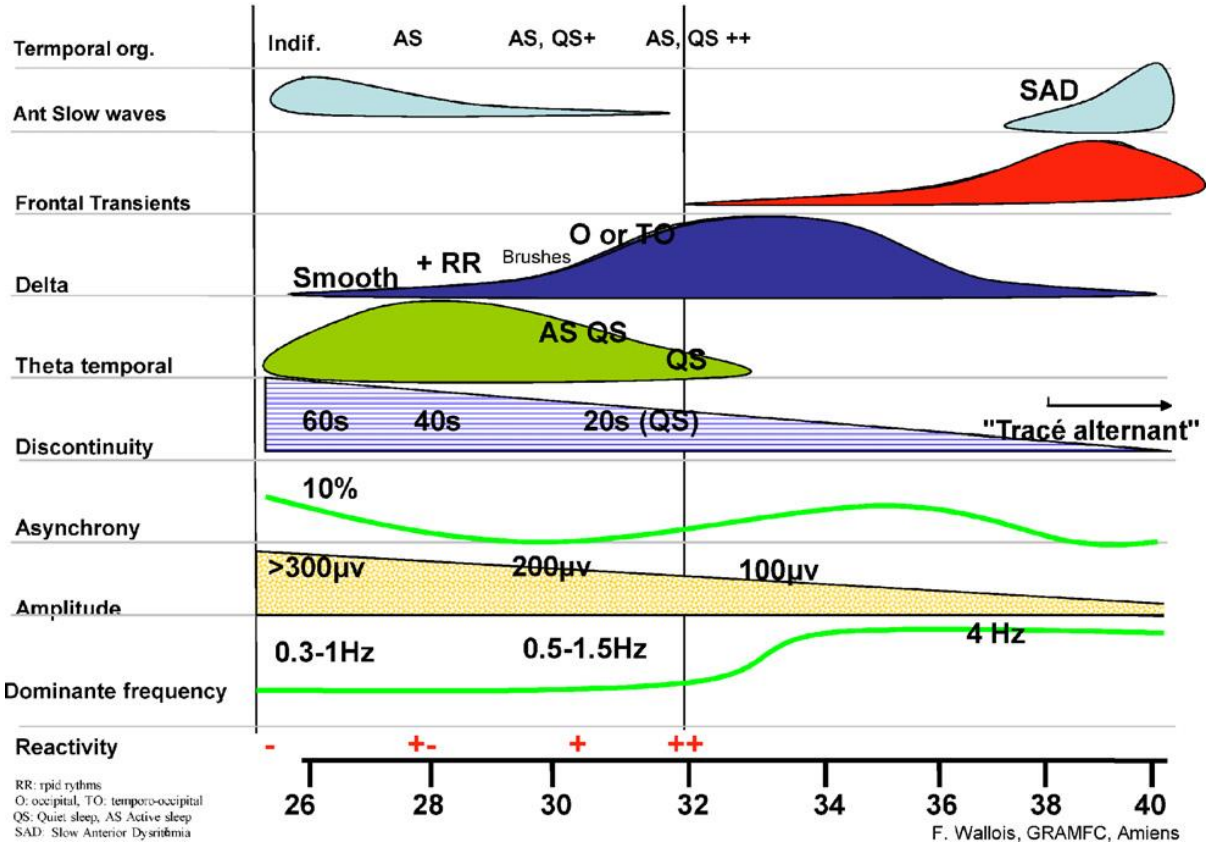

Fig.4 *Synopsis of maturation of specific features in EEG of premature neonates (Wallois, 2010).*

1.1.5.1 The development of the subplate and thalamocortical connections in neonatal brain

By 5–6 wGA, neuroblasts, or neuronal precursors, are proliferating rapidly within the ventricular zone (de Graaf-Peters and Hadders-Algra, 2006). The radial and tangential neuronal migrations continue to be completed. The disturbances of this migration could explain the disorders observed at the 25th wGA in the periventricular zone which will affect brain development. Cortical connectivity is set up corresponding to the growth of axons and dendrites and will be influenced by surrounding neuronal and synaptic activity (Le Bé and Markram, 2006).

As early as 9-11 wGA, and before maturation of the brain connections, a transitional structure is set up called "*subplate"* (Fig.5). This sub-plate is located under the cortical plate which is four times thicker than the cortical plate. It consists of well-differentiated post-migratory neurons, migrating neurons, glial cells and especially thalamocortical axons "waiting" before they penetrate to the cortical plate. It contains pre-synaptic elements, synapses, and postsynaptic elements. This contrasts with the cortical plate that does not contain synapses during this developmental period. At this time, the subplate is an essential site of synaptic interaction (Tau and Peterson, 2010). In addition, it receives information conveyed by the thalamocortical fibers capable of activating the subplate in response to peripheral sensory stimulation. When the electrical activity of subplate neurons is recorded from cerebral fetal tissues (20-21 wGA), several types of activity have been identified (Moore et al., 2011). These activities are recorded in vitro from brain slices even at 20 wGA, while functional synaptic contacts at the cortical level are still scarce. This suggests that subplate neurons play a crucial role in the activities recorded in EEG. Thus, the generation of a discontinuous activity could be an intrinsic property of the subplate neurons.

Before 26 weeks GA, thalamocortical afferents accumulate in the subplate without penetrating to the cortical plate. They establish connections with the neurons of the subplate, which constitutes the emergence of the first neural networks with the appearance of a spontaneous endogenous activity. Between 28 and 30 weeks, the thalamocortical afferents invade the cortical plate where they establish the first synapses with the final cortical neurons. The subplate that already processed the information from the thalamus would play an essential role in providing a thalamic, sensory influence in the development of neural circuits of the cortical plate (Kanold and Luhmann, 2010).

Between 31 and 33 weeks of GA, the thalamocortical axons establish synapses with the neurons of the layer IV and have their activity which begins to be modulated by the sensory afferents. In parallel with this cortical synaptogenesis, the theta temporal activities on the EEG tend to disappear and to be replaced by slow waves surmounted by fast rhythms: the delta-brushes. It is interesting to note that these delta-brushes were recently considered as neurobiomarkers of sensory synaptogenesis in the somaesthetic and visual modalities without demonstrating that subplate is involved (Colonnese et al., 2010). This period is marked by a revival of inter-hemispheric asynchrony.

During the period from 28 wGA up to 33-34 wGA maximum, pathological elements, specific to periventricular leukomalacia, called positive rolandic spikes may appear. These are slow, high amplitude waves that share specific shape features with theta temporal activities (Laura paper 2017). In addition to their morphological characteristics, these pathological elements provide additional arguments on the role of the subplate in the activities recorded in EEG. Indeed, the source localization of these activities is related to an activation of structures located under the cortical plate that could very well correspond to the subplate and the usual locations of white matter lesions of periventricular leukomalacia (Sarnat and Flores-Sarnat, 2002).

Between 34 and 37 weeks of GA, the subplate disappears, the neurons of the subplate join the layer VI or die by apoptosis. This period is dominated by the growth of inter-hemispheric connections. At the same time, inter-hemispheric synchronization are taking place. The EEG inter-hemispheric asynchrony disappears, the amplitude of the delta-brushes decreases. The rolandic positive spikes of periventricular leukomalacia are no longer recorded by EEG.

Thus in the age group 28-32 wGA, we can observe the initiation of the functional and sensory connectivity of the cortical plate. Nevertheless, the subplate is the most active structure in preterms and could participate in the recorded brain activity on the surface of the scalp. The subplate could also participate in the development of the functional organization of neural networks of the cortical plate. It could participate in the guidance of neuronal axons of cortical layers V and VI, as well as in inter-hemispheric synchronization. We are thus in a situation of two networks operating in parallel: *subplate* and *cortical plate*, both of which receive sensory information and have synaptic substances capable of interacting with each other and producing signals recorded on the surface of the scalp.

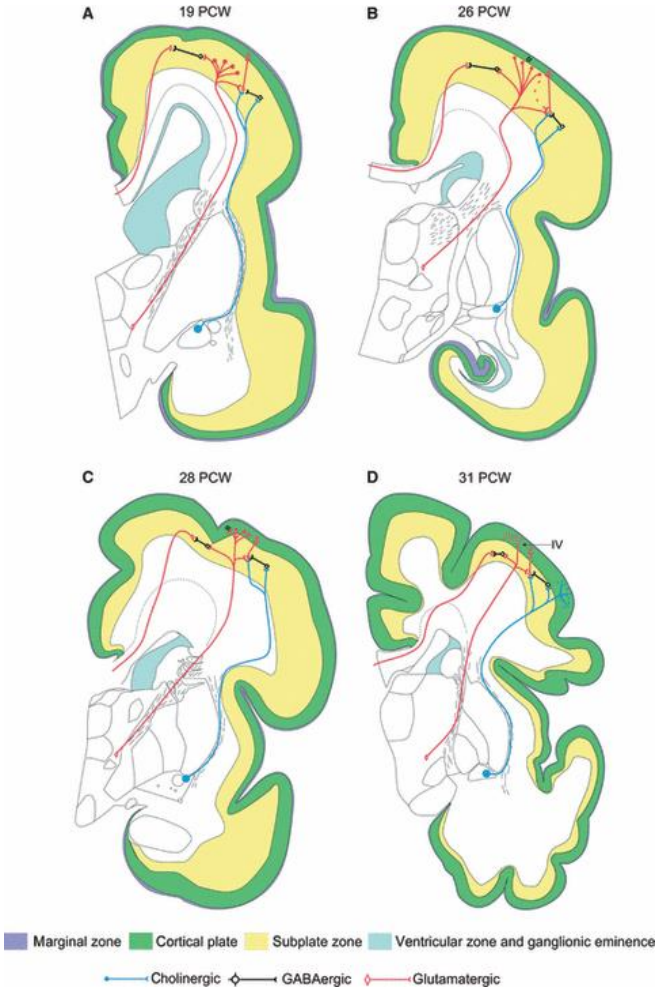

Fig.5 *The organization of afferent systems and transient cortical circuitry in preterm infants. (A); the accumulation of afferents in the superficial subplate (i.e. below the cortical plate) in very early preterm (22–23 postconceptional weeks). (B); the penetration of afferents into the cortical plate after 24 postconceptional weeks (C); intra-cortical elaboration of thalamocortical fibers after 29 postconceptional weeks (D). All major pathways 'cross' vulnerable periventricular zone. Note that afferent axons and cells in the subplate zone are involved in all stages of circuitry development and reorganization. Laminar shifts of thalamocortical and basal forebrain afferents together with the laminar development of synapses in the cortical plate cause changes in cortical electric responses (Kostovic and Judas, 2010).*

1.1.5.2 Burst of activities

One of the essential characteristics of the newborn's cerebral activity (especially in the premature infants) is the discontinuity (Fig.6). These specific EEG patterns serve as useful markers for determining the CA of the infant's nervous system.

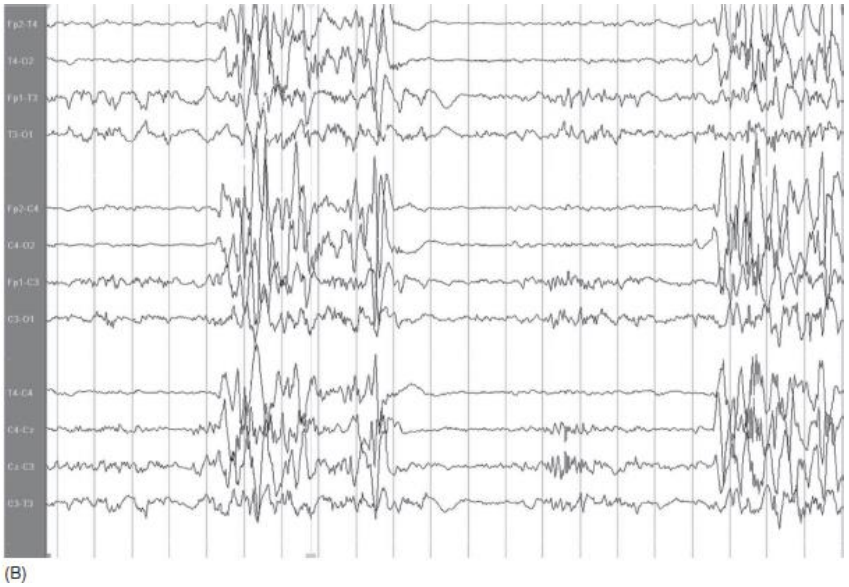

Fig.6 *Burst of activities pattern during sleep, the background is discontinuous with excessive discontinuity more prominent over the right hemisphere*[1].

The mean duration of this discontinuity (interburst intervals) in the healthy premature infant decreases with increasing gestational age; the mean IBI at 27 to 29 wCA is approximately 6 seconds, and at 30 to 34 wCA is approximately 4 to 5 seconds. The maximum IBI should not exceed approximately 30 seconds at any age and ay any sleep stage beyond 27 wCA (Hayakawa et al., 2001; Selton et al., 2000). The excessive discontinuity can be considered as a neuorobiomarker of cerebral disorder, so the time dimension must be taken into account. This discontinuity suggests complex maturation processes that play an essential role in endogenous brain oscillators. The patterns of EEG burst of activities can be specified based on age in the preterm infant (Fig.7, Fig.8).

At 23 to 26 wCA, bursts can be longer and IBI shorter. Biagioni et al. (Biagioni et al., 2000) found that the maximum IBI duration ranged between 20 - 62 seconds and the minimum burst length was 1 - 2 seconds, while, Hayakawa et al. found the maximum IBI duration about 87 seconds at 23-24 w CA and 44 seconds at 25-26 wCA (Hayakawa et al., 2001).

At 27 to 29 wCA, the maximum IBI are generally less than 30 seconds and there may be EEG differentiation of active sleep (REMs are observed with a burst of slow waves admixed

[1]http://www.demosmedical.com/media/samplechapters/9781620700457/mobile/9781620700457_Chapter1.html

with theta activity) and quiet sleep states (REMs are absent, and the background becomes more discontinuous) (Selton et al., 2000).

At 30 to 32 wCA, discontinuous background composed of an admixture of the occipital delta, theta, and alpha range activity occurs in quiet sleep. More continuous background occurs in active sleep (Hahn, 2012).

At 33 to 35 wCA, discontinuous activity is associated with quiet sleep, and continuous background occurred in active sleep.

At 36 to 38 wCA, discontinuous pattern separated by low to medium amplitude background represents quiet sleep.

At 38 to 42 wCA, sleep, and waking cycles are well established (Hahn, 2012).

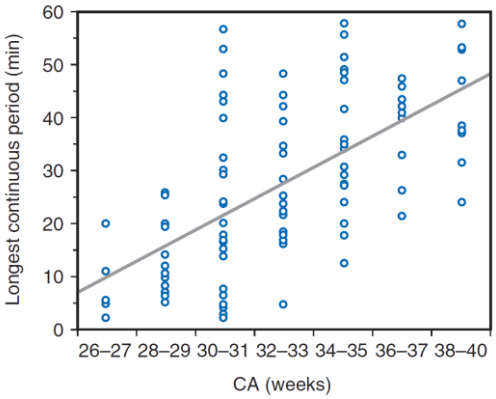

Fig.7 *Longest continuous period of cerebral activity at various conceptional ages (CAs). Image source: (Hahn JS et al., 1989).*

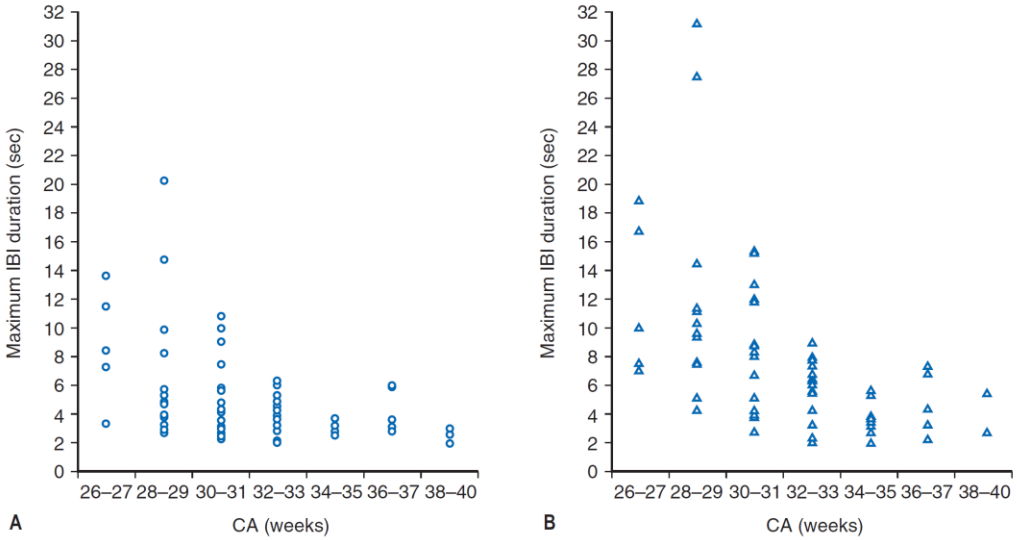

Fig.8 *The maximum interburst interval (IBI) versus conceptional age (CA). A, For type 1 IBIs (intervals of at least 2 seconds containing no cerebral activity greater than 15 mV in any channel). B, For type 2 IBIs (similar to type 1 IBIs, except for a transient lasting less than 2 sec in one or two electrodes or continuous cerebral activity greater than 15 mV in one electrode) (Hahn JS, et al. 1989).*

1.1.6 Vascular network development

Parallel to the maturation of brain structures and neural networks, there is a maturation of the vascular system in newborns. At birth, there is an increase in vascular volume and approximately 30% decrease in the distance between any point of the brain tissue and the nearest vessel (Risser et al., 2009). Different studies suggest that vascular proliferation may be partly related to metabolic demand and structures requiring increased energy demand (Weber et al., 2008). Some studies in preterm infants demonstrated that functional small vessel density changes over the first postnatal month and directly correlates with hemoglobin concentration and environmental temperature. In the neonatal brain, vascular density growth is rapid between 26 and 35 wGA and continues beyond 36 weeks (Miyawaki et al., 1998). From the 28th to the 32nd wGA, the irrigation of the CBF decreases in the germinal zone in favor of the cortex. The arteries increase in size to irrigate the white substance, and small cortical arteries appear to irrigate the gray matter (Saliba, 2003). Before 30th wGA, the vessels are still immature, and the immaturity prevents them from participating in the regulation of CBF and makes them vulnerable to sudden changes in intraluminal pressure. Also it was reported, the aminergic systems which release the transmitters as vasoconstrictors for the maintenance of resting vascular tone, expand postnatally (Goldman-Rakic and Brown, 1982).

In neonates, the highest glucose uptake was observed in the sensorimotor cortex, with low functional activity over of the other regions. Increased glucose uptake in the parietal, temporal and primary visual cortices were observed during the second and third months of neonatal life, coinciding with improvements in motor, auditory and visual skills (Albers and Grieve, 2007; Ferry, 1987) in addition to changes in the neonatal EEG (Kellaway, 2003). Moreover, similar developmental dynamics have been observed in CBF (Altman et al., 1988; Tokumaru et al., 1999). Increasing in regional myelination is accompanied by increases in glucose uptake and CBF (Peterson et al., 2003), accompanying with the augmentation of energy demand and cerebral activity in myelinated regions. CMRO2 was reported higher in term neonates compared to premature neonates (Elwell et al., 2005; Skov et al., 1993; Yoxall and Weindling, 1998). The reaction of CBF to acute changes in CO2 would be strongly attenuated in the

preterm infants supported by mechanical ventilation for about the first 24 hours of life, for reasons which are not explicitly established (Pryds et al., 1989).

During the first six weeks of life whatever the GA, Labarbe et al. show (i) a constant decrease in SO2 due to the decrease in hemoglobin (HGB) while CBV remains stable, and (ii) a constant increase in CBF to maintain appropriate brain oxygenation despite the HGB decrease (Roche-Labarbe et al., 2010). Lin et al. show that hemodynamic (CBV, CBFi, and SO2) and metabolic (CMRO2i) parameters were higher in the temporal and parietal regions than in the frontal region and that these differences increased with postmenstrual age (PMA). Also, all these parameters were significantly higher in the right hemisphere than in the left (Lin et al., 2013b). Labarbe et al. show that cerebral hemoglobin oxygenation (SO2) is not correlated with postmenstrual age (PMA) but varies with chronological age and HGB; suggesting that SO2 depends on systemic changes whereas CBF and rCMRO2 correlate better with PMA. CBF and rCMRO2 are more accurate biomarkers of the brain development than SO2 in the premature newborns (Roche-Labarbe et al., 2012).

Since the density of neuronal and vascular networks and also the neurovascular coupling itself are not as mature in the preemies as in the adult, the responses to neuronal activation may have different hemodynamic characteristics depending on age (Harris et al., 2011).

1.1.6.1 Cerebral hemodynamic response in developmental brain

It is commonly accepted the hypothesis that regional brain activation is accompanied by increases in CBF and CMRO2. As the increase in rCBF exceeds the increase in rCMRO2, this results in a decrease in the HbR in venous blood and increases in HbO (Fig .9). Several studies (Hoshi and Tamura, 1993; Kato et al., 1993; Kleinschmidt et al., 1996) have shown either an absence of HbT variation with an increase in HbO/decrease in HbR, or an increase/absence of HbR accompanying HbT and HbO increases. Besides, the initial dip may correspond to an increase in HbR due to a mismatch between CMRO2 and CBF (Kim and Kim, 2011), or increases in CBV (Buxton et al., 1998).

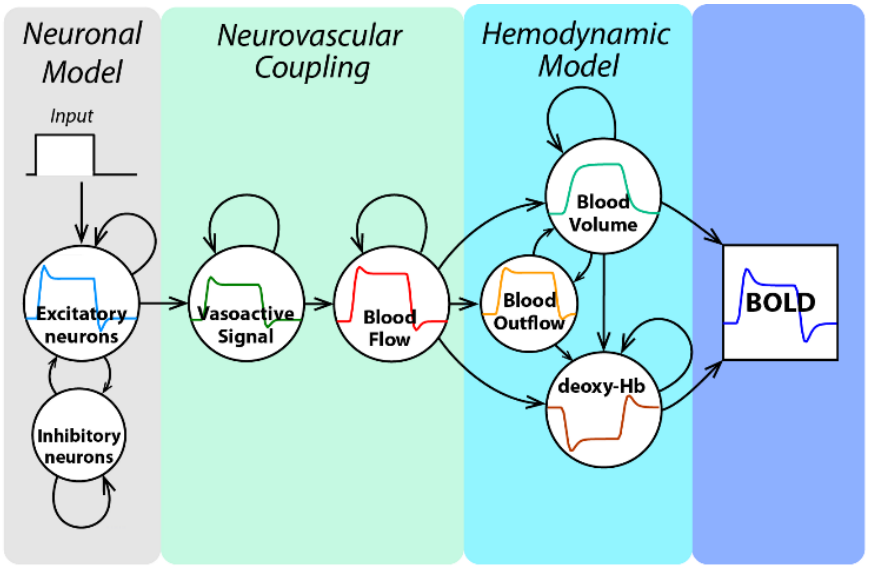

Fig.9 *Schematic illustration of physiological variables and their interactions in FMRI.*

Both negative and positive hemodynamic responses to stimulation have been observed in the developing human brain using NIRS as well as fMRI BOLD responses. An increase in HbT, HbR, and HbO suggest insufficient hyperemia to meet oxygen demands (Fig. 10B). Further, a decrease in HbT and HbO with an HbR increase, suggest that the local vasoconstriction reinforce HbR increases (Fig. 10C).

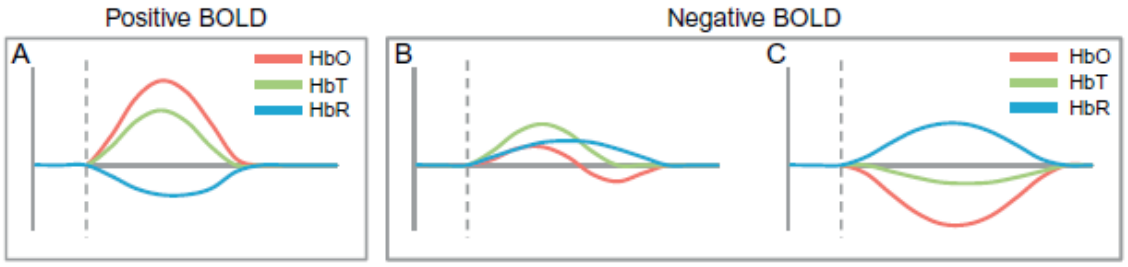

Fig.10 *Diagrams of different types of hemodynamic response to stimulus reported in the developing human brain. (A) Hemodynamic response with an increase in oxygenated (HbO) and total hemoglobin (HbT) and a corresponding decrease in deoxygenated hemoglobin (HbR). (Positive BOLD in fMRI). B and C are negative BOLD in fMRI. (B) The pattern suggests that functional hyperemia is insufficient to meet oxygen demands of the tissue, resulting in an increase in HbT, HbO, and HbR. (C) A decrease in HbT accompanies an increase in HbR suggesting vasoconstriction amplifying increases in HbR (M. Kozberg, 2016).*

fNIRS reflects Hb oxygenation in arterioles, capillaries, and venules because fNIRS is more sensitive to small vessels since light is almost entirely absorbed by large vessels (Mancini et al., 1994). Although there is no precise vascular specificity of fNIRS, one argument is that fNIRS signals particularly corresponds to capillary oxygenation (Rasmussen et al., 2007).

Alternatively another argument is that fNIRS corresponds to venous, capillary, and arterial blood within the sampling volume (Murkin and Arango, 2009) (Fig.11). Different studies of the developing brain indicated differences in postnatal brain hemodynamic responses compared to the adult brain as it was shown in (Fig.12) (M. Kozberg, 2016). The newborn brain was observed to have a lower baseline synaptic and vascular density, a lower CBF and CMRO2, which increases to adolescence rates by increasing age. These values then decline to adulthood values by the late teenage years. But capilary density increas after childhood (Fig.12).

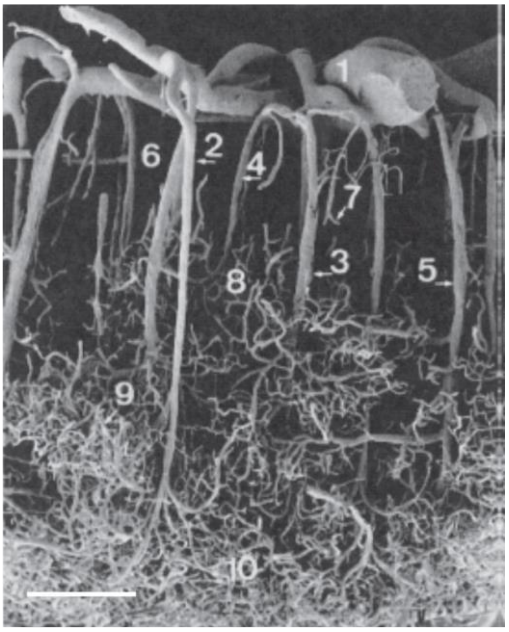

Fig.11 *Vascular structure in the human temporal cortex obtained by vascular casting and electron scanning microscopy. 1, pial artery; 2, long cortical artery; 3, middle cortical artery; 4, short cortical artery; 5, cortical vein; 6, subpial zone; 7, precapillary vessels with blind endings; 8, superficial capillary zone; 9, middle capillary zone; 10, deep capillary zone. Scale bar=375um (Reina-De La Torre et al., 1998).*

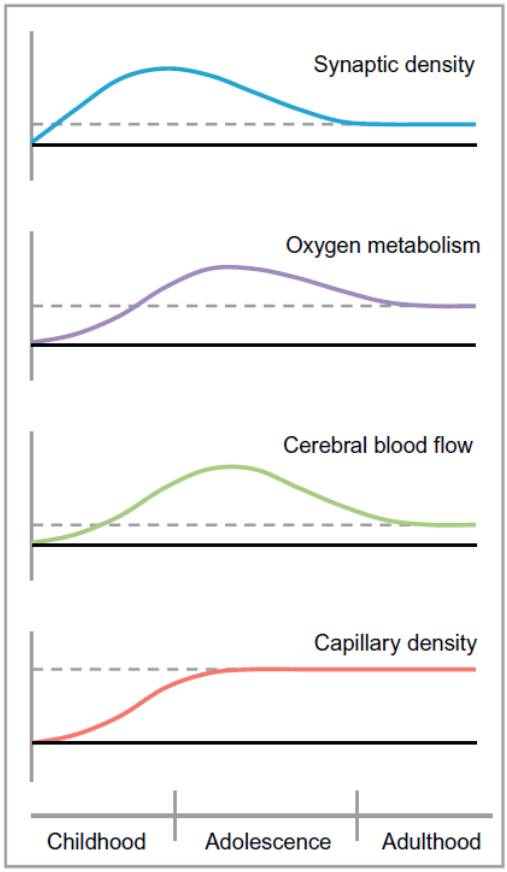

Fig.12 *Developmental changes in neural and vascular density, oxygen metabolism, and cerebral blood flow (M. Kozberg, 2016).*

1.1.6.2 Neurovascular coupling in resting state

Much of what we currently know about brain function and neurovascular coupling have been derived from studies using external stimulus. In recent years, another rapidly growing approach called *resting-state* is being used to understand the neuronal and vascular function of the brain in the absence of an externally provoked task (Fox and Raichle, 2007; Power et al., 2014). The goal of a resting state study is to evaluate spontaneous brain activity without presenting any external task or stimuli, i.e., measuring brain activity at "rest". The initial studies of the spontaneous brain activity were met with doubt, as it was suspected that this signal was driven by noise and was not explicitly organized as it is in response to tasks. In 1995, Biswal and colleagues were the first group that showed spontaneous hemodynamic fluctuations in the absence of a task, occurring in the same brain regions that were active during finger tapping (Biswal et al., 1995). Other groups have been worked on resting state in other brain regions as

well (Cordes et al., 2000; Hampson et al., 2002; Lowe et al., 1998; Stein et al., 2000; Xiong et al., 1999).

Using combined fNIRS-EEG, Hoshi et al. (Hoshi et al., 1998) demonstrated that the changes in HbO in the frontal and occipital regions during a 15-min resting period in healthy adult brains could correspond to brain activities.

Relatively recent findings in premises, at rest, performed in our laboratory, show that there is a correlation between EEG discontinuity of prematurity and cerebral metabolic activity in resting-state (Roche-Labarbe et al., 2007a). The results suggest that the interactions between the two neuronal and vascular networks are likely to participate in the modulation of the cerebrovascular activity.

1.1.7 Cardiovascular development

Fetal circulation is characterized by low systemic vascular resistance with high systemic blood flow and high pulmonary vascular resistance with low pulmonary blood flow. Given the low oxygen tension in the fetus, fetal circulation with the placenta helps to provide more oxygenated blood to the vital organs. The arterial canal (ductus arteriosus) is a vessel that connects the left pulmonary artery with the descending aorta in the fetus. The foramen ovale is a small hole located in the wall between the two upper chambers of the heart. The most of the right ventricular output is passed through the patent ductus arteriosus (PDA) to the systemic circulation. The pulmonary blood flow constitutes 11-25% of the combined cardiac output that supplies blood to the lungs with the peak around 30 wGA. The systemic blood flow depends on the connections between the systemic and pulmonary circuits via the foramen ovale and PDA during fetal life (Mielke and Benda, 2001).

1.1.7.1 Transitional physiology

At birth, the systemic vascular resistance increases due to the removal of low resistance placental circulation and the increase in catecholamines and other hormones. The pulmonary vascular resistance and CBF decrease due to the act of breathing air and pressure of oxygen. A drop in CBF in the first few minutes after birth in normal term neonates was also reported (Noori et al., 2012b). This decrease in CBF was due to the increase in arterial blood oxygen, a possible role of PDA and the inability of the immature myocardium to pump against the suddenly increased systemic vascular resistance (Noori et al., 2012b).

After birth, in term infants, PDA will be closed and the circulation changes from parallel to series. However in very preterm infants, due to the inability of the ductus arteriosus to close, the left and right ventricular outputs could not become equal. Due to the persistence of the PDA, the hemodynamics significantly alters during the transition.

1.1.7.2 Microcirculatory physiology

Under resting physiologic conditions, CBF is regulated by a baseline vascular tone under the influence of the autonomic nervous system. On the other hand, microcirculation (the small arteries and arterioles and the venules and small veins) plays a significant role in regulating systemic and local hemodynamics. The inverse relationship between microvascular CBF and systemic vascular resistance (SVR) and mean BP immediately after delivery was no longer present by the fifth day of postnatal life (Kroth et al., 2008).

Oxygen delivery is dependant on the oxygen content of the blood, on the cardiac output and on the blood pressure. It is determined by the interaction between SVR and cardiac output (systemic blood flow). In fact, if systemic vascular resistance is too low, blood pressure may decrease below a critical level where oxygen delivery becomes compromised despite normal or even high cardiac output. Some studies have described the possible lower limits of BP below which autoregulation of CBF are impaired in very low birth weight in preterm infants (Munro et al., 2004; Victor et al., 2006). When the supply of oxygen to the tissues does not meet oxygen demand, neuroendocrine compensatory mechanisms and increased oxygen extraction maintain perfusion pressure and blood flow, to compensate oxygen delivery. The uncompensated phase of oxygen delivery results in the loss of vital organ blood flow autoregulation and the development of lactic acidosis, and then cellular function become compromised.

The circulatory function is dependant on the neural, hormonal, and metabolic mechanisms at the central and local levels, and is regulated by peripheral baroreceptors and chemoreceptors in the aortic arch and carotid sinus as well as by the mechanoreceptors to balance between sympathetic and parasympathetic outflow. Even though many of these mechanisms have been identified, much work remains to better define this complexity and the developing aspects of the cardiovascular control in the immature infant. The effect of gestational and postnatal age, the patient's ability to compensate with increased cardiac output and regulation of CBF, and the underlying pathophysiology on the dependency of CBF on BP in premature infant remain to be determined (Noori et al., 2012a).

1.1.8 The pathophysiology of neonates

The hemodynamic disturbance in preterm neonates can be caused by the impact of immaturity and pathologic events on the physiology of the neonatal cardiovascular regulation, which lead to the end-organ damage caused by the decrease in oxygen delivery to the organs. Patent ductus arteriosus (PDA) and intraventricular hemorrhage (IVH), are the main neurological pathological situations of preterms.

1.1.8.1 Patent ductus arteriosus in premature infants

PDA is a common problem in preterm infants with less than 30 weeks GA. During fetal life, increased pulmonary vascular resistance, decreased pulmonary blood flow, diversion of the blood from the pulmonary to the systemic circulation (right-to-left) through ductus arteriosus occurred. After birth, increased pressure and blood flow in the pulmonary vascular bed would occur (Fig.13). In term infants, the PDA within the first 48 hours after birth will be closed. In contrast, preterm infants frequently fail to constrict their ductus. As it was explained in transitional physiology part, this will happened due to the effect of the separation of placental, the pressure of oxygen and hormonal secretions. The direction of flow in the PDA in preterm infants depends on the relative resistances in the systemic and pulmonary circulation. 52% of neonates less than 30 weeks GA have left-to-right ductal shunts, 43% of neonates during the transitional period left-to-right bidirectional shunts, and only 2% have right-to-left shunts by 5 hours of postnatal life (Greisen, 2012).

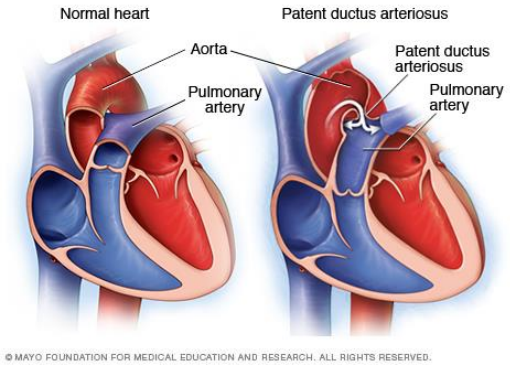

Fig. 13 *The direction of flow in the PDA in preterm infants*[2].

[2] https://www.mayoclinic.org/diseases-conditions/patent-ductus-arteriosus/symptoms-causes/syc-20376145

Signs of PDA: The degree of PDA depends on the size and direction of the shunt and on the duration of the ductal patency that can be measured by Doppler. A PDA size ≥1.6 or ≥2 mm at 5 hours of postnatal life in preterm infants younger than 30 weeks GA is considered as a hemodynamically significant patent ductus arteriosus (hsPDA) (Kluckow and Evans, 1995). More recently, diastolic flow velocity in the left pulmonary artery, transductal velocity ratio, the ratio of left ventricular output to superior vena cava flow, the presence of holodiastolic retrograde flow in the descending aorta, have been used to quantify the hsPDA (Flynn et al., 2005).

Cardiovascular Adaptation to PDA: The presence of a PDA with a left-to-right shunt, results in an increase blood flow to the lungs. Consequently, venous return from the pulmonary circulation to the left atrium is also increased and leads to an increase in the preload of the left ventricle. The increase in myocardial muscle fiber stretch from higher preload results in a higher cardiac output and augments stroke volume (since there is no change in heart rate). The increase in cardiac output may offset the hsPDA, at least initially. However, this compensatory mechanism may fail in some very low birth weight infants, and systemic perfusion may become inadequate. In infants with very low birth weights and hsPDAs, have significantly lower systolic, diastolic and mean blood pressures. When this occurs, signs of tissue hypoperfusion may occur in the form of decreased urine output (Clyman and Noori, 2012).

CBF and PDA: Some studies suggest that CBF is maintained in the presence of an hsPDA, but the most studies have demonstrated a decrease in CBF. In preterm infants with the presence of hsDPA, Perlman et al. showed a decrease in diastolic blood flow velocity in the anterior cerebral artery (Perlman et al., 1981). Besides, Lemmers et al. demonstrated a decrease in cerebral oxygenation that resolved after treatment with indomethacin (Lemmers et al., 2008). Moreover, Shortland et al. found no difference in anterior CBF velocity between infants with or without a PDA (Shortland et al., 1990). There is a study suggesting that CBF progressively decreases as left-to-right shunts across the PDA become larger (Jim et al., 2005). Further, in the presence of a PDA, CBF is maintained at a constant level as long as the left ventricular output is increased (Shimada et al., 1994). In contrast, Baylen et al. demonstrated a decrease in CBF when cardiac output was compromised in preterm lambs with a PDA (Baylen et al., 1983). To sum up, it seems that the increase in cardiac output can compensate cerebral perfusion at least to a certain point in patients with a PDA.

PDA treatment: To treat PDA, surgical ligation produces definitive ductus arteriosus closure, but it is associated with its own set of illness. Indomethacin and ibuprofen have been used as the preferred therapy instead of surgery for closing a PDA. Indomethacin reduces CBF and cerebral oxygenation in experimental animals, adults, and preterm neonates (Pryds et al., 1988). Although indomethacin decreases the severity of peri-intraventricular hemorrhage (PIVH), this may affect long-term neurodevelopmental outcomes (Schmidt et al., 2001). Contrary to indomethacin, ibuprofen does not have significant cerebrovascular effects (Mosca et al., 1997). However, it is not known whether the use of ibuprofen for the treatment of patent ductus arteriosus (PDA) affects long-term neurodevelopmental outcomes. Dopamine increases blood pressure and effects on CBF, without a (dilatory) effect on brain vessels (Zhang et al., 1999). In infants with a large PDA, dopamine at doses of 8 to10 mcg/kg/min may increase systemic blood pressure and pulmonary vascular resistance resulting in a reduction of left to right shunt (Bouissou et al., 2008). But autoregulation might also be impaired during high concentrations of dopamine (Alderliesten et al., 2013).

1.1.8.2 Intraventricular hemorrhage in premature infants

Intraventricular hemorrhage is the neurological pathology of prematurity in the neonatal period (Fig.14). The occurrence of intraventricular hemorrhage is 50% in the first 8 hours of life. 75% of cases occur in the first 24 hours and 95% before the 4th day of life. The cerebral hemorrhages are more frequent in the premature with low weight and the gestational age lower than 32 wGA. The cerebral hemorrhages are classified into four stages according to Sarnat (Johnson, 2000):

Stage I: subependymal hemorrhage,

Stage II: intraventricular hemorrhage with normal ventricles,

Stage III: intraventricular hemorrhage with dilatation,

Stage IV: intraventricular hemorrhage with intraparenchymal extension.

50-60% of children with hemorrhage (lower than 32 wGA) with ventricular dilatation or parenchymal involvement develop cerebral palsy. The primarily imaging technique (such as CT and MRI) used for the diagnosis of IVH in the newborn.

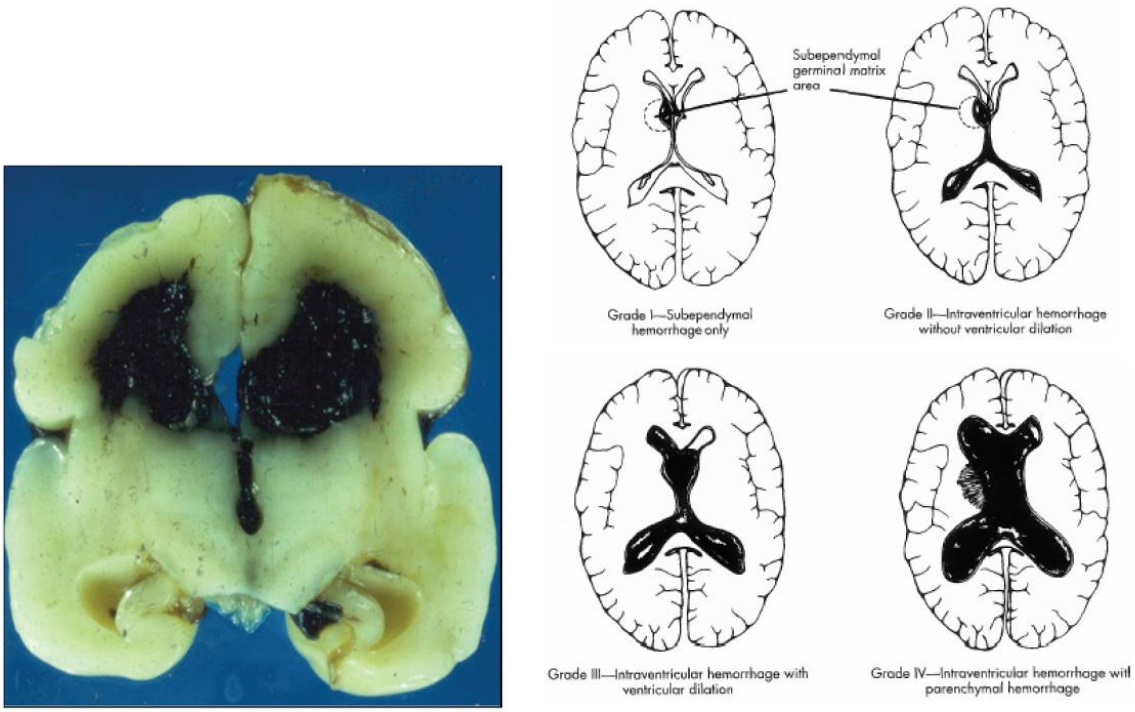

Fig. 14 *Left, Massive intraventricular hemorrhage distending the lateral ventricles (Whitelaw, 2011). Right, IVH grades I-IV (Merestein, 1998).*

Mahmoudzadeh et al. tested how preterm neonates with IVH react to external stimulation (i.e., speech syllables). By combined EEG and fNIRS, a neural response to syllables was observed in IVH infants but did not induce a vascular response in contrast with healthy neonates. These results clearly demonstrate that the cerebral vascular network in IVH preterm neonates was unable to compensate for the increased metabolism resulting from neuronal activation in response to external stimulation (Fig.15) (Mahdi Mahmoudzadeh, 2017).

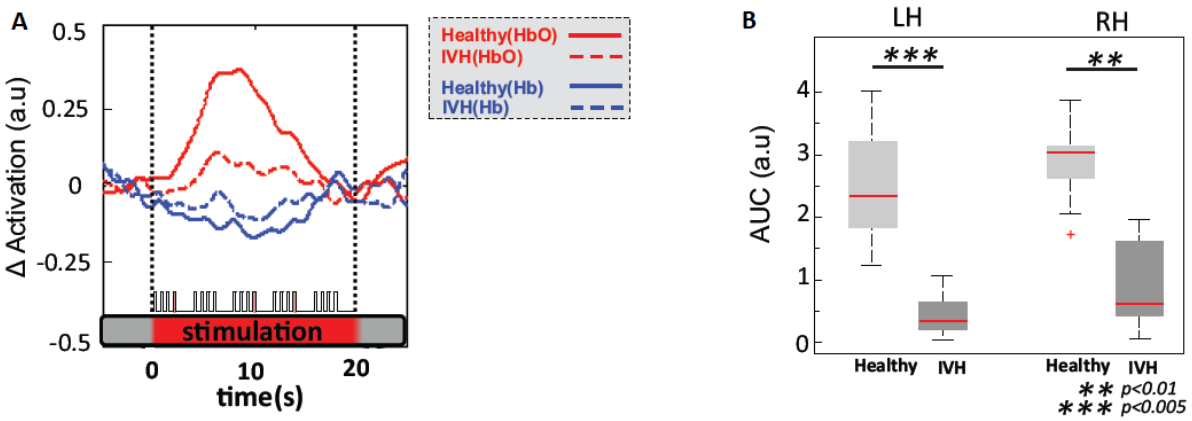

Fig. 15 *(A) shows one sample fOI channel of grand-average of HbO (red lines), Hb (blue lines) changes for healthy (solid lines) and IVH (dotted lines) neonates during auditory stimulation. Horizontal red thick bars indicate the period of the stimulation (20 seconds). This response was pronounced for the healthy neonates, with a significant increase in HbO. (B) Comparison of the mean AUC changes of Oxy-Hb induced by auditory stimulation between healthy and IVH infants. For each hemisphere, activations were significantly reduced in the IVH group compared to the healthy group.*

1.2 Objective and Approach

Understanding the relationship between hemodynamic responses and neural activity in the resting-state immature brain, is so complex. The maturation of the many components related to the mechanism of neurovascular coupling in the neonatal brain is unstable and at varying pace, that has inspired a wide array of investigations ranging from the systems level to the molecular level. In this thesis, we have focused on the following questions:

It makes sense to assume that there is a coupling between hemodynamic and neuronal activity in the premature neonatal brain in resting state (Roche-Labarbe et al., 2007a), but whether the hemodynamic responses to the burst of activities have the same patterns or not has to be analyzed? Is it possible to predict the hemodynamic response of neural activity in resting state in the premature infant considering all the complexity of the immature brain? Is the neurovascular coupling age-dependent at resting state? Does neurovascular coupling occurs in pathological cases in immature infants? Under resting-state conditions, what are the causality and linear/nonlinear relationship between cerebral blood flow and cerebral blood volume and cerebral metabolic rate of oxygen? What is the impact of the different gestational ages and/or pathologic events on the cerebral hemodynamic changes/disturbance in the immature neonatal brain?

In this thesis, we have focused on the following general points:

Multimodal hybrid EEG-NIRS-DCS: to answer these questions, we used multimodal hybrid EEG-NIRS-DCS and non-invasive beat-to-beat blood pressure monitoring techniques, since the multimodal imaging is a suitable approach for monitoring different aspects of hemodynamic and neural activities in the neonatal brain. Multimodal simultaneous recording suggests a complementary approach and makes it possible to minimize the inaccuracies related to each of the individual techniques.

Resting state: our analysis is based on the assumption of only minor alterations from the baseline condition (resting-state) rather than the hemodynamic response for task-evoked conditions. Chen et al. (e.g., Chen et al. Neuroimage 2015), suggest that HRF (Hemodynamic Response Function) models should be modified for resting-state conditions compared to traditional task-based models implying different hemodynamic behaviors in these two conditions. This is even more important considering immature neonates.

Complexity of the immature neonatal brain: our knowledge concerning cerebral autoregulation in preterm neonates remains limited and how cerebral oxygenation develops over time is unknown. Moreover, given the very limited knowledge concerning the spontaneous activity of the premature brain at present, the mechanisms underlying the present observations have not been elucidated, which would be a fascinating subject for future studies.

Thermal impact of near-infrared laser: Increasing temperature as a result of the propagation of laser light in human tissues is an essential issue in functional optical imaging. The purpose of this part was to model the photothermal interaction of NIR laser on human tissues. The results presented in this part could be useful to optimize laser spot size and power for a variety of laser applications of functional imaging systems (e.g., DCS which need NIR light with relatively high laser power). A combination of simulation and adequate in vitro experiments could help to develop a more effective optical imaging to avoid any possible tissue damage.

1.3 Thesis overview

This thesis beginning with a general introduction in the first chapter and I provided an overview of the neuronal and vascular components likely to be involved in the neurovascular coupling and their roles in mediating blood flow changes. The mechanism

underlying the neurovascular coupling (aerobic and anaerobic mechanisms) are also described. Then I rapidly reviewed fetal, transitional, and post-transitional neuronal/vascular and cardiovascular physiology and described some pathophysiological aspects of neonates with IVH or PDA.

I briefly present the different chapters of the thesis in sequence, that aims to evaluate the neurovascular coupling in premature infants in resting state through a non-invasive multimodal approach that combines the evaluation of neuronal activity (EEG), local hemodynamic activity (fNIRS-DCS) and systemic hemodynamic activity (non-invasive beat-to-beat blood pressure monitoring).

Chapter 2: Material and Methods. In Chapter 2, I provided an overview of the multimodal imaging systems used in our study. Their underlying principles were also briefly described. This chapter contains a general methodological introduction to near-infrared spectroscopy, diffusion correlation spectroscopy together with the mathematical and physical basis of photon propagation in biological tissue. Calculating the parameter of the cerebral metabolic rate of oxygen (CMRO2), measuring and estimating the blood pressure with the Finometer device (non-invasive beat-to-beat blood pressure monitoring) were also explained.

Chapter 3: Thermal impact of near-infrared laser in advanced noninvasive optical brain imaging. In Chapter 3, we modeled the photothermal interaction of NIR laser of advanced optical imaging, on neonatal and adult quasi-realistic head models. We modeled the thermal effect of different laser powers with various spot sizes and different head tissue characteristics by numerical simulation using finite-element analysis. The results of chapter 3 can be useful to optimize laser parameters for a variety of laser applications in the adult and neonatal brain.

Chapter 4: Relationship between relative cerebral blood flow, relative cerebral blood volume, and relative cerebral metabolic rate of oxygen in the preterm neonatal brain. In Chapter 4, directionality and a causal relationship between relative cerebral blood flow and relative cerebral blood volume rCBF–rCBV (also between relative cerebral blood flow and relative cerebral metabolic rate of oxygen rCBF − rCMRO2) in preterms at resting state were identified by using transfer entropy. This help to elucidate the principles of cortical hemodynamics during development.

Chapter 5: Neurovascular Coupling in the Developing Neonatal Brain in Resting State. The coupling between spontaneous physiological burst of activity with a transient stereotyped hemodynamic pattern in resting state premature infants, consisting of deoxygenation, oxygenation, cerebral blood flow, cerebral blood volume and cerebral metabolic rate of oxygen is identified, which help to elucidate the principles of neuronal and cortical hemodynamic during development. The multi-frequency aspect of neurovascular coupling was presented using wavelet coherence analysis, in comparing between two normal and pathological groups and represent as a function of age.

Chapter 6: Conclusion and Perspective. In the final chapter 6, I summarize the main conclusions and consider the perspectives for future research.

CHAPTER

Material and Methods 2

2.1 Introduction

The simultaneous acquisition of electroencephalography (EEG), near-infrared spectroscopy (NIRS) and diffuse correlation spectroscopy (DCS) is a potentially powerful multimodal imaging technique for measuring the functional activity of the human brain. Non-invasive beat-to-beat systemic blood pressure was simultaneously recorded by Finometer®. The Finometer® is a solution for accurate blood pressure monitoring. Given that EEG measures the electrical activity of neural populations while NIRS and DCS measure local cerebral hemodynamics via a blood oxygenation and blood flow signal related to neuronal activity. Simultaneous EEG/NIRS/DCS offer a unique modality to investigate the relationship between these three phenomena within the context of noninvasive neuroimaging. The rationale for combining EEG/NIRS/DCS and systemic blood pressure monitoring is the fact that the individual modalities measure obviously different physiological phenomena at the same time. That is, there is a need for a more comprehensive understanding of the specific mechanisms underlying neurovascular coupling in neonates.

2.2 Cortical electrical activity measurements in premature infants by EEG

The cortical neurons that are activated or inhibited by stimulation or in resting state appear to be involved in basal forebrain-mediated changes in electroencephalogram (EEG) activity (Lee and Dan, 2012). The EEG is presumed to reflect the synchronized synaptic activity of large numbers of neurons (Buzsaki et al., 2012). The EEG oscillations have been subdivided into five frequency

bands: delta (0.5–4 Hz), theta (4–8 Hz), alpha (8–12 Hz), beta (12–30 Hz), and gamma (>30 Hz). It has been suggested that ongoing activity in the EEG (background activity), plays a decisive role in functional communication in the brain (Basar et al., 2001). EEG records all brain's spontaneous electrical activity over a period from multiple electrodes placed on the scalp.

2.3 Cortical hemodynamic measurements in premature infants by fNIRS and DCS

The basic idea from the propagation of light through tissues to probe tissues such as tumors has been around since about 1930s. In the late 1970s, Jobsis founded out that there exists a "window" (range 700 to 900 nm), in the near-infrared spectrum wherein photons, could deeply penetrate into tissue because of the reduced absorption of water (Fig.1) (Jobsis, 1977). The measurements of scattering and absorption of the photon were used in the late 1980s for different applications ranging from imaging of breast tumors to functional imaging of the brain (A. G. Yodh, 2003). By the diffuse optical technique, it is possible to measure oxyhemoglobin (HbO), deoxyhemoglobin (HbR), water, lipid, and scattering as well as some less common variants of hemoglobin and other tissue chromophores (A. Yodh, 1995).

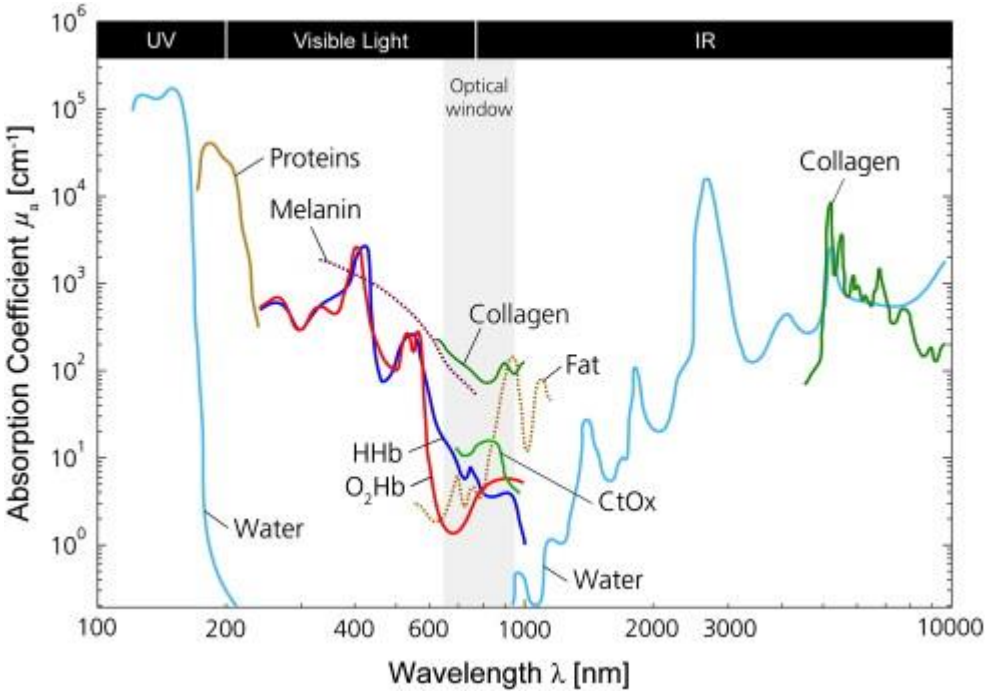

Fig. 1. *Absorption spectra (natural logarithm base!) for different chromophores present in human tissue. Shown are the spectra for O2Hb, HHb, proteins, water, collagen, fat, and cytochrome oxidase (CtOx) in the region from 100 nm to 10,000 nm. The spectra are given with respect to the specific concentration in mM. (Scholkmann et al. 2014)*

This has been only possible for a few clinical applications in the preterm infants' neuroimaging such as hemorrhage detection (Gibson et al., 2006) or disturbed cerebral autoregulation detection in newborns. NIRS is portable and provides bedside monitoring. It is noninvasive and safe as it uses nonionizing radiation with less energy than a head ultrasound.

2.3.1 Methodology for oxy and deoxy-hemoglobin measurement (NIRS)

To probe tissue by the diffuse optical technique, three main paradigms can be used: Continuous wave (CW), Time domain (TD) and Frequency domain (FD) functional near-infrared spectroscopy (fNIRS).

2.3.1.1 Continuous wave NIRS

CW-NIRS makes use of a steady state light beam that is continuously injected into the tissue. The reduction in transmitted light amplitude modulated at a low (a few kHz) frequency is measured. CW methods are becoming increasingly popular also in clinical due to their simplicity, low cost, size and speed (Siegel et al., 1999).

In CW-NIRS, changes in tissue chromophore concentrations from the baseline value can be obtained from the modified Beer-Lambert law. The original Beer-Lambert law describes the absorption of light in a medium. The attenuation of light is related to the change in concentration of the compound and to the optical pathlength: $A = E \times C \times P$, where A is absorbance (no units), E is extinction coefficient or molar absorptivity (measured in L/ mol/cm), P is pathlength of the sample (measured in cm), and C is concentration of the compound (measured in mol/L) (Victor and Weindling, 2012).

The modified Beer-Lambert law, include an additive term, K, due to scattering losses, is expressed as $A = P \times L \times E \times C + K$, where L is the differential pathlength factor. K is a constant value and is unknown because K is dependent on the measurement geometry and the scattering coefficient of the tissue investigated. This equation cannot provide the absolute value of the concentration of the chromophore, but if K is constant during the measurement period, it is possible to calculate a change in concentration (ΔC) of the chromophore, with following formula:

$$\Delta A = P \times L \times E \times \Delta C \text{ or } \Delta C = \Delta A / P \times L \times E \quad (1)$$

In a medium containing several chromophores (C_1, C_2, and C_3) the overall absorbance is:

$$A = (E_1C_1 + E_2C_2 + E_3C_3)\, P \times L, \quad (2)$$

$$\Delta C_1 = Q_1\Delta A_1 + R_1\Delta A_2 + S_1\Delta A_3 + T_1\Delta A_4, \quad (3)$$

$$\Delta C_2 = Q_2\Delta A_1 + R_2\Delta A_2 + S_2\Delta A_3 + T_2\Delta A_4, \quad (4)$$

$$\Delta C_3 = Q_3\Delta A_1 + R_3\Delta A_2 + S_3\Delta A_3 + T_3\Delta A_4, \quad (5)$$

Where ΔA_1, ΔA_2, ΔA_3, and ΔA_4 represent changes in absorption at different wavelengths such as 774 nm, 825 nm, 843 nm, and 908 nm. ΔC_1, ΔC_2, and ΔC_3 represent changes in the concentrations of C_1, C_2, and C_3 (such as HbR, HbO, and Cytochrome aa3). Because the pathlength is wavelength dependent, the inverse matrix coefficients is presented in Table.1 (Victor and Weindling, 2012).

Table 1. *INVERSE MATRIX COEFFICIENTS FOR HB, HBO2, AND CYTOCHROME AA3 AT DIFFERENT WAVELENGTHS*

	774 nm	825 nm	843 nm	908 nm
Hb	1.363	−0.9298	−0.7538	0.6747
HbO_2	−0.7501	−0.5183	−0.0002	1.8881
Cyt aa3	−0.1136	0.7975	0.4691	−1.0945

The CW method allows only relative measurements, to solve this problem (for a pathlength correction) multiple optodes operating are placed simultaneously around the head, but the tissue should assume to be homogeneous. This modification is called *spatially resolved spectroscopy* with the reasonable signal-to-noise ratio and with the depth from the surface between 1 and 3 cm. If the distance between the light source and the detector is large enough (> 3 cm), it can be assumed that scatter distribution becomes so homogeneous that the loss due to scattering is the same at all the detectors. Tissue oxygenation index (TOI) is calculated as follows:

$$\text{TOI}\ (\%) = \frac{K.HbO2}{K.HbO2 + K.HbR} \quad (6)$$

Where K is the constant scattering contribution.

The NIRO-200NX (Hamamatsu Photonics, Hamamatsu City, Japan) was used to monitor cerebral tissue oxygenation. This instrument uses three light emitting diodes with wavelengths of 735, 810 and 850 nm, respectively, and two detecting photodiodes to measure light attenuation at different distances from the source. The emitter and receiver were fixed to the probe holder to ensure an inter-optode distance. This spectrometer uses both the modified Beer-Lambert law (MBL) –to measure changes in oxyhemoglobin and deoxyhemoglobin concentrations (HbO and HbR)– and

spatially resolved spectroscopy (SRS) method –to measure an absolute ratio of oxyhemoglobin to total hemoglobin, known as the tissue oxygenation index (TOI) (Wong et al., 2008). The SRS method uses a mathematical model based on the light diffusion equation to calculate TOI. SRS assumes a homogeneous pathlength and uniform light scattering for all emitted light frequencies. Although it does not entirely eliminate the contribution from extracranial contents, the use of multiple detectors and the thinness of the neonatal skull minimizes this component from the overall measurement.

2.3.1.2 Time domain NIRS

Time domain (TD) methods use the pulsed laser and photo-detection techniques with picosecond resolution. This method uses a mathematical approximation based on diffusion theory to allow better estimation of light scattering properties by measurement of differential pathlength factors. Thus the method permits differentiation of one tissue from another. This system can provide the absolute quantification of hemodynamic variables. TD fNIR provides the highest information with a large amount of data, which means that data are collected and analyzed relatively slowly (in minutes), but it has the reputation of being cumbersome, bulky, and very expensive (F. E. W. Schmit, 1998).

2.3.1.3 Frequency domain NIRS

Frequency domain (FD) methods provide an amplitude modulated sinusoid at a single (generally 100-1000 MHz) frequency. Even though FD techniques provide less information than TD, it provides a direct measurement of absorption and scattering coefficients of the tissue by the reduction in amplitude and the phase shift of the transmitted light (Yang et al., 1997). This method allows for the different scattering effects of the fluid and tissue components of the brain.

2.3.2 Methodology for cerebral blood flow measurement (DCS)

Additional information can be obtained from the monitoring of the fluctuations of the scattered light in tissue which reflects the dynamics of the scatterers such as red blood cells. Measuring the electric field temporal autocorrelation function or its Fourier Transform reflects the motions of scatterers within the tissue; the most significant signal is from blood flow (Durduran et al., 2010b).

DCS is similar to NIRS, uses near-infrared light to penetrate through tissue (~1 cm) to noninvasively measure CBF in small vessels, in comparaison to the transcranial Doppler (TCD) that estimates blood flow only in the main arteries. By incorporating NIRS with DCS, the cerebral

metabolic rate of oxygen (CMRO2) can be estimated. DCS was presented in the early 1990s and has been accredited in some animal and human studies for CBF measurement.

Historically, optically regional CBF in neonates using NIRS was measured by either changing the inspired oxygen in ventilated infants, or by injection of an indocyanine green bolus (Patel et al., 1998) have ethically limitation for the healthy infants. Although these methods give reliable estimates of CBF, they are not ethically applicable in all infants. Diffuse correlation spectroscopy (DCS) is a more succeeding technique, providing a measure of CBF based on the movement of scatters such as blood cells inside the tissue. DCS can directly measure CBF without injecting bolus or oxygen manipulations.

2.3.2.1 Photon diffusion in tissues

The physical basis of the optical properties can be explained by the "diffusion equation", where the measurable, near-infrared photon fluence rate, $\boldsymbol{\Phi}(r, t)$ (photons/[cm^2.s]) obeys the following diffusion equation (Durduran et al., 2010b):

$$\nabla.\big(D(r)\nabla\Phi(r,t)\big) - v\mu_a(r)\Phi(r,t) - \frac{\partial\Phi(r,t)}{\partial t} = -vS(r,t) \quad (7)$$

Here $\boldsymbol{\Phi}(r, t)$ is proportional to the photon number density (U(r, t) (photons/cm^3)), v is the speed of light in medium (cm/s), $\mu_a(cm^{-1})$ is the absorption coefficient, $\mu_s'(cm^{-1})$ is the reduced scattering coefficient and $D=\frac{v}{3\mu_s'}$ is the photon diffusion coefficient. S(r, t) is an isotropic source term which gives the number of photons emitted at position r and time t per unit volume per unit time. The equation 7 represents the rate of change of photons within a sample volume element, the number of photons scattered minus the number of photons absorbed per unit time, plus the number of photons emitted per unit time from any sources within the volume element. Since, the frequency domain methods were employed the amplitude and phase of the AC component of the transmitted diffuse light waves were measured. In this case, the source term is written as:

$$S(r,t) = (S_{DC} + S_0 e^{-iwt})\delta(r) \quad (8)$$

The reduction in amplitude and the phase shifts of diffuse light density are detected with multiple source-detector separations (Fig.2). Then by plotting the detected amplitude and fitting the slope, the optical properties are extracted (Durduran et al., 2010b).

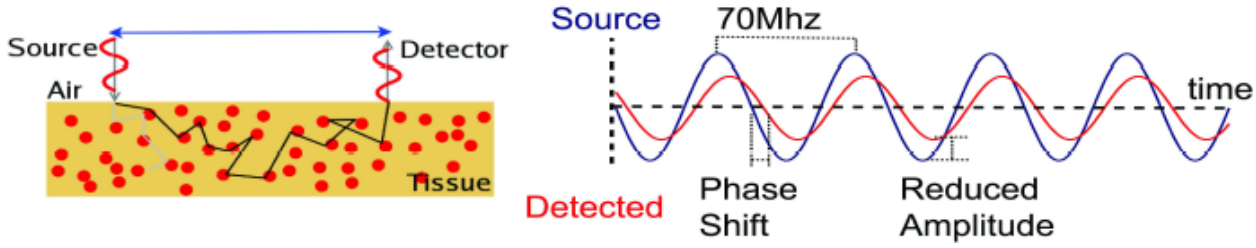

Fig.2 *The photons are injected at the source position and detected some distance away. The reduction in amplitude and the phase shifts of diffuse photon density waves are detected at multiple source-detector separations.*

2.3.2.2 Diffuse correlation spectroscopy (DCS)

To find the index of blood flow and learn about the motions of red blood cells, the electric field temporal autocorrelation function is measured and analyzed by DCS device. E(r, t) represents the temporal variations of the light electric field at time t and position r, which propagate through tissue. The decline of the autocorrelation function by a factor of 1/e occurred when the scatters particles such as the red blood cells have moved (Durduran and Yodh, 2014).

The temporal electric field autocorrelation function diffuses through tissue in a manner that is similar to light fluence rate, so diffusion equation are used for transport of autocorrelation function. Thus, many tissue optical properties such as tissue absorption (μa) and scattering coefficient (μ′s), are the same. The difference between them is an additional absorption term that is dependent on the dynamics of the scatterers. Diffuse correlation spectroscopy is a measure of tissue perfusion that depends on both the movement of scatterers inside the blood vessels and the optical tissue properties. The diffusion equation of autocorrelation function:

$$\left[\nabla . D(r)\nabla - v\mu_a(r) - \frac{\alpha}{3} v\mu_s' k_0^2 \langle \Delta r^2(\tau)\rangle\right] G_1(r,\tau) = -vS(r) \qquad (9)$$

Here τ is the correlation time, α is the ratio of moving scatterers such as red blood cells to the total number of scatterers in the sample, k_o is the wave-number of the light in the sample, and $D(r) \equiv \frac{v}{3\left(\mu_s'(r)+\mu_a(r)\right)} \approx \frac{v}{3\left(\mu_s'(r)\right)}$ is the photon diffusion coefficient, $G_1(r,\tau) = \langle E^*(r,t).E(r,t+\tau)\rangle^2$ is the temporal field autocorrelation function, $\langle \Delta r^2(\tau)\rangle$ is the mean-square displacement of these moving red blood cells in time τ. Here the angle brackets denote ensemble averages or averages over time. The mean-square particle has been found as a Brownian motion, i.e., $\langle \Delta r^2(\tau)\rangle = 6D_B\tau$ where D_B is the effective diffusion coefficient of the moving scatterers. It is assumed that the measured relative changes of D_B are equal to the relative changes in blood speed, and that α is proportional

to the tissue blood volume fraction. With these assumptions, the relative change of αD_B equals the relative change of the cerebral blood flow (CBF).

In practice, the light intensity is more accessible to measure than the light electric field. The measured normalized intensity auto-correlation function $g_2(\tau) \equiv \langle I(r,t)I(r,t+\tau)\rangle / \langle I(r,t)\rangle^2$ is related to the normalized electric field correlation function $g_1(\tau) = \langle E^*(r,t).E(r,t+\tau)\rangle / \langle |E(t)|^2\rangle$ by the Siegert relation ($g_2(\tau) = 1 + \beta|g_1(\tau)|^2$). DCS intensity auto-correlation curves has a delay time range of 200 ns~1 s. The intensity, $I(r,t) \sim |E(r,t)|^2$ and β is a constant in an ideal experiment setup that depends on the source coherence, detection optics, ambient light and other external factors.

By fitting the measured intensity autocorrelation functions to solutions of Eq. (1), it can be possible to estimate blood flow from DCS data. The best-fit defines a tissue blood flow index (BFI) from the data. Relative changes in BFI (i.e., rBFI) at time t are defined as $rBFI(t) = BFI(t)/BFI(t_0)$, where t_0 denotes a time during the baseline period. Percent changes in BFI (i.e.,ΔBFI) are sometimes defined with respect to zero, i.e $\Delta BFI(\%) = (rBFI - 1) \times 100$.

The theoretical solutions of equation (1) is (Boas et al., 1995b);

$$g_2(r_s, r_d, \tau) = (1 + \exp\left(-(3\mu_s'\mu_a + (P_{RBC}\mu_s')^2 k_0^2 \langle \Delta r^2(\tau)\rangle)^{\frac{1}{2}} |r_s - r_d|\right)) \quad (10)$$

Where the source is at position r_S, the detector is at position r_d, the correlation time is τ, the reduced scattering coefficient is μ_s', the absorption coefficient is μa, the wave number for the laser light is k_0, $\langle \Delta r^2(\tau)\rangle$ is the mean square displacement of the scatters (such as the red blood cells), and P_{RBC} is the probability of scattering from a moving red blood cell. Brownian motion is the most common model for the mean square displacement of the moving particles:

$$\langle \Delta r^2(\tau)\rangle = 6D_B\tau \quad (11)$$

Where D_B is the Brownian diffusion coefficient. Since P_{RBC} is generally unknown, these two parameters ($D_B P_{RBC}$) to assign a blood flow index (CBF_{ix}) (Yu et al., 2005). Relative changes in D_B are correlated with relative changes in tissue blood flow.

The curves decay faster with increasing D_B, i.e. increased flow, and increased source-detector separation. The slope and/or the decay rate provides information about the optical properties and the motion of the scatterers (Fig.3).

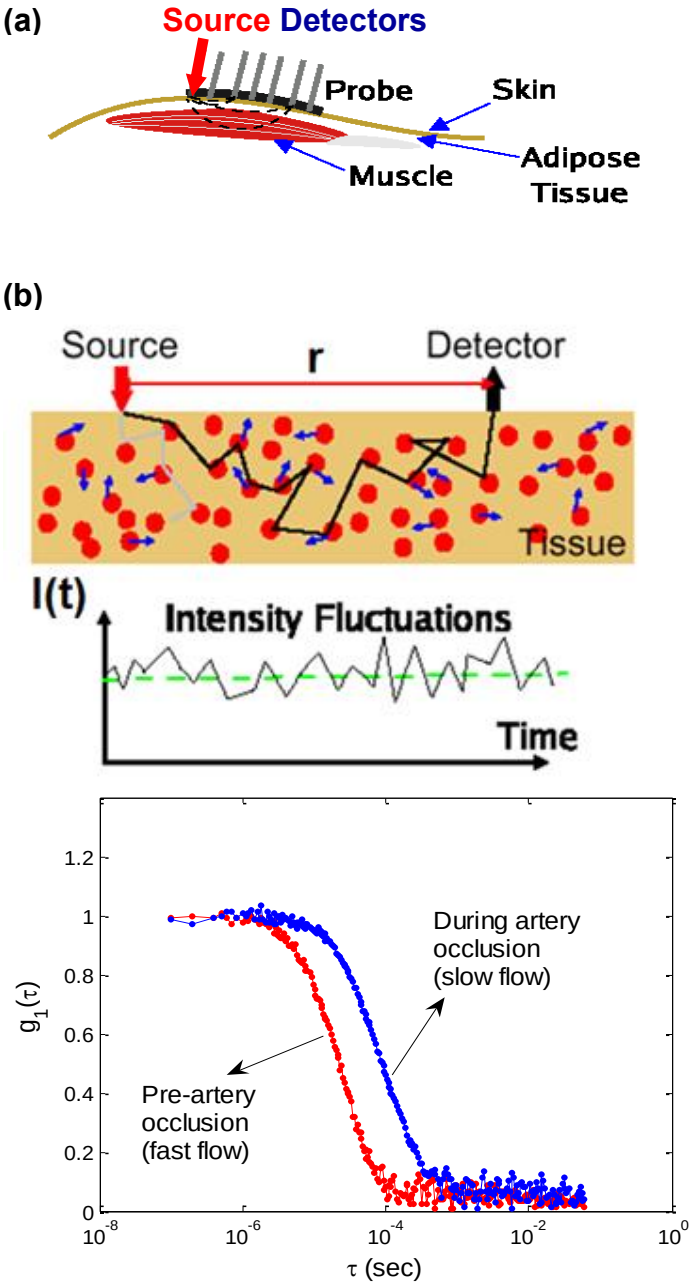

Fig.3 *(a) Schematic of a diffuse correlation tomography in a turbid medium. Sources and detectors are placed on the "air-side" of the tissue. The photons undergo scattering, absorption and experience Doppler shifts when they scatter from moving particles. The motion of the scatterers leads to fluctuations in intensity which are detected by a photon counting detector. (b) The temporal autocorrelation functions of the intensity are then calculated using an autocorrelator (Durduran and Yodh, 2014).*

2.3.3 Methodology for cerebral metabolic rate of oxygen ($CMRO_2$) measurement

Measuring the parameter of the cerebral metabolic rate of oxygen (CMRO2), finding the relationship between CMRO2 and CBF, and the mechanisms of oxygen transport from the blood to the brain is an important issue to understand the underlying mechanisms of neurovascular coupling. Based on a theory of Crone (1963) (Crone, 1963), because the only source of oxygen is blood (i.e., hemoglobin), the oxygen extraction from blood to cerebral tissue could be related to the arteriovenous concentration difference (Ca − Cv) by detecting tracer amounts of an exogenous indicator's dilution (within the blood) or diffusion (into the tissue). According to Fick's principle CMRO2/CBF was defined (Siesjo, 1978);

$$CMRO2/CBF=(Ca - Cv) \quad (12)$$

Hill (1913) found the relation between saturation of hemoglobin with oxygen and the changing of the color of erythrocytes: the fully oxygenated hemoglobin being bright red whereas the fully deoxygenated hemoglobin being nearly black (Hill, 1913). Penfield (1933) found that cerebral arterial vessels were almost always red whereas venous ends were purple, and veins became redder when neuronal activity increased (Chorobski and Penfield, 1932). These findings provided an essential contention about the equation of CMRO2 during neuronal activity.

In an activated region, the difference between Ca and Cv become smaller, because the blood is almost fully oxygenated at the arterial end, venous oxygenation is increased and accompanied with a drop in deoxyhemoglobin concentration at the venous end of the capillary. Thus the arteriovenous difference in capillaries decreased. It has been known for several decades that blood oxygenation raised with increased neuronal activity. In other words, in the activated region, there is a more substantial increase in CBF than CMRO2, which is commensurate with a decrease in OEF.

2.3.3.1 CMRO2 calculation

1) rCMRO2 calculation can be estimated from the difference in oxygen saturation between arterial and venous blood(relative oxygen extraction fraction, rOEF), and from the relative cerebral blood flow, which can be estimated from DCS data. The relative cerebral metabolic rate of oxygen was estimated as (Culver et al., 2003):

$$rCMRO_2 = rCBF \times rOEF \quad (13)$$

Where rOEF is defined as:

$$rOEF = \frac{SaO_2(t) - SvO_2(t)}{SaO_{2\mathrm{bl}}(t_0) - SvO_{2\mathrm{bl}}(t_0)} = \frac{SaO_2(t) - SO_2(t)}{SaO_{2\mathrm{bl}}(t_0) - SO_{2\mathrm{bl}}(t_0)} \quad (14)$$

With venous oxygenation $SvO_2 = (SO_2 - a \times SaO_2)/b$, where a+b=1, a and b are the arterial and venous contributions that are constant over time (Watzman et al., 2000). SO2 is the microvascular tissue oxygen saturation (Wray et al., 1988) ($SO_2 = HbO_2/HbT$), ($HbT = HbO_2 + Hb$, where Hb is the deoxy-hemoglobin concentration and HbO_2 is the tissue oxy-hemoglobin concentration that measure by NIRS). "bl" is used to indicate baseline values. Baseline SO_2 (SO_{2bl}) is estimated from the literature values. S_aO_2 is the arterial blood oxygen saturation which can be estimated by pulse-oximetry or by blood gas sampling. Mechanical ventilation parameters and inspired oxygen concentrations can be maintained constant at sufficiently high levels to saturate arterial hemoglobin (SaO2 ≈ 100%). If SaO2 is not considered equal to 100%, the $rCMRO_2$ was estimated as:

$$rCMRO_2 = rOEF \times rCBF = \left(\frac{S_aO_2(t) - SO_2(t)}{S_aO_{2bl}(t_0) - SO_{2bl}(t_0)}\right)\left(\frac{\gamma_{bl} S_aO_{2bl}}{\gamma S_aO_2}\right) rCBF \approx \left(\frac{S_aO_2(t) - SO_2(t)}{S_aO_{2bl}(t_0) - SO_{2bl}(t_0)}\right)\left(\frac{S_aO_{2bl}}{S_aO_2}\right) rCBF \quad (15)$$

γ is an empirical parameter that is constant and can be estimated by optical methods such as spiroximety (denotes the percentage of blood in the venous compartment).

2) rCMRO2 can generally be calculated by combining relative changes in rCBF and oxygen extraction fraction, but monitoring rCBV independently of rCBF by the NIRS device allows rCMRO2 to be evaluated independently of rCBF (Roche-Labarbe et al., 2010) by using $(rCBV)^{\beta}$ instead of rCBF in relation (1). By considering Grubb's relation between changes in rCBF and rCBV (Davis et al., 1998), the relative cerebral metabolic rate of oxygen was estimated as:

$$rCBF = \frac{CBF_i(t)}{CBF_i(t_0)} = \left(\frac{CBV(t)}{CBV(t_0)}\right)^{\beta} = (rCBV)^{\beta} \quad (16)$$

$$rCMRO_2 = (rCBV)^{\beta} \times rOEF \quad (17)$$

As 'beta' could be time-variant, time-invariant characteristic of beta should be validated statistically. In some studies (Roche-Labarbe et al., 2010) a constant power law relation between changes in CBF and CBV was assumed. Kida and Hyder et al. (Kida et al., 2007), reported the variation of β, ranging from 0.19 to 0.23 for the plateau CBF during stimulation, although it was not statistically significant.

CBV (cerebral blood volume) was defined as: $\frac{(HbT \times MW_{Hb})}{HGB \times D_{bt}}$, where CBV is expressed in ml/100 g, HbT in µmol, MW_{Hb} (64,500 g/mol) is the molecular weight of hemoglobin, D_{bt} (1.05 g/ml) is the brain tissue density and HGB (g/dl) is the blood hemoglobin concentration. The control state at time t0 was defined as the mean value of the signal and was considered to be the reference value. The standard normal values for HGB were used, as HGB was not available in clinical charts (de Alarcón and Werner, 2005; Wolff and Goodfellow, 1955). Some studies have been reported about uncertainties in the above physiologic parameters (Franceschini et al., 2007). rCBV was calculated using the following equation:

$$rCBV = \frac{HbT(t)}{HbT(t_0)} \tag{18}$$

3) The index of the absolute value of CMRO2 was estimated as (Dehaes et al., 2014):

$$\mathrm{CMRO}_{2i} = CBF_i.(CaO_2 - CvO_2) = CBF_i.\frac{HGB}{MW_{Hb}}.(SaO_2 - SvO_2) = CBF_i.\frac{HGB}{MW_{Hb}}.\frac{1}{b}.(SaO_2 - SO_2) \tag{19}$$

Where CaO2 and CvO2 [mol/dl] are the arteriolar and venous O2 concentrations, where venous oxygenation is $\mathrm{SvO_2} = (\mathrm{SO_2} - \mathrm{a} \times \mathrm{SaO_2})/\mathrm{b}$ (a+b=1), and the arterial: venous (a:b) contribution ratio is 1/4:3/4. In the formula CMRO2i = (HGB × CBFi × (SaO2 - SO2)) / (4 × MWHb × β), the factor 4 implies the four O2 molecules bound to each hemoglobin and b is the percent contribution of the venous compartment to the hemoglobin oxygenation measurement.

4) To assign different fractions of functional changes versus baseline values of HbR and HbT concentrations in the venous compartment with respect to the total volume fractions, the rCMRO2 was estimated as:

$$rCMRO_2 = \left(1 + \gamma_r \frac{\Delta HbR}{HbR}\right) \times \left(1 + \gamma_t \frac{\Delta HbT}{HbT}\right)^{-1} \times \left(\frac{\Delta CBF + CBF}{CBF}\right) \tag{20}$$

$$\gamma_r = \frac{\Delta HbR_v/\Delta HbR}{HbR_v/HbR} \; and \; \gamma_t = \frac{\Delta HbT_v/\Delta HbT}{HbT_v/HbT} \tag{21}$$

Γr and γt may range from 0.5 to 2, with 0.75 to 1.25, and under the assumption SaO2=100%, γr, and γt equal to 1 (Jones et al., 2001).

5) To assign the effect of the blood transit time from the arterial to venous compartment on the OEF, the rOEF and then rCMRO2 was estimated as (Buxton et al., 1998; Hoge et al., 2005);

$$rOEF = \frac{rHbR}{rCBV} + \frac{\tau}{rCBF}\left(\Delta rHbR - \frac{rHbR}{rCBV} \times \Delta rCBV\right) \quad (22)$$

$$rCMRO_2 = rCBF \times rOEF \quad (23)$$

Where τ is the mean transit time through the venous compartment. The value of τ in adults has been estimated to be 3–4 s.

2.4 Systemic pressure measurements in preterm infants by Finometer®

The Finometer® is a non-invasive instrument that can be used in clinics and laboratories. Ambulatory Finometer enables measuring of the equivalent of brachial blood pressure (brachial BP) from the finger blood pressure (finger BP). Although the primary problem resides in the non-invasive aspect of the Finometer®, as noninvasive methods are usually associated with reduced accuracy, this innovative device has many potentials to measure the different parameters. It has the potential for providing estimates of stroke volume (SV) and cardiac output (Q) from the finger blood pressure. The Finometer® monitors hemodynamic by using three different main steps: measuring finger BP, estimating brachial BP and then, estimating Q.

2.4.1 Monitoring finger blood pressure

Finger blood pressure is measured with a cuff wrapped around the finger. The blood pressure is measured with the method of volume-clamp presented by Juan Peñáz [Peñáz, 1973] that is based on keeping fixed the finger arterial diameter (Fig.4.A).

A

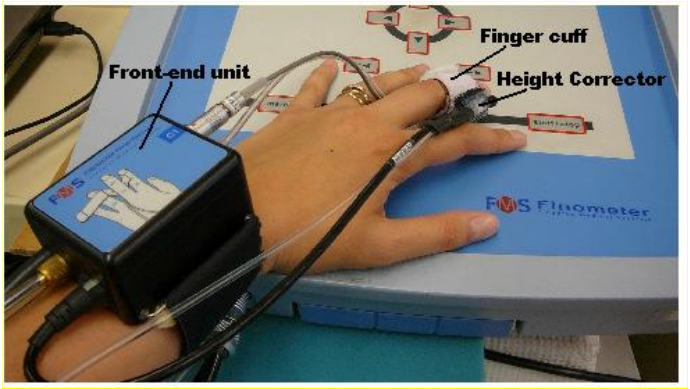

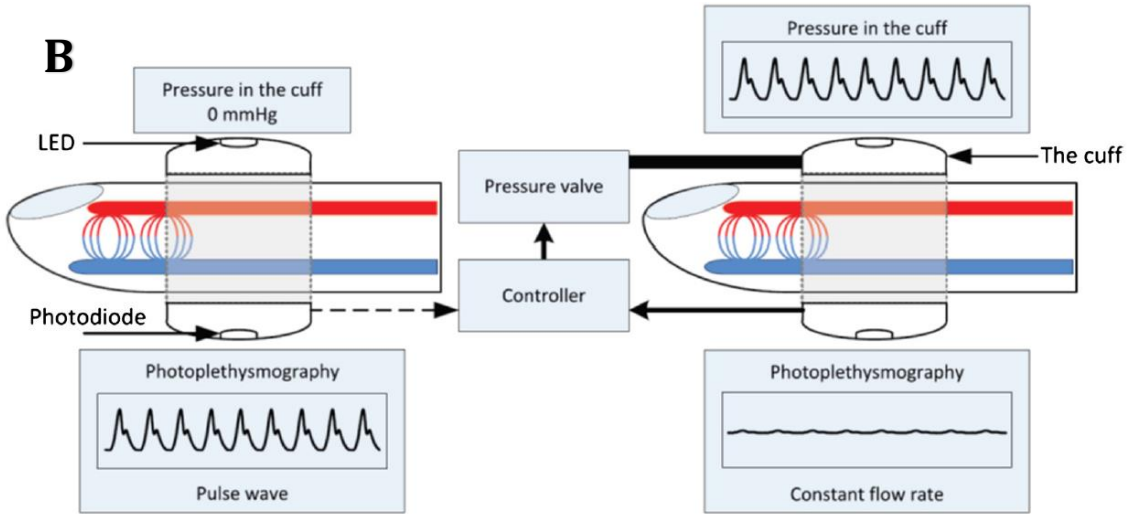

Fig.4 *A) Wrist and finger Cuff, B) Finger photoplethysmography (Fantini et al., 2016).*

The finger arterial diameter is kept constant at a preset point that is defined by an algorithm, in which search for the "unloaded" diameter when the pressure of the arterial wall is zero; meaning that the pressure inside is the same as the pressure outside the artery [Wesseling et al., 1995]. So, the pressure applied by the servo controller to the cuff to hold constant the artery diameter will represent the finger blood pressure. The pressure in the finger cuff is tuned by an air control unit placed around the wrist of a subject (Fig.4.A). Because the changes in hematocrit, stress and the tone of smooth muscle in the arterial wall will influence the unloaded diameter, the defined algorithm will recalibrate the unloaded diameter after each several heartbeats.

The information of changing in diameter is detected by an infrared photo-plethysmograph and sent to the servo-controller located in the finger cuff [Boehmer et al., 1987]. A photoplethysmography sensor consists of a light emitting diode (LED) and an optical detector (photodiode). The features of the detected optical signal related to the dynamic changes in arterial blood volume. When the finger cuff is not inflated (Fig.4.B, left panel), the plethysmography sensor which built into the finger cuff, detects the oscillations of light intensity due to the arterial expansion and contraction at the cardiac rate. Then a pulsating pressure is applied to the finger cuff by means of a fast pneumatic servo system that lets for arterial unloading. When the finger cuff is inflated to achieve arterial unloading at zero transmural pressure and the optical signal flattens out (Fig.4.B, right panel). In this state, there is no change in the arterial blood volume and the arterial pressure equals the cuff pressure. In this condition the temporal trend applied to the cuff pressure equals the temporal trend of ABP (Fantini et al., 2016).

In order to automatically determine the setpoint value at which to clamp the arteries under the cuff, a strategy was designed to determine this unloaded volume from the pressure-volume pulsations over a limited number of heartbeats when the counter pressure is gradually varied from zero to supra-systolic. This strategy was called “Physiocal”, that calibrates the physiology of the finger arteries under the cuff (K.H. Wesseling, 1995). The counter pressure generated in the cuff and the volume signal from the plethysmograph was shown in the (Fig.5).

The optical signal detected is also sensitive to the systolic and diastolic phases of the heart cycle. In this step, the servo controller of Finometer can estimate the heart rate (HR) with a new waveform.

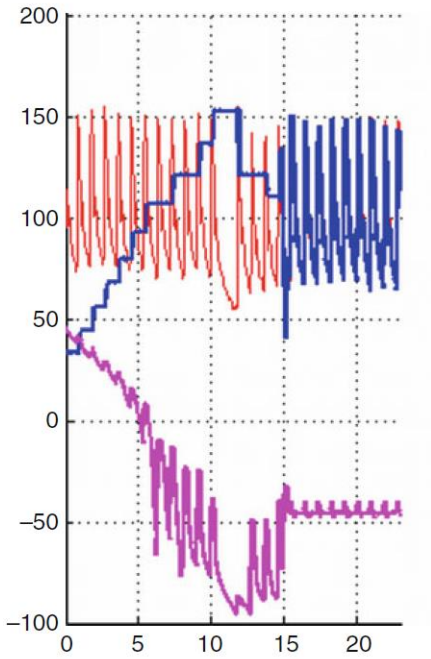

Fig.5 *Volume clamp setpoint by Physiocal: determine the unloaded volume setpoint from the pressure volume pulsations over a limited number of heartbeats when the counter pressure is gradually varied from zero to supra-systolic. Left panel: intra-arterial pressure (red), counter pressure generated in the cuff (blue) and the volume signal from the plethysmograph (purple) for 15 beats (Ehrenfeld and Cannesson, 2013).*

2.4.2 **Estimation of brachial blood pressure**

To estimate the brachial blood pressure from the finger blood pressure, an inverse modeling correction is used [Bos et al., 1996] because the pressure waveforms change in the path of going from brachial to finger arteries (Fig.6). The inverse modeling correction is a frequency dependent transfer function used as a filter, which has been developed by Gizdulich et al. in 1997 (Fig.7).

There is a distortion due to resonating at a frequency ranging from 4.26Hz to 10.58Hz depending on the subject (with the mean value of 8Hz). A frequency-dependent filter with an anti-resonance frequency of 8Hz was used in Finometer device to remove this distortion [Gizdulich et al., 1997].

Figure 7.A shows the transfer function amplitude (top line), the frequency-dependent filter amplitude (bottom line) and the expected result of the overall transfer function amplitude (middle line) of one subject. It is substantial that the transfer function amplitude should be as close as possible to 1. A deviation from this value will apply amplification or attenuation on the signal and make the distortion on the signal. As a fixed anti-resonance frequency at around 8Hz is used for all subjects, it will create discrepancies in the case subjects having their transfer function resonating at 5 Hz for example.

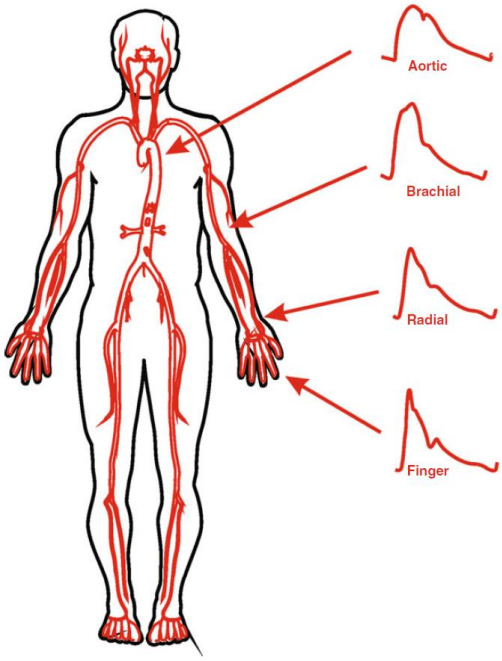

Fig.6 *Site of pressure measurement: because of reflections at the periphery (arterioles, capillaries), the arterial pressure waveform shapes change from rounded at the aortic sites to slightly peaked at the brachial site to more peaked at the more peripheral radial and finger artery sites (Ehrenfeld and Cannesson, 2013).*

In the case of an average person, figure 7 shows the effect of the inverse model on the shape of the brachial blood pressure with different frequencies. As shown, the inverse model would have a little bit effect on the shape of the brachial blood pressure in the low frequencies. But it will have a more significant influence in the high frequencies, which means the significant influence of the systolic pressure [Bos et al., 1996] (Fig. 7B).

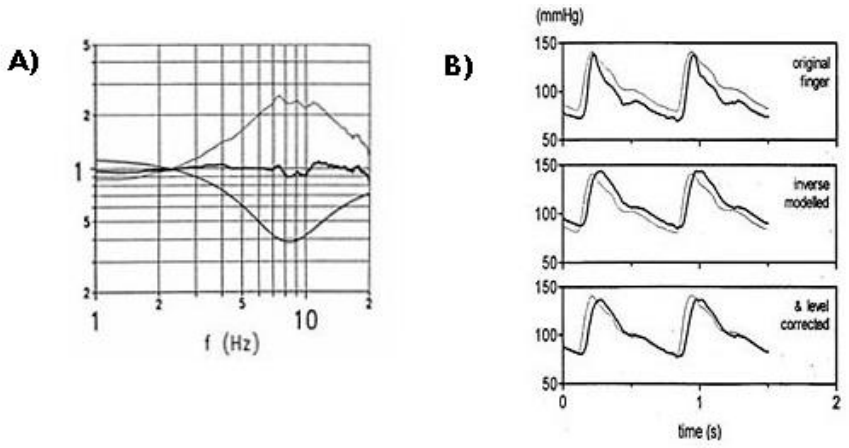

Fig.7 *A) Transfer Function Amplitude Comparison; B) Reconstruction of brachial blood pressure (gray line) from the finger blood pressure (black line) [from FMS website].*

The hydrostatic pressure is caused by the force of gravity on blood and has effect in the pressure gradient. So a height corrector is necessary to equilibrate the pressure gradient driving the flow from the brachial artery to the finger artery (Fig. 7B). This correction was applied by using two sensors for the finger and the brachial level (in upper-arm cuff). The return to flow calibration is done by an upper arm cuff positioned on the same arm as the finger cuff. Such as the idea of a standard sphygmomanometer, the upper arm cuff will completely stop the flow through the brachial artery if its pressure is higher than the systolic blood pressure (SBP). The pressure is then reduced until it reaches the SBP and lets the first pulsation that will be sensed and recorded by the finger cuff.

Therefore the parameters such as: the systolic blood pressure (SBP), the diastolic blood pressure (DBP), the mean arterial pressure (MAP), and the pulse pressure (PP) can be estimated with the Finometer.

2.4.3 Estimation of stroke volume and cardiac output

Cardiac output and Stroke Volume are estimated from finger arterial blood pressure by using the Langwouters' equation and the Model flow method. The Model flow method is a non-linear method by using the three elements model of the systemic vascular resistance (R_P), the aortic input impedance (Z0) and Windkessel arterial compliance (CW) [Wesseling et al., 1993].

The impedance element (Z0) displays the aortic opposition to the flow from the contracting left ventricle, the Windkessel arterial compliance element (CW) represents to the aortic elastic storing capacity and the resistance to an increase in blood volume, and the systemic vascular

resistance element (R_P) refers to the Poiseuille resistance of all vascular beds entirely [Wesseling et al., 1993; Harms et al., 1999]. Both elements of (Z0) and (CW) are dependent to the pressure as the elastic behavior of the aorta changes nonlinearly with the changing pressure [Langwouters et al., 1985; Bogert et al., 2005]. The values of (Z0) and (CW) are then calculated with an algorithm to achieve the aortic diameter from the intra-arterial pressure [Langwouters et al., 1984].

$$A(p) = A_{max}\left[0.5 + \frac{1}{\pi} arctan\left(\frac{p - p_0}{p_1}\right)\right] \quad (24)$$

Where A_{max}, $p_{0,}$ and p_1 are the parameters related to the age and the sex of the subject.

The aortic flow waveform will be estimated from the finger arterial blood pressure waveform in the modelflow (Fig.8). Stroke volume (SV) will be calculated from the integral (area under the curve) of the aortic flow waveform and cardiac output (Q) can be calculated from the following equation:

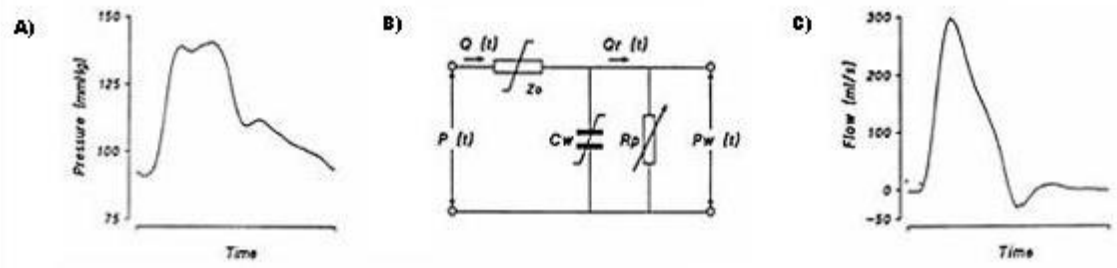

Fig.8 *A) Pressure waveform; B) Model flow method; C) Aortic flow waveform*

Figure 9 present all the process of the monitoring finger blood pressure and the estimation of brachial blood pressure, stroke volume and cardiac output in flowchart

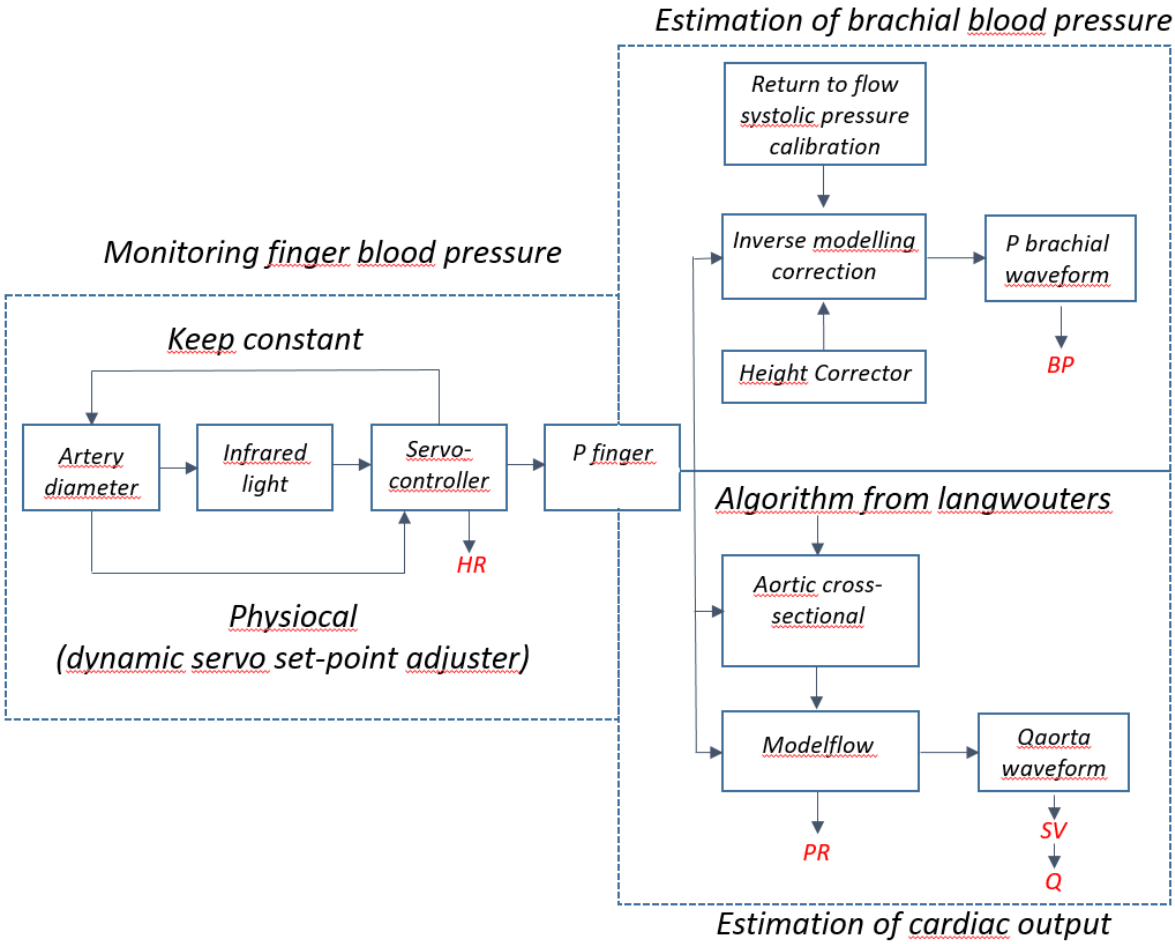

Fig.9 *Schematic Representation of the FinometerTM Layout.*

CHAPTER

Safety of multimodal brain imaging methods 3

Safety issues in EEG

At present, there are not any known safety issues associated with EEG measurements. The only limitation is to use amplifiers which are designed and built on a high standard quality basis. For instance, EEG amplifiers should meet all obligatory requirements for medical devices to avert adverse effects created by electrical short circuits, voltage variations, or other forms of device failure. EEG is considered as being non-obtrusive, non-harmful, and non-invasive. Therefore, there are no serious medical or ethical restraints related to this device. Thus, this device can regularly be used to investigate cerebral processes of normal and abnormal adult subjects as well as neonates.

Safety issues of optical imaging

The propagation of laser light energy through the tissues is an important issue in optical imaging. Thus, the impact of lasers is a critical factor that requires being considered to evaluate the effectiveness and laser safety of these systems, especially with high power consumption. Due to the specificity of neonatal head tissues, it is therefore essential to test the safety of our new optical imaging set up (e.g., DCS lasers) in preemies as a very specific, sensitive population.

Increasing the body temperature leads to several effects such as hyperthermia, coagulation, and other irreversible tissue effects. The thermal impact on tissue changes drastically when the temperature rise exceeds 42 °C (Jeong et al., 2003a). No evident thermal impacts are detected from 37 to 41°C. By increasing the temperature, the first effect is hyperthermia (Table 1). The

hyperthermia mechanism by which some molecular bonds are destroyed and the membrane is altered ranging from approximately 42–50°C. However, these effects in this temperature range are reversible. Beyond 50°C, a measurable reduction in enzyme activity is observed. From 60°C, denaturation of proteins and collagen occurs which leads to tissue coagulation and cell necrosis. From 100°C, water molecules start to vaporize. At temperatures exceeding 100°C, carbonization is observable. Finally, beyond 300°C, melting might occur. Table 1 depicts the summarized heat effects for different temperatures.

Table 1. *Thermal effects of laser radiation. Adapted from Niemz (2003)(Niemz, 2004)*

Temperature	Biological effect
37°C	Normal
45°C	Hyperthermia
50°C	Reduction in enzyme activity, cell immobility
60°C	Denaturation of proteins and collagen, coagulation
80°C	Permeabilization of membranes
100°C	Vaporization, thermal decomposition (ablation)
> 100°C	Carbonization
> 300°C	Melting

However, the ability to perceive changes in skin temperature depends on a number of variables including the location of the simulation, the amplitude and rate of the temperature change, and the baseline temperature of the skin. The rate that skin temperature changes influences how readily people can detect the change in temperature. If the temperature changes very slowly, for example at a rate of less than 0.5 °C per minute, then a person can be unaware of a 4-5 °C change in temperature (Kenshalo and Scott, 1966), providing that the temperature of the skin remains within the neutral thermal region of 30-36 °C. If the rate of energy deposition is faster

than the rate of thermal diffusion (thermal confinement), then the temperature of the exposed tissue rises. If a critical temperature is reached (typically about 10°C above basal), then thermal damage occurs (Glickman, 2002). This critical temperature varies very slowly with time and is a function of the thermal reaction considered.

In this study, we investigated the thermal effect of different laser powers with various spot sizes and different head tissue characteristics on neonatal and adult quasirealistic head models, that has been published in Neurophotonics journal;

Nourhashemi M, Mahmoudzadeh M, Wallois F. "Thermal impact of near-infrared laser in advanced noninvasive optical brain imaging. Neurophotonics". *2016 Jan;3(1):015001. doi: 10.1117/1.NPh.3.1.015001. Epub 2016 Jan 14.*

Thermal impact of near-infrared laser in advanced noninvasive optical brain imaging

Mina Nourhashemi
Mahdi Mahmoudzadeh
Fabrice Wallois

3.1 Abstract

The propagation of laser light in human tissues is an important issue in functional optical imaging. We modeled the thermal effect of different laser powers with various spot sizes and

different head tissue characteristics on neonatal and adult quasi-realistic head models. The photothermal effect of NIR-laser (800nm) was investigated by numerical simulation using finite-element-analysis. Our results demonstrate that the maximum temperature increase on the brain, for laser irradiance between 0.127W/cm^2 (1mW) and 12.73W/cm^2(100mW) at a 1mm spot size, ranged from 0.0025 to 0.26°C and from 0.03 to 2.85°C at depths of 15.9mm and 4.9mm in the adult and neonatal brain, respectively. Due to the shorter distance of the head layers from the neonatal head surface, the maximum temperature increase was higher in the neonatal brain than in the adult brain. Our results also show that, at constant power, spot size changes had a lesser heating effect on deeper tissues. While the constraints for safe laser irradiation to the brain are dictated by skin safety, these results can be useful to optimize laser parameters for a variety of laser applications in the brain. Moreover, combining simulation and adequate in-vitro experiments could help to develop more effective optical imaging to avoid possible tissue damage.

3.2 Introduction

Conventional optical imaging systems typically include certain basic components such as various types of lasers and flexible fiber optics (Scholkmann et al., 2014). Over recent decades, optical methods have been used to monitor brain function (Izzetoglu et al., 2004), neurovascular coupling that is correlated with brain activity, brain hemodynamics, cerebral blood volume and oxygenation (Goldman, 1990), (Duarte, 2008). Such modalities have a broad range of practical imaging applications, in both adults and neonates (Ferrari and Quaresima, 2012), (Obrig, 2014), particularly in premature neonates (Roche-Labarbe et al., 2007a), (Mahmoudzadeh et al., 2013b), ranging from changes in tissue oxygenation (by Near-Infrared Spectroscopy, NIRS) and cerebral blood flow measurement (by Diffuse Correlation Spectroscopy, DCS) (Durduran et al., 2010c), (Duarte et al., 2012) to changes in membrane configuration such as neuron swelling and shrinking (Fast Optical Signal, FOS) (Manoochehri et al., submitted). The photothermal impact of lasers is a critical parameter that needs to be determined in order to evaluate the effectiveness and laser safety of these systems especially with high power consumption, (50mW) (Roche-Labarbe et al., 2010), (Boas et al., 1995a), (Boas and Yodh, 1997), (Pine et al., 1988), (~60mW) (Lin et al., 2013a) and (300mW)(Milej et al., 2014). Laser has photothermal interactions with tissues (Dua and Chakraborty, 2005), caused by the temperature rise due to laser irradiation, which may cause damage to the tissues (Welch and van Gemert, 1995), including protein denaturation, increased mitochondrial

membrane permeability and ultimately vaporization (Ganguly, 2012). Temperature increases can also lead to changes in cellular metabolism, electrical membrane capacitance and, in the long term, can lead to necrosis (Fujii and Ibata, 1982), (Seese et al., 1998), (Thompson et al., 2012), (LaManna et al., 1989), (Dewey et al., 1977), (Ito et al., 2000). However, the mechanisms responsible for tissue damage from heat exposure are complex and still poorly understood. Although no obvious thermal impacts are detected at skin temperatures of 37 to 41°C, a temperature increase above 41°C and up to 50°C likely results in reversible membrane alterations (Dewey et al., 1977), (Kim et al., 1982), (Jeong et al., 2003b). The normal skin surface temperature, depending on environmental conditions, is usually around 31°C; a sustained temperature increase by more than 10°C can therefore lead to tissue damage (Ito et al., 2000), (Vander et al., 2001). Irreversible mechanisms then occur, resulting in cell death (Jeong et al., 2003b). The temperature known to induce cell injury is 10°C when studied *in vitro*, resulting in vascular damage such as angiogenesis or necrosis (3°C)(Seese et al., 1998), aberrant neuronal activity in guinea pig olfactory cortical slices (2°C) (Fujii and Ibata, 1982), cortical spreading depression (3.4°C) (Ueda et al., 1977) or axonal injury (1°C). Furthermore, temperature increases greater than 1°C can have long-term effects on brain tissue (LaManna et al., 1989), (Denda et al., 2010).

The propagation of laser light energy through the tissues is therefore an important issue in optical imaging. Effective functional optical imaging can be achieved by tailoring the laser parameters to the optical characteristics of the target tissue (heat capacity, thermal conductivity, absorption coefficient, scattering coefficient). Laser parameters (e.g. radiant energy, frequency, spot size, pulse duration) should be carefully chosen to optimize imaging efficacy while minimizing undesirable tissue damage. The energy delivered to the tissues must be determined in order to ensure safety standards in optical imaging. The specific limits of laser power that determine the harmful effects of heat on neonatal tissue are poorly elucidated. Due to the specificity of neonatal head tissues, such as thin skin and skull, tissue absorption coefficients may be different from those observed in adults (Cope and Delpy, 1988). It is therefore essential to test the safety of optical imaging lasers in this specific, sensitive population.

The purpose of this study was to model the photothermal interaction of NIR laser on human tissues. We investigated the influence of heat and fluence rate of various laser radiant powers on two head models (adult vs neonate). The temperature distribution inside the tissue was modeled using FEM simulations and the bio-heat transfer equation to determine the transient

temperature function required to calculate the photothermal interaction. A range of different laser powers (1mW-100mW) with various spot sizes, different skin and brain absorption coefficients, temperature distribution profiles in adults vs neonates and the influence of blood perfusion were investigated using the simulated model. Laser irradiation was simulated using the diffusion theory and was validated by comparing with Monte-Carlo method.

Laser wavelength and power are the effective parameters in tissue-delivered energy. These properties, using wavelengths longer than 950 nm, have been extensively used for laser surgery (Bozkurt and Onaral, 2004). In this paper, we investigate the effect of laser on neonatal and adult head tissues in the lower NIR spectrum [600nm-900nm] used in functional optical imaging. We also discuss our mathematical approach and its limitations.

The laser hazard class depends on the potential to cause biological damage (ANSI Z136.1-2014, IEC 825-1)(Institute, 2014). Accessible Emission Limit (AEL) and Maximum Permissible Exposure (MPE) for a given wavelength and exposure time were considered to evaluate the risk of injury (Table 1) (AEL= MPE × Area of Limiting Aperture). According to the above standards, the MPE (frequency and time-dependent) is the highest power (W/cm^2) of a light source that is considered to be safe and is usually about 10% of the dose associated with a 50% chance of causing damage (Schröder, 2000) under worst-case conditions.

According to ANSI[3], the 3.5 mm Limit Aperture Diameter (LAD) of irradiated laser was selected, as, for Near-IR exposures to the skin lasting longer than 10 seconds, involuntary movements of the body and heat conduction will result in an average irradiance profile over an area of about 10 mm^2 (even when the irradiated body part is intentionally kept still) (Protection).

Table 1. *Maximum permissible exposure (MPE) for skin exposure to a laser beam (From ANSI Z136.1-2014), t is the laser exposure duration, CA =* $10^{0.002(\lambda-700)}$

Wavelength (nm)	Exposure time, t (s)	MPE
400-1400	10^{-7} to 10	$1.1\times CA\times t^{0.25}(J.cm^{-2})$
400-1400	10 to 3.0×10^4	$0.2\times CA$ ($W.cm^{-2}$)

[3] https://www.rli.com/resources/articles/classification.aspx

3.3 Materials and Methods

To evaluate the thermal impact of NIR laser light in optical imaging in human head tissues, we used Finite Element Analysis (FEA), using the laser radiant power and exposure time. Two quasi-realistic six-layered models of neonatal and adult head tissues were simulated during irradiation by a focal infrared laser beam. To simulate the thermal interaction due to laser irradiation by different laser radiant powers and head model tissues (neonate vs adult), the bio-heat diffusion model was calculated by finite-element solver COMSOL Multiphysics. The resulting thermal distribution under steady-state conditions and their time profiles were investigated. As blood flow is a factor with a major impact on heat, we further investigated the influence of blood perfusion on local heating induced by laser irradiation.

3.3.1 Numerical analysis and modeling of heat transfer in the tissues due to the laser source

Heat transfer from the laser source to the surrounding tissues was simulated by using the FEA method and bio-heat equation. This model includes heat conduction, convection through blood flow, metabolic heat generation in the tissue, and heat generation by the laser source. In this model, the tissues were assumed to be homogeneous and isotropic. The temperature distribution was obtained by solving the bio-heat transfer equation (BHTE) (Pennes, 1948):

$$C\rho\frac{\partial T}{\partial t} = \nabla.(k\nabla T) + A_0 - B_0(T - T_B) + Q_{ext}[\frac{w}{m^3}] \quad (1)$$

Where T is temperature (◦C), C is specific heat [J/ (kg ◦C)], ρ is tissue density (kg/m^3), k is thermal conductivity [J / (m s ◦C)], A_0 is the basic metabolic rate [J / (m^3 s)], B_0 ($\rho_b c_b \omega_b$) is the blood perfusion coefficient [J / (m^3 s ◦C)] that includes blood specific heat $C_b(\frac{j}{kg.K})$, blood perfusion rate $w_b(\frac{1}{s})$ and mass density of blood $\rho_b(\frac{k}{m^3})$, T_B is the temperature of blood (◦C), and Q_{ext} is the external heat source (W/m^3). This equation computed the temperature distribution within the tissue at different times during laser irradiation.

To solve the bio-heat equation, the boundaries of the model, except for the surface of the skin layer exposed to air, were considered to be at body temperature. At the surface in contact

with air, it was assumed that heat transfer occurred as a result of free convection into air (heat transfer by radiation into the air would be negligible), which is described by:

$$n.(k\nabla T) = h(T_{ext} - T) \quad (2)$$

Where n is the outward normal vector, h is a heat transfer coefficient to control convective cooling to the model ($W/m^2.K$), defined as 5 $W/m^2.K$ for air, T_{ext} is the external temperature defined as 24°C for air, T is the internal temperature of model, and k is the thermal conductivity (W/m.K) (2006; Kim et al., 2007).

3.3.2 Modeling the Laser Source

To simulate the heat generated by the laser irradiation (the source term Q_{ext}), a spatially Gaussian and temporally continuous laser beam was modeled perpendicular to the surface of the model to simulate an optical fiber positioned orthogonally to the surface.

Light propagation in biological tissue results from the diffusion approximation of the radiative transfer equation and is defined by (Saouli and Mansour, 2013):

$$\frac{1}{c}\frac{d}{dt}\phi(r,t) - \nabla\left(\frac{1}{3(\mu_a+\mu_s)}\right)\nabla\phi(r,t) + \mu_a\phi(r,t) = S(r,t) \quad (3)$$

Where: c is the light speed in a vacuum, μa is the absorption coefficient, μs is the reduced scattering coefficient, $\boldsymbol{\phi}$ is the photon intensity and S(r, t) is the local photon source ($Q_{ext}=\mu_a.\boldsymbol{\phi}$). The photon-diffusion equation was used to calculate photon propagation in strong-scattering media such as biological tissues. The diffusion approximation can correctly predict light transport in a region far from the laser source, where all photons are scattered at least several times (Farrell and Patterson, 2001; Gobin et al., 1999). In skin, these conditions are only satisfied in the deeper levels of the dermis and do not apply to the epidermis, where scattering of radiation remains highly anisotropic. A skin depth of 0.4mm was therefore used for further skin investigation. Different power levels were investigated and the results were compared between neonatal and adult head models. Dirichlet and Robin boundary conditions were applied by equations (4), (5).

$$\phi(r,t) = 0 \quad (4)$$

$$\phi(r,t) + 2\frac{1}{3(\mu_a + \mu_s)}\frac{1+R}{1+R}\frac{\partial\phi(r,t)}{\partial n} = 0 \quad (5)$$

Where, n is the normal vector and (R= 0) is the reflection parameter.

3.3.3 Model

Two quasi-realistic six-layer head models in a 3-D Cartesian (x, y, z) coordinate, were simulated to solve light propagation equations in neonatal and adult head tissues, as shown in Figure 1. The thickness of the skin, fat, skull, dura, CSF and brain were defined as shown in Table 2, for the adult and neonatal models. The minimum thickness of neonatal skin was extracted from the distribution of skin thicknesses measured *in vitro* as a function of gestational maturity (Saidi, 1992b). For the sake of simplicity, the curvature of the 6 layers was not considered. To assume that the temperature at the boundary of the selected region was equal to body temperature (37 °C), a sufficiently large thickness (80mm) of brain tissue was selected. The model size was defined as (radius=80mm, height=80mm), fourfold larger than the area affected by laser radiation, in order to conserve the semi-infinite nature of the model (X. Ronghou, 2014). The optical source was simulated in which the laser source emits a Gaussian and temporally continuous laser beam. Different radii of laser spots (0.2, 0.4, 0.6, 1, 3, 5, 7, 11, 15mm) for different powers (from 10 to 200mW) were investigated.

Table 2 *Tissue thickness (mm) of six-layer adult and neonatal head models*

	Skin	Fat	Skull	Dura	CSF	Brain
Adult	**5**(Bamett et al., 2003; Kiguchi et al., 2007; Madsen, 2012)	**1.4**(**Khodabakhshi and Cheldavi, 2010; Rahmat-Samii and Kim, 1998**)	**7**(Bamett et al., 2003; Kiguchi et al., 2007; Madsen, 2012)	**0.5**(Genina et al., 2005; Khodabakhshi and Cheldavi, 2010)	**2**(Kiguchi et al., 2007; Rahmat-Samii and Kim, 1998)	**80**
Neonate	**0.5**(Saidi, 1992b)	**1.4**(Khodabakhshi and Cheldavi, 2010; Rahmat-Samii and Kim, 1998)	**2**(Kiguchi et al., 2007)	**0.5**(Genina et al., 2005; Khodabakhshi and Cheldavi, 2010)	**0.5**(Kiguchi et al., 2007)	**80**

The adult and neonatal models consisted of 1,564,530 and 1,024,918 tetrahedral elements, respectively. The maximum element size of the refined mesh around the light source was 0.01 mm. The diffusion equation is valid in the case of large scattering compared to absorption and

when studying diffuse light propagation, i.e. at sufficient distances from any light sources. These considerations were applied to the physics of the model.

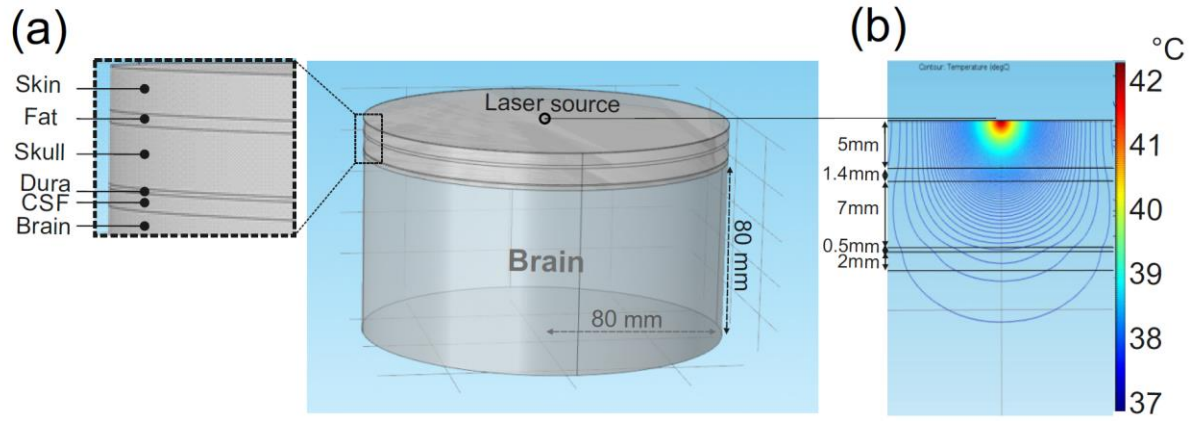

Fig. 1 (a) *Geometrical structure of 3D-CAD composed of six layers (skin, fat, skull, dura, CSF and brain) (inset shows a zoom up region). The origin was situated immediately under the source.* ***(b)*** *Distributions of the photon-fluence rate in the head calculated in the head model.*

3.3.4 Thermal and optical properties for various tissues

The tissue parameters of the model, such as thermal conductivity, density, heat capacity at constant pressure, metabolic rate, blood perfusion for the six different layers, are shown in Table 3, 4 (DeMarco et al., 2003). The brain perfusion rate used in this study was 0.00932 s^{-1} ≈ 0.56 min^{-1}, which is comparable to the value measured *in vivo* with ASL-fMRI (Rowland and Tozer, 1995; Shargel et al., 2004). Grey and white matter were considered to have the same thermal properties (Kim et al., 2007). The effect of cerebral metabolism on brain temperature was considered to be negligible (Iwata et al., 2014; Kauppinen et al., 2008), allowing the metabolic rate for adults and neonates to be considered to be identical. Brain function and metabolic activity are indicated by oxygen concentration and glucose intake in brain cells (Gordon et al., 1976; Scheinberg et al., 1954).

The NIR laser wavelength in the middle of biological optical windows (600nm-900nm) was selected for further investigation (isosbestic point: 800 nm) (Vo-Dinh, 2014). The scattering coefficients were acquired by the following equation:

$$\mu_s' = a.(\lambda / 500nm)^{-b} \quad (6)$$

Where a, b, λ are scattering amplitude (related to scatterer density (cm^{-1})), scattering power (related to scatterer size distribution) and wavelength in nm, respectively. a and b coefficients

for different tissues were selected according to (Jacques, 2013). Absorption and scattering coefficients of different adult and neonatal tissues are given in Table 5. For the 800 nm wavelength, similar optical properties for neonatal and adult skin were obtained from (Jacques, 2013) and (Vo-Dinh, 2014), respectively.

Discrepancies were observed concerning the precise value of absorption and scattering coefficients. This difference could be derived from the discrepancy between theoretical and experimental results. In general, *in vivo* μ_a and μ_s values for human skin were significantly smaller than those obtained *in vitro* (about 10 and 2 times, respectively (Tuchin and Engineers, 2007)). For μa, the discrepancy may be attributed to the low sensitivity of the double-integrating sphere, and goniometric techniques were applied for *in vitro* measurements at weak absorption combined with strong scattering ($\mu_a << \mu_s$) and sample preparation methods.

The absorption coefficients in our study were adopted from the most recent complete reference concerning the optical properties of tissues (Vo-Dinh, 2014). Different percentages of melanin [Melanosomes per unit volume]%=0.87, 1.15, 1.65% corresponding to the skin absorption coefficient $\mu_{a(skin)}$= 0.52cm^{-1}, 0.65cm^{-1}, 0.88cm^{-1} (Jacques, 2013) were applied in our model. A wide range of skin absorption coefficients (0.5 cm^{-1} also including 0.1 cm^{-1}, 0.2 cm^{-1}, 0.3 cm^{-1}, 0.4 cm^{-1}) was investigated. In addition, different ranges (0.01 cm^{-1}, 0.05 cm^{-1}, 0.1 cm^{-1}, 0.5 cm^{-1}) of adult brain absorption coefficients were considered (Tuchin and Engineers, 2007).

Table 3 *Thermal properties of the six layers of the head (skin, fat, skull, dura, CSF and brain) (DeMarco et al., 2003).*

	Thermal conductivity (W/m.K)	**Density (kg/m^3)**	**Heat capacity at constant pressure (J/(kg.K))**
Skin	0.420	1010	3500
Fat	0.250	920	2500
Skull	0.30	1810	1300
Dura[4]	0.44	1174	3364
CSF[4]	0.57	1007	4096

[4] Taken from: www.itis.ethz.ch/itis-for-health/tissue-properties/database/database-summary/

Brain	0.503	1043	3600

Table 4 *Heat equation parameters of the six layers of the head (skin, fat, skull, dura, CSF and brain) (DeMarco et al., 2003).*

	Blood temperature $T_b(K)$	**Blood specific heat $C_b(\frac{j}{kg.K})$**	**Blood perfusion rate $w_b(\frac{1}{s})$ (Bernardi et al., 2000; DeMarco et al., 2003; Duck, 2013; Williams and Leggett, 1989)**	**Mass density of blood $\rho_b(\frac{k}{m^3})$**	**Metabolic rate $Q_{met}(\frac{w}{m^3})$**
Skin	310.15	3840	0.00257	1060	1000
Fat	310.15	3840	0.00023	1060	180
Skull	310.15	3840	0.00004	1060	0
Dura[4]	310.15	3840	0.00744	1060	6914
CSF[4]	310.15	3840	0	1060	0
Adult brain	310.15	3840	0.00932	1060	10000
Neonatal brain	310.15	3840	0.00166 (Altman et al., 1988; Edwards et al., 1988; Kusaka et al., 2005)	1060	10000

Table 5 *Optical properties of the tissue components, corresponding to the six layers of the head (skin, fat, skull, dura, CSF and brain): absorption coefficient (Vo-Dinh, 2014), scattering coefficient (Jacques, 2013), (Saidi, 1992a), (van der Zee et al., 1993).*

	Absorption coefficients (cm^{-1})	**Scattering coefficients (cm^{-1})**
Skin	0.52 (Jacques, 2013; Vo-Dinh, 2014)	23.58 (Jacques, 2013)
Fat	0.11 (Vo-Dinh, 2014)	13.41 (Jacques, 2013)
Skull	0.11 (Vo-Dinh, 2014)	16.35 (Jacques, 2013)
Dura	0.70 (Vo-Dinh, 2014)	12.61 (Jacques, 2013)
CSF	0.01 (Vo-Dinh, 2014)	3.2 (Okada and Delpy, 2003)
Adult Brain	0.90 (Vo-Dinh, 2014)	11.34 (Jacques, 2013)

Neonatal Skin	0.52[Saidi, 1992a]	23.58[Saidi, 1992a]
Neonatal Brain	0.08[Tuchin and Engineers, 2007]	8.42[Tuchin and Engineers, 2007]

3.4 Results

The first section describes the light-induced heating due to exposure from various laser powers and the distribution profile due to photothermal interactions in various types of adult and neonatal head tissues. The following sections describe the effects of blood perfusion, various skin and brain absorption and scattering coefficients, laser spot size and different tissue thickness on the temperature distribution in head tissues. Moreover, Monte Carlo simulation was used to validate the diffusion theory.

3.4.1 Effect of various laser radiant powers on neonatal and adult head models

Figure 2 shows the various temperature change profiles as a function of the radial distance around an optical fiber tip (Laser spot size=1mm) in six different layers of the head models (skin, fat, skull, dura, CSF, brain) under steady-state conditions (Fig. 2a: Adult, Fig. 2b: Neonate). The maximum temperature increase, using NIR for laser powers between 1 mW and 100 mW (laser irradiance, I, between 0.127 W/cm^2 and 12.73 W/cm^2), with 10 mW increments, ranged from 0.16 to 16.12°C (on the adult head) and 0.13 to 13.51°C (on the neonatal head) at a skin depth of 0.4mm. However, the maximum temperature increase on the brain for laser powers between 1 mW and 100 mW ranged from 0.0025 to 0.26°C and from 0.03 to 2.85°C at depths of 15.9 mm and 4.9 mm in the adult and neonatal brain, respectively. Fig. 2c demonstrate the temperature changes at the depth of 0.4mm with various powers: 10 mW to 100 mW in 10 mW increments over time.

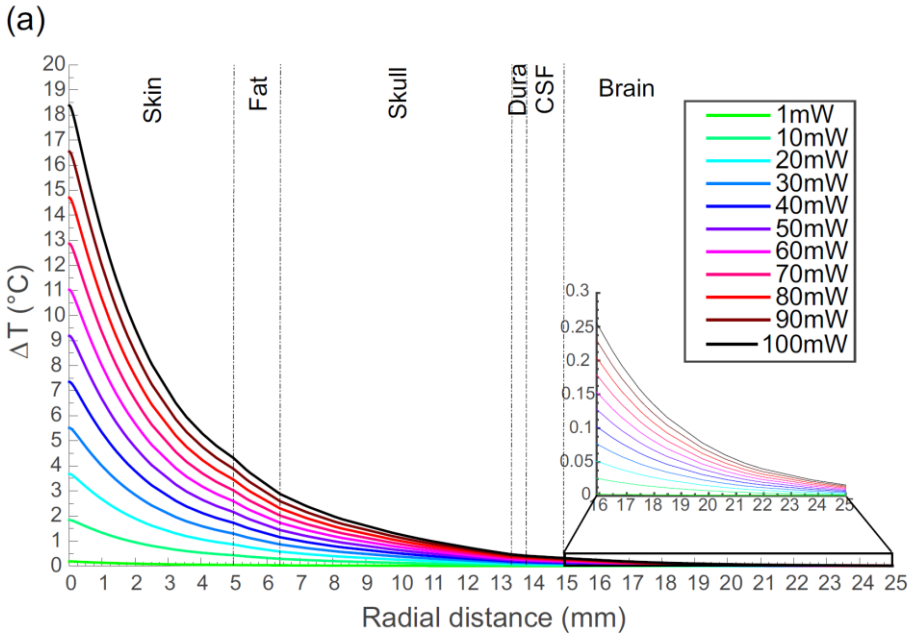
(a)
Skin
Fat
Skull
Dura
CSF
Brain
1mW
10mW
20mW
30mW
40mW
50mW
60mW
70mW
80mW
90mW
100mW
ΔT (°C)
Radial distance (mm)

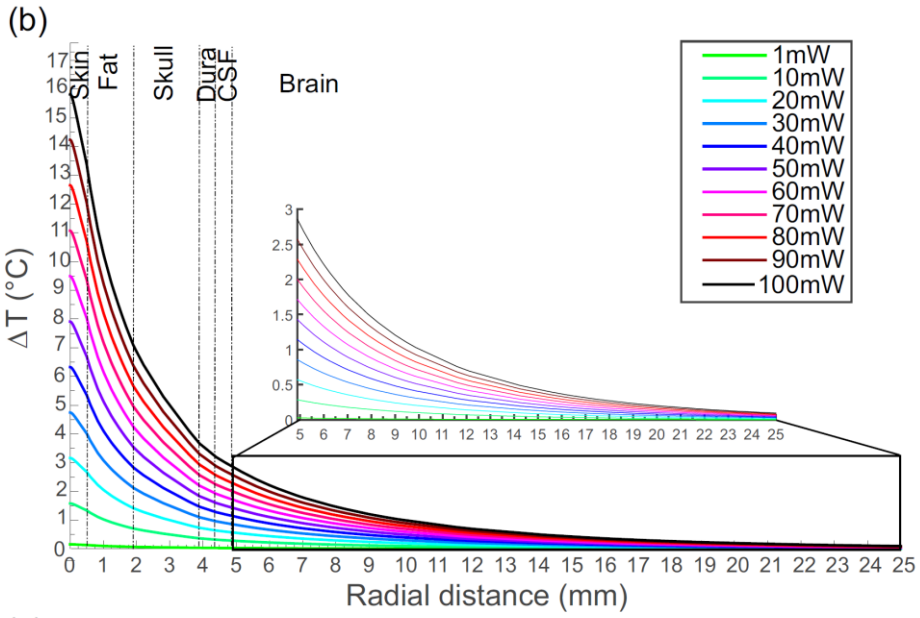
(b)
Skin
Fat
Skull
Dura
CSF
Brain
1mW
10mW
20mW
30mW
40mW
50mW
60mW
70mW
80mW
90mW
100mW
ΔT (°C)
Radial distance (mm)

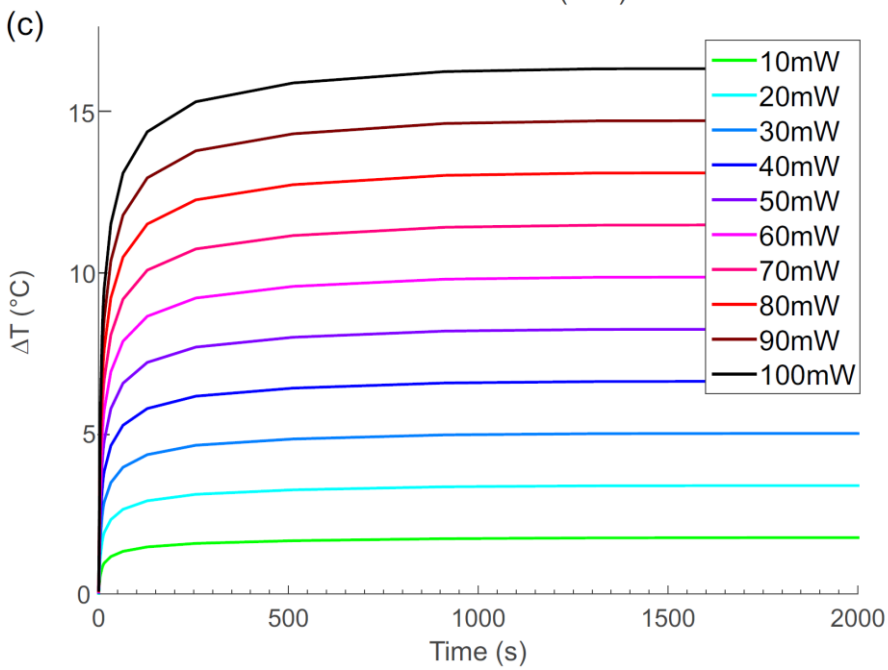
(c)
10mW
20mW
30mW
40mW
50mW
60mW
70mW
80mW
90mW
100mW
ΔT (°C)
Time (s)

Fig. 2 *Temperature changes according to radial distance from the laser source with various powers: 1 mW, 10 mW to 100 mW ten by ten (0.127 W/cm2 < I < 12.73 W/cm2), for a six-layered head model (skin, fat, skull, dura, CSF and brain) obtained from numerical simulations (inset shows a zoom up region). (a) Adult head model. (b) Neonatal head model. (c) Temperature changes at the depth of 0.4mm with various powers: 10 mW to 100 mW in 10 mW increments over time .*

3.4.2 Effect on neonatal vs adult tissue

The intensity and correlative temperature changes in adult and neonatal head tissues according to the depth from the surface under steady-state conditions were evaluated in order to compare temperature distribution profiles in the adult versus the neonatal model (Fig. 3). For instance, Figures 3 and 4 show the heat distributions for 3.81 W/cm^2 and the magnitude of laser penetration, respectively. As the skin and skull are much thinner in neonates, more light reaches the neonatal brain than the adult brain, which consequently results in a more marked temperature increase in the neonatal than in the adult brain. In the present study, using similar characteristics for neonatal and adult skin, the temperature increase was obviously the same in the two models. Due to the shorter distance of the other tissues from the surface in the neonatal head, the maximum temperature increase for 3.81 W/cm^2 was higher in the neonatal brain (ΔT=0.85°C) than in the adult brain (ΔT=0.07°C) (Fig. 3).

The light-distribution profiles on the brain surface for the respective models are presented in Figure 4, which shows the comparative distributions of the normalized intensity of photons (I/I_0) from the laser source (30 mW) for six layers of adult (lower diagram) and neonatal head models (skin, fat, skull, dura, CSF and brain). The depths of the brain from the skin surface were 15.9 mm for the adult model and 4.9 mm for the neonatal model. The horizontal axis represents the distance along the surface of the brain from the source. Comparison of the adult and neonatal models showed deeper scattering of light in the neonatal brain.

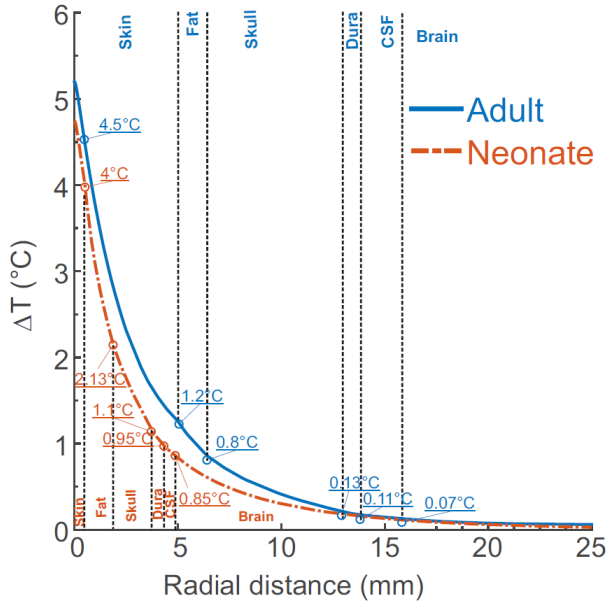

Fig. 3 *Temperature changes according to the radial distance from the laser source (I = 3.81 W/cm^2) for six layers of adult and neonatal head model (skin, fat, skull, dura, CSF and brain) obtained from numerical simulations.*

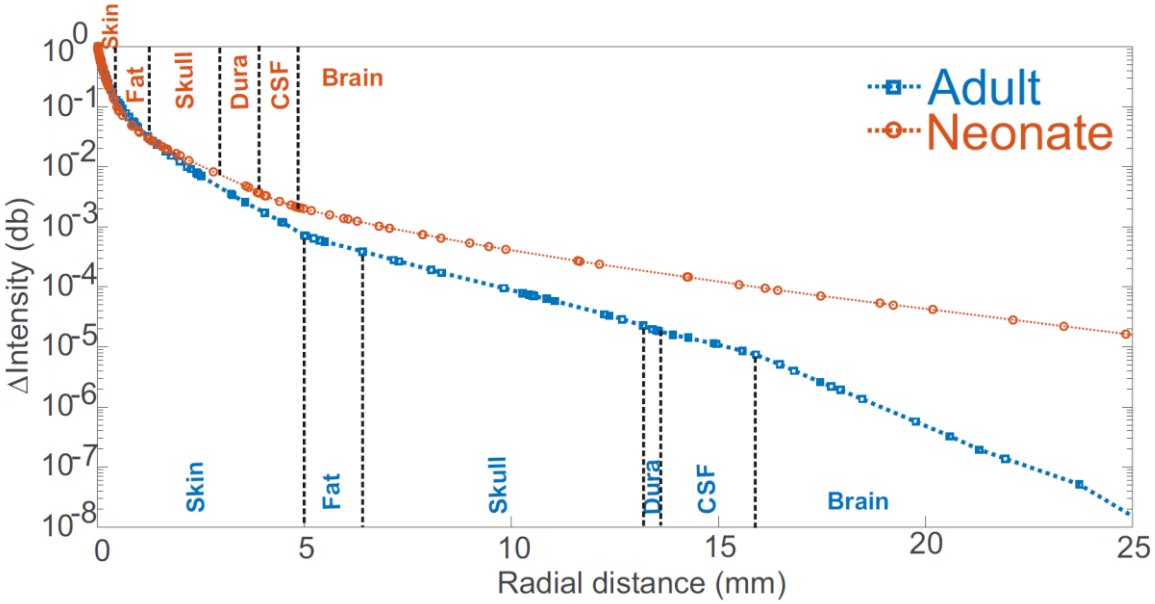

Fig. 4 *Comparative distributions of the normalized intensity of photons (I/I_0) according to the radial distance from the laser source (I = 3.81 W/cm2) for six layers of adult (lower diagram) and neonatal head models (skin, fat, skull, dura, CSF and brain) obtained from numerical simulations.*

3.4.3 Effect of blood perfusion

As blood flow has a major impact on tissue temperature regulation, we simulated two different conditions (presence and absence of blood perfusion) in the adult model to investigate the influence of blood perfusion on local heating induced by laser irradiation (Fig. 5a). The maximum temperature increase in the brain in the presence of blood perfusion (ΔT=0.07°C) was lower than in the absence of blood perfusion (ΔT=0.5°C), suggesting that, based on the numerical simulation, blood perfusion decreases the temperature rise by 0.43°C for 3.81 W/cm^2. Figure 5b shows the effect of different blood perfusion and metabolic rates on induced heat distribution in neonatal brain. Doubling the blood perfusion rate decreased temperature changes in the brain by about 0.1°C (Fig. 5b), whereas the laser-induced heat changes in the brain when the normal adult metabolic rate (10000 W/m^3) is decreased by one half can be considered to be negligible.

3.4.4 Effect of different skin and brain absorption coefficients

As accurate *in vivo* measurements of optical properties are not available, a wide range of these values had to be modeled. Figure 6 presents the evolution of the temperature profile as function of radial distance for different skin (Fig. 6a) and brain (Fig. 6b) absorption coefficients for 3.81 W/cm^2. The curves depict the temperature distribution in the skin and brain, in which a variation of the absorption coefficient ($\mu_{a(skin)}$: 0.1 cm^{-1} to 0.88 cm^{-1}; $\mu_{a(brain)}$: 0.01 cm^{-1} to 0.5 cm^{-1}) had a significant influence at a depth of 0.4mm in the skin (ΔT = 1.8°C to 6.9°C) but not in brain tissue (ΔT = 0.07100°C to 0.7148°C).

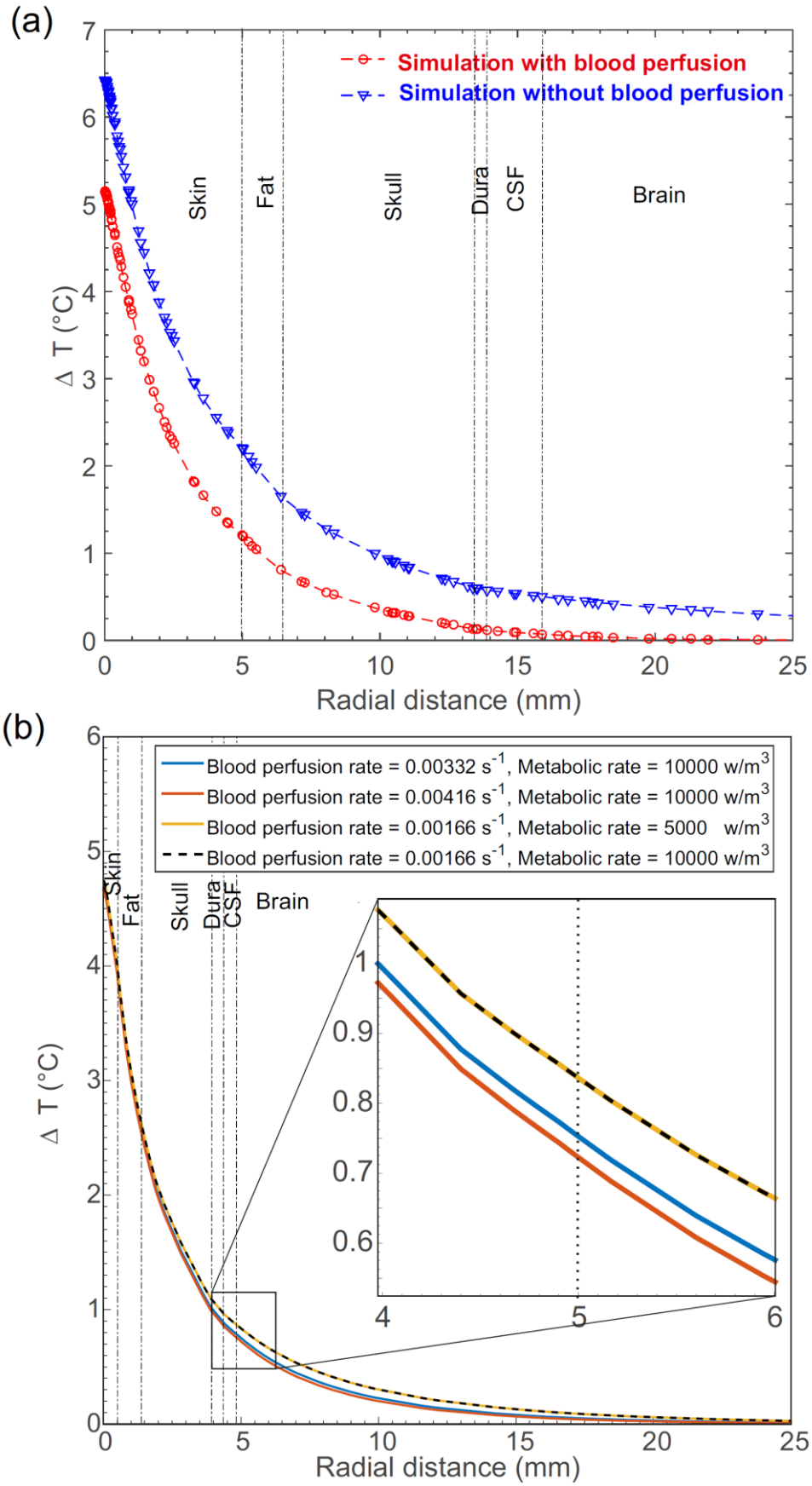
(a)
Simulation with blood perfusion
Simulation without blood perfusion
Skin
Fat
Skull
Dura
CSF
Brain
Δ T (°C)
Radial distance (mm)
(b)
Blood perfusion rate = 0.00332 s-1, Metabolic rate = 10000 w/m3
Blood perfusion rate = 0.00416 s-1, Metabolic rate = 10000 w/m3
Blood perfusion rate = 0.00166 s-1, Metabolic rate = 5000 w/m3
Blood perfusion rate = 0.00166 s-1, Metabolic rate = 10000 w/m3
Skin
Fat
Skull
Dura
CSF
Brain
Δ T (°C)
Radial distance (mm)

Fig. 5 *Comparative temperature changes according to the radial distance from the laser source (I = 3.81 W/cm^2) between six layers of the head model (skin, fat, skull, dura, CSF and brain)* ***(a)*** *with blood perfusion and without blood perfusion in adult* ***(b)*** *the effect of different blood perfusion rates and metabolism on induced heat distribution in neonatal brain.*

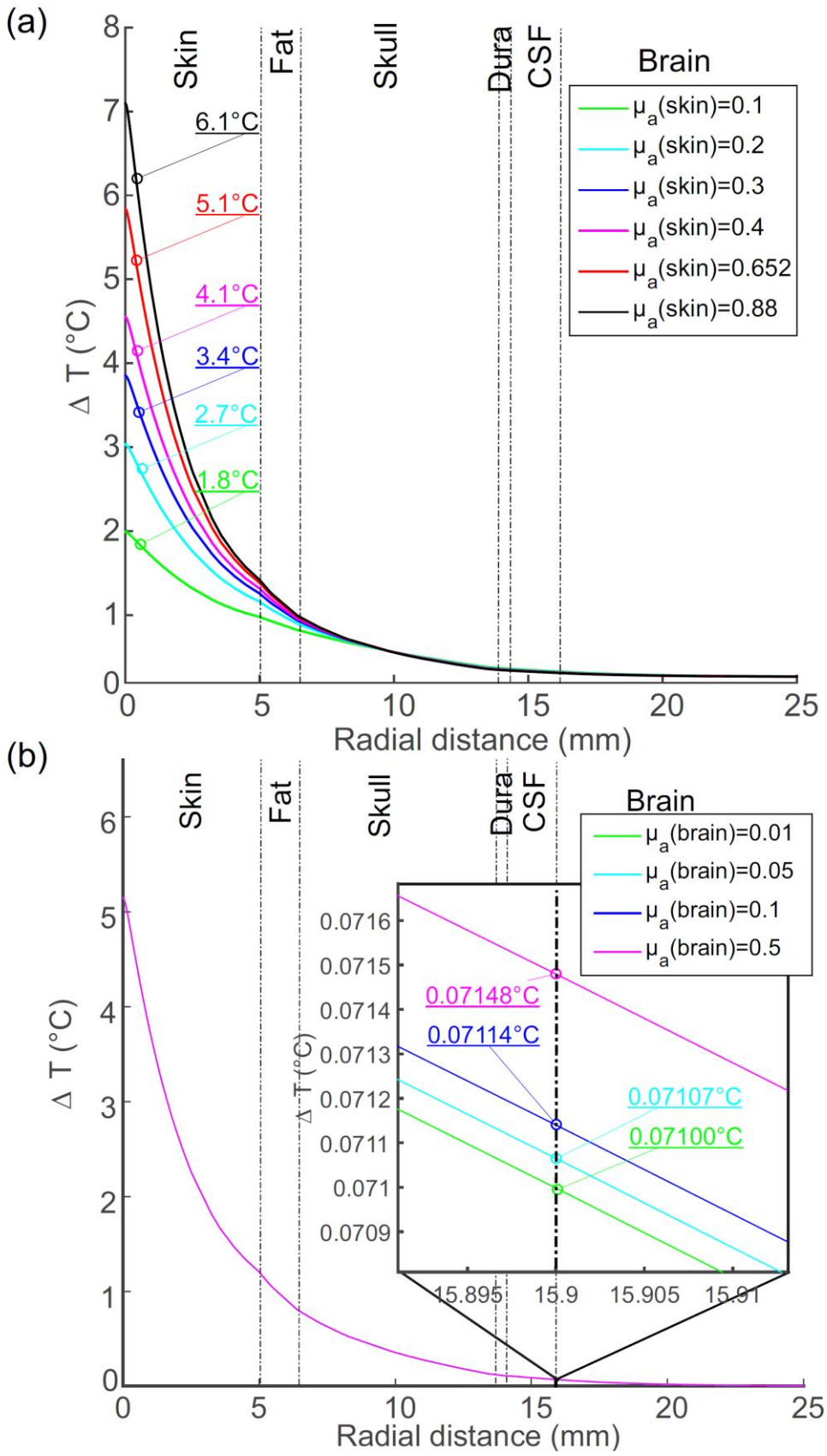
(a)
Skin
Fat
Skull
Dura
CSF
Brain
μa(skin)=0.1
μa(skin)=0.2
μa(skin)=0.3
μa(skin)=0.4
μa(skin)=0.652
μa(skin)=0.88
6.1°C
5.1°C
4.1°C
3.4°C
2.7°C
1.8°C
Δ T (°C)
Radial distance (mm)
(b)
Skin
Fat
Skull
Dura
CSF
Brain
μa(brain)=0.01
μa(brain)=0.05
μa(brain)=0.1
μa(brain)=0.5
0.07148°C
0.07114°C
0.07107°C
0.07100°C
Δ T (°C)
Radial distance (mm)

Fig. 6 *The temperature changes according to the radial distance from the laser source (I = 3.81 W/cm^2) with various absorption coefficients are shown; the lines correspond to different skin (a) and brain (b) absorption coefficients. (Inset shows a zoom up region)*

3.4.5 Effect of different Laser spot sizes

Laser spot size impacts the temperature profile. The effect of laser spot size on the temperature distribution in the skin and brain tissue of the adult and neonatal head models was investigated in the laser power range of 10 - 200mW (in order to investigate the effect of higher powers on the temperature profile by changing spot size). Figure 7 shows a more marked temperature decrease as the laser spot size was increased from 0.2mm to 15mm.

Figure 8 shows the temperature changes vs. irradiance (Fig. 8a: skin, Fig. 8b: brain). Temperature changes in the brain were 0.6059°C and 0.7182°C for the same irradiance of 0.113W/cm^2 with different powers and spot sizes (150mW, spot size=13mm) and (200mW, spot size=15mm), respectively. Higher powers and larger spot sizes (but with the same irradiance) therefore induced higher temperatures, implying that temperature changes depend not only on the magnitude of irradiance but also on the photon distribution (which depends on both power and spot size).

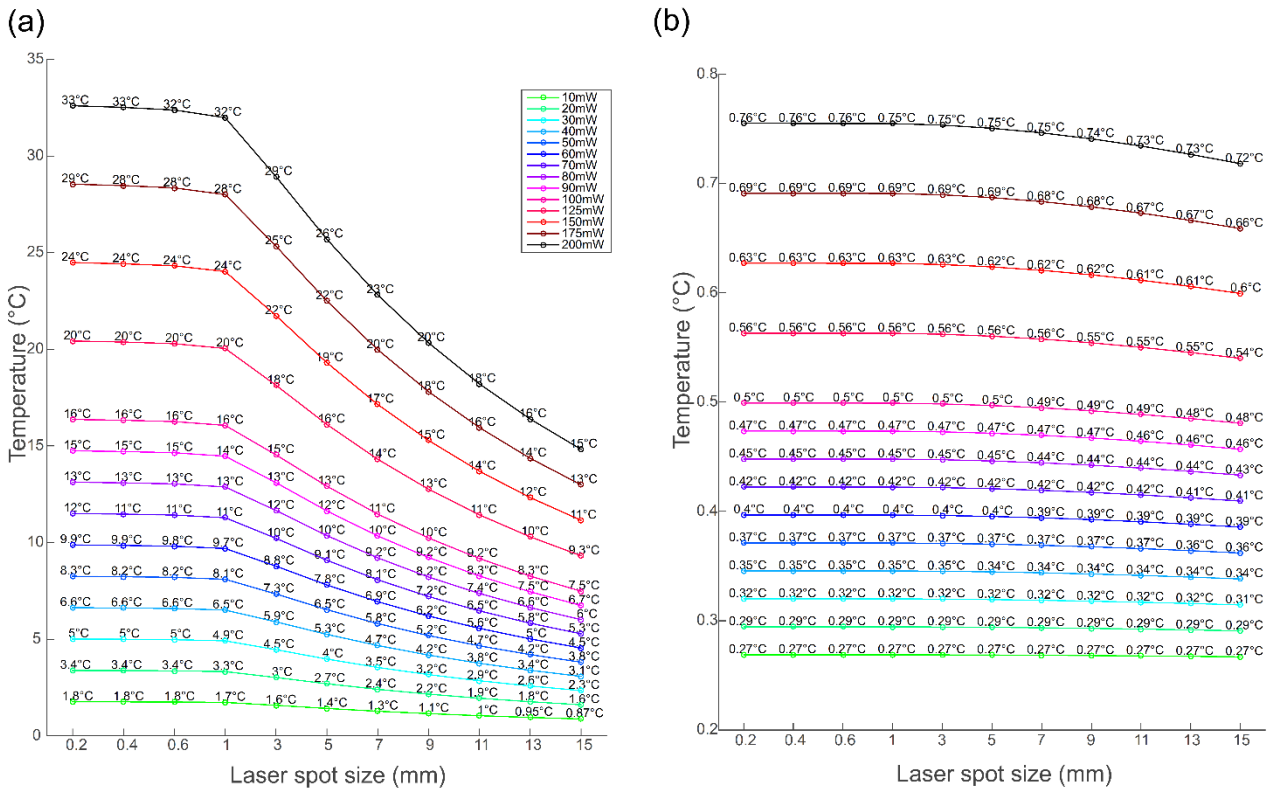

Fig. 7 *The effect of laser spot size on the temperature distribution in (a) adult skin and (b) adult brain tissue.*

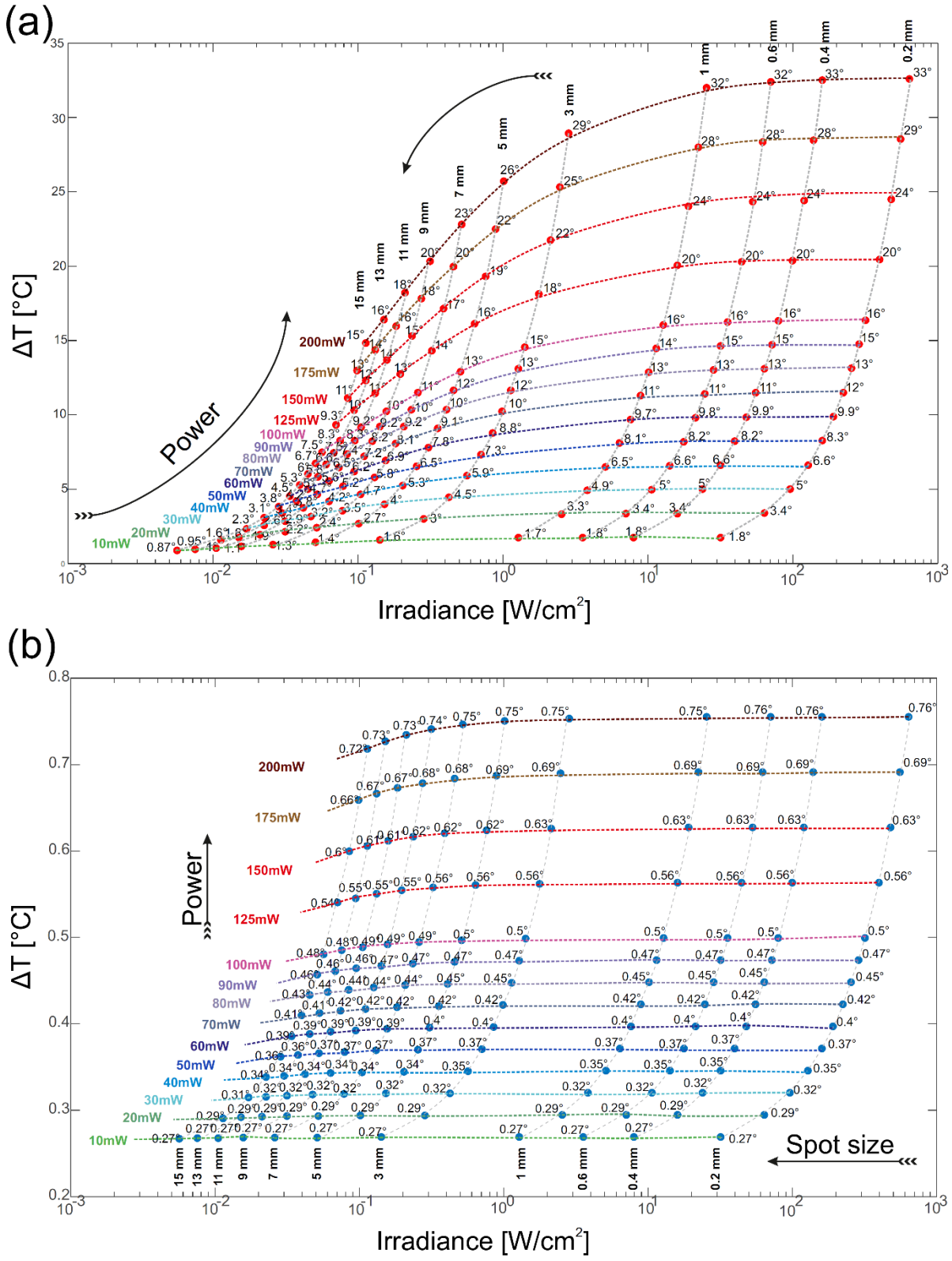

Fig. 8 *The effect of laser irradiance on the temperature distribution in (a) adult skin and (b) adult brain tissue.*

3.4.6 Effect of different tissue thicknesses

Different thicknesses were investigated, as tissue thickness is one of the parameters that needs to be accurate and they are estimated and variable according to different individuals and medical conditions. Figure. 9 shows the analysis of temperature changes in different tissues due to variations of the thickness of individual layers. Temperature changes were not largely affected by variations of the thickness of each layer: skin (3, 4, 5, 6 mm), fat (0.4, 1.4, 2, 3 mm), skull (5, 6, 7, 8 mm), CSF (0.1, 1, 2, 3 mm). In particular, the effect of thickness variations on deep tissues is negligible.

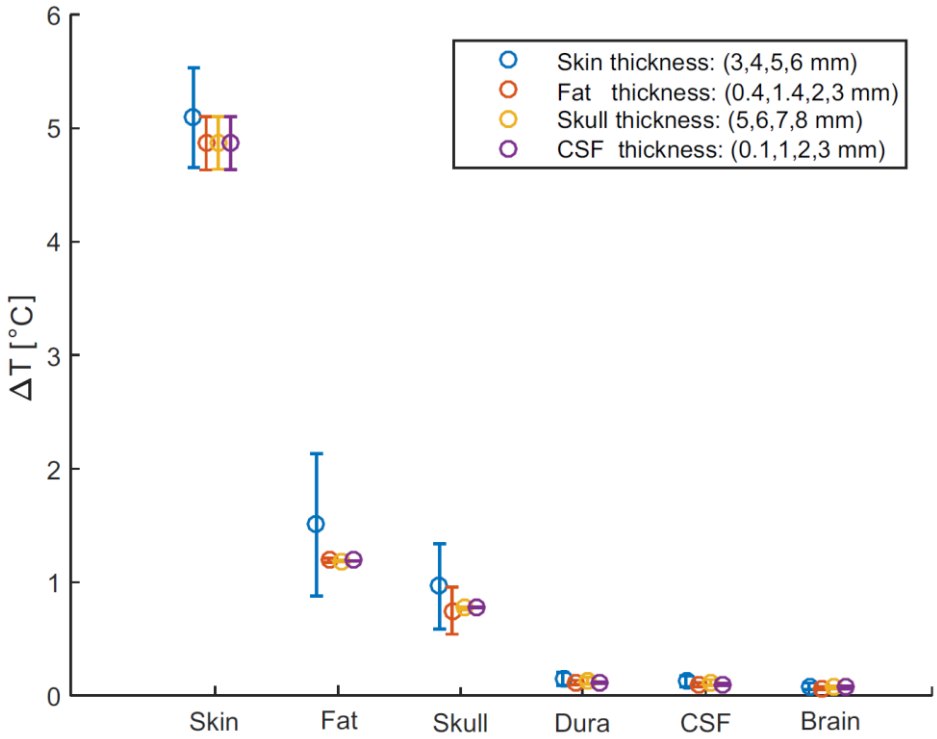

Fig. 9 *Temperature changes in different tissues due to variations in the thickness of individual layers.*

3.4.7 Validation of Diffusion Theory

The diffusion theory and the Monte Carlo approach have complementary attributes for modelling photon transport in a scattering medium. The Monte Carlo approach is precise but computationally inefficient, whereas the diffusion theory is inaccurate but computationally efficient. A trade-off must therefore be reached between the computational accuracy and efficiency of the two models. Using Monte Carlo improves the computational accuracy at the expense of computational efficiency. Although the diffusion theory is acceptable when the

isotropic point source is situated far from the surface of the scattering medium, it becomes less accurate as the source approaches the surface (Fig. 10). To demonstrate this point, we compared the results obtained with the Monte Carlo method (http://omlc.org/software/mc/) and the diffusion theory. In this section, we evaluate each step of the approximation described above using the accurate Monte Carlo method. The optical properties from table 5 were used. As shown in Figure 8, the fluence derived from the diffusion theory was only accurate when r was greater than 0.3cm. Deviations caused by each step of the approximation are illustrated in Figure 10. Curves M are derived from the Monte Carlo method, whereas curve D is derived from the diffusion theory.

The error due to the approximation of Fig. 10a right with Fig. 10b left is shown in Fig. 10c. Curves M and D were calculated by the Monte Carlo method and the diffusion theory, respectively; they show relatively small systematic differences. The relative error decreased with increasing r; it was >100% close to r=0 and 20% close to r = 0.35 cm.

3.5 Discussion

To the best of our knowledge, this is the first study to use two quasi-realistic models (six-layered neonatal vs adult head models) to quantify the temperature distribution by bio-heat diffusion modelling. Furthermore, despite the use of animal models (Kim et al., 2007), this is the first study to use an FEA approach to investigate the influence of heat and fluence rate of various laser radiant powers on human head models (adult and neonatal) with blood perfusion.

3.5.1 Effect of various laser radiant powers on neonatal and adult head models

By ignoring the optical discontinuity and anisotropic properties of the tissues, the temperature distribution showed a higher surface temperature for a highly scattering medium during laser irradiation. Current research into laser-induced tissue damage has focused on damage generated in superficial tissues in adults (Ito et al., 2000). Ito et al. (2000) investigated the heating effect of near-infrared irradiation at 789 nm. A 0.101°C/mW temperature elevation was detected at a depth of 0.5 mm in the human forearm in which $\mu_{a(forearm)}= 0.2cm^{-1}$ (Vo-Dinh, 2014).

In agreement with the results of this previous study (Ito et al., 2000), our results show a 2.7°C temperature increase at a depth of 0.4 mm in the skin (using $\mu_{a(skin)}=0.2cm^{-1}$, NIR-light at 800 nm and a power of 30mW, I = 3.81 W/cm^2) (Fig 6a). On the other hand, for a power of

1 mW (I= 0.127 W/cm^2), a 0.16°C temperature increase was detected at a depth of 0.4 mm in the skin (using $\mu_{a(skin)}$=0.5cm^{-1}). In our simulation, the total fluence rate, especially in the superficial area of skin, was overestimated when the diffusion approximation was used (Motamedi et al., 1989). Although the main aim of our study was to investigate thermal effects on brain tissue (situated far away from the laser source), we compared the results obtained in superficial tissue in a previous experimental study in order to validate our model (Ito et al., 2000).

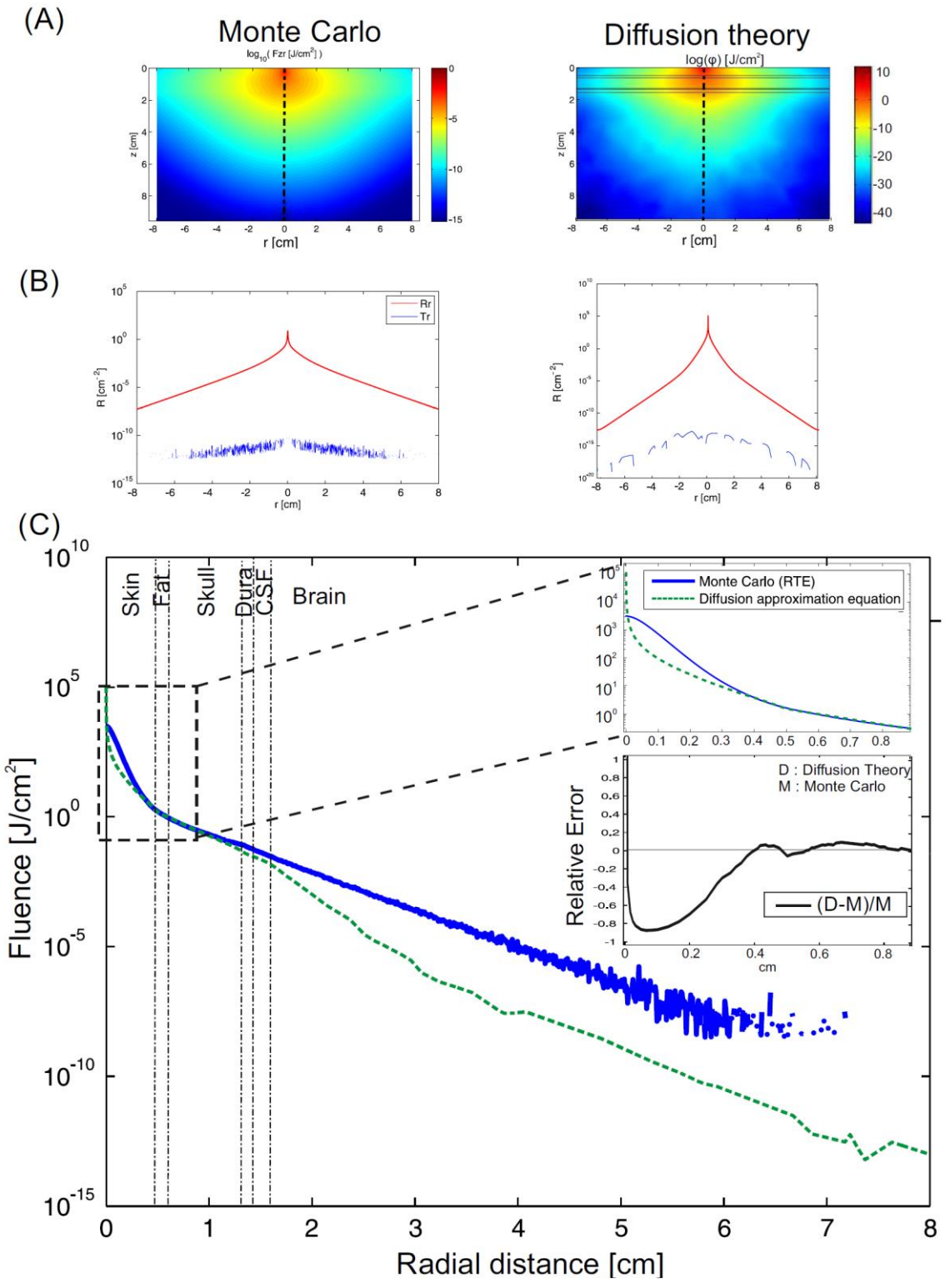

Fig. 10 *Comparisons between the Monte Carlo method and the diffusion theory in terms of (a) distribution of fluence rate (b) the diffuse Reflectance, Transmittance. (c) Fluence J/cm2 (inset shows relative errors between the results of the Monte Carlo method and the diffusion theory).*

In adults, a 10°C temperature increase is considered to be the safety limit to avoid skin injury (Widmaier et al., 2004) (assuming a skin surface temperature of around 31°C). Consequently, our results show a temperature increase of up to 10°C at a power of about 50 mW (I= 6.36 W/cm2) and 60 mW (I= 7.63 W/cm^2) under steady-state conditions on adult and neonatal skin, respectively.

Considering a 1mm spot size and assuming a brain blood perfusion rate equal to 0.00166 s^{-1}, the temperature increase in the adult brain for powers ranging from 1mW to 100mW (0.127 W/cm^2 < I < 12.73 W/cm^2) was much lower (ΔT = 0.002°C to 0.26°C) than the temperature known to induce cell injury when studied *in vitro* (10°C). In contrast, in the neonatal brain, the temperature increase was lower (ΔT = 0.03°C to 0.86°C) than the critical temperature (1°C) for powers ranging from 1 to 30mW (0.127 W/cm^2 < I < 3.81 W/cm^2) and a 1 mm spot size.

3.5.2 Effect on neonatal vs adult tissue

As expected, with an irradiance of 0.31Wcm^{-2}, the temperature increase in the neonatal brain was higher than that in the adult brain (when comparing the ΔT of each neonatal head layer with the same layer in the adult model), notably because of the thinner skin and skull in neonates, facilitating penetration of photons into the brain. Despite similar optical properties of neonatal and adult skin at 800 nm (Saidi, 1992b), (Vo-Dinh, 2014), additional factors predisposing to a more marked temperature increase are the greater transparency and lower absorption coefficient of neonatal brain tissues (Tuchin and Engineers, 2007).

Nevertheless, the temperature increase at 3.81 W/cm^2 was about 4.5°C vs 4°C at a depth of 0.4 mm in skin (neonate vs adult) and 0.85°C vs 0.07°C on the brain (neonate vs adult), which is still much lower than the previously reported limit for the skin (10°C) and the brain (1°C) under steady-state conditions (LaManna et al., 1989) and also well below the safety limits adopted for laser-induced tissue injury. However, if the temperature changes very slowly (e.g. at a rate of less than 0.5 °C per minute), the subject may can be unaware of a 4-5 °C change in temperature (Kenshalo and Scott, 1966), provided the skin temperature remains within the neutral thermal range of 30-36 °C.

3.5.3 Effect of blood perfusion

Blood perfusion plays a significant role in thermal regulation of a living body. In the present study, blood perfusion removed heat away from the laser source and appeared to

constitute a cooling mechanism for the brain. Local heating of the model was considerably reduced when blood perfusion in the tissues was taken into account. Body fluids, transporting heat throughout the tissues, act as a convection mechanism. The present study did not consider the blood flow increase induced by vasodilatation resulting from the temperature rise (Charkoudian, 2010), which would have further reduced laser-induced heating of the skin as a result of the normal physiological thermoregulation processes. In addition, the superficial brain is spontaneously cooled by the environment and is cooler than arterial blood. Under physiological conditions, an increase in CBF may lead to an increase in superficial brain temperature and a simultaneous decrease in deep brain temperature, emphasizing the complexity of the effects of blood perfusion rate.

Our results show that changes in cerebral metabolism had no significant impact on local brain temperature changes congruent with the experimental results (Sukstanskii and Yablonskiy, 2006) (Fig 5b). However, changes in brain temperature were linked with cerebral blood perfusion and blood perfusion contributed to maintain a low brain temperature.

3.5.4 Effect of various skin and brain absorption and scattering coefficients

Discordant values have been reported for the exact absorption and scattering coefficients. These discordant values could be due to the discrepancies between theoretical and experimental investigations. In general, *in vivo* μ_a and μ_s values for human skin are significantly lower than those obtained *in vitro* (about 10-fold and 2-fold lower, respectively (Tuchin and Engineers, 2007)). The discordant values for μ_a may be related to the low sensitivity of the double-integrating sphere, the goniometric techniques used for *in vitro* measurements at low absorption combined with strong scattering ($\mu_a << \mu_s$) and sample preparation methods (Tuchin and Engineers, 2007). Consequently, in the absence of accurate absorption coefficients, these values need to be chosen cautiously, and our temperature profiles were probably overestimated, as data were presented as the maximum temperature rise resulting from intentional selection of the maximum absorption coefficients available in the literature. As skin absorption is usually dominated by melanin absorption, various melanin levels in the skin have therefore been investigated to study the effect of darker skin. Figure 6 presents the temperature distributions with broad ranges of skin (Fig. 6a) and brain (Fig. 6b) absorption coefficients and shows that changes in brain or skin absorption coefficients had a greater impact on superficial layers,

closer to the source, and a lesser impact on deeper tissues. Nevertheless, as the brain is situated far from the source, this impact is limited to the brain surface (Fig. 6b inset).

Photons are less scattered and penetrate much more deeply for lower values of scattering coefficient, as they are able to travel over a longer distance with greater step size before they interact with the tissue at a new position. As the value of the scattering coefficient increases, scattering increases and photons undergo frequent scattering with smaller step sizes, resulting in a more circular profile of fluence rate. For lower scattering coefficients, photon penetrate much more deeply with intensity decreasing outwards according to the radial distance. While changes in scattering coefficients can impact on the photon density distribution, their effect on temperature is negligible, in view of the small range of scattering coefficients of these head layers is low (brain scattering coefficient:8.74_12.17cm^{-1}, skin:15.09_26.75cm^{-1}, fat:8.30_22.12cm^{-1}, skull: 8.89_19.24cm^{-1}, CSF: 0.1_3.2cm^{-1}(Okada and Delpy, 2003)) (Jacques, 2013).

3.5.5 **Effect of various Laser spot sizes**

The mechanisms involved in the interaction between laser and biological tissue are also intimately related to the Laser characteristics (e.g. wavelength, energy density, and spot size). By increasing the beam spot size, Laser light can be diffused over larger areas and, in these situations, laser power can be increased while maintaining safe levels of skin irradiation. Figure 7 shows that the temperature decreased as the laser spot size increased from 0.2mm to 15mm. This figure shows that, for a specific Laser power, Laser spot size should be kept above a specific limit to avoid skin temperatures exceeding safety limits (e.g. in adults, assuming a skin safety threshold of 10°C, if Laser power = 100mW, the spot size should be ≥ 11 mm).

In the brain, a few orders of magnitude of difference in spot size does not induce any change of brain temperature, but smaller differences in laser power cause measurable differences in brain temperature, due to smaller spot size leading to higher irradiance but smaller penetration depth. Laser beam spot size determines the depth of penetration. A larger spot size decreases scattering of light and increases the depth of penetration. A larger spot size therefore results in deeper penetration, while smaller spot size induces more rapid scatter and more rapid decay of fluence with depth (Keijzer et al., 1989). Since the e^{-1} depth of scattered light is unclear when scattering dominates absorption ($\mu_a << \mu_s'$), the exact depth of light penetration in tissue has not been determined (Welch and van Gemert, 1995). Therefore, by

maintaining the same power, using larger spot size (sp↑) decreases irradiance (I↓), but increases the depth of penetration of the light (depth↑), resulting in insignificant temperature changes in deeper tissues (e.g brain). By maintaining the same spot size, higher power (P↑) increases irradiance (I↑) and the depth of penetration of the light (depth↑), resulting in significant brain temperature changes. The temperature in the brain therefore depends on the laser power more than on the spot size.

Figure 7 (A, B) shows that spot size changes at constant power have a lesser intense heating effect on deeper tissue.

Figure 8 illustrates the temperature changes vs. irradiance and shows higher temperature due to higher power and higher spot size with the same irradiance. In skin tissue, for small spot sizes, cooling of surrounding non-irradiated tissue is much more effective than for large spot size. With larger spot sizes, heat transfer from the center of the spot size cannot occur radially (sideways). Consequently, for the same level of skin irradiance, larger spots produce higher temperatures than smaller spots. This effect of higher temperatures for larger spot sizes reduces the exposure limit, since the effect of cooling means that the damage threshold does not simply depend on the skin irradiance. Exposure limits decrease with increasing spot sizes, reflecting the fact that, for the same level of irradiance, larger spots are more hazardous than smaller spots. However, this dependence of the risk threshold on spot size diameter does not apply to very large spot sizes, since the temperature profile in the center of the spot has a more or less flat profile, and this value is not affected by any further increase in the actual spot size, as the edges that are cooled radially are situated too far away from the center. Consequently, for large sources, the risk threshold depends only on the irradiance and no longer on the spot diameter (Schulmeister, (Taylor & Francis, 2004).).

During exposure of the skin to IR radiation for several seconds, involuntary body movements and heat conduction disperse the irradiance profile over an area of at least several square millimetres (~3.5mm), even when the irradiated body part is intentionally kept still, even the smaller spot sizes (0.2 to 1mm) has been considered in our model in order to study the effect of these range of spot size (i.e. which is below the 10°C limit skin temperature at 3mm but not below the 10°C limit at 1mm at the same power). For a wavelength of 800 nm used in our study, with the maximum anticipated exposure time (Table 1), with an ANSI standard MPE equal to 0.3Wcm^{-2}, larger power would be allowable with larger spot size.

3.5.6 Systematic model errors

Our simulated model remains a mathematical model, meaning that errors could be come from the simplifications. These errors are essentially due to the following causes:

The inaccuracy of the optical and thermal properties is main point in the model's set of equations, as these properties are essential for the accuracy of the simulated model's outcome. Many approaches have been demonstrated to estimate these properties, but various authors have reported very discordant values, reflecting the difficulty of estimating these properties. In addition, the inaccuracy is further increased by the dependency of the properties on the various parameters (temperature) over time, resulting in a nonlinear difference.

The error of Pennes' bio-heat equation is that it does not account for directionality of blood perfusion, which is an important factor in the energy exchange between vessels and tissue. In addition, Pennes' equation does not consider the local vascular geometry. While Pennes' bio-heat model is based on incorrect anatomical views about the temperature distribution of blood through the tissues, it is still universally employed and its relative accuracy in tissue situated away from large vessels which introduce local convection has been confirmed (Arkin et al., 1994).

Another error is related to computer performance limitations: accessible memory, the size of mesh nodes used to make the model. Our simulated model was established on the basis of the above conditions, with COMSOL standard refining processes at the crucial areas (around the heat source).

Absolute numeric tolerance: Whole numerical approaches have a permitted error (absolute numeric tolerance) that expresses the reference point of the convergence. Different solvers commonly use different absolute tolerances. In our model, we used the COMSOL default tolerance value of 0.01 which leads to a final error of 1%, considered to be a reasonable criterion for modelling.

Diffusion theory limit: Despite the fact that diffusion theory suggests a fast approach, it is not valid close to the light source or the boundary, where the photon intensity is strongly anisotropic. This is due to the fact that, at short distances, the radiance rate is not linearly anisotropic and the basic assumptions required for the diffusion approximation to Boltzman transport equation are not satisfied. On the other hand, strong absorption prevents photons from

engaging in an extended random walk and the approximation $\mu_t = \mu_s'$ becomes insufficient. The diffusion approximation is therefore only valid in highly scattering media (i.e., $\mu_a << \mu_s'$) and when the point of interest is situated far from sources or boundaries.

The simulated head model consists of six types of tissues. However, the sophisticated geometry of the tissue structure is ignored and tissue layers are parallel to each other. In a real head, the thickness of superficial tissue, such as the scalp and skull, is not uniform and brain surface is folded with sulci. The thickness of the skull is known to vary significantly around the head and between individuals. In addition, the thickness of the CSF can vary because the brain can move to a limited degree within the skull, this change is more prominent in the neonatal head. Moreover, there is a relationship between skin thickness and the neonate's gestational maturity (Saidi, 1992a).

3.6 Conclusion

A laser-tissue interaction model was developed to predict the spatial dynamic changes in temperature rise during laser exposure of human head tissues. We describe the bases necessary to calculate the effects of the temperature changes caused by the absorption of light energy in the tissues, using the bio-heat equation and including the cooling effects of blood perfusion in tissue in order to model the photothermal interaction of NIR laser on human tissues.

The temperature changes of the radiated zone calculated from our simulation and in vitro experiments presented a small deviation. Two of the main reasons for this deviation are the lack of accurate values of the tissue optical properties and diffusion approximation theory in superficial surfaces.

Further studies under different conditions are necessary to achieve full agreement with in vivo data, and, if necessary, define error correction factors to be added to the equation set. However, this would not eliminate the need for precise values for the optical and thermal properties of the tissue. On the other hand, our model remains practical, as it introduces a step in using simulated head tissues as a basis for much more detailed NIR laser photothermal interaction experiments.

The results presented in this work should be useful to optimize Laser spot size and power for a variety of laser applications of functional imaging systems (e.g. Diffuse Correlation Spectroscopy (DCS) which need near-infrared (NIR) light with relatively high laser power). A

combination of simulation and adequate in vitro experiments could help to develop a more effective optical imaging to avoid any possible tissue damage.

3.7 Supplementary

In the following we explained some parts of study in more details:

1) *Model Geometry included:*

The head (with 6 layers) was modeled in a 3-D Cartesian (x, y, z) coordinate, as shown in the following figure. The thickness of the skin, fat, bone, dura, CSF and brain were set according to the following table, for the adult and neonatal models. The minimum thickness of neonatal skin (in the different gestational maturity) was selected as measured in vitro (Sajjadian et al., 2012), as shown in the following figure. For the sake of simplicity, the curvature of 6 layers was not considered. To assume the temperature at the boundary of the selected region is equal to body temperature (37 °C), the thickness of brain tissue was selected sufficiently large (80mm). Optical source was simulated in which the laser source sends out a Gaussian and temporally continuous laser beam and Q_{ext} in bioheat equation for each layer of tissue was defined as absorption coefficient × $\boldsymbol{\Phi}$ (photon intensity). Different radii of laser spot (0.2, 0.4, 0.6, 1, 3, 5, 7, 11, 15mm) were investigated (refer to chapter 3).

Table 7. *Tissue thickness (mm) (H. Khodabakhshi, 2010; Kiguchi et al., 2007)*

	Skin	Fat	Bone	Dura	CSF	Brain
Adult	5	1.4	7	0.5	2	80
Neonate	0.5	1.4	2	0.5	0.5	80

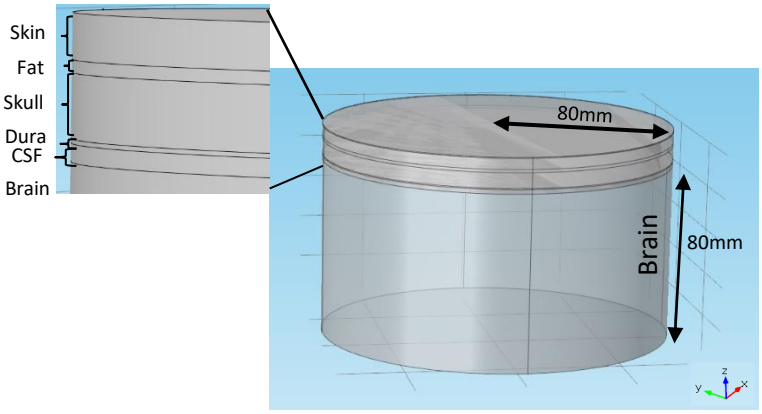

Fig. 11 *Geometrical structure of 3D-CAD composed of six layers (skin, fat, skull, dura, CSF and brain)*

- *Boundary conditions:*

The cylindrical volume was simulated with six head layers. The curved surface of the cylindrical volume (model sampled inner head volume involved laser radiation region) specify the internal temperature of the head, while third boundary condition (heat balance by convection) was applied to the circular plane surface of the cylindrical volume which was exposed to the air.

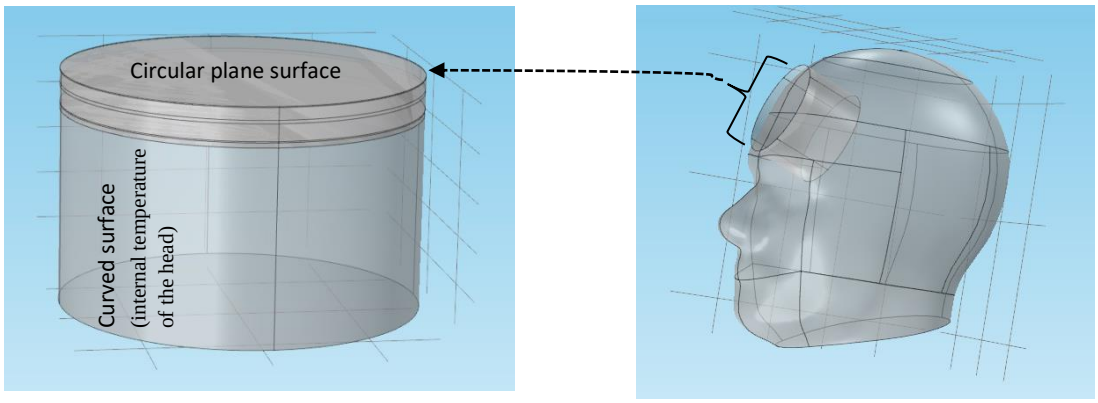

Fig. 12 *Geometrical structure of 3D-CAD composed of six layers (skin, fat, skull, dura, CSF and brain)*

The boundaries of the selected region (except the surface exposed to the air), was considered to be at the body temperature. This is reasonable since the volume to be analyzed chosen to be sufficiently large and the boundaries are not affected by the heating source. The third boundary condition corresponds to convection at a surface was considered to solve the bioheat equation, at the surface contacting with air, assumed

that the heat transfer occurs in the form of free convection into the air (Heat transfer by radiation at the surface into the air was neglected) (Alawadhi, 2010):

$$n.(k\nabla T) = h(T_{ext} - T) \tag{7}$$

- *Semi-infinite domain:*

To have sufficient distances from light sources in case of large scattering, a semi-infinite domain was required. The layer sizes of the model were selected sufficiently large to be able to assume a semi-infinite domain. The model size was taken as (radius=80mm, height=80mm), which by being 4 times larger the area affected by the laser radiation, conserves the semi-infinite nature of the model. The same relative dimensions (4 times larger) for a semi-infinite domain have been used by Wilson et al., Bianco et al., and Ronghou et al. (Bianco, 2008; Ogoh, 2010; Ronghou, 2014).

To demonstrate that the domain is large enough to assume a semi-infinite geometry, it should calculate solutions for different sizes of the domain and show that the lateral and depth profiles of temperature and light do not change as extend the domain. The following figure shows that the lateral and depth profiles of temperature and light do not change when the dimensions are changed to 70, 80, 90 mm.

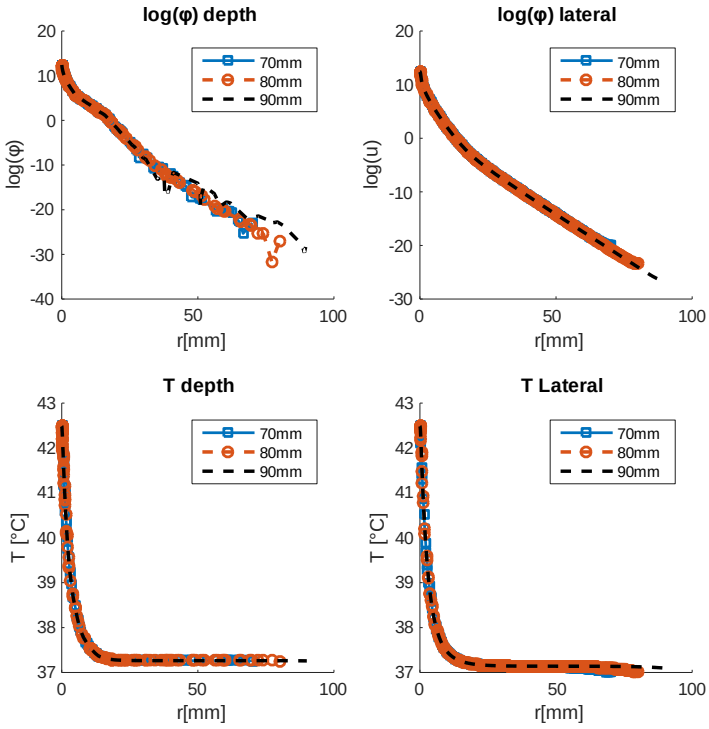

Fig.13 *The lateral and depth profiles of temperature and light for different sizes of the domain.*

- *The thermal equilibrium between the 'head' and the 'ambient':*

For an ambient temperature that is lower than the skin surface temperature, heat loss from the skin to the environment takes place via convection. Heat transfer by radiation into the air would be negligible. The boundary condition in the above surface is:

$$n.(k\nabla T) = h(T_{ext} - T) \tag{8}$$

- *The assumptions that lead to simplifying the diffusion approximation from the radiative transfer equation (RTE):*

Two assumptions permit the diffusion approximation as a simplification of the radiative transfer equation: (1) Relative to scattering events, there should be very few absorption event, and the radiance will become nearly isotropic. (2) In a primarily scattering medium, the time for substantial current density change is much longer than the time to traverse one transport mean free path. Thus, over one transport mean free path, the fractional change in current density is much less than unity. This property is sometimes called temporal broadening (Wang and Wu, 2007).

To reduce the complexity of the RTE, a standard method for approximating equation called the *PN* approximation was employ. When $L(r,\Omega,t)$ (source) is nearly isotropic, the so-called *P1* approximation:

$$\nabla\Phi(r,t) = -\frac{3}{v}\frac{\partial J(r,t)}{\partial t} - 3\mu_t J(r,t) + 3\int Q(r,\Omega,t)\,\Omega\,d\Omega + 3\mu_s g J(r,t). \tag{9}$$

Assuming isotropic sources $(Q(r,\Omega,t) = Q(r,t))$, the integral over Q in equation above is zero. Furthermore, if we also **assume slow temporal variations in the photon flux J**, then $(1/v)\partial J/\partial t$ in equation above can be neglected compared with $(\mu_t - \mu_{sg})J$. results in the photon diffusion equation for the photon fluence rate:

$$\nabla.\big(D(r)\nabla\Phi(r,t)\big) - v\mu_a(r)\Phi(r,t) - \frac{\partial\Phi(r,t)}{\partial t} = -vS(r,t) \tag{10}$$

Here we defined the photon diffusion coefficient $D(r)\equiv v/3(\mu'_s(r) + \mu_a(r))$ (Durduran et al., 2010a).

The diffusion equation is valid according to the assumptions that (1) the scattering is large compared to the absorption and (2) studying diffuse light propagation at sufficient distances from any light sources which is the case in our study. However, the main aim of current study is to investigate the thermal effect of the laser source on brain tissue.

- *The limitations of using the diffusion approximation:*

  According to Lorenzo and Schweiger (Munro, 2013; Schweiger, 1994), the applicability of the diffusion equation can be restricted by the limitation of the expansion of the transfer equation to the first two terms (P1 approximation), and the above assumptions.

  In biological tissue ($\mu_a \ll \mu'_s$), the P1 approximation can be acceptable. The directionality of the laser beam diminishes across a tiny distance, afterward light propagation changes state to isotropic, because of high scattering in tissue. This permits the diffusion approximation to be applied. Inconsistency between the diffusion model and experimental measurements are expected in the region close to the laser source. Based on the assumptions and approximations, the diffusion equation will go wrong very close to the surfaces or laser sources (this would, in theory, abolish the angular dependence and perhaps make the contribution of the term $\partial J/\partial t$ not negligible).

  Commonly, these (flexible) restrictions are determined by comparing the outcomes of the diffusion approximation to the RTE, and not the whole solution to Maxwell equations and generally ignore the contribution from the reduced intensity. By comparing the outcomes of the diffusion approximation to the RTE, and not the whole solution to Maxwell equations and generally ignore the contribution from the reduced intensity, commonly these (flexible) restrictions can be determined.

  In this manner, we are not doing an equitable comparison: the RTE suffers from many approximations of its own which are clearly not being accounted for. If a strict comparison of theories is to be performed, it should be with regards to the exact problem using Maxwell equations, since the diffusion equation is not something unique to the RTE, it is an equation which can also be extracted directly from Maxwell.

On the other hand, when cautiously applied (in the presence of high absorption for instance, or very close to laser sources) the diffusion approximation has produced experimentally very good results, in most cases better than what was expected.

This could be because we are facing with volume averaged quantities measured with real detectors. Thus the question still remains: what are the limits of validity of the diffusion approximation? According to the reference, there is no straight answer to this question. Distances smaller or equivalent to the average distances between particles does not hold much significance neither in the context of the RTE nor the context of the diffusion approximation. Similarly, time scales that confine light propagation to such small volumes should not be considered when dealing with diffuse light.

Moreover, as occurred with the RTE, results predicted by the diffusion approximation are assumed to deviate significantly in cases where there might be a highly coherent contribution. What we can clearly determine is when the diffusion approximation is expected to hold (far away from source and detectors, at long time-scales, and in the absence of coherent effects). Determining where it does not hold is a different matter since there are no rigorously defined limits.

The diffusion approximation can predict light transport correctly far from the light source and far from the air-tissue boundary (Farrell and Patterson, 2001; Gobin et al., 1999). In the skin, this is only satisfied in the deeper level of the dermis and does not apply to the epidermis and the upper level of the dermis where the scattering of radiation is anisotropic. Therefore, the total fluence rate, especially in the superficial area of skin, is overestimated when the diffusion approximation is used (Motamedi et al., 1989). Although the main aim of our study is to investigate the thermal effect on brain tissue (far away laser source), to verify our results of superficial tissue with the experimental study (Ito et al., 2000) we consider temperature changes at 0.4 mm radial distance from the laser source (considering epidermis thickness is 0.06mm).

- *To solve heat and light diffusion equations:*

The finite element method was used to simultaneously solve the diffusion equations of light and heat (Shafirstein et al., 2003). In this study, the diffusion and bio-heat equations were solved simultaneously, and results are shown at steady state. To obtain

the transient as well as the steady-state temperature profile, a time-dependent analysis of heat transfer and light diffusion was performed (the following figure). The time to reach steady state for light diffusion was 0.7ns but was 500s for heat transfer. The light fluence in tissue is constant at the scale of one second. Power per unit volume was therefore defined as a stationary heat source in the thermal equation; this was shown the light source was define constantly ON.

(a)

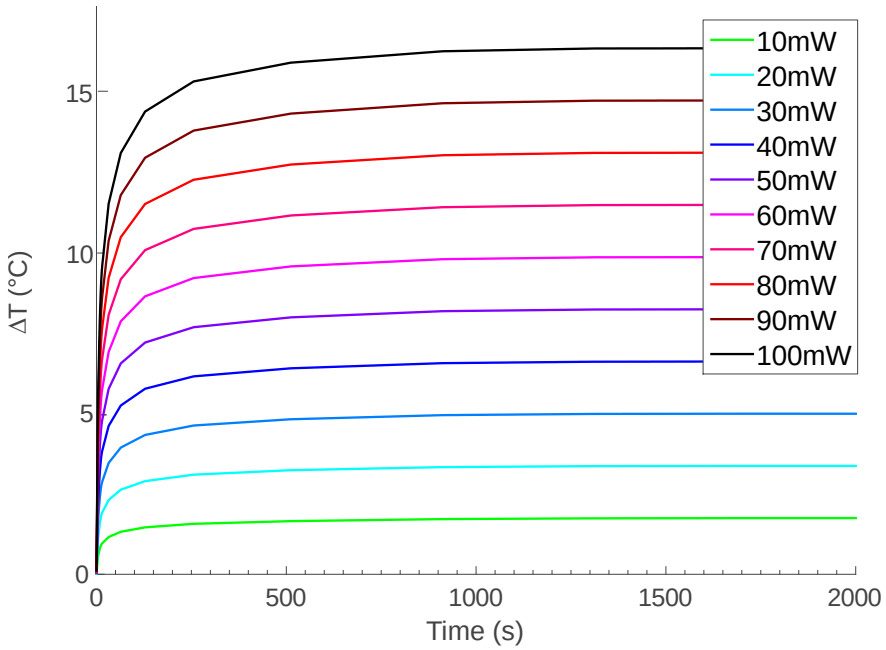

(b)

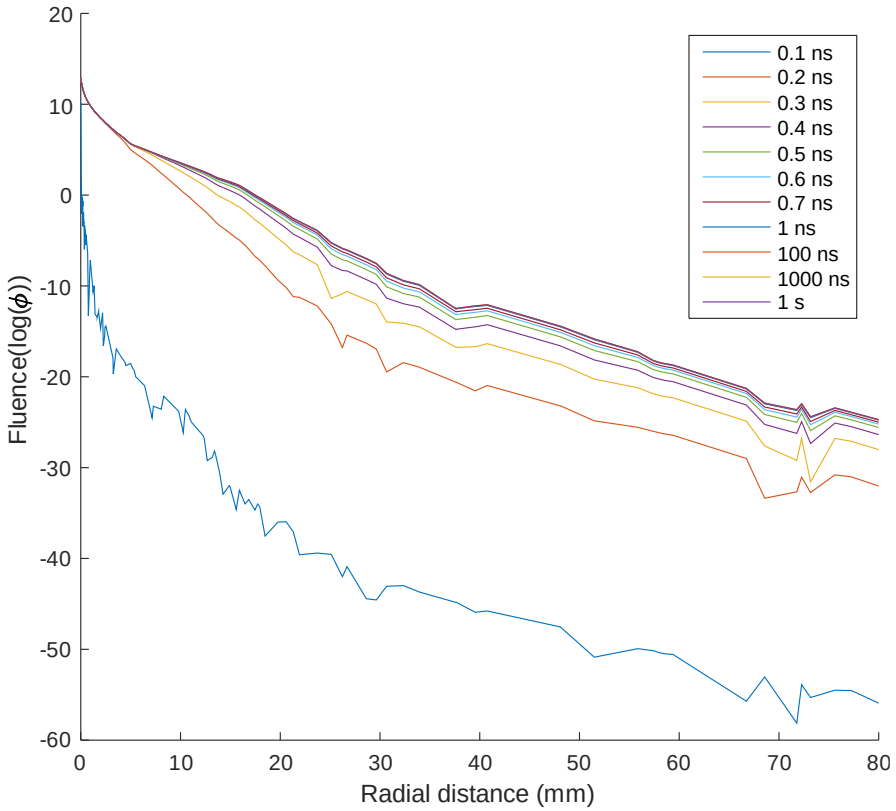

Fig.14 *(a) Temperature changes at the depth of 0.4mm with various powers: 10 mW to 100 mW in 10 mW increments over time and (b) fluence changes for a constant power over time.*

- *The effect of different level of melanin in skin, hair, Moles and Birthmarks on temperature investigation:*

  The different level of melanin in the skin, the darker skin, Moles and Birthmarks has been effected on temperature sensation. The hair effect should be estimated by considering a wide range of melanin absorption coefficient. The skin absorption coefficient is usually dominated by melanin absorption. In this study, in order to investigate the thermal effects of laser on skin, we considered the temperature increase in relation to the different volume fraction of the epidermis occupied by melanosomes in the skin[5] (Melanosomes per unit volume in the epidermis [M]%=0.87 ,1.15, 1.65% correspond to the skin absorption coefficient μa(skin)= 0.52cm^{-1}, 0.65cm^{-1}, 0.88cm^{-1}, respectively).

- *Eye safety:*

[5] http://omlc.org/news/jan98/skinoptics.html

The particular mechanism activated depends on the wavelength and exposure duration of the injuring light. According to the ANSI standard document: Z136.1-2014, Standard for the safe use of a laser[6], the retina has the potential of causing ocular damage in the wavelengths of 400nm, 1400nm. Since many of the thermal energy would be absorbed directly through the skin and scalp before reaching the eye, indirect exposures are less likely to cause damage the retina, and the retina temperature is much lower than the critical temperature.

Wavelengths with the Potential of Causing Ocular Damage	Ocular Structure
400nm to 1,400nm (Visible & Near Infrared)	Retina
1,400nm to 3,000nm (3.0μ) (Near Infrared)	Lens
1,400nm to 1mm (Near, Mid, & Far Infrared)	Aqueous Humor
3,000nm (3.0μ) to 1mm (Mid & Far Infrared)	Cornea

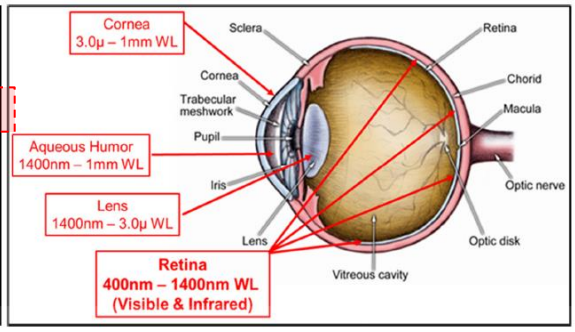

Fig.15 *Eye safety of laser (https://www.laserdentistry.org/uploads/files/conference/2014/Handouts/Benjamin-LeBeau--Laser%20Safety%20Officer%20Training%20Handout.pdf)*

- *Compare the ANSI 2014 standard to the ISO standards:*

According to the Steen (Steen, 2003), the Technical Committee No. 76 of the International Electrotechnical Commission (IEC) drew up the basic standard from which most others have been developed (IEC 825-1). The European Committee for Electrotechnical Standardization (CENELEC) adopted the IEC 825 standard as the European Norm EN 60825 (EN 60825-1, which is identical to IEC 825-1 and was approved in 1994).

The American National Standards Institute (ANSI) issued ANSI Z136.1- 1993. These standards evolved into the next generation in which there is a closer fit between Europe (EN 60825-1:2001) and the US norms (ANSI Z136.1-2007). There are no updates in ANSI 2014 (compare to the ANSI 2000) revision about Maximum Permissible

[6] https://www.laserdentistry.org/uploads/files/conference/2014/Handouts/Benjamin-LeBeau Laser%20Safety%20Officer%20Training%20Handout.pdf

Exposure (MPE) for Skin Exposure to a Laser for Wavelengths from 400 nm to 1400 nm used in our study (Table 7b, ANSI 2014).

Table 8 *– Maximum permissible exposure (MPE) of skin to laser radiation, INTERNATIONAL STANDARD IEC 60825-1*

60825-1 © IEC:1993+A1:1997 +A2:2001(E)

Table 8 – Maximum permissible exposure (MPE) of skin to laser radiation [1) 2)]

Wavelength λ nm \ Exposure time t s	<10^{-9}	10^{-9} to 10^{-7}	10^{-7} to 10^{-3}	10^{-3} to 10	10 to 10^{3}	10^{3} to 3×10^{4}
180 to 302,5	3×10^{10} W·m^{-2}	30 J·m^{-2}				
302,5 to 315		C_1 J·m^{-2} ($t > T_1$)		C_2 J·m^{-2} ($t > T_1$)	C_2 J·m^{-2}	
315 to 400		C_1 J·m^{-2}			10^{4} J·m^{-2}	10 W·m^{-2}
400 to 700	2×10^{11} W·m^{-2}	200 J·m^{-2}		$1{,}1\times10^{4}\ t^{0,25}$ J·m^{-2}	2 000 W·m^{-2}	
700 to 1 400	$2\times10^{11}\ C_4$ W·m^{-2}	200 C_4 J·m^{-2}		$1{,}1\times10^{4}\ C_4\ t^{0,25}$ J·m^{-2}	2 000 C_4 W·m^{-2}	
1 400 to 1 500	10^{12} W·m^{-2}	10^{3} J·m^{-2}		5 600 $t^{0,25}$ J·m^{-2}	1 000 W·m^{-2} [3)]	
1 500 to 1 800	10^{13} W·m^{-2}	10^{4} J·m^{-2}				
1 800 to 2 600	10^{12} W·m^{-2}	10^{3} J·m^{-2}		5 600 $t^{0,25}$ J·m^{-2}		
2 600 to 10^{6}	10^{11} W·m^{-2}	100 J·m^{-2}		5 600 $t^{0,25}$ J·m^{-2}		

1) For correction factors and units see "Notes to tables 1 to 4".

2) There is only limited evidence about effects for exposures of less than 10^{-9} s. The MPEs for these exposure times have been derived by maintaining the irradiance applying at 10^{-9} s.

3) For exposed skin areas greater than 0,1 m^2, the MPE is reduced to 100 W·m^{-2}. Between 0,01 m^2 and 0,1 m^2, the MPE varies inversely proportional to the irradiated skin area.

Table 7b. Maximum Permissible Exposure (MPE) for Skin Exposure to a Laser for Wavelengths from 400 nm to 1400 nm

	Wavelength λ (nm)	Exposure Duration t (s)	MPE (J·cm^{-2})	MPE (W·cm^{-2})	Notes
Visible & Near IR	400 to 1400	10^{-9} to 10^{-7}	$2.0\ C_A \times 10^{-2}$	-	NOTE 1 NOTE 2
		10^{-7} to 10	$1.1\ C_A\ t^{0.25}$	-	
		10 to 3×10^{4}	-	$0.2\ C_A$	

NOTE 1—A 3.5 mm diameter limiting aperture is to be used for hazard evaluation. (Table 8a).

NOTE 2—See Table 6a for the wavelength dependent correction factor C_A.

- *Considering Limiting Apertures (3.5mm):*

According to ANSI standard (ANSI 2014, page 88), Limiting Apertures (3.5mm) are based on beam “hotspots” (1mm) since for most all exposures to the skin and IR exposures to the eye lasting greater 10 seconds, the involuntary movement of the eyes and the body as well as heat conduction will average an irradiance profile over an area

of about 10 mm^2, even if the irradiated body part is kept intentionally still[7] (ANSI, 2014; ICNIRP, 2013).

- *Considering the different between experimental measurements and simulation:*

  According to the Ashley 2011, we should consider the errors between experimental measurements and simulation results. There are thermocouple-specific errors, the error of probe-based transducers and measurement errors in the presence of spatial tissue temperature gradients, etc. In addition, the difference between thermal measurement in the forearm by Ito et al. and our head model study may also due to the different absorption coefficients between forearm ($\mu_{a(800nm)}$[forearm]=0.23cm^{-1}) and scalp ($\mu_{a(800nm)}$[scalp] = 0.5cm^{-1})(Vo-Dinh, 2014).

  On the other hand, the diffusion approximation can predict light transport correctly in a region far from the light source and far from the air-tissue boundary where all photons are scattered at least several times (Farrell and Patterson, 2001; Gobin et al., 1999). In the case of skin, this is only satisfied in the deeper level of the dermis and does not apply to the epidermis and the upper level of the dermis where the scattering of radiation remains highly anisotropic. Therefore, the total fluence rate, especially in the superficial area of skin, is overestimated when the diffusion approximation is used (Motamedi et al., 1989). Although the main aim of our study is to investigate the thermal effect on brain tissue (far away laser source), to verify our results of superficial tissue with the experimental study (Ito et al.) we consider temperature changes according to 0.4 mm radial distance from the laser source (considering epidermis thickness is 0.06mm).

- *The distributions of the photon-fluence rate between experimental measurements (Ito et al.) and our simulation:*

  The measured spatial temperature distribution reported by Ito et al. is in agreement approximately with our result (both in the shape and attenuation ratio). Following figure (a, on left) shows the delta temperature attenuation is almost one order of magnitude

[7] https://www.rli.com/resources/articles/classification.aspx

per mm for 9.8mw, and figure (b, on right) shows the delta temperature attenuation (from 42°C to 39°C equal to delta temperature=3°C) at 3mm depth from the surface.

Ito et al. studied the heating effect of near-infrared irradiation at 789 nm, a 0.101°C/mW temperature elevation was detected at a depth of 0.5 mm in the human forearm ($\mu_{a(forearm)}$ = 0.2cm^{-1} (Vo-Dinh, 2014)). Our results are showing temperature increases on the scalp (with $\mu_{a(skin)}$ =0.2cm^{-1}) NIR-light at 800 nm with 30mW power, a 2.7°C temperature elevation was detected at a depth of 0.4 mm in the scalp. On the other hand, for 1 mW power the temperature increase at the depth of 0.4 mm in the scalp (with $\mu_{a(skin)}$ =0.5cm^{-1}) equal to 0.16°C. This has been added to the discussion.

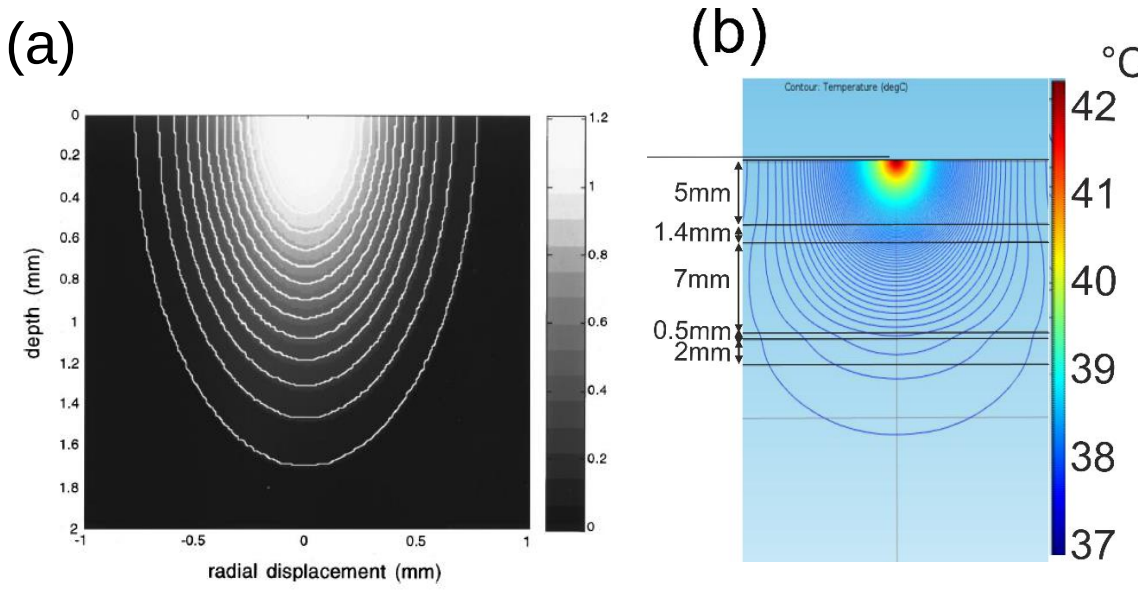

Fig.16 *Interpolated temperature map with overlayed contour map, (a) adapted from Ito et al. for 9.8 mW irradiation in human forearm, (b) Spatial temperature distribution of our model for 30 mW.*

- *Comparing the chosen perfusion value of brain with values measured in vivo with ASL-fMRI:*

The brain perfusion rate used in the current study is 0.00932 s^{-1} ≈ 0.56 min^{-1} which is comparable with the value measured in vivo with ASL-fMRI (Rowland and Tozer, 1995; Shargel and Yu, 1999).

Table.11 *The brain perfusion rate measured in vivo with ASL-fMRI.*

Organ	Perfusion Rate (mL/min/mL of tissue)	Percent of cardiac output (CO)
Brain	0.5 - 0.55	14 - 15
Fat	0.01 - 0.03	2 - 4

- *Effect of brain metabolic rate:*

According to these studies (Gordon et al., 1976; Scheinberg et al., 1954), the brain function and metabolic activity are indicated by oxygen concentration and glucose intake to the brain cells.

The variation in cerebral metabolism had no significant effect on regional brain temperature (Iwata et al., 2014) and the effect of cerebral metabolism on brain temperature is considered to be small (Kauppinen et al., 2008).

About the effect of the complexity of blood perfusion rate, the superficial brain is spontaneously cooled by the environment and is cooler than the arterial blood. This suggests that, under physiological conditions, an increase in CBF may lead to an increase in superficial brain temperature and a simultaneous decrease in deep brain temperature. In addition, the neonatal perfusion rates have been used for infant model (by taking and not taking account the perfusion rate) (Altman et al., 1988; Edwards et al., 1988; Kusaka et al., 2005).

- *The chosen absorption and scattering coefficients:*

There is a discrepancy over the precise value of absorption and scattering coefficients. The difference may derive from the discrepancy between the theoretical and experimental results. In general, in vivo μ_a and μ_s values for human skin proved to be significantly smaller than those obtained in vitro (about 10 and 2 times, respectively (Tuchin, 2000)). For μ_a, the discrepancy may be attributed to the low sensitivity of the double-integrating sphere, and goniometric techniques have been applied for in vitro measurements at weak absorption combined with strong scattering ($\mu_a << \mu_s$) and sample preparation methods. In our study, the absorption coefficients are adopted from the most recent complete reference about optical properties of tissue (Vo-Dinh, 2014).

The absorption coefficient of tissue is between 10^{-2} and 10^{-1} cm^{-1} due to the fact that they did not consider melanin absorption of the skin (In figure 16, Steve Jacques). By

considering in vivo tissue parameter (table 3, Steve Jacques) and following equation (Steve Jacques):

$$\mu_a = BS\mu_{a,oxy} + B(1-S)\mu_{a,deoxy} + [W]_{\%}\mu_{a,Water} + [F]_{\%}\mu_{a,Fat} + [M]_{\%}\mu_{a,\text{melanosome}} \quad (9)$$

Skin absorption coefficient would equal to $\mu_{a\,(skin)}$= 0.52cm^{-1}, 0.65cm^{-1}, 0.88cm^{-1}. These skin absorption coefficients (including also 0.1, 0.2, 0.3, 0.4 cm^{-1}) have been investigated in our study.

Table.12 *absorption and scattering coefficients.*

(μM), B = blood volume fraction × 100% (assuming 150 g HGb L^{-1} saturation of HGb × 100%, W = water volume fraction × 100%, M = fraction × 100%. Human tissues unless otherwise labeled. (na = not availat

rence)	C_{HGb} (μM)	B%	S%
rmal (Tromberg *et al* 1997)	23.6	1.02	67.6
rmal (Bevilacqua *et al* 2000)	24.2	1.04	75.5
rmal (Durduran *et al* 2002)	34.0	1.46	68.0
rmal (Jakubowski *et al* 2004)	16.0	0.69	62.6
rmal (Spinelli *et al* 2004)	15.7	0.67	66.4
nor (Jakubowski *et al* 2004)	41.0	1.76	61.1
(Jakubowski *et al* 2004)	12.5	0.54	76.0
houdhury *et al* 2010)	4.7	0.20	39.0
(Choudhury *et al* 2010)	0	0	0
(500–600 nm) (Tseng *et al* 2011)	1.1	0.05	75.7
(600–1000 nm) (Tseng *et al* 2011)	7.9	0.34	98.5
IV (500–600 nm) (Tseng *et al* 2011)	8.2	0.35	96.2
IV (600–1000 nm) (Tseng *et al* 2011)	9.6	0.41	99.2
VI (600–1000 nm) (Tseng *et al* 2011)	2.7	0.12	99.3
(Matcher *et al* 1997)	117.0	5.03	64.1
atcher *et al* 1997)	78.0	3.35	64.1
tcher *et al* 1997)	84.0	3.61	69.0
brain (Zhao *et al* 2004)	39.7	1.71	58.7
brain (Ijichi *et al* 2005)	64.7	2.78	70.0
(Svensson 2007)	215.0	9.24	76.0
owel (Solonenko *et al* 2002)	119.0	5.11	80.0
idney (Solonenko *et al* 2002)	340.0	14.61	70.0

On the other side, by considering volume fraction of melanosomes in the epidermis in another reference for optical properties of tissue[8] (Steven L. Jacques), the absorption coefficient of skin is higher (μ_a=17) than chosen one in our study. For example, a moderately pigmented adult with a 10% volume fraction of melanosomes will have absorption coefficients as listed below:

Table.13 *absorption coefficients.*

[8] http://omlc.org/news/jan98/skinoptics.html (Oregon Medical Laser Center)

wavelength [nm]	mua.skinbaseline [cm^-1]	mua.mel [cm^-1]	mua.epi [cm^-1]
694 nm	0.268	228	23
755 nm	0.254	172	17
1064 nm	0.244	55	5.7

In addition, different range (0.01, 0.05, 0.1, 0.5 cm^{-1}) of adult brain absorption coefficients is considered (Tuchin, 2000).

- *The maximum exposure times and the repetition frequency can use:*

To avoid the temperature of the exposed tissue rises, the rate of energy deposition should be slower than the rate of thermal diffusion. Therefore, the maximum exposure duration should be shorter than time point of critical temperature. Hence, the inter-exposure interval should be at least twice than time duration reaches critical point. However, in our study, thermal effect of laser on brain is the main objective thus for skin effect refer to ANSI standard.

- *Effect of different scattering coefficient on temperature:*

Photons are less scattered and penetrate much more deeply for lower values of scattering coefficient, as they are able to travel over a longer distance with greater step size before they interact with the tissue at a new position. As the value of the scattering coefficient increases, scattering increases and photons undergo frequent scattering with smaller step sizes, resulting in a more circular profile of fluence rate. For lower scattering coefficients, photons penetrate much more deeply with intensity decreasing outwards according to the radial distance. While changes in scattering coefficients can impact on the photon density distribution, their effect on temperature is negligible, in view of the small range of the scattering coefficients of these six head layers (brain scattering coefficient: 8.74_12.17 cm^{-1}, skin: 15.09_26.75cm^{-1}, fat: 8.30_22.12cm^{-1}, skull: 8.89_19.24cm^{-1}, CSF: 0.1_3.2_8cm^{-1} (8cm^{-1} scattering caused by the arachnoid trabeculae)) (Jacques, 2013).

Despite the insignificant effect of scattering coefficient on temperature, the following figure shows that higher value of scattering coefficient leads to a higher temperature; on the other hand, the other studies show that increasing temperature leads to a decrease of scattering coefficient in the tissue (Kim and Jeong, 2014).

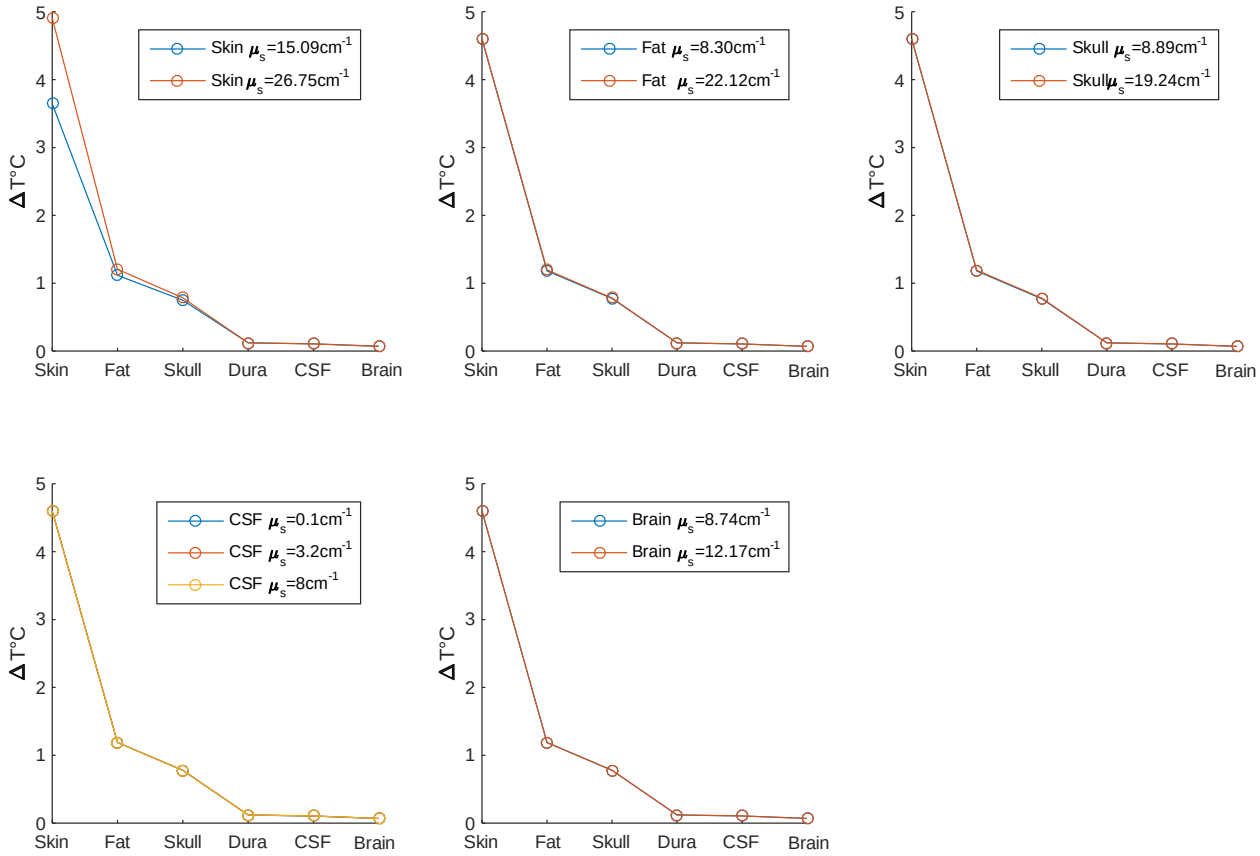

Fig.17 *Temperature changes in different tissues due to variations in scattering coefficient of individual layers.*

- *Scalp thickness:*

  According to (Kiguchi et al., 2007), scalp thickness is 5 to 7 mm, by considering the maximum value of 7mm for the scalp and 1.4mm (or less) for fat, skin thickness can be considered to be 5 mm. However, the error analysis for different skin thicknesses shows that temperature changes were not largely affected by variations the thickness of skin on the brain. In a real head, the thickness of superficial tissue, such as the scalp and skull, is not uniform.

- The brain scattering coefficient:

  Jacques et al. (Jacques, 2013) indicate that brain scattering ranges from 10 to 40 cm^{-1} for a wavelength of 500nm. By using this equation [$\mu_s' = a.(\lambda / 500nm)^{-b}$ with the parameters of Table 1 in (Jacques, 2013)] at a wavelength of 800nm, the brain scattering coefficient

was equal to 9.55, 9.31, 8.74, 9.3, 15.04, 9.99, 9.05, 12.17 cm^{-1} for Brain, Cortex (frontal lobe), Cortex (temporal lobe), Astrocytoma of optic nerve, Normal optic nerve, Cerebellar white matter, Medulloblastoma, and Brain, respectively. The value of 11.34 cm^{-1} was chosen according to Table 2 in (Jacques, 2013) (with the average parameters for reduced scattering coefficient of the brain). The skin scattering coefficient at 500nm is higher than brain scattering (Table 1, (Jacques, 2013)).

- *Irradiance, power and spot size:*

The temperature in the skin and brain depends on the laser power more than on the irradiance. For example, the temperature changes were 0.6059°C and 0.7182°C for the same irradiance of 0.113W/cm2 with different powers and spot sizes (150mW, spot size=13mm) and (200mW, spot size=15mm), respectively. A higher temperature due to a higher power and higher spot size (but with the same irradiance), implying that temperature changes depend not only on the magnitude of irradiance but also on the distribution of photons (which depends on both power and spot size). (It is similar to the temperature changes shown in the following figure, Ashley J. Welch, 2011, page 865 (Welch and van Gemert, 2011)).

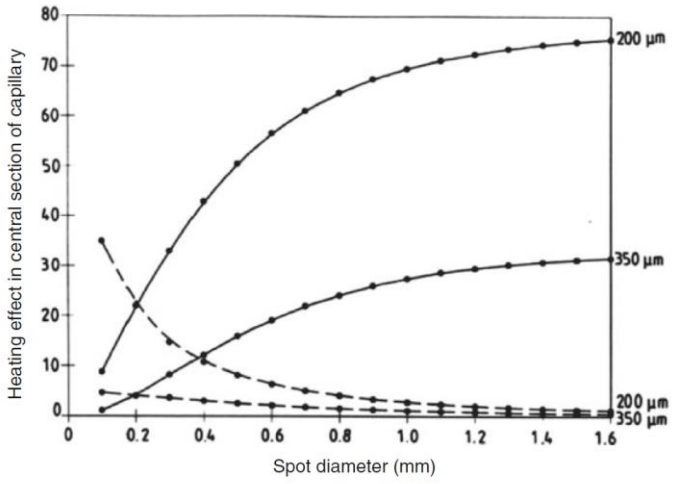

Fig. 23.2 Heating effect on the axis of central capillaries at depths of 200 and 350 µm, as a function of laser beam diameter, *D*. For constant radiant exposure *H* [J/cm^2] greater heating is obtained with increasing *D* (solid lines). For constant energy of the pulse [J] the heating effect always decreases with *D* (dashed lines). Results from numerical simulation for $\lambda = 577$ nm [30]

Fig.18 *Ashley J.Welch, 2011, page 865. 1989.*

The primary source of tissue irradiation is typically a laser beam, and the delivered light is characterized by its spot size and power. Smaller spot size leads to higher irradiance,

but the smaller depth of penetration. The spot size of a laser beam determines its depth of penetration. A larger spot size reduces scattering of light and achieves deeper penetration. Hence, the larger the spot size, the deeper will be the penetration and the smaller the spot size, the more rapid the scatter and the more rapid the decay of fluence by depth (Figure 19) (Keijzer et al., 1989)). Since the e-1 depth of scattered light is unclear when scattering dominates absorption ($\mu a << \mu s$), the exact depth of light penetration in tissue cannot be determined ((Welch and van Gemert, 2011), page 53).

Therefore, by maintaining the same power, using larger spot size (sp↑) decreases irradiance (I↓) but increases the depth of penetration of light (depth↑), resulting in insignificant temperature changes in deeper tissues (e.g. brain). By maintaining the same spot size, higher power (P↑) increases irradiance (I↑) and depth of penetration of the light (depth↑), resulting in significant brain temperature changes, which is why a 4 orders of magnitude difference in irradiance in the brain does not change brain temperature, but smaller differences in laser power induce measurable differences in brain temperature. At constant power, changes in spot size have a lesser heating effect on deeper tissues ((Welch and van Gemert, 2011), page 865).

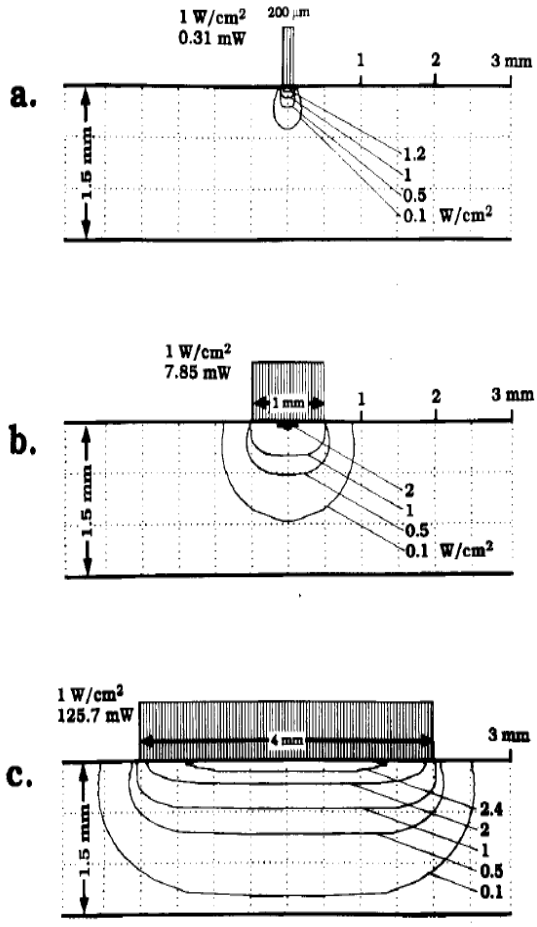

Fig.19 *The source of tissue irradiation of laser beam and the delivered light by its spot size and power.*

A higher temperature is observed due to a higher power and higher spot size with the same irradiance in the skin. In skin tissue, for small spot sizes, cooling to neighboring non-irradiated tissue is a lot more effectual than for large spot sizes. For larger spot sizes, heat transfer from the center of the spot size cannot occur radially (sideways), as illustrated schematically in the following figure. Hence, for the same level of skin irradiance, larger spots produce a higher temperature than smaller spots. This impact of higher temperatures for larger spot sizes decreases the exposure limit since the effect of cooling means that the damage threshold does not depend simply on the skin irradiance. The exposure limit would decrease with increasing spot sizes, reflecting the fact that, for the same level of irradiance, larger spots are riskier (have a lower exposure limit) than smaller spots. However, this dependence of hazard threshold on spot size diameter does not apply to very large spot sizes, since the temperature profile in the center of the spot has a more or less flat profile, and this value is not influenced by any

further increase in the real spot size, as the borders that are cooled radially are located too far away from the center. Hence, for large sources, the hazard threshold depends only on the irradiance and no more on the spot size (Henderson and Schulmeister, 2003).

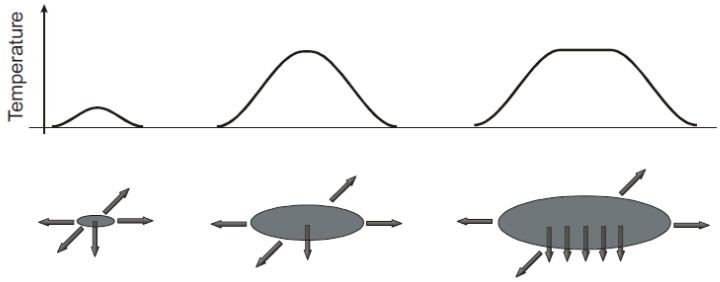

Fig.20 *Relation of temperature, power and spot size with the same irradiance in the skin. (R. Henderson, 2004).*

CHAPTER

Relationship between relative cerebral blood flow, relative cerebral blood volume, and relative cerebral metabolic rate of oxygen in the preterm neonatal brain

4

Mutual information is a statistic used to measure the relatedness between two variables. It provides a general measure based on the joint probabilities of two variables assuming no underlying relationship such as linearity. Mutual information can detect a wider range of relationships compared with traditional measures, such as correlation. For example, zero correlation coefficient does not necessarily imply that two variables are independent, while zero mutual information is mathematically equivalent to independence. One advantage of using information entropy in the present study for uncertainty analysis was that it combines the probabilities for multiple outcomes to one meaningful measure and that it does not assume a specific statistical distribution or an estimate of a mean. In this study, to investigate the relative cerebral blood flow, volume and relative metabolic rate of oxygen relationship in the premature neonatal brain at rest, we used information entropy, which has been published in Neurophotonics journal;

Mina Nourhashemi, Guy Kongolo, Mahdi Mahmoudzadeh, Sabrina Goudjil, Fabrice Wallois. "Relationship between relative cerebral blood flow, relative cerebral blood volume,

and relative cerebral metabolic rate of oxygen in the preterm neonatal brain. Neurophotonics. *2017 Apr;4(2):021104. doi: 10.1117/1.NPh.4.2.021104. Epub 2017 Apr 18.*

Relationship between relative cerebral blood flow, relative cerebral blood volume, and relative cerebral metabolic rate of oxygen in the preterm neonatal brain

Mina Nourhashemi
Guy Kongolo
Mahdi Mahmoudzadeh
Sabrina Goudjil
Fabrice Wallois

4.1 Abstract

The mechanisms responsible for coupling between relative cerebral blood flow (rCBF), cerebral blood volume (rCBV) and relative cerebral metabolic rate of oxygen ($rCMRO_2$), an important function of the microcirculation in preterm infants, remain unclear. Identification of a causal relationship between rCBF-rCBV and rCBF-$rCMRO_2$ in preterms may, therefore, help to elucidate the principles of cortical hemodynamics during development. We simultaneously recorded rCBF and rCBV and estimated $rCMRO_2$ by two independent acquisition systems: Diffuse Correlation Spectroscopy (DCS) and Near Infrared Spectroscopy (NIRS), respectively, in 10 preterms aged between 28 and 35 weeks of gestational age. Transfer entropy was calculated in order to determine the directionality between rCBF-rCBV and rCBF-$rCMRO_2$. The surrogate method was applied to determine statistical significance. The results show that

rCBV and $rCMRO_2$ have a predominant driving influence on rCBF at the resting state in the preterm neonatal brain. Statistical analysis robustly detected the correct directionality of rCBV on rCBF and $rCMRO_2$ on rCBF. This study helps to clarify the early organization of the rCBV-rCBF and rCBF-$rCMRO_2$ interrelationship in the immature cortex.

4.2 Introduction

Coupling between cerebral blood flow (CBF), cerebral blood volume (CBV) and cerebral metabolic rate of oxygen ($CMRO_2$) is an important primary function of the microcirculation(Kleinman and Seri, 2012; Roy and Sherrington, 1890), as the brain requires a continuous supply of glucose and oxygen (O_2) provided by CBF and blood oxygen content to meet cellular oxygen requirements (Kleinman and Seri, 2012). Identification of a causal relationship between relative cerebral blood volume (rCBV)-relative cerebral blood flow (rCBF) and relative cerebral metabolic rate of oxygen ($rCMRO_2$)-relative cerebral blood flow (rCBF) under resting physiological conditions in the neonatal brain could help to elucidate the principles of cortical hemodynamic function during development.

High coupling between changes in CBF and CBV has been demonstrated in both resting state and stimulus-induced activity. The relationship between CBF and CBV has been shown to be adequately quantified by a simple power law equation in both steady state and dynamic state (Grubb's law which assumes a constant relationship between rCBF and rCBV: $rCBV = (rCBF)^{1/\beta}$) (GRUBB et al., 1974a). Several groups have observed different values of β when measured during functional challenges (Jones et al., 2001). Under steady-state conditions, CBF and CBV have been shown to have steady values in response to a physiological challenge such as hypercapnia or hypocapnia (GRUBB et al., 1974a; Ito et al., 2003). Grubb's exponent has often been measured under dynamic conditions during neural stimulation experiments, in which both CBF and CBV changed following stimulation (Jones et al., 2001). Previous stimulation studies have reported that CBV increased progressively during the first few seconds of stimulation, while CBF did not change. After several seconds, CBF started to increase much more rapidly than CBV and returned to baseline before CBV returned to baseline (Roche-Labarbe et al., 2014), (Buxton et al., 1998). Under resting state conditions, the causality and nonlinear relationship between CBF and CBV changes can be used to determine whether CBV drives CBF or *vice versa*.

Roy and Sherrington (Roy and Sherrington, 1890) proposed the hypothesis of stimulus-induced increases in CBF driven by local metabolic demand. Strong coupling between CBF and $CMRO_2$ is observed during neural stimulation in adults (Buxton and Frank, 1997), but a mismatch in CBF-metabolism coupling was reported by Fox et al., who described that, during neuronal activation, regional cerebral blood flow (CBF) increased by 50%, while $CMRO_2$ increased by only 5% (Fox and Raichle, 1986). In fact, CBF can increase in the absence of any significant variations of $CMRO_2$ (Fujita et al., 1999), and inversely, $CMRO_2$ can increase with no significant increase of CBF (Vafaee MS, 2001). Whether or not a precise coupling exists between CBF and $CMRO_2$ during neural stimulation has been the subject of numerous studies in both adults (Raichle, 1998) and preterms (Mahmoudzadeh et al., 2013a; Mahmoudzadeh M). While the linear relationship between CBF and $CMRO_2$ changes at the resting state has been demonstrated in adults (Roy and Sherrington, 1890), it remains a subject of debate in preterms (Wong et al., 2009). This study was designed to address whether rCBV drives rCBF in preterms or *vice versa* and to provide information about the directionality and causality between measured changes in rCBV and rCBF (also, between evaluated $rCMRO_2$ and rCBF).

We used the transfer entropy (TE) method based on information theory (Shannon, 1948) to evaluate the nonlinear interactions between rCBV-rCBF and rCBF-$rCMRO_2$ in resting preterm infants. Transfer entropy determines the intensity and direction of the relationship and the dominance between two discrete random variables (Gourevitch and Eggermont, 2007) (i.e. rCBF and $rCMRO_2$). Based on the concept of causality (Wiener, 1956), we investigated a possible causal interaction between rCBF and rCBV by predictive analysis of time-series of rCBF (or rCBV) measurements by incorporating data from another previous rCBV (or rCBF) time-series.

Near-infrared spectroscopy (NIRS) (Wolf and Greisen, 2009) and diffuse correlation spectroscopy (DCS) (Durduran et al., 2010d) are optical imaging techniques that noninvasively and repeatedly measure cerebral vascular parameters at the bedside in preterms (Nourhashemi et al., 2016a; Roche-Labarbe et al., 2010). NIRS device allows to monitor relative changes in ([HbT] ([HbO]+[Hb]) that is equivalent to relative changes in CBV. The relative changes in CBF are proportional to the relative changes in tissue blood flow related to the motion of red blood cells that can be measured by the DCS device (Durduran et al., 2010d).

Estimation of $rCMRO_2$ by optical imaging requires measurement of rCBF and oxygen extraction fraction (OEF). According to Boas and Payne (Boas and Payne, 2009), CBF can be estimated from CBV by inverting Grubb's equation, which allows $CMRO_2$ to be estimated from CBV. To evaluate $rCMRO_2$ independently from rCBF it required calculated $rCMRO_2$ by rCBV and OEF. This can be achieved due to the independent measurement of rCBV by NIRS and rCBF by DCS. Although Leung *et al.*(Leung et al., 2009) suggested that Grubb's relation cannot be inverted to estimate CBF from CBV. Using independent estimation of $rCMRO_2$ by rCBV (Franceschini et al., 2007), the causality investigation could be performed by analyzing the interactions between estimated $rCMRO_2$ (NIRS) and directly measured rCBF (DCS). rCBF and $rCMRO_2$ are linked in a complex way, notably, they are affected by autoregulation mechanisms (Paulson et al., 1990). These adaptive mechanisms act to preserve constant CBF over a range of blood pressures by adapting cerebrovascular resistances or vasodilation. The mechanisms of cerebral autoregulation in preterm infants remain unclear and may involve a combination of myogenic, neurogenic, and metabolic processes that regulate cerebrovascular resistance to maintain CBF (Paulson et al., 1990). In the present study, we evaluate the possible relationships and causalities between rCBF, rCBV, and $rCMRO_2$ in resting state in preterms.

4.3 Materials and Methods

Ten preterm neonates (6 females; mean gestational age (GA) at birth: 28.5 weeks GA and 4 males; mean gestational age (GA) at birth: 27.5 weeks GA) were tested in the supine position (recording age: 31 wGA, Table 1). This study is part of the French public hospital Clinical Research Project (PHRC National). The study was approved by the Amiens University Hospital local ethics committee according to the guidelines of the Declaration of Helsinki of 1975 (CPP Nord-Ouest II-France IDRCB-2008-A00704-51). Parents were informed about the study and provided their written informed consent.

Table.1 *Clinical features of the tested infants*

Infant number	Gender	GA at birth (wk)	GA at test (wk)	Birth Weight (g)	Test Weight (g)	Apgar (1 min)	Apgar (5 min)	Multiple Birth	Delivery	Patent ductus arteriosus	Clinical conditions (Etiology)	Brain US	Drug use	EEG	Vascular resistance index
1	M	31 1/7	32 1/7	1250	1285	7	8	No	caesarean	Closed ductus	HELLP syndrome preeclampsia	normal	_	normal	0.70
2	F	25 5/7	28 1/7	750	1110	7	8	No	vaginal	Closed ductus	Multiple pregnancy - second twin died - chorioamnionitis	bilateral IVH-II + Intraventricular cysts	ibuprofen	PRS	0.84

3	M	26 6/7	30 2/7	900	1350	9	9	Yes	caesarean	Closed ductus at 27 wk	chorioamnionitis- T-T syndrome multi gestation	expanding precerebral areas	_	normal	0.85
4	M	26 6/7	32	1200	NA	2	5	Yes	caesarean	Closed ductus at 27 1/7 wk	Chorioamniotitis- T-T syndrome multiple pregnancy	normal	_	normal	0.76
5	F	28 4/7	30 5/7	1600	NA	7	8	No	caesarean	Patent ductus	prolapsed cord	suprasystemic PAH	ibuprofen	PRS	0.79
6	F	29	33 3/7	1000	2180	8	10	Yes	caesarean	Closed ductus at 29 1/7 wk	maternal hypertension, preeclampsia, and twin pregnancy	minor cerebral edema	_	normal	0.77
7	F	29	34	1249	1690	8	10	Yes	caesarean	Closed ductus at 29 4/7 wk	maternal hypertension, preeclampsia and twin pregnancy	normal	_	normal	0.85
8	F	33 3/7	35	1300	1360	10	10	Yes	caesarean	Closed ductus	Birth spontaneous triple	minor cerebral edema_ cardiac congenital abnormalities CIV	_	normal	0.61
9	M	26 4/7	29 3/7	790	1150	2	7	No	caesarean	Closed ductus	Diabetes gravidis; uterine bleeding; Preterm labor	bilateral IVH-III + hydrocephalus	Dopamine-ibuprofen-lorazepam	normal	0.90
10	F	26 1/7	27	950	1150	7	9	No	vaginal	Patent ductus	metrorrhagia+ threat of premature delivery	bilateral IVH-II	ibuprofen	normal	0.69

M: Male, **F**: Female, **GA**: Gestational Age, **Brain US:** Brain ultrasonography, **PAH:** pulmonary arterial hypertension, **PRS:** positive rolandic spikes.

4.3.1 DCS and NIRS instrumentation

DCS and NIRS devices were synchronized and all events detected by DCS were also recorded by the NIRS devices (Fig. 1). The overall measurement duration was between 30 and 40 minutes for each subject. NIRS/DCS data were acquired simultaneously from the frontal area providing large volumes of data in order to converge transfer entropy and investigate the relationships between rCBF-rCBV and rCBF-rCMRO$_2$ at the resting state.

4.3.1.1 Diffuse Correlation Spectroscopy (DCS)

DCS is an optical blood flow measurement modality that uses intensity fluctuations of near-infrared (NIR) light to noninvasively quantify CBF. The light scattered by moving red blood cells causes temporal fluctuation of the detected light intensity. The time lag of these fluctuations is quantified by the intensity-time autocorrelation function of the detected light.

The correlation diffusion equation is applied to fit the autocorrelation function in order to calculate a cerebral blood flow index (CBFi). Neuro-Monitor-FloMo (Hemophotonics SL, Spain) consists of a narrowband CW laser (785 nm, Crystalaser Inc., NV) with a long coherence length (> 50 meters), four fast photon-counting avalanche photodiodes (APD) (SPCM-AQR-14-FC, Pacer Components Inc., UK), and a four-channel autocorrelator board (Flex03OEM-4CH, Correlator Inc., NJ). The system uses continuous-wave (CW) lasers in the NIR range (~785 nm) with an acquisition rate of 0.3921 Hz (one sample every 2.55 s). The light was delivered to the brain surface via multi-mode fibers and light on the head surface was detected by 4 single-mode fibers d_{DCS}=2 cm away from the source. The light was detected by single-photon counting avalanche photo-diodes (SPADs) (SPCM-AQR(H) series, Excelitas, Canada).

4.3.1.2 Continuous wave tissue oximeter (NIRS)

Near-infrared spectroscopy probes NIRO-200NX (Hamamatsu Photonics Corp., Tokyo, Japan) were placed on the infant's forehead to measure cerebral oxygenation in the frontal cortex. The NIRO 200 NX uses spatially resolved spectroscopy at three wavelengths (λ=735 nm, 810 nm, and 850 nm). It is based on the solution of the diffusion approximation for a highly scattering semi-infinite homogeneous medium. The effective light attenuation coefficient can be estimated by measuring the decrease in reflected light as a function of distance. By assuming wavelength dependence of the reduced scattering coefficient, the spectral shape of the absorption coefficient can then be calculated and tissue oxygen saturation can be estimated (Matcher et al., 1995b). The average output power of the lasers was less than 2 mW and the CW acquisition rates were 5 Hz (200 ms).

4.3.1.3 The DCS and NIRS probe

To simultaneously measure rCBF and rCBV dynamics, we developed a specific probe that supports DCS and NIRS emitters and detectors. Recording sites on the subject's head and a diagram of the two combined probes are shown in Figure 1(a). The infants were placed in the supine position on a comfortable pad in a dark and quiet incubator. The incubator was further protected against ambient light by dark sheets. The probe was smoothly secured to the infant's head with straps and foam padding. Figure 1(b) shows the diagram of the combined DCS-NIRS probe. DCS probe: The tips of the source and detector fibers were angled to 90º and tightly held in place by a flexible rubber material. Four detectors (blue circles) were set up in a multicore arrangement away (d_{DCS} = 2 cm) from the emitter (red circle), creating 4 measuring

points (channels) over the frontal area. A special DCS probe made of soft, flexible rubber (3 mm thick) was designed to comfortably hold the source and detector fibers on the infant's head. NIRS probe: The NIRS probe comprising 2 detectors and 1 source and the emitter-detector distance of the continuous-wave optical NIRS probe was 3 cm. The NIRS source contained three wavelength emitters (735, 810 and 850 nm) (bottom right_hand corner) SO_2 (tissue oxygenation) was measured by using the Spatially Resolved Spectroscopy(SRS) method. SRS is a method used to calculate concentrations by measuring the change of light attenuation (A) over distance (d), i.e. $\frac{\partial A}{\partial d}$, as shown in Figure 1(b).

4.3.2 Data processing and statistical analysis

Off-line analysis was performed using in-house MATLAB scripts for CBF measured by Neuro-Monitor-FloMo (Hemophotonics SL, Spain), and for CBV (total hemoglobin, HbT=HbO+HbR) and oxygen extraction fraction (OEF) measured by NIRO-200NX (Hamamatsu Photonics Corp, Tokyo, Japan).

A z-score-based algorithm was used to reject artifact signals (Mahmoudzadeh et al., 2013a). As individual features, such as skull thickness and hair color, influence signal strength, the signal was first homogenized in each participant by computing a z-score across all measurement periods for each channel. A z-score greater than 4 in any channel was considered to be an artifact, in which case, the entire artifact time-window was excised from the data for all channels (Mahmoudzadeh et al., 2013a). The mean value of rCBF signals recorded from 4 paired source-detectors was calculated. The remaining cleaned rCBV, rCBF signals were band-pass filtered [0.03–0.5 Hz] using a zero phase filter (Butterworth, order: 3) to eliminate physiologic noise (e.g. slow drifts, arterial pulse oscillations).

4.3.2.1 rCMRO$_2$ calculated by NIRS data

$CMRO_2$ can generally be calculated by combining relative changes in CBF and oxygen extraction fraction, but monitoring rCBV independently of rCBF by the NIRS device allows $rCMRO_2$ to be evaluated independently of rCBF (Roche-Labarbe et al., 2010) by using $(rCBV)^{\beta}$ instead of rCBF in relation (1) (Fig. 1c). The relative cerebral metabolic rate of oxygen was estimated as (Culver et al., 2003):

$$rCMRO_2 = rCBF \times rOEF \quad (1)$$

Where rOEF is defined as:

$$rOEF = \frac{SaO_2(t)-SvO_2(t)}{SaO_2(t_0)-SvO_2(t_0)} = \frac{SaO_2(t)-SO_2(t)}{SaO_2(t_0)-SO_2(t_0)} \quad (2)$$

With venous oxygenation $SvO_2 = (SO_2 - a \times SaO_2)/b$, where a+b=1, a and b are the arterial and venous contributions that are constant over time (Watzman et al., 2000), and arterial oxygenation SaO_2=100%. Mechanical ventilation parameters and inspired oxygen concentrations were maintained constant at sufficiently high levels to saturate arterial hemoglobin (SaO2 ≈ 100%).

SO_2 is the microvascular tissue oxygen saturation (Wray et al., 1988) ($SO_2 = HbO_2/HbT$). By considering Grubb's relation between changes in rCBF and rCBV (Davis et al., 1998) (β=0.9) (Roche-Labarbe et al., 2010) (time invariant characteristic of beta has been validated statistically),

$$rCBF = \frac{CBF_i(t)}{CBF_i(t_0)} = (\frac{CBV(t)}{CBV(t_0)})^{\beta} = (rCBV)^{\beta} \quad (3)$$

$$rCMRO_2 = (rCBV)^{\beta} \times rOEF \quad (4)$$

CBV (cerebral blood volume) was defined as: $= \frac{(HbT \times MW_{Hb})}{HGB \times D_{bt}}$, where CBV is expressed in ml/100 g, HbT in µmol, MW Hb (64,500 g/mol) is the molecular weight of hemoglobin, Dbt (1.05 g/ml) is the brain tissue density and HGB (g/dl) is the blood hemoglobin concentration. The control state at time t0 was defined as the mean value of the signal and was considered to be the reference value.

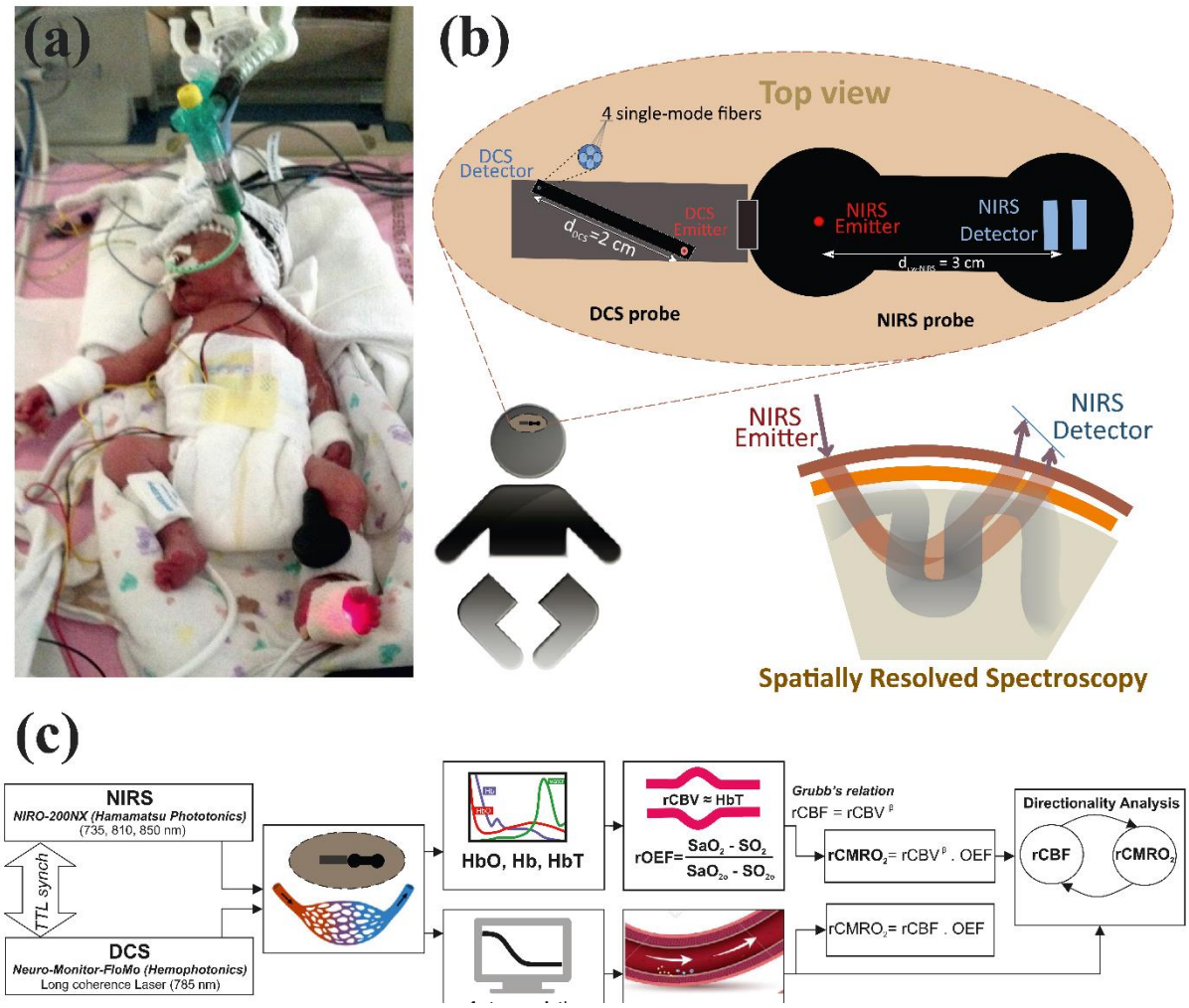

Fig. 1 ***(a)*** *The infants were tested with the DCS and CW-NIRS systems,* ***(b)*** *Diagram of the combined DCS-NIRS probe,* ***(c)*** *Diagram of the calculation of $rCMRO_2$ by NIRS data and rCBF by DCS data.*

4.3.3 Nonlinear Flow-Metabolism interaction by transfer entropy

Transfer entropy was used to define the strength of causality and the coupling between rCBV-rCBF and rCBF-$rCMRO_2$. The concept of entropy is related to the degree of uncertainty associated with a signal random variable (i.e. rCBF). In other words, it provides a measure of the average uncertainty in a random variable. The determination of entropy of a random variable rCBF with a probability mass function P(rCBF) is defined by the following equation:

$$H(\mathrm{rCBF}) = \sum_{i=1}^{N} -P(rCBF_i).log[P(rCBF_i)] \quad (5)$$

The first step consisted of the evaluation of the entropy (H) corresponding to the uncertainty associated with one of the 2 variables, rCBV, and rCBF. The analysis was based

on times-series with identical probability variables and a flat distribution of quantized values. The original normal distribution of the two variables (rCBF and rCBV) is shown in Figure 2(a). In order to produce time-series with identical probability variables of rCBF and rCBV, raw rCBF and rCBV data were quantized using 25th, 50th, 75th and 100th percentiles and rCBF and rCBV values between the (0, 25th), (25th, 50th), (50th, 75th) and (75th, 100th) percentiles, corresponding to 1, 2, 3, 4, respectively in Figure 2(b). The quantized rCBF and rCBV values presented the required flat distribution, (Fig. 2c).

The reduction of the uncertainty of one random variable obtained by the addition of a second variable (i.e. rCBV) (where rCBV is not completely independent of rCBF), is defined as mutual information (MI). Mutual information is a measure of the amount of information that one random variable provides about another random variable, defined by H(rCBF, rCBV) corresponding to the entropy of the two variables, rCBF, and rCBV.

$$MI(\mathrm{rCBF}, rCBV) = H(\mathrm{rCBF}) + H(\mathrm{rCBV}) - H(\mathrm{rCBF}, \mathrm{rCBV}) \quad (6)$$

The second step consisted of the evaluation of the Mutual Information (MI) shared by the 2 variables. To evaluate the interdependency between the 2 variables, rCBV, and rCBF, the Mutual Information MI was compared to the Entropy (H) of each variable. When MI between these 2 variables is less than entropy (H), it can be concluded that the 2 variables are dependent.

As MI is symmetrical for the exchange of signals, it captures the information shared by two signals but is unable to distinguish the driving signal. The reduction in the uncertainty of rCBF due to the information provided by rCBV can also be obtained by introducing a third variable, resulting in conditional mutual information (CMI). The mutual information between rCBF and rCBV conditioned by a third variable corresponds to the part of the information derived from simultaneous analysis of rCBF and rCBV that is unrelated to the third variable (i.e. Z).

$$CMI(rCBF, rCBV|Z) = H(rCBF, Z) + H(rCBV, Z) - H(rCBF, rCBV, Z) - \mathrm{H(Z)} \quad (7)$$

To obtain an asymmetrical measure, the bivariate version of CMI was used, wherein the third variable is a lagged version of variable rCBF or rCBV (delayed mutual information). It states that a signal rCBF is caused by signal rCBV when the future of signal rCBV is more accurately predicted by appending information from the past and present of signal rCBF than by using information from the present and past of signal rCBV alone (Wiener, 1956). Delayed

MI shows a causal dependence related to the information exchanged rather than the information shared (for instance, due to a common drive of both signals by a third, external source) (Schreiber, 2000). Transfer entropy from rCBF to rCBV is defined by the following formula, where t is a discrete time-index value:

$$TE(rCBV \rightarrow rCBF) = CMI(rCBF_t, rCBV_{t-1} | rCBF_{t-1}) = H(rCBF_t, rCBF_{t-1}) + H(rCBV_{t-1}, rCBF_{t-1}) - H(rCBF_t, rCBV_{t-1}, rCBF_{t-1}) - H(rCBF_{t-1}) \quad (8)$$

$$TE(rCBF \rightarrow rCBV) = CMI(rCBV_t, rCBF_{t-1} | rCBV_{t-1}) = H(rCBV_t, rCBV_{t-1}) + H(rCBF_{t-1}, rCBV_{t-1}) - H(rCBV_t, rCBF_{t-1}, rCBV_{t-1}) - \mathrm{H}(rCBV_{t-1}) \quad (9)$$

The information transfer between rCBV and rCBF was measured by the time-lagged Conditional Mutual Information (CMI). By applying time-lagged CMI to the two variables (rCBF and rCBV), if $TE(\mathrm{rCBF} \rightarrow \mathrm{rCBV})$ is less than $TE(\mathrm{rCBV} \rightarrow \mathrm{rCBF})$, it can be concluded that rCBF is more dependent on rCBV.

Then, because transfer entropy is based on transition probabilities, it can be used to determine the dominant direction in the relationship between two variables. The directionality index (DI) between two variables rCBF and rCBV is calculated by:

$$\mathrm{DI}(\%) = \frac{TE(rCBV \rightarrow rCBF) - TE(rCBF \rightarrow rCBV)}{TE(rCBV \rightarrow rCBF) + TE(rCBF \rightarrow rCBV)} \times 100 \quad (10)$$

When DI> 0, it was concluded that the rCBV was predominant over rCBF. Contrariwise, when DI <0, rCBF controlled rCBV and, DI = 0 indicates balanced bilateral interactions between the two variables. The statistical significance of TE and MI measurements was evaluated by using a surrogate method by measuring the dependency of two time-series (rCBF and rCBV) with one of the signals randomly shuffled and reorganized and with each sample replaced in a random position in the series. The limit of statistical confidence corresponding to the 95th percentile was found by repeating a different permutation on one of the signals 300 times.

The third step consisted of the evaluation of the direction of the relationships between rCBF and rCBV, which can be determined by the directionality index (DI) on both measured and surrogate data. The confidence intervals can be used to calculate statistical power in order

to conclude that a surrogate explains at least a certain proportion of the correct direction. If the test statistic from the data is higher than the 95th percentile of the surrogate, it demonstrates the reliability of the estimation procedure (Fig. 2d). All steps were identical for investigation of the relationship between rCBF and rCMRO2.

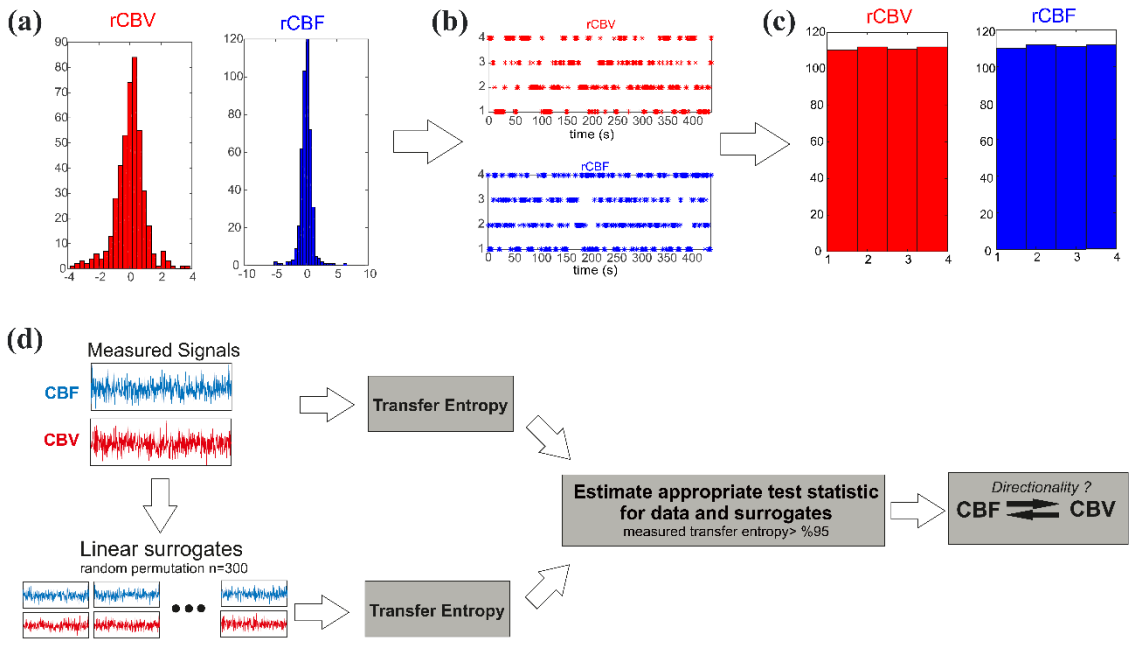

Fig. 2 (a) *Distribution histogram of rCBV and rCBF,* ***(b)*** *Time-series of rCBV and rCBF expressed as quantized values to produce time-series with identical probability variables,* ***(c)*** *Flat distribution of rCBV and rCBF,* ***(d)*** *Diagram of the surrogate data approach to the rCBF-rCBV coupling hypothesis.*

4.4 Results

4.4.1 Linear interaction between rCBF-rCBV and rCBF-rCMRO$_2$

Changes in rCBV were plotted as a function of rCBF for 10 subjects (Fig. 3a), resulting in a fluctuating correlation between rCBV and rCBF with a tendency towards a positive correlation in 6/10 preterms and a negative correlation in the remaining 4 preterms with an average slope of 0.02±0.12.

4.4.2 Computation of transfer entropy

The entropy (H) of rCBF and rCBV for each subject and each parameter was equal to 2. For each subject, the mutual information MI of rCBF and rCBV was less than the entropy (H)

of rCBV and rCBF ($MI_{(rCBF, rCBV)} < H_{(rCBV)}$ and $MI_{(rCBF, rCBV)} < H_{(rCBF)}$), (Fig. 3b). By considering $rCMRO_2$ as a product of the measured HbT and HbO_2, the same analysis was performed to test the relationship between rCBF and $rCMRO_2$ (Fig. 4). Selected parts of $rCMRO_2$ and rCBF for subjects #4 and #10, illustrating the evaluation of TE from $rCMRO_2$ to rCBF as indicated by circles on signals in the dark gray box, suggest that the source signal ($rCMRO_2$) drives the target signal (rCBF) (Fig. 4a). The entropy (H) of rCBF and $rCMRO_2$ for each subject and each parameter was equal to 2. For each subject, MI of rCBF and $rCMRO_2$ was less than the entropy (H) of $rCMRO_2$ and rCBF. The average value of Mutual Information (MI=0.0343) was less than the entropy (H=2) (Fig. 4b). These results indicate that rCBF and rCBV (also, rCBF and $rCMRO_2$) can be considered to be dependent variables at the resting state in the preterm brain.

4.4.3 Causal relationship between rCBF-rCBV and rCBF-$rCMRO_2$

Transfer Entropy (TE) was used to identify a causal relationship between rCBF and rCBV, as it detects the relationship between the past of one signal (rCBV) and the present of another signal ($rCBF_{t+}$). For each subject, $TE_{(\mathrm{rCBF}\rightarrow\mathrm{rCBV})}$ was less than $TE_{(\mathrm{rCBV}\rightarrow\mathrm{rCBF})}$ and the average value of $TE_{(\mathrm{rCBF}\rightarrow\mathrm{rCBV})}$ (0.0476) was less than the average value of $TE_{(\mathrm{rCBV}\rightarrow\mathrm{rCBF})}$ (0.2702) (Fig. 3b). These results demonstrate that $rCBF_{t+}$ appears to be more dependent on rCBV than $rCBV_{t+}$ on rCBF, suggesting that rCBV drives rCBF at the resting state in the preterm brain.

This relationship can be summarized by the Directionality Index (DI) between rCBF and rCBV (Fig. 3b). The negative values of the Directionality Index (DI<0) suggest that rCBV was predominant over rCBF. Statistical analysis with a limit of statistical confidence corresponding to the 95th percentile of the 300 trials was performed according to the surrogate method. As the Directionality Index (DI) measured in each of the 10 subjects was higher than the 95th percentile, statistical analysis robustly detected the correct direction of rCBV on rCBF. By applying the same analysis to the relationship between the rCBF and $rCMRO_2$, the negative values of DI<0 suggest that estimated $rCMRO_2$ would be predominant over measured rCBF (Fig. 4c, d).

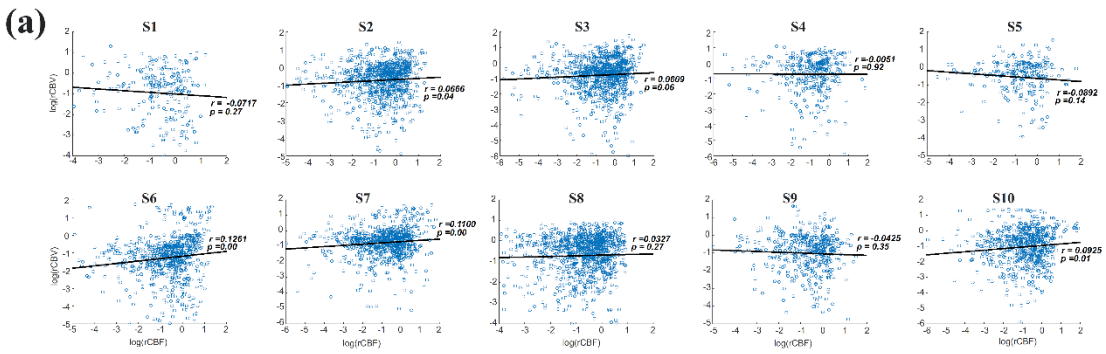

(b)

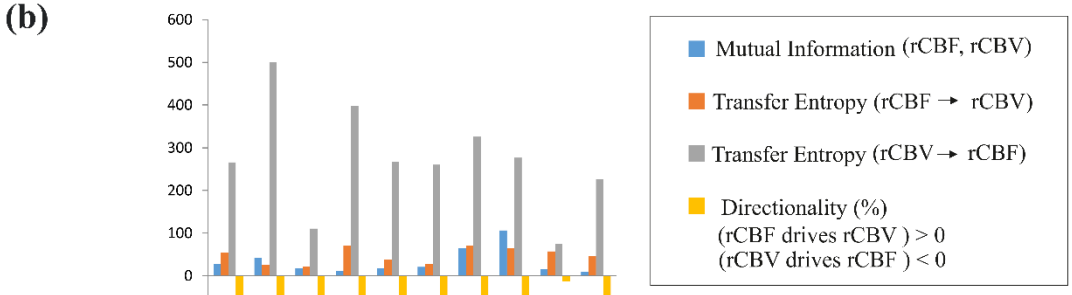

	Sub1	Sub2	Sub3	Sub4	Sub5	Sub6	Sub7	Sub8	Sub9	Sub10
MI (rCBF, rCBV)	27.4	42.3	18	11.3	17.1	20.6	64.3	106.2	15.4	9
TE (rCBF-> rCBV)	55	25.3	21.3	70	38	27.6	71.4	65	57.4	45.7
TE (rCBV -> rCBF)	266	500.4	110.7	398.7	267.1	260.1	325.7	276.7	74.3	226.5
D (%)	-65.5	-90.3	-67.6	-70.1	-75	-80.8	-64.02	-61.96	-12.8	-66.4

Fig. 3 ***(a)*** *Correlation between log(rCBV)_log(rCBF),* ***(b)*** *Amount of information shared between rCBF and rCBV measured by MI, TE indicates the amount of information exchanged from rCBF to rCBV and vice versa and Directionality index(D). (*all values are multiplied by 10^3).*

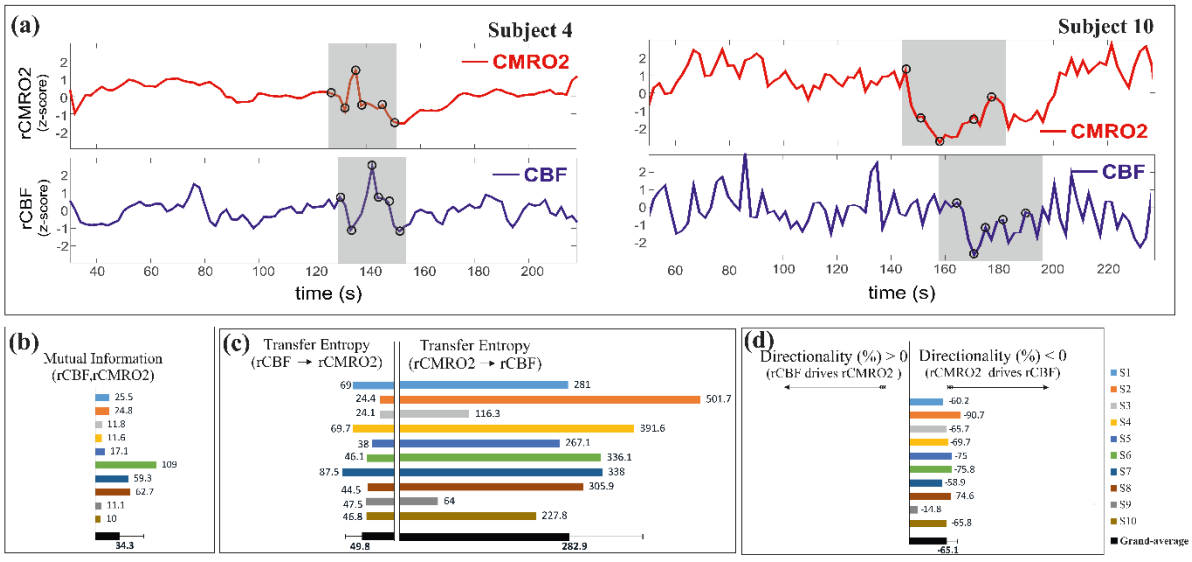

Fig. 4 ***(a)*** *A selected part of $rCMRO_2$ and rCBF (subjects #4, #10), illustrating evaluation of TE from $rCMRO_2$ to rCBF,* ***(b)*** *Mutual information shared between rCBF_$rCMRO_2$,* ***(c)*** *Rate of information (TE) exchanged from rCBF to $rCMRO_2$ and vice versa,* ***(d)*** *Directionality index (D). (*all values are multiplied by 10^3).*

4.4.4 Directionality from rCBV to rCBF with GA at the time of the test, vascular resistance index, Apgar score at 1 min and at 5 min, bilateral IVH-III in preterm neonates

Relationship of Directionality from rCBV to rCBF with GA at the time of the test, vascular resistance index, Apgar score at 1 min and at 5 min, bilateral IVH-III in preterm neonates was investigated. Figure 5 shows the directionality between rCBV and rCBF as a function of gestational age at the time of the test (R^2 = 0.003, P-value = 0.78) (Fig. 5a), a function of vascular resistance index (R^2 = 0.072, P-value = 0.26) (Fig. 5b), a function of Apgar score (1 min) (R^2 = 0.254, P-value = 0.100) and Apgar score (5 min) (R^2 = 0.046, P-value = 0.518) (Fig. 5c), The results do not demonstrate any significant relationship between maturational stage, vascular resistance index, Apgar score and developmental dynamics of the relationship between rCBF and rCBV. More subjects could be recruited in future studies in order to investigate the impact of gestational age, vascular resistance index, Apgar score, bilateral IVH-III on TE.

4.4.5 Relationship between rCMRO2 and mean arterial blood pressure at the resting state in preterm neonatal brain

Figure 6 shows the relationships between $rCMRO_2$ and mean arterial blood pressure. The nonzero mutual information between $rCMRO_2$ and mean arterial blood pressure demonstrates that the two variables are partially dependent on each other, suggesting that $rCMRO_2$ might also partly be dependent on other systemic variables.

On the other hand, the grand averages of 10 subjects for the linear correlation between ($rCMRO_2$ and mean arterial blood pressure (MABP)) and ($rCMRO_2$ and heart rate (HR)) were not statistically significant (Y_{rCMRO2}=-0.0059 .X_{MABP}+0.0005, P = 0.4 and Y_{HR} =-0.0056 . X_{rCMRO2}+0.00056, P = 0.6, respectively).

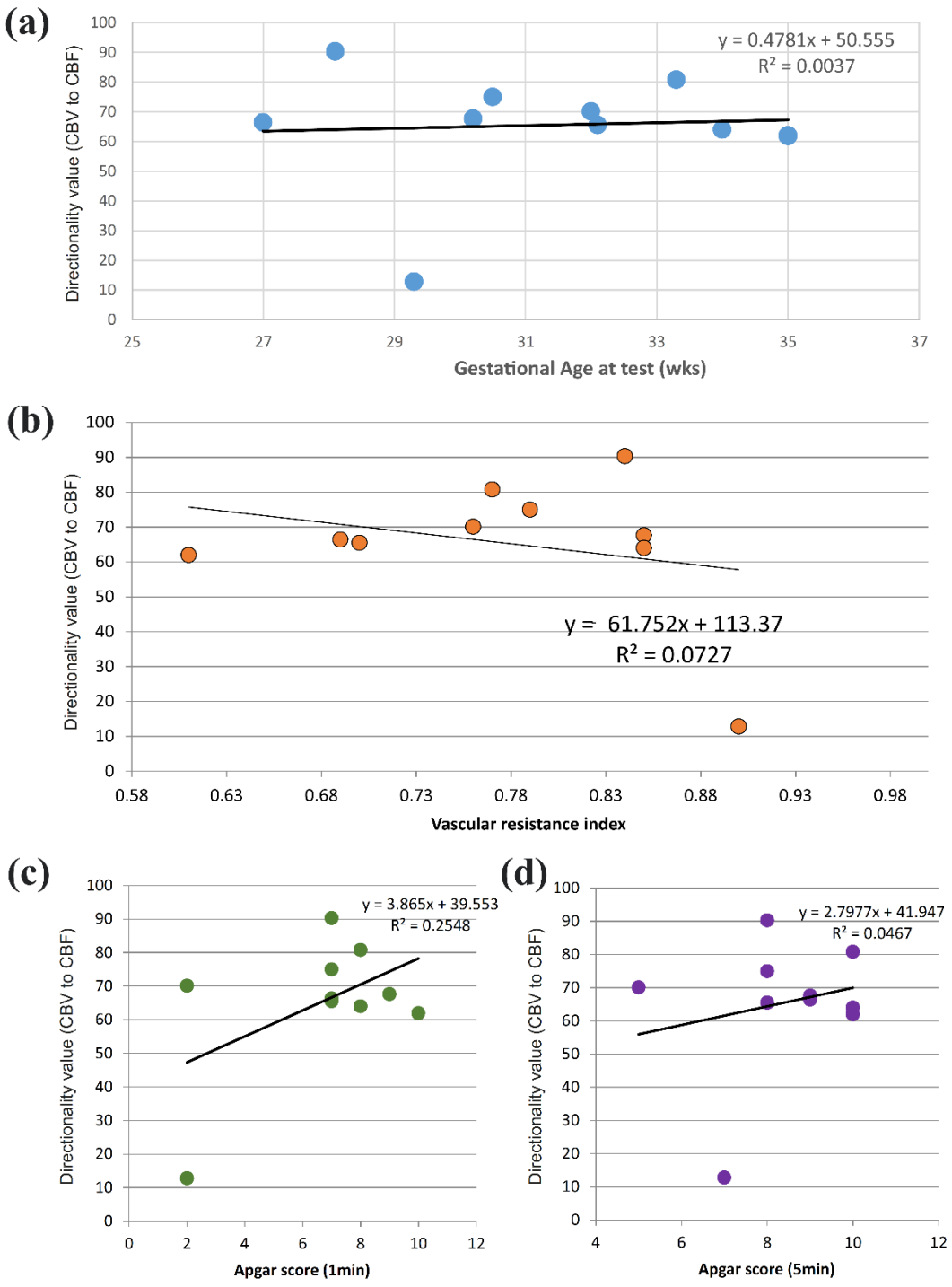

Fig. 5 *Directionality% (rCBV to rCBF) as a function of* ***(a)*** *GA at the time of the test (weeks),* ***(b)*** *Vascular resistance index,* ***(c)*** *Apgar score at 1 min and* ***(d)*** *Apgar score at 5 min. R^2 and the linear regression equation are indicated in the upper right corner of the graph.*

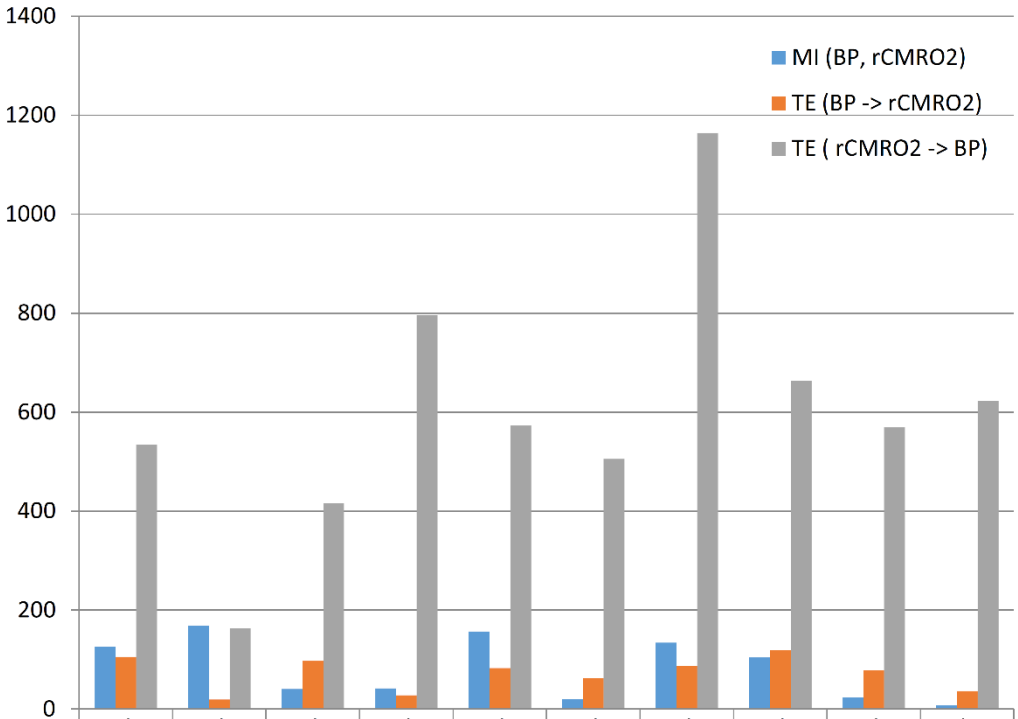

	Sub1	Sub2	Sub3	Sub4	Sub5	Sub6	Sub7	Sub8	Sub9	Sub10
MI (BP, rCMRO2)	126.1	168.8	40.8	41.7	156.8	20.5	134.3	103.9	23.6	8
TE (BP -> rCMRO2)	105.2	19.4	97.4	28	82.7	62	87.3	118.7	78	36
TE (rCMRO2 -> BP)	533.9	163.5	415.4	795.4	572.4	505.7	1164	663.9	568.9	623.2

Fig. 6 *Amount of information shared between $rCMRO_2$ and mean arterial blood pressure measured by mutual information (MI), Transfer entropy (TE) indicates the amount of information exchanged from $rCMRO_2$ to mean arterial blood pressure and vice versa.*

4.4.6 Impact of possible time lag variability

Analysis of directionality is often based on synchrony assumptions of the two signals, suggesting that time lag variability would have an impact on the conclusions. It is therefore important to assess this time lag effect by means of sensitivity analyses. We considered different time lags between 0.8s to 2.4s (DCS sampling period (2.5s) is the maximum possible time lag). Figure 7 shows that time lag changes had a negligible impact on the directionality index. The consistency between the results of primary analysis and the results of maximum possible time lag analysis therefore support the conclusions and the credibility of the results.

4.4.7 The effect of different beta values on transfer entropy

We used a constant value for beta in Grubb's equation (β=0.9) (Roche-Labarbe et al., 2010). The effect of different constant β values (0.1, 0.2, 0.3, 0.4, 0.75, 1, 2) on transfer entropy

(TE) between rCBF and $rCMRO_2$ was investigated (Fig. 8). Regardless of the β value considered, the directionality of $rCMRO_2$ was predominant over rCBF.

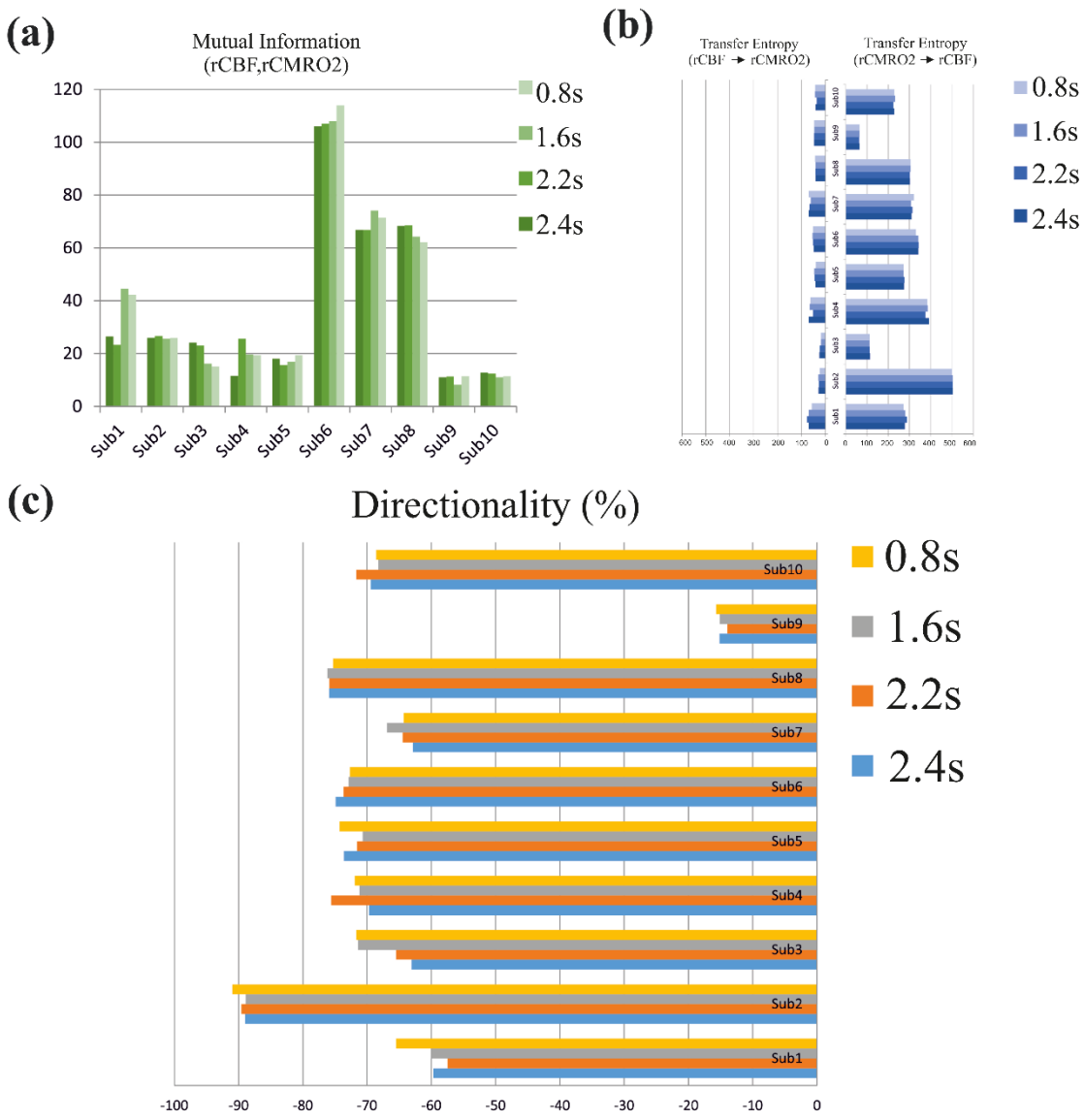

Fig. 7 *Impact of time-lagged rCBF on $rCMRO_2$ with different time lags (0.8s, 1.6s, 2.2s, 2.4s)* ***(a)*** *Amount of information shared between rCBF and $rCMRO_2$ measured by mutual information (MI),* ***(b)*** *Transfer entropy (TE) indicates the amount of information exchanged from rCBF to $rCMRO_2$ and vice versa with different time lags,* ***(c)*** *Directionality index D indicates the dominant direction of the transfer, the negative sign indicates the dominance of $rCMRO_2$ over rCBF and vice versa.*

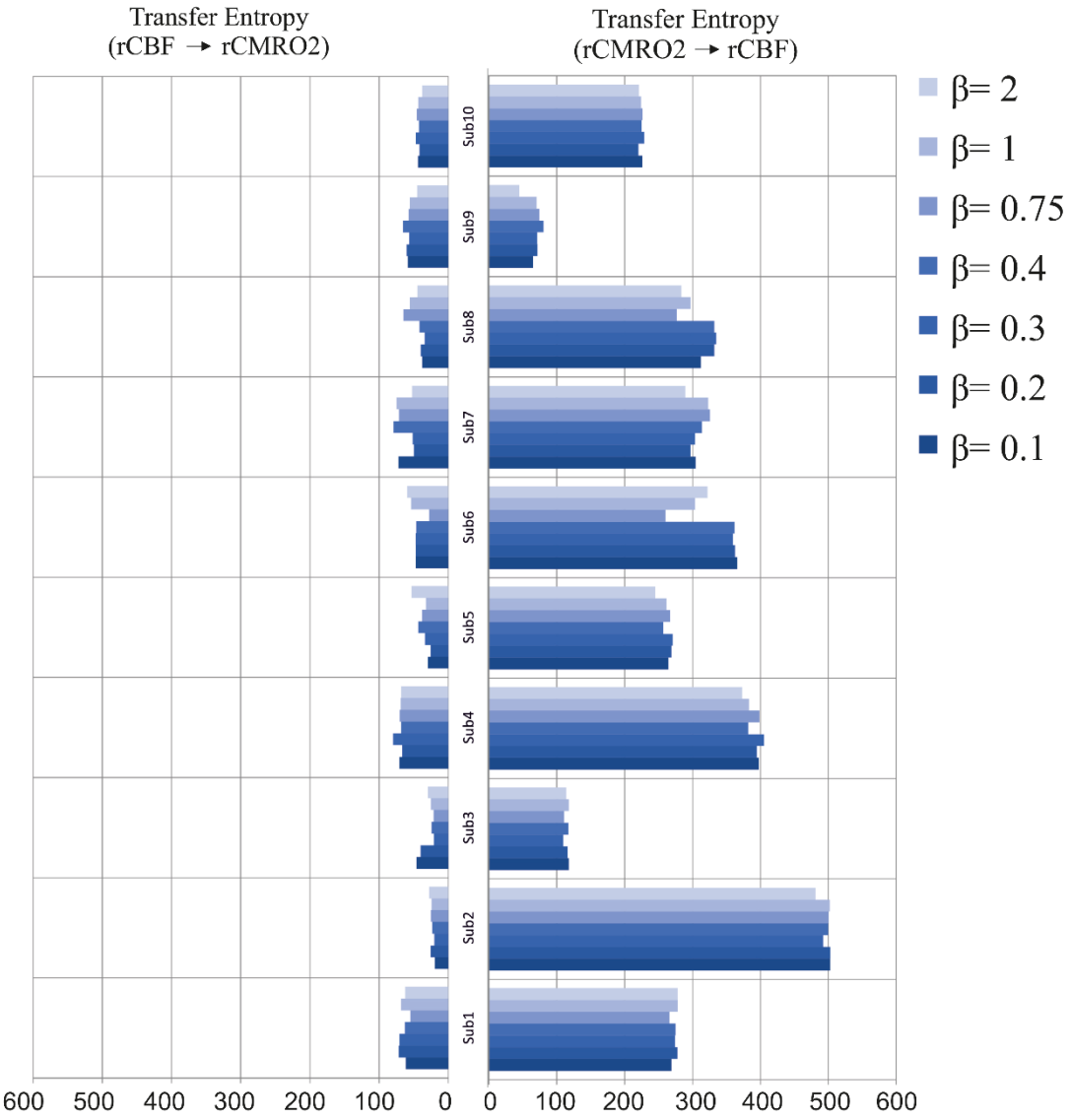

Fig. 8 *Transfer entropy (TE) indicates the amount of information exchanged from rCBF to $rCMRO_2$ and vice versa, (10 subjects with 7 different values of β).*

4.5 Discussion

This study demonstrates that, in very preterm newborns (<32 wGA), rCBV is predominant over rCBF and that neurovascular interactions appear to be sufficiently efficient for $rCMRO_2$ to be already able to drive rCBF at rest.

While our previous data (Mahmoudzadeh et al., 2013a; Mahmoudzadeh M) supported the existence of neurovascular coupling in response to neuronal activations by auditory stimuli in very preterm infants, little is known about the interactions between rCBF and rCBV (and

between rCBF and $rCMRO_2$) in preterms at rest (Wong et al., 2009), in whom the cardiovascular and autonomic nervous systems remain largely immature. The linear relationship between rCBF and rCBV (rCBF and $rCMRO_2$) has been extensively studied at rest in adult humans (Ito et al., 2003) (during sleep (Madsen et al., 1991) and under general anesthesia (Lam et al., 1995)) and in animals (GRUBB et al., 1974b; Sokoloff et al., 1977), showing that CBF and CBV (as well as CBF and $CMRO_2$) (Cohen et al., 1995) are tightly coupled under normal conditions. In the present study, the linear correlation between rCBF and rCBV was fluctuating with a tendency to be either positive (n=6) or negative (n=4) (Fig. 3a), which is consistent with the results in preterm infants reporting rather stable rCBV whatever the changes in rCBF (Roche-Labarbe et al., 2010). In comparison to the mature adult brain, presenting high coupling between CBF and CBV, a weaker correlation between these two variables was observed in the developing neonatal brain.

Most studies have explored the linear relationships between rCBF and rCBV (Roche-Labarbe et al., 2010) (rCBF and $rCMRO_2$ (Wong et al., 2009)). To the best of our knowledge, this is the first study to evaluate the nonlinear relationships between rCBF and rCBV in preterm infants, demonstrating the intensity and asymmetry of the interactions between these two autonomic variables, ie, rCBF and rCBV, using transfer entropy (TE) analysis derived from information theory (Shannon, 1948). To ensure the independency of the recorded parameters, rCBF and rCBV were simultaneously recorded by two separate devices using two different approaches, DCS and NIRS, respectively.

In preterms, the negative Directionality Index (DI<0) between rCBV and rCBF suggests that rCBV has a more predominant driving influence on rCBF (*vs.* rCBF to rCBV) at the resting state. We tested to what degree the maximum time lag between the two separate devices would affect the results, despite the fact that the acquisition devices were synchronized by an external event trigger. The maximum possible lag changes (Fig. 7) and the effect of different constant values of β (Fig. 8) had a negligible impact on the directionality index. Our results at resting state are in agreement with those reported by Roche-Labarbe et al., (Roche-Labarbe et al., 2014), although their study was conducted under different conditions, with large in-flow modeled related to task-evoked conditions such as somatosensory stimulation (Roche-Labarbe et al., 2014). During the first few seconds of stimulation, rCBV increased progressively, while changes in rCBF started to increase abruptly after only a few seconds (Roche-Labarbe et al., 2014), suggesting a lag between changes in rCBV and rCBF.

Notwithstanding the methodological limitations ((i) small differences in tissue volume sampled, (ii) optimization of the distances between emitters and detectors of the NIRS and DCS probes to minimize light interferences, (iii) higher integration time for DCS than for NIRS to achieve a balance between signal quality and temporal resolution) and the physiological complexity (arteriole resistance, arterial/venous/capillary compartment), the use of information entropy has the advantage of combining the probabilities for multiple outcomes to one meaningful measure, ie the directionality from rCBV to rCBF, and it does not assume a specific statistical distribution or an estimate of a mean.

Transfer entropy implies to quantify the causal relationship between the variables (i.e. rCBV and rCBF). The causality does not necessarily imply that two variables have a time lag, they also could have taken place simultaneously. Increased volume followed by increased flow with a slight delay (i.e. time lag between the rCBV and rCBF), direct us to explore for a suitable physiological underlying mechanism. Although the reports of relative CBV and CBF dynamics have been controversial (Jones et al., 2001; Malonek et al., 1997b; Sheth et al., 2005), our finding (rCBV followed by rCBF changes) support the assumption of a process of capillary filling (increase in rCBV) (Malonek et al., 1997b) followed by a delayed neurovascular regulation of rCBF in the capillary bed. Functional recruitment of capillaries is the changeover of low blood flow to high blood flow capillaries (Kuschinsky and Paulson, 1992). An initial phase of activation can be expected when local capillary blood volume increases, but at a time when arterioles have not yet dilated and the blood flow has not yet increased (Malonek et al., 1997b). This type of lagged relationship between blood volume and blood flow has been described to be valid if the outflow from the capillary compartment in the activated regions is briefly lower than the inflow to this capillary compartment (Malonek et al., 1997b). Following the neuronal activation, the capacitance of the capillaries was to raise and their resistance was to reduce (i.e. the capillary bed might play as a ‘‘sink’’ for red blood cells) (Malonek et al., 1997b). This in turn allows the outflow from the compartment to decrease, before the occurrence of upstream arteriolar dilatation that would provoke an increased inflow. Thereafter, when the arteriolar part has dilated, the increased inflow causes a flow increase in the entire capillary compartment, oxyhemoglobin increases, and deoxyhemoglobin decreases (Malonek et al., 1997b).

Leung *et al.*(Leung et al., 2009) suggested that Grubb’s relation cannot be used to estimate $CMRO_2$ because the variances in $\log(CBF/CBF_0)$ and $\log(CBV/CBV_0)$ measurements would

be different, but, in contrast, Boas and Payne noted that: “both of these calculations assume that the dependent variables are functionally dependent on the independent variable and that the variance in the linear regression is exclusively derived from the variance in the dependent variable”. rCBF can therefore be estimated from rCBV, allowing $rCMRO_2$ to be estimated when only rCBV measurements are available(Boas and Payne, 2009).

By considering the neurovascular coupling cascade (multiple signaling pathways encompassing perivascular astrocytes, vasoactive chemical agents, and direct neuronal connections)(Cauli and Hamel, 2010; McCaslin et al., 2011) and estimation of $rCMRO_2$ index by rCBV (Boas and Payne, 2009), the linear correlation between rCBF and $rCMRO_2$ was also fluctuating with a tendency to be either positive (n=6) or negative (n=4). This fluctuation in the linear correlation between rCBF and $rCMRO_2$ has already been described in preterm infants, with no relationship observed in healthy preterms, while a strong relationship was observed after dopamine treatment (Wong et al., 2009), suggesting that the underlying mechanisms of the interactions between rCBF and $rCMRO_2$ in preterms are fairly complex, immature and have yet to be determined (Greisen, 1986). The direction of the nonlinear relationship between rCBF and $rCMRO_2$ is an accepted hypothesis in adults(Roy and Sherrington, 1890) and supports the idea that rCBF could be controlled by oxygen demand (Baumgartner, 2006).

Nonlinear analysis can be used to detect a wider range of interactions between variables compared to conventional analysis, such as linear correlation. Analysis of the nonlinear relationship between rCBF and $rCMRO_2$, and the negative values of DI suggest that $rCMRO_2$ is significantly predominant over rCBF in the resting state in the preterm healthy brain. As $rCMRO_2$ depends on the degree of brain activity at the resting state (Kuschinsky, 1991), rCBF variations may be partly driven by brain activity at rest. This hypothesis is now being tested in the laboratory by combining EEG, NIRS and DCS in preterms.

The relationship between $rCMRO_2$ and mean arterial blood pressure were also assessed. The nonzero mutual information between $rCMRO_2$ and mean arterial blood pressure implies that, although $rCMRO_2$ might be affected by changes in systemic variables, some of the variations of $rCMRO_2$ depend on other variables such as rCBF. This study also demonstrates a possible relationship between rCBF and $rCMRO_2$ with a directionality from estimated $rCMRO_2$ to measured rCBF.

The already functional directionality between rCBF and rCBV or between rCBF and $rCMRO_2$ suggests that the intimate cellular mechanisms observed in adults, such as the participation of astrocytes and the various signals arising from activated neuronal assemblies and transmitted to perivascular glial endfeet, might be already functional in preterms from 28 wGA, resulting in changes in arterial tone(Paulson et al., 2010).

This type of analysis could be applied in clinical practice to investigate whether this relationship between rCBF and rCBV (rCBF and $rCMRO_2$) persists in patients at risk of neuronal or vascular brain injury (IntraVentricular Hemorrhage (IVH), hydrocephalus, etc.). The results of this study demonstrate the lowest directionality value ($rCMRO_2$ to rCBF) for neonate #9 with bilateral IVH-III and hydrocephalus. Although a greater number of subjects must be included in future studies, this result is in agreement with those we reported in Mahmoudzadeh et al (Mahdi Mahmoudzadeh and Kongolo, 2016), showing the absence of hemodynamic responses induced by phoneme stimuli in IVH III-IV preterms. The results also demonstrate the highest directionality value (rCBV to rCBF) and ($rCMRO_2$ to rCBF) in neonate #2, who was one of the two patients of our study with abnormal EEG (positive rolandic spikes). Further studies are also required to assess the developmental dynamics of the relationship between rCBF and rCBV (rCBF and $rCMRO_2$) at different postnatal ages. The various treatments administered to preterm infants in this study may have influenced the relationship between rCBF and rCBV (rCBF and $rCMRO_2$). For example, opioids (morphine) may have decreased $CMRO_2$ (Uchino et al., 2015). Moreover, it is widely accepted that neurovascular modulations are highly dependent on sedative treatment including direct cerebral vasodilation and significantly reduce cerebral metabolic demand, which would reduce rCBF in response to neuronal activation during anesthesia (Kuroda et al., 1997). Strict coupling between rCBF and $rCMRO_2$ cannot be expected under such conditions. Nevertheless, the directionality from rCBF to rCBV (rCBF to $rCMRO_2$) was preserved even in lightly sedated preterms.

4.6 **Conclusions**

This study focused on the nonlinear relationship between rCBF and rCBV (rCBF and $rCMRO_2$) in preterm infants recorded before 32 wGA. The mechanisms by which rCBV drives rCBF ($rCMRO_2$ drives rCBF) are already functional at this early age of development regardless of whether or not these two variables are strictly correlated. As the directionality was observed in all preterm infants regardless of the type of anesthesia, it would be interesting to test the

application of this technique in routine clinical practice as a potential index of neurovascular coupling in a larger population of preterms at risk of neuronal or vascular brain injury.

4.7 Supplementary

In the following we explained some parts of study in more details:

2) *The different time constant of the NIR measurements (CBFi and Hb changes were measured with two separate devices):*

The first part concerns how we synchronized the various acquisition devices. The second part evaluates the maximum time lags between the two systems. The third part that explained in above part evaluates to what degree this time lag may affect our analysis.

I) Measuring instrument synchronization

To simultaneously measure hemodynamic activities, the various measuring systems must be accurately synchronized. Synchronization was achieved by an external event trigger that produces TTL signals via a parallel port (LPT) using an in-house *Matlab*® code. This system produces markers simultaneously on both systems to precisely indicate the beginning and the end of data acquisitions. Synchronization was performed using the *Level triggering* mode. In this mode, a device monitors the A/D converter for an increase in the voltage level applied to the marker/trigger pins. When the appropriate increase in voltage is reached (TTL “high” signal), the measuring system records the event.

II) Phantom test

The *Instruction Manual* of NIRO-200NX (*page* 99) noted that maximum pulse duration of the NIR-light sources is 18µs. In addition, the *Technical Description* (08/2014, *page* 2) of HemoFloMo (http://hemophotonics.com/HemoFloMo_technical_06102014.pdf) noted that switching times of DCS source is less than < 10ms.

Moreover, to evaluate the time lags between the two systems, DCS and CW-NIRS, a circuit/code was designed with Arduino® comprising an on/off LED switch at 5-second intervals, as shown below. For high temporal precision, a microcontroller board was used, based on the ATmega2560 with a 16 MHz crystal oscillator. The Arduino also set 2 other *Low*

and *High* pins to simultaneously send the markers to DCS/CW-NIRS. In this mode, the A/D converter acquire data in intervals based on the integration time set in the software.

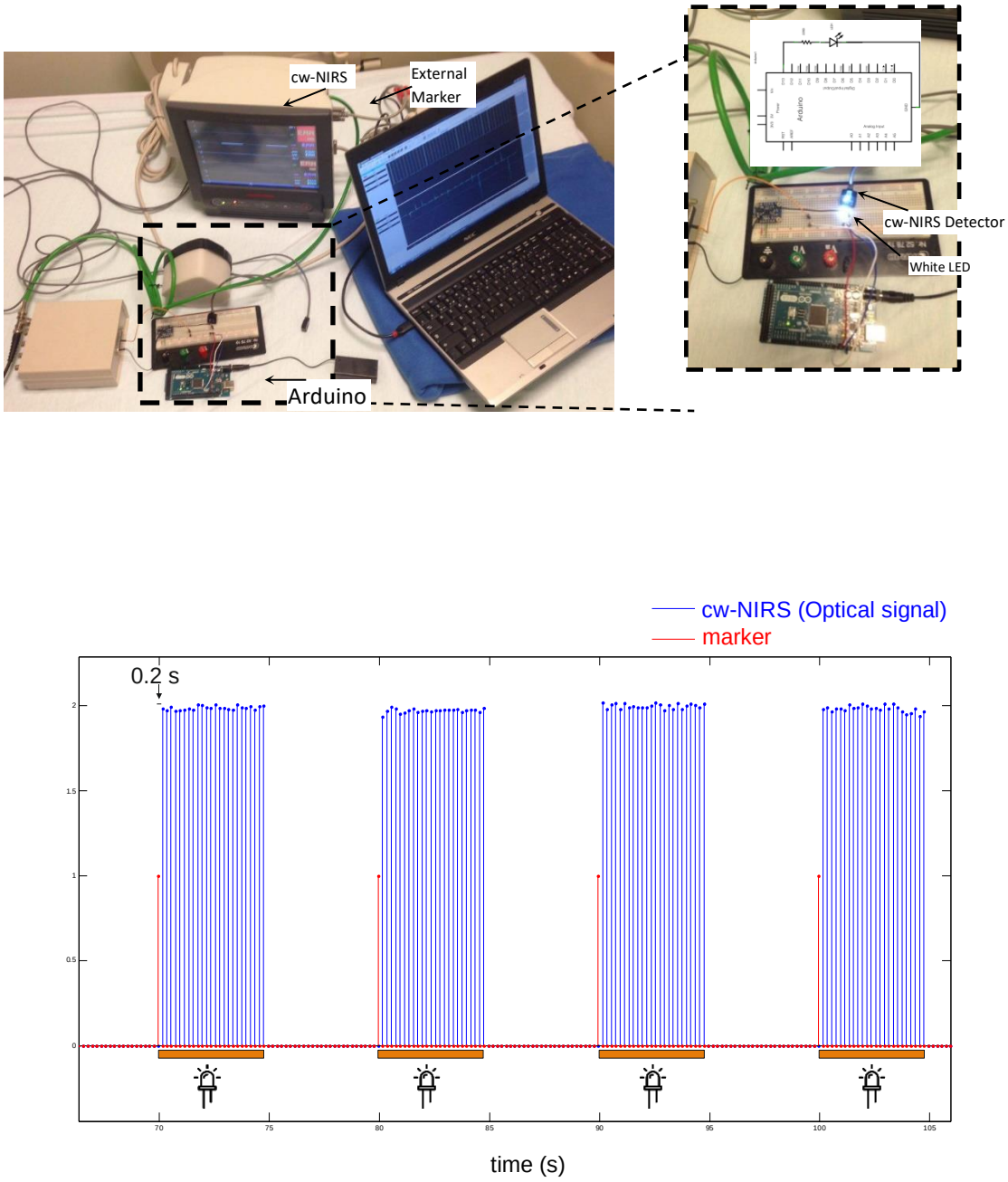

Fig.9 *Phantom test designed to check the system time-lag. Top: An Arduino® causes a connected LED to flash off and on at 5-second intervals. Bottom: time lag between the marker and the optical signal in CW-NIRS (200ms)*

A balance was also achieved between signal quality and temporal resolution. The integration time was therefore set 200 ms (sampling period) in the CW-NIRS (Hamamatsu®), and 2.5s in DCS. Due to the low signal-to-noise ratio (SNR), a higher integration time was set for the DCS than for the CW-NIRS. Signal-to-noise ratio and depth of penetration are two interrelated and important experimental parameters.

Larger source-detector separations are required to obtain a sufficient depth of penetration. However, the use of larger source-detector separation configurations is challenging, since DCS optimally requires single-mode detection fibers to measure the intensity autocorrelation function. The throughput of single-mode fibers is relatively low and leads to a low SNR.

Two approaches were used in this study to resolve the issue of low SNR: 1) *Spatial* integration and 2) *Temporal* integration.

1) *Spatial integration*: To resolve the issue of low SNR, we implemented a multi-speckle scheme for DCS detection, which substantially improved the DCS signal-to-noise ratio. In this set-up, we employed parallelized detection, e.g. multiple detector fibers bundled together in the same position (4 detectors in the same holder), and the autocorrelation curves from all detectors were then averaged to obtain a single curve.

2) *Temporal integration*: Additionally, improved SNR were achieved by increasing the amount of light delivered to the tissue by increasing integration time (2.5s). In practice, a low SNR means that repeated measurements of physiologic activity need to be averaged. The effect of averaging over different ranges of measurements constitutes a trade-off between high SNR and high temporal and spatial resolution.

3) *Linear correlation plots on measured parameters:*

We wanted to detect non-linear correlations between parameters rather than simply linear correlations. The following plots would provide additional information about fluctuations of hemodynamic variables. However, one subject (subject #10) will be presented as an example. Figure 10 shows the significant linear correlations between z-score-rCMRO2 and z-score-rCBF (p=0.02) and between z-score-SO2 and z-score-rCBF (p=0.00), but the linear correlations between variables (z-score-rCBF, z-score-HbT), (z-score-rCBF, z-score-HR), (z-score-CBF, z-score-BP), (z-score-CMRO2, z-score-HR), (z-score-CMRO2, z-score-BP) were not statistically significant (P = 0.4, 0.9, 0.2, 0.9, 0.4, respectively).

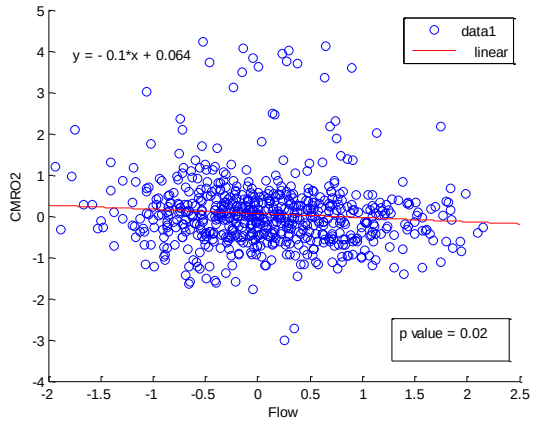
y = - 0.1*x + 0.064
data1
linear
p value = 0.02
CMRO2
Flow

(A)

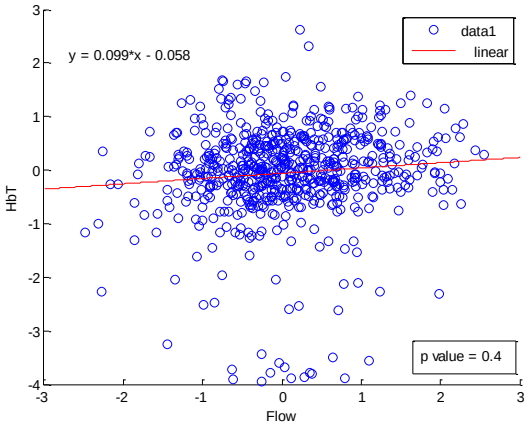
y = 0.099*x - 0.058
data1
linear
p value = 0.4
HbT
Flow

(B)

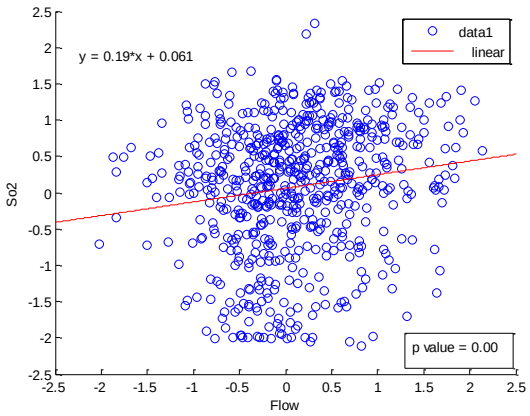
y = 0.19*x + 0.061
data1
linear
p value = 0.00
So2
Flow

(C)

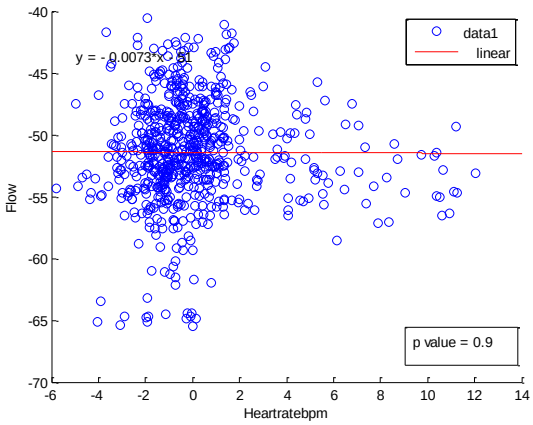
y = - 0.0073*x - 51
data1
linear
p value = 0.9
Flow
Heartratebpm

(D)

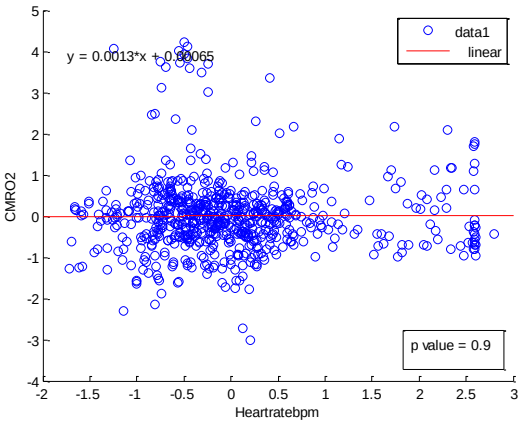
y = 0.0013*x + 0.00065
data1
linear
p value = 0.9
CMRO2
Heartratebpm

(E)

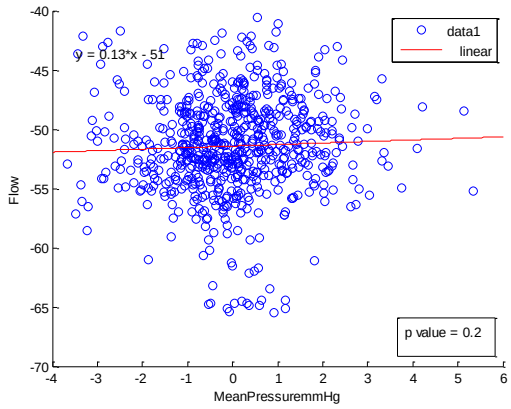

(F)

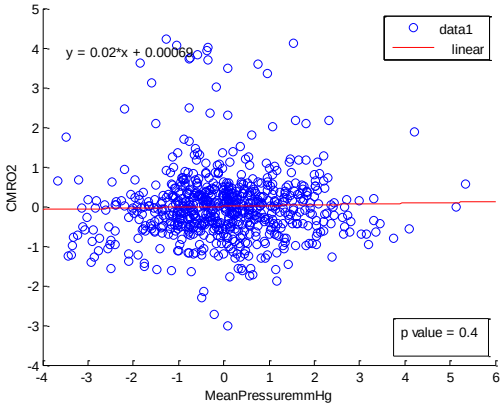

(G)

Fig.10 *Scatterplots of A) z-score-rCMRO2 and z-score-rCBF, (B) z-score-rCBF and z-score-HbT, (C) z-score-SO2 and z-score-rCBF, (D) z-score-rCBF and z-score-HR, (E) z-score-rCMRO2 and z-score-HR, (F) z-score-rCBF and z-score-MBP, (G) z-score-rCMRO2 and z-score-MBP.*

4) Comparing our results with Roche-Labarbe et al.:

Roche-Labarbe et al. used eq. (rCMRO2 = rCBF. rOEF) which means that changes in CBF and CMRO2 are correlated by default. In our study, we used rCBV instead of rCBF to calculate rCMRO2. Our results can be compared with those presented in Figure 3 (rCBF and rCBV) of Roche-Labarbe's paper. However, the study conditions are different. In our study, we evaluated changes in the various variables at the resting state, whereas Roche-Labarbe et al. analyzed the impact of somatosensory stimulation.

In the following figure from Roche-Labarbe's study, the first few seconds of stimulation also show that rCBV increased progressively, while rCBF did not change, but started to increase abruptly after 2 seconds while rCBV reached a critical value of 1.005. These results suggest a threshold beyond which CBV triggers CBF dynamics. This part of Figure 3 in Roche-Labarbe's paper is therefore in agreement with our results.

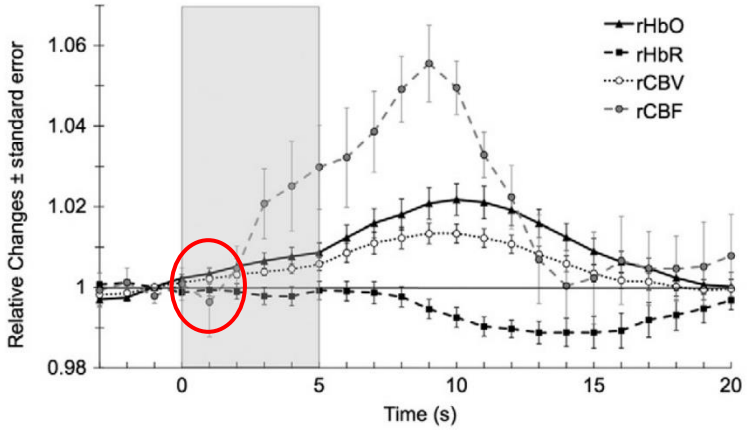

Fig. 3. Grand average of relative changes in blood flow, oxy-, deoxy- and total hemoglobin.

Fig.11 *Grand average of relative changes in blood flow, oxy, deoxy and total hemoglobin.*

5) *The absorption and reduced scattering coefficient (mua, mus), as input for the DCS analysis:*

We considered μa = 0.1 cm-1 and μs' = 10 cm-1, which are typical values for biological tissue. Although rCBF is influenced by both tissue absorption and scattering coefficients, μa and μs', respectively, uncertainties in μa lead to relatively small errors in rCBF (<20%), whereas uncertainties in μs' can result in substantial errors in rCBF (Mesquita et al., 2013). In neonates, Jain et al. observed a strong correlation between rCBF and CBF in the sagittal sinus despite assuming a fixed μs' across the entire cohort (Jain et al., 2014), which may have been at least partly due to the homogeneity of the patient cohort, i.e., all subjects were < 1-week-old neonates, which is also the case in the present study (< 34 wGA). Moreover, the effects of uncertainties in μa and μs' on rCBF are decreased when monitoring relative changes in CBF over time, as these tissue parameters change little except in the case of extreme interval blood loss/gain, edema, etc. Clearly, in future studies, we plan to combine DCS with the frequency-NIRS method to determine absolute μa and μs' for the tissue of interest, e.g., in all subjects whenever possible.

6) *The linear and non-linear correlations between rCMRO2 and rCBV:*

Linear correlations: Although there are high linear correlations between rCMRO2 and rCBV (p-value=0.00), but the figure 12 confirms that the rCMRO2 index does not solely represent fluctuations of HbT (rCBV). Since the data points do not follow the exact linear trend, rCMRO2 does not just represent rCBV.

Sub.2 *Sub.8*

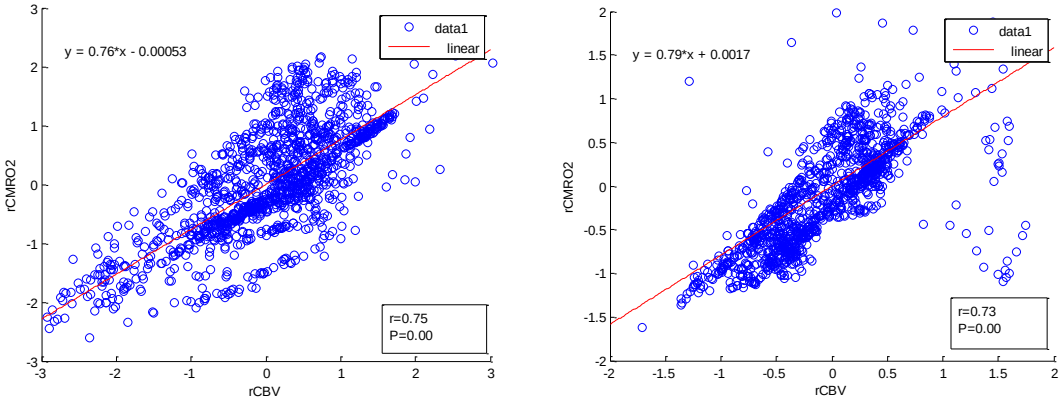

Fig.12 *Scatterplots of A) z-score-rCMRO2 and z-score-rCBV (subject #2, 8).*

Non-linear relationship*:* Moreover, the non-linear relationship was investigated by the entropy (H). The entropy (H) of rCMRO2 and rCBV for each subject was equal to 2000. For each subject, the mutual information MI of rCMRO2 and rCBV was less than the entropy (H) of rCMRO2 and rCBV (MI (rCMRO2, rCBV) < H (rCBV) and MI(rCMRO2, rCBV) < H(rCMRO2)). rCMRO2 and rCBV can, therefore, be considered to be dependent variables but not totally dependent, (i.e., rCMRO2 index is related to signal fluctuation of HbT but not solely represents fluctuations of HbT).

Table.2 *Amount of information shared between rCMRO2 and rCBV by mutual information (MI).*

	Sub1	**Sub2**	**Sub3**	**Sub4**	**Sub5**	**Sub6**	**Sub7**	**Sub8**	**Sub9**	**Sub10**
MI(rCBV;rCBMRO2)	216.3	462.8	1057.5	1471.9	844.4	81.8	1525.9	635.2	1580.5	1533.3

7) To validate the constant beta over the measured periods using actual time traces of the concurrently measured CBF and CBV:

The following figure 13 shows the time trace plots of beta in two sample subjects. To validate the constant beta over the measured periods, a t-test was used to determine whether data are significantly fluctuate. The t-test does not reject the null hypothesis at 5% significance level for each subject. Thus we accept the null hypothesis that the beta is constant over the time traces of the measured CBF and CBV.

Table.3 *t-test on beta*

	Sub1	**Sub2**	**Sub3**	**Sub4**	**Sub5**	**Sub6**	**Sub7**	**Sub8**	**Sub9**	**Sub10**

***p* value**	0.3196	0.2988	0.3183	0.1291	0.5606	0.8447	0.1008	0.6958	0.1770	0.2978

Sub.2

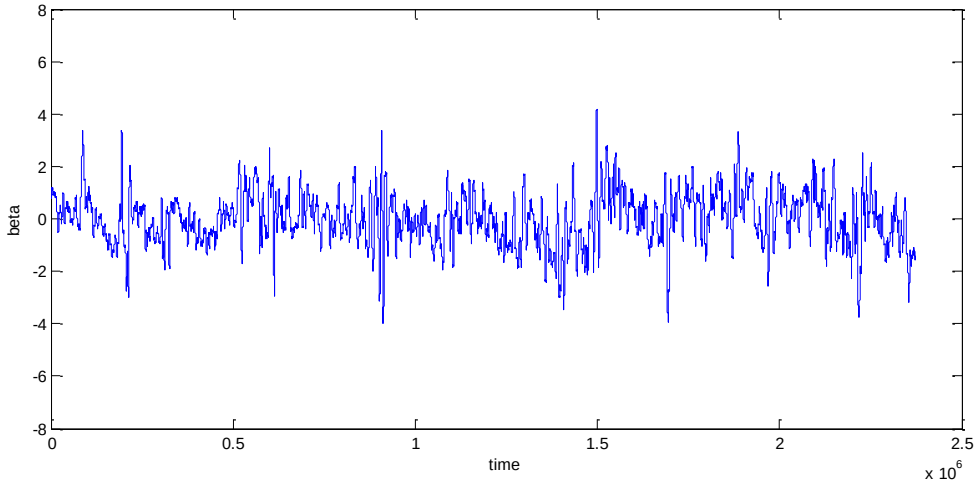

Sub.10

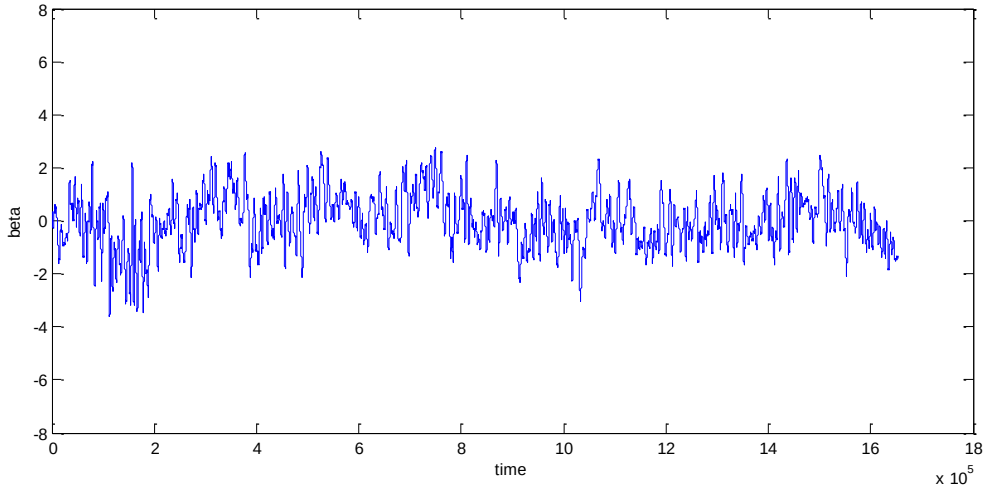

Fig.13 *The time traces of Z-score-beta (subject #2, 10)*

8) The correlation between CBF and HbT:

The relation between HbT and CBF is complex and not simply direct. The following figures (14, 15) shows the non-significant linear correlation between $HbT\ vs.\ CBF$ (p-value =0.4) and the significant linear correlation of $\log(HbT)\ vs.\ \log(CBF)$ (p-value=0.01). Although the linear correlation of $\log(HbT)\ vs.\ \log(CBF)$ is not significant for subjects 6 and 7.

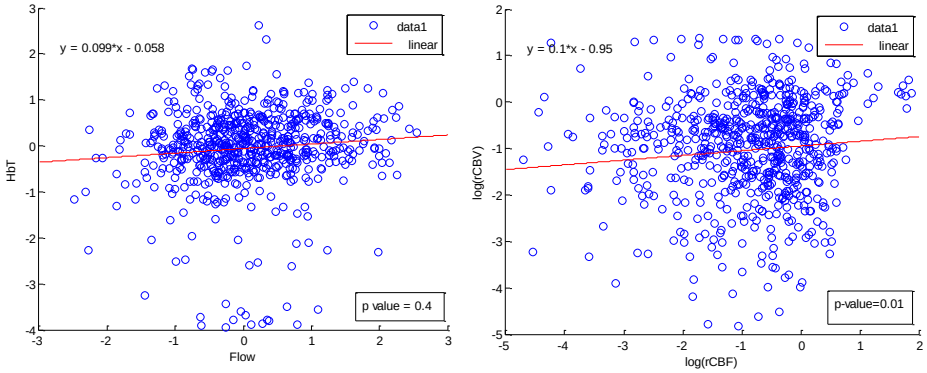

Fig.14 *Comparing between the correlation of (HBT-CBF) and (log(HBT)-log(CBF)) (subject #10).*

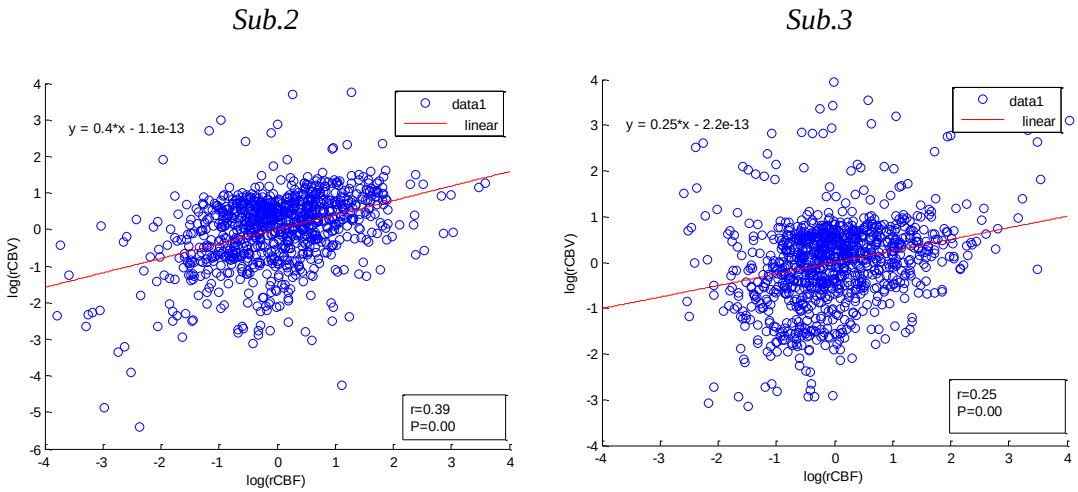

Fig.15 *Scatterplots of $log(HbT) - log(CBF)$ (subject #2, 3).*

9) *rCBV has a more predominant driving influence on rCBF (with more detail):*

Transfer entropy implies to quantify the causal relationship between the variables (i.e., relative CBV and CBF). The causality does not necessarily imply that two variables have a time lag, they also could have taken place simultaneously. Increased volume followed by increased flow with a slight delay (i.e., the time lag between the relative CBV and CBF), direct us to explore for a suitable physiological underlying mechanism.

Although the reports of relative CBV and CBF dynamics have been controversial. Malonek et al. (Malonek et al., 1997a) reported that CBV increased before CBF, whereas Sheth et al. (Sheth et al., 2005) reported CBV lagged CBF and Jones et al. (Jones et al., 2001) reported CBV and CBF had similar onset times and times to peak. Our finding (rCBV followed by rCBF

changes) support the assumption of a process of capillary filling (increase in rCBV) followed by a delayed neurovascular regulation of rCBF in the capillary bed (Malonek et al., 1997a).

Functional recruitment of capillaries is the changeover of low blood flow to high blood flow capillaries (Kuschinsky, 1992; Villringer, 1995). An initial phase can be expected when local capillary blood volume increases, but at a time when arterioles have not yet dilated and the blood flow has not yet increased. This type of lagged relationship between blood volume and blood flow is considered to be valid if the outflow from the capillary compartment in the activated regions is briefly lower than the inflow to this capillary compartment (Malonek et al., 1997a). Following the neuronal activation, the capacitance of the capillaries was to raise, and their resistance was to reduce (i.e., the capillary bed might play as a ‘‘sink’’ for red blood cells). This would, in turn, allows the outflow from the compartment to decrease, before the occurrence of upstream arteriolar dilatation that would provoke an increased inflow. Thereafter, when the arteriolar part has dilated, the increased inflow causes a flow increase in the entire capillary compartment, oxyhemoglobin increases, and deoxyhemoglobin decreases (Malonek et al., 1997a).

Some studies (Jones et al., 2001) also suggested that CBV changes lead to CBF changes. These findings are discussed in the frame of the most refined model of the vascular response, the “balloon model” (based on the venous balloon the origin of the change in CBV and deoxy-Hb). As mentioned in (Vanzetta and Grinvald, 2008); “Exchanging the roles of CBV and CBF in the Balloon Model equations thus improved the fit of the model predictions to the experimental data, but without attaining satisfactory agreement, probably also because the largest CBV changes occur in arterioles rather than in venules or veins (Vanzetta et al., 2005). In any case, it becomes increasingly apparent that CBV and CBF are linked in a more complex way than by a simple power-law $CBV=CBF^{\alpha}$ (“Grubb’s law,” Grubb et al., 1974), and that they also depend on state of activation, vessel type, and size (Hutchinson et al., 2006).”

Following figures show different studies in which changes in rCBV leads to changes in rCBF:

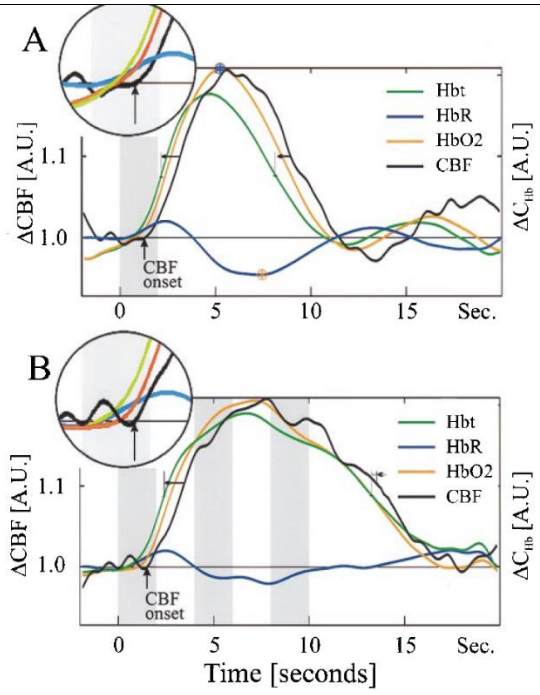

Fig.16 *Dynamics of various vascular responses. Total hemoglobin concentration (Hbt, green line) leads CBF response (black line) throughout the response cycle for both the short stimulus (A) and the repeated stimuli (B). Each curve is the average response to 24 stimulation periods during a single experiment. Horizontal arrows mark the temporal difference between the curves when they had reached 50% of their maximal amplitude (marked by thin, vertical lines) during the uprising phase and during the decay to baseline. HbR curve appears to lead all other components, and it reaches its peak before all other curves. Notice the delays of both the CBF (marked by arrow) and the HbO2 onsets after the stimulus onsets. At onset, Hbt change is entirely composed of HbR elevation, whereas at the later phase it is predominantly HbO2. Because of fluctuations of HbO2 (and thus Hbt) before stimulation, its onset is determined as time when its rate of change increased. Asterisks mark the maximum of HbO2 and the minimum of HbR (Malonek et al., 1997a).*

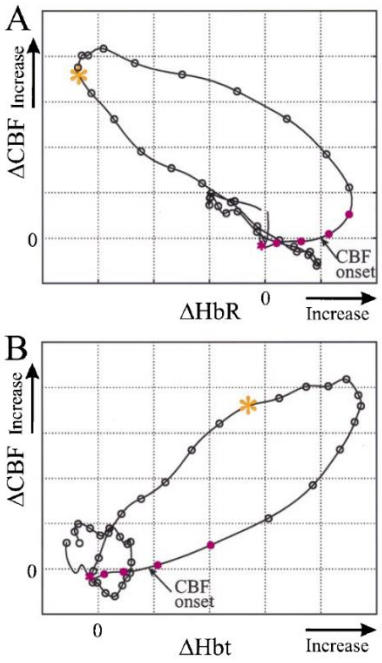

Fig.17 *Correlated dynamics of CBF to HbR and to Hbt for short stimulus. Phase plots show the dependence of CBF changes on HbR and Hbt after 2 sec of stimulation. Along the curves, intervals between the circles represent 0.5 sec, and the first four segments (five circles) are during stimulation. An asterisk marks the stimulus onset, and an arrow marks the onset of CBF, when an observable change in its rate of change is detected. (A) After stimulation onset (pink asterisk), HbR increases, whereas no observable change in CBF is seen for more than a second. As CBF starts to increase (arrow), the rate of change of HbR starts to decrease and becomes negative 1 sec later. At the last phase of the response (red asterisk), an inverse relation between the parameters is seen; an increase in CBF is accompanied by a decrease in HbR and vice versa. (B) An exponential dependence of CBF on Hbt is seen during the first 4.5 sec after stimulus onset. Throughout the response cycle, changes in Hbt lead changes in CBF by about 1–2 sec (Malonek et al., 1997a).*

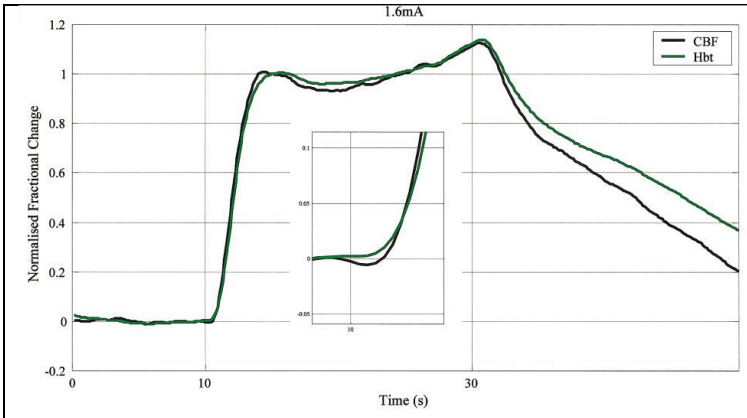

Fig.18 Temporal comparison of the time series of CBF and Hbt. The mean time series of CBF and Hbt normalized between 0 and 1, with respect to the baseline control period and peak, are depicted. (A) The time series of CBF and Hbt following electrical stimulation (1.6 mA, 20 s) of the whisker pad (Jones et al., 2001).

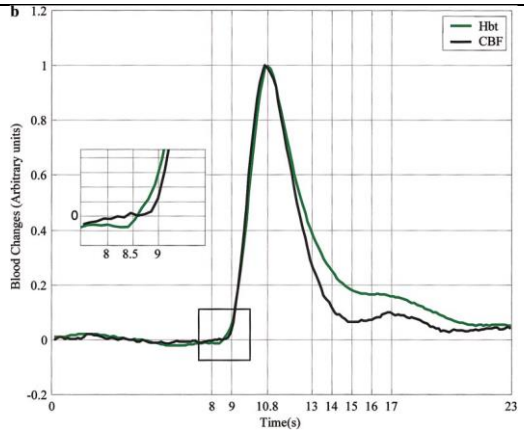

Fig.19 Comparison of the time series of CBF and Hbt following electrical stimulation of the whisker pad. (b) The mean time series of CBF and Hbt for all stimulation intensities normalized with respect to to the baseline control period and peak. This allows further comparison of the temporal dynamics of flow and volume. The inset shows an enlarged view at the time of stimulation onset (Jones et al., 2002).

CHAPTER

Neurovascular Coupling in the Developing Neonatal Brain in Resting State 5

5.1 Abstract

The neonatal brain is an extremely dynamic organization undergoing essential development in connectivity and function. The developmental course of cortical hemodynamics in the neonatal brain reflects, to a certain extent, the gradual maturation of neurovascular coupling. Several functional imaging investigations of the developing brain have found patterns of hemodynamic responses that contrast from adult. This discrepancy is partly due to that neurovascular coupling that is still developing in the neonatal brain. Both neural and vascular organizations spread and are then highly selectively pruned in early brain development. The elaboration and refinement of both neural and vascular networks need exogenous inputs as well as endogenous spontaneous activity within the primary developed wiring. These modifications are presumably to influence early neonatal neurovascular coupling, and likewise may influence functional imaging measurements in this population.

The identification of coupling between the spontaneous physiological neuronal activity with the transient stereotyped hemodynamic pattern in premature infants, consisting of deoxygenation, oxygenation, and cerebral blood flow is a complex issue, which helps to elucidate the principles of neuronal and cortical hemodynamic coupling during development.

We simultaneously recorded (EEG, HbO, HbR, TOI, CBF and estimated CMRO2) in 32 preterms, to determine how the changes in the hemodynamic responses were coupled to the

occurrence of spontaneous bursts of cerebral electric activity. Data were acquired by using the multimodal EEG-NIRS-DCS technique adapted for neonatal imaging. The bursts of electroencephalographic activity in neonates (<35 wGA) in resting state were found to be coupled to a transient hemodynamic response involving different types of hemodynamic response including (a) positive stereotyped hemodynamic responses (increases in HbO, decreases in HbR together with increases in CBF and CMRO2), (b) negative hemodynamic responses (increases in HbR, decreases in HbO together with decreases in CBF and CMRO2), (c) Increases and decreases in both HbO-HbR and CMRO2 together with no changes in CBF.

To assess the multi-frequency aspect of dynamic neurovascular coupling *wavelet coherence analysis* was applied on simultaneously-measured signals. We observed the establishment of neurovascular coupling system as a function of age. High coherence was observed between the cerebral hemodynamic (vascular) and electrical (neuronal) oscillations in the frequency range of 0.003–0.125 Hz in the non-encephalopathic newborns than in two pathological groups (i.e., PDA and IVH). Likewise, NVC coherence (CBF-EEG) was significantly decreased in IVH group vs. normal newborns (median IQR 20.3[17.2–22.8] vs. 22.2[21.2–26.9], p = 0.03).

Conclusively, different patterns of cerebral hemodynamic response to the neuronal burst of activities coupled with dynamics in neurovascular coupling with ages, reflect the immaturity and complexity of both neonatal vasculature and neuronal networks.

A comprehensive understanding of the variation of the neurovascular patterns could add fresh insights into the clinical assessment of newborn infants. Although maturational differences in early neurovascular coupling may puzzle classical interpretation of functional hemodynamic studies, neurovascular development could provide a biomarker for evaluation of healthy or altered developmental pathways that could be measurable using functional imaging.

5.2 Introduction

The dynamic interactions among the components of neurovascular unit balance and control complex brain function. The co-development of neural and vascular networks is more rational, rather than separate maturation or primary blueprint of the arrangement of blood vessels before neural elaboration/refinement. Likewise, embryonic neuronal and vascular networks may serving simillar guidance cues as each is maturing (Gelfand et al., 2009). The neuronal and vascular networks constitute the two halves of the same functional unit relying on the neurovascular unit that tightly

couple regional blood flow in response to local metabolic demands known as the Neurovascular Coupling (NVC) well characterized in adults by an increase in blood flow in response to neuronal activation (Nourhashemi et al., 2017a). The balance between local consumption and arterial supply related to neuronal activation is much more delicate in the developing brain (Kozberg and Hillman, 2016). Further, how this NVC is affected by particular metabolic and vascular disorder (Attwell and Iadecola, 2002; Sheth et al., 2004), in the immature brain is clinically relevant in respect to the neurodevelopmental consequences of its dysfunction.

Functional hemodynamic imaging research in neonates have determined evidently distinct response in preterm and term new-borns, contrast to canonical adult hemodynamic responses (Arichi et al., 2012). More information indicates that these discrepancies in hemodynamic responses related to the immaturity of neurovascular coupling (Roche-Labarbe et al., 2007a). The massive cortical maturation known to develop after childbirth hence contains the progressive postpartum developing of neurovascular coupling. Structurally, during the last trimester of human gestation, both the neuronal and the vascular system still undergo drastic developments. The processes of neuronal migration, synaptogenesis, short and long-range connectivity, pruning and cell death, neuronal dendritic differentiation, neurochemical maturation, myelination are gradually building the neuronal networks, providing in premature a dual innervation of pyramidal cells by both subplate and thalamic axons (Arichi et al., 2010). Neural networks first experience a potent epoch of axonal prolongation and synaptogenesis (Lewis et al., 2013), proceed by wiring refinement with synapse elimination (Huttenlocher et al., 1982). These epochs of elaboration/refinement differ locally, but mostly progress in the human brain well into young adulthood (Harris et al., 2011). In parallel, the vascular system itself develops remarkably morphologically during the early neonatal period. While neurons and vasculature share guidance cues as each is developing (Gelfand et al., 2009), the grey matter perforating vessels establish rich intrinsic capillary plexuses that parallel the growth and complexity of the structurally and functionally developing cortical grey matter (Marin-Padilla, 1983). These vessels constitute the physiological locus of regulation of blood flow in response to change in metabolic demands of local networks (Iadecola et al., 1996). The underlying plexus progressively differentiate into the different vascular compartment (Herken et al., 1989; Wang et al., 1992). This occurs together with capillary bed expansion, remodeling and pruning. Whether this immature network is able to respond to metabolic demands by an increase in blood flow in premature neonate at rest is not entirely elucidated.

Functionally, the maturation of the neonatal neuronal network is associated with characteristic age-dependent transient features, high amplitude mixed frequency activities and discontinuous pattern (Wallois, 2010) reflecting the interaction between genetically encode transient generators of the subplate and cortical plate, permanent generators that progressively built up and exogenous inputs from the external world (Routier et al., 2017). Some studies has also presented that spontaneous endogenous activity may also be critical to wiring development (Feller, 1999) and provoking neural activity which may help in early wiring elaboration and refinement (Ackman et al., 2012). The discontinuous spontaneous EEG bursts of activity constitute discernible events offering the opportunity to monitor non-invasively and passively the hemodynamic responses to endogenous cortical activation in premature neonates, avoiding exogenous stimulation (Roche-Labarbe et al., 2007a).

The adaptation of the immature vascular network to neuronal activation is still a matter of discussion. fNIRS and fMRI studies in animals have suggested that it develops postnatally (Colonnese et al., 2007). In contrast, in premature neonates we observed a neurovascular coupling from 28wGA on, in response to spontaneous endogenous bursts of activity (Roche-Labarbe et al., 2007b) or exogenous phonemes or voices stimulations (Mahmoudzadeh et al., 2013b). While in adult the response of the vascular network is well established as a positive neurovascular coupling, in immature populations, increase-decrease of blood flow or blood volume have been reported in response to exogenous stimulation in neonates or premature (see for example (Allievi et al., 2016; Anderson et al., 2001; Born et al., 2000; Erberich et al., 2006; Heep et al., 2009; Kozberg et al., 2013; Mahmoudzadeh et al., 2017a; Martin et al., 1999; Sakatani et al., 1999; Sie et al., 2001; Zaramella et al., 2001) as well as in immature animals (Colonnese et al., 2008) pointing to interstudy, intersubject, and even intrasubject regional variability in early development (Kozberg and Hillman, 2016).

The potentiality that neurovascular coupling itself may be matured parallel to neuronal development in the early infancy suggests that in this developmental span the neonatal brain may be undergoing variations in energy supply and demand dynamics in comparison to the adult brain. It makes sense to assume that there is a coupling between hemodynamic and neuronal activity in the premature neonatal brain in resting state (Roche-Labarbe et al., 2007b), but whether the hemodynamic responses to the burst of activities have the same patterns or not has to be analyzed? Is it possible to predict the hemodynamic response of neural activity in resting state in the premature infant considering all the complexity of the immature brain? What is the impact of the different

gestational ages and/or pathologic events on the cerebral hemodynamic changes/disturbance in the immature neonatal brain? Is the neurovascular coupling age-dependent at resting state? Does the neonate cerebrum run into a situation of lacking of energy accessiblity that altering the capability of cortical neurons to fire? To answer these questions, in this study, we will mainly focus on the coupling between spontaneous physiological burst of activity with a transient hemodynamic pattern in resting state premature infants, consisting of deoxygenation, oxygenation, cerebral blood flow, cerebral blood volume and cerebral metabolic rate of oxygen, which help to elucidate the principles of neuronal and cortical hemodynamic coupling during development.

The multifaceted progress of neurovascular development prolongs occur after childbirth in natural development, suggesting attention to the potential contribution of this co-developing networks in normal and abnormal pathways of cerebral maturation. Since the early postpartum brain seems to work with a sensitive stability of cortical oxygenation, the establishment of functional hemodynamic response at the right moment in maturation is presumably an essential phase of development. Disconnetion or lags in the onset of neurovascular coupling could promote anomalies in both neural and vascular networks.

To better characterize the dynamics of the vascular network at rest in relation to spontaneous neuronal activity two approaches are considered in premature. The first approach is classic and considers the NVC in response to a neuronal activation. For this we took the opportunity of the spontaneous bursts in the discontinuous cortical activity of prematurity to trigger the analysis of the hemodynamic response. To better explore the different type of hemodynamic responses (direction of changes in [HbO] and [HbR], cerebral blood flow and cerebral oxygenation), a combined simultaneous, multimodal multiscale approach using Electroencephalography (EEG) with Diffuse Correlation Spectroscopy (DCS), Continuous Wave and Frequency Domain (CW and FD) functional Near-infrared spectroscopy (fNIRS) and monitoring of arterial blood pressure at bedside was developed. Another more recent, approach, is to consider the interaction between spontaneous oscillations of the neuronal and the vascular compartments in the time-frequency domain. This approach was applied on our multimodal multiscale data's using wavelet analysis method that has been proved to be adequate in neonates to provide clinical arguments to discriminate healthy neonates from asphyxiated newborns with encephalopathy (Grinsted, 2004). Therefore the method was also applied to a subgroup of Patent Ductus Arteriosus (PDA) patients to test if the method might be helpful in situations in which autoregulation is considered to be altered (Tian et al., 2016).

To perform these monitoring's a hybrid EEG-NIRS-DCS patch was built and placed on the infant's forehead (Fig1.A)**.** To define the onset of the burst of spontaneous activity and quantify the neuronal activation at rest, eight EEG channels were recorded at the bedside. To acquire [HbO] and [HbR] concentration changes and to calculate the cerebral tissue oxygenation index (TOI), a CW near-infrared spectroscopy probe was ls attached. To control spatially the change in HbO and HbR, in depth and at different locations, a multidistance, multichannel frequency-domain-based optical imaging system was used. To control for systemic effects, the peripheral arterial blood pressure was monitored continuously. To non-invasively quantify CBF, a DCS device was connected which further allows an estimate of CMRO2 changes. All the data were acquired simultaneously providing the multimodal and multiscale (neuronal and hemodynamic) approach. To evaluate the effect of the burst on the hemodynamic parameters, the burst onset was defined as the moving average of the EEG envelope-derivative value remaining over a given threshold. This was used to define time =0 for further analysis of the NVC, related to bursts of activity. Then, to extract the directional changes of HbO and HbR, all the trials of hemodynamic responses related to EEG bursts within the time window: [-20 to 30 sec] are passed through a classification algorithm, before grand averaging. The algorithm categorizes the blocks of HbO_HbR if the most samples of the HbO and HbR were over or under the threshold levels of 0.05 or -0.05 after 0 sec, and classifies the HbO_HbR into 3 main conditions; in opposite changes in HbO_HbR (Condition A), increase in both HbO_HbR (Condition B) and decrease in both HbO_HbR (Condition C) (Fig1.B). Condition A was further subdivided into 3 subconditions (i) subcondition A1; bursts are separated by InterBurst Intervals (IBIs) of more than 20s, (ii) subcondition A2; bursts are separated by IBIs of less than 20s, including only one burst in the reference period [-20s to 0s], (iii) subondition A3; bursts are separated by IBIs of less than 20s, including more than one burst in the reference period [-20s to 0s] (Fig1.B). To estimate the linear dynamics between the bursts of activity and the hemodynamic response we compared the root mean quare (*rms*) of HbO, HbR, TOI, CBF and CMRO2 with the *rms* of the envelope-derivative of the EEG bursts. To evaluate the nonlinear interactions between EEG and NIRS changes (EEG-HbO) in resting-state preterm infants, as previously (Nourashemi et al., 2017), we used the transfer entropy (TE) method based on information theory (Shannon, 1948). To estimate the directionality in resting-state between spontaneous oscillations in HbO, HbR, TOI, CBF and CMRO2 and the spontaneous EEG oscillations, and to analyse whether it might help to discern between healthy and pathological neonates a new time-frequency domain wavelet analysis was applied to healthy and a subgroup of PDA patients (Tian et al., 2016). To evaluate the effect of age, the different parameters were evaluated in the course of the development in healthy patients.

5.3 Methods

Thirty-two preterm neonates (12 females; mean gestational age (GA) at birth: 29.3 weeks GA [27-34wGA]) were tested in the supine position (recording age: 31.3 wGA, Table 1) (Fig.S.1).

5.3.1 EEG data processing

Off-line analysis was performed using in-house MATLAB scripts for all signals. The artifacts from EEG data detected and rejected visually by trained an experimented clinical neurophysiologist (FW).

5.3.1.1 Automated detection of spontaneous burst of activity

In order to detect EEG burst of activity, we used a non-linear energy operator (NLEO) algorithm. The NLEO combines information's from both the amplitude and the frequency content of the signal, which makes it more sensitive for detection of preterm bursts rather than other estimators of signal energy with information's extracted from amplitude or frequency only (Vanhatalo et al., 2005).

To provide a moving average signal, the absolute value of NLEO output was then smoothed by calculating the average in a sliding window with a length of 1.5 seconds. In order to better detect the interburst intervals (IBIs), a baseline correction was applied; the value of each EEG sample was subtracted by the minimum value of the moving averaged calculated from 1 min prior each considered sample. Then EEG bursts of activity was extracted from the discontinuous trace when the moving average of the EEG envelope-derivative value remains over a given threshold (1.5 μV^2) for longer than a defined duration as a time limit (1s). The optimal values for the threshold level, the time limit for EEG burst extraction and the length of the window for the moving average were provided by Palmu et al. (Palmu et al., 2010). EEG bursts detection were validated by an experimented clinical neurophysiologist (FW). Burst onset time (time zero, t_0) was then determined when the moving averaged of the EEG envelope-derivative cross the threshold (1.5μV^2) (Fig.S.2).

5.3.2 Hemodynamic data processing; HbO, HbR, TOI, HbT, CBF, and CMRO2

A z-score-based algorithm was used to reject artifact from optical signals (Born et al., 2000). As individual features, such as skull thickness and hair color, influence signal strength, the signal was first homogenized in each participant by computing a z-score across all measurement periods for each channel. A z-score greater than 4 in any channel was considered to be an artifact, in which

case, the entire artifact time-window was excised from the data for all channels (Born et al., 2000). The mean value of rCBF signals recorded from 4 paired source-detectors was calculated. The remaining cleaned hemodynamic signals were band-pass filtered [0.03–0.5 Hz] using a zero phase filter (Butterworth, order 3) to eliminate physiologic noise (e.g., slow drifts, arterial pulse oscillations).

While CBF can be independently measured by DCS, it has been proposed that the relative cerebral metabolic rate of oxygen (CMRO2) can be theoretically estimated by combining relative changes in CBF and oxygen extraction fraction (Culver et al., 2003):

$$rCMRO_2 = rCBF \times rOEF \quad (1)$$

Where rOEF is defined as:

$$rCBF = \frac{CBF_i(t)}{CBF_i(t_0)}, \qquad rOEF = \frac{SaO_2(t)-SvO_2(t)}{SaO_2(t_0)-SvO_2(t_0)} = \frac{SaO_2(t)-SO_2(t)}{SaO_2(t_0)-SO_2(t_0)} \quad (2)$$

With venous oxygenation $SvO_2 = (SO_2 - a \times SaO_2)/b$, where a+b=1, a and b are the arterial and venous contributions that are constant over time (Watzman et al., 2000), and arterial oxygenation SaO_2=100%. Mechanical ventilation parameters and inspired oxygen concentrations were maintained constant at sufficiently high levels to saturate arterial hemoglobin (SaO2 ≈ 100%). SO_2 is the microvascular tissue oxygen saturation (Wray et al., 1988) ($SO_2 = HbO_2/HbT$). The control state at time t_0 was defined as the mean value of the signal and was considered to be the reference value.

Hemodynamic analysis

The hemodynamic responses (i.e. HbO, HbR, TOI, CBF and CMRO2) time-locked to the EEG signal were averaged (time window: [-20 to 30 sec]). Because the hemodynamic responses to EEG bursts last around 15s, we defined a reference period of -20s to 0s, to be able to define a reference (condition.A1, see below), during which hemodynamic changes are unlikely to be related to the previous burst. The first 10 sec period [-20 to -10 sec] was defined as the baseline for further analysis.

All the trials of hemodynamic responses related to EEG bursts with the time window: [-20 to 30 sec], are passed to a classification algorithm with threshold levels of 0.05 and -0.05. The algorithm categorizes the trials of HbO_HbR if the most samples of the HbO and HbR were over or under the threshold levels of 0.05 or -0.05 after 0 sec, and classifies the HbO_HbR into 3 main

conditions; in opposite changes in HbO_HbR, increase in both HbO_HbR and decrease in both HbO_HbR.

5.3.2.1 Classification of Hemodynamic responses

Hemodynamic responses related to EEG bursts were classified into 3 main conditions according to the direction of the changes in HbO and HbR. In condition A, they were further classified according to the number of burst occurring within the reference period [-20s to 0s].

- Condition A; The hemodynamic response consist in opposite changes in HbO and HbR.
    - Condition A1; bursts are separated by IBIs of more than 20s (Fig.2.A1).
    - Condition A2; bursts are separated by IBIs of less than 20s, including only one burst in the reference period [-20s to 0s], (Fig.2.A2).
    - Condition A3; bursts are separated by IBIs of less than 20s, including more than one burst in the reference period [-20s to 0s], (Fig.2.A3).
- Condition B; The hemodynamic response consist in an increase in HbO and HbR, (Fig.2.B).
- Condition C; The hemodynamic response consists in a decrease in HbO and HbR, (Fig.2.C).

Statistical analyses were performed on the amplitude of the hemodynamic signals. For all selected hemodynamic segments [-20 to 30 sec], we used Student's t-test for paired samples to compare the hemodynamic response to the baseline (the first 10 s of each segment). We calculated the mean baseline value by averaging this 10 s of baseline, which provided a reference value for each segment, then compared values for every second of each segment to its own reference. The result is a significance level (p-value) for each comparison.

5.3.3 Wavelet coherence analysis of neurovascular coupling (NVC)

To estimate the cross-correlation in resting state between spontaneous oscillations in CBF, HbO, HbR, TOI and CMRO2 on one side and the spontaneous EEG oscillations on the other side, a new time-frequency domain wavelet analysis was applied (Grinsted, 2004). The peak to peak of z-scored EEG amplitudes were first smoothed using a moving average of 0.5 seconds.

The wavelet transform coherence is a method for analyzing the coherence and phase lag, with squared cross-wavelet coherence, R^2, between two time series as a function of both time and

frequency without priori assumptions of linearity and stationarity (Chang and Glover, 2010; Torrence and Webster, 1999). R^2 (squared wavelet coherence) ranges between 0 and 1 (the color scale represents the magnitude of R^2) and can be conceptualized as a localized correlation coefficient in the time-frequency domain between the recorded hemodynamic responses and the EEG bursts. The two variables selected for evaluation of NVC were (i) the amplitude of the hemodynamic responses (either CBF, HbO, HbR, TOI or $CMRO_2$) and (ii) the amplitude of the EEG burst. NVC is represented as the significant in-phase coherence ($\Delta\phi \approx 0$) between the hemodynamics and the EEG bursts oscillations. The percentage of significant coherence is quantified as the percentage of the time-frequency area during which the HbO_EEG burst, HbR_EEG burst, TOI_EEG burst, CBF_EEG burst, $CMRO_2$_EEG burst coherence is statistically significant from the background.

The percentage of significant coherence was further calculated as a function of age and compared between two groups of normal and pathological premature neonates (with IVH and PDA).

5.3.4 Linear and Nonlinear EEG_hemodynamic responses interactions

The linear correlation between *rms* of EEG and *rms* of hemodynamic responses and the nonlinear relationship between EEG and NIRS (DCS) data by using transfer entropy (TE) were investigated. The TE was used to define the strength of causality and the coupling between EEG and NIRS (DCS) data. The concept of entropy is related to the degree of uncertainty associated with a signal random variable. In other words, it provides a measure of the average uncertainty in a random variable. The analysis was based on times series with identical probability variables and a flat distribution of quantized values. Because TE is based on transition probabilities, we used TE to determine the dominant direction in the relationship between two variables EEG and NIRS (DCS) data. Statistical analysis with a limit of statistical confidence corresponding to the 95th percentile of the 300 trials was performed according to the surrogate method (Nourashemi et al., 2017).

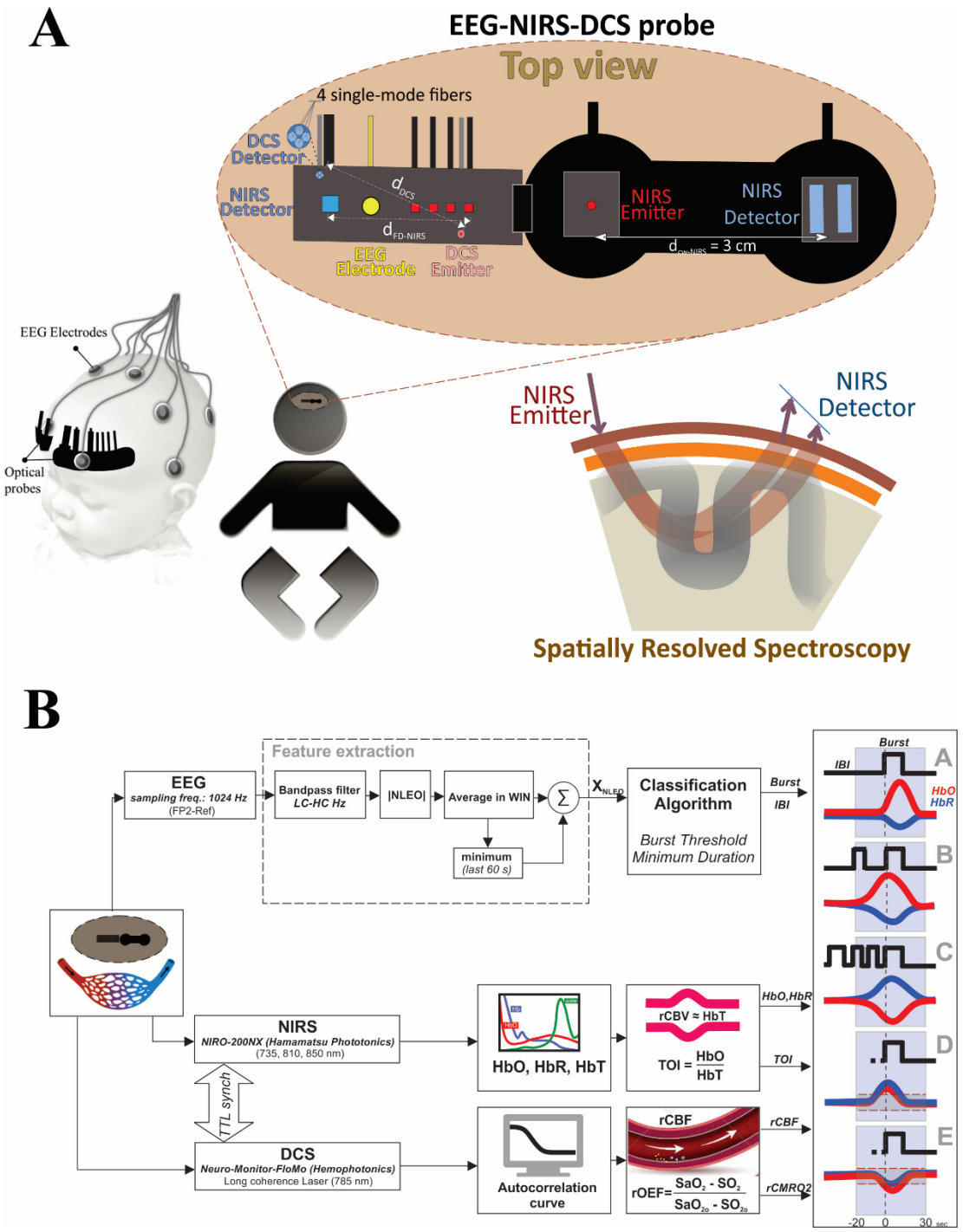

Fig.1 *(A) Schematic representation of the location of the EEG and optical probes on an infant's head. (UP) View of the hybrid optical probe constructed with a flexible hypoallergenic material and composed by three sectors, one for the DCS probe (The tips of source and detector fibers were bent 90º and tightly held in place by rigid plastic material), one EEG and the other for the NIRS. Diagram of the frequency-domain multiple-distance (FDMD); the four emitters (red squares) are arranged on multi-distance patch far from detector (Gray square), creating 4 points of measure (channels) over frontal area. (B). Diagram of the hemodynamic responses (HbO, HbR, calculated HbT and TOI by NIRS data, rCBF by DCS data and calculation of rCMRO2 by NIRS data) and Schematic presentation of the algorithm. |NLEO| applied on EEG signal, Classification of Hemodynamic responses to EEG bursts.*

5.4 Results

The discontinuous bursts of EEG activity were first detected by NLEO algorithm and then validated by an experienced neurophysiologist (FW). The percentages of the number of classified hemodynamic responses to EEG bursts in each condition (in all subjects healthy and PDA) are presented in Table 2 (SI).

5.4.1 Cerebral hemodynamic responses to burst of activities in premature neonates

The grand average (n=32) of the changes in the different hemodynamic parameters were calculated (HbO-HbR, TOI, CBF) and estimated (CMRO2) relatively to the onset of the detected burst of activity after grand average of the envelope-derivative of the EEG and a moving average of this envelope over all bursts (Fig.2). 4 types of responses were observed. They consisted either in a CBF response with either a positive/negative change in CBF (Conditions A1, A2 and A3) or in a CBV response with a positive/negative change in CBV (Conditions B and C). The most frequent responses were observed in condition A during which the hemodynamic CBF response consisted in opposite changes in HbO and HbR. Also more frequent was the condition A1and A2 with a positive neurovascular coupling and increase in CBF. In condition A1 the bursts were separated by interburst intervals (IBI) of more than 20s (Fig.2.A1). In such condition (A1), the hemodynamic changes started well before the burst onset. It consisted in an initial decrease (starting -12s from the onset of the burst (t0), significant ($p<0.001$) between -8 and -3s)) followed by an increase in HbO starting from -1s before t0, significant ($p<0.001$) between -0 and 15s). The following increase is concomitant to the burst of activity (Fig.2.A1.II). A slight, nonsignificant, increase in HbR was followed by a decrease in HbR starting at -3.5s before t0, being significant ($p<0.001$) from -0.7s to 19s (Fig.2.A1.II). The increase in TOI also started before the burst onset (-2s) but is only significant ($p<0.001$) from 1.2s to 20s (Fig.2.A1.IV). The decrease in regional CBF (and rCMRO2) also started before the burst onset (-13s and -16s, respectively) and was significant ($p<0.001$) from -10s to -2.3s and again from 1.7s to 9.6s for CBF and from -9.7s to -1.4s and 6s to 9s for CMRO2. Then rCBF (rCMRO2) starts to increase at the onset (t0) of the EEG burst (Fig.2.A1.V-VI). CBF and CMRO2 returned to the baseline faster than HbO_HbR. The decrease in CBV (HbT) started before the burst onset (-12s) and was significant ($p<0.001$) from -7.5s to -5.1s. No significant changes in CBV were observed (Fig.2.A1.VII). To evaluate the effect of the previous bursts on the hemodynamic responses we considered conditions A2 and A3. In condition A2 the bursts were separated by IBIs of less than 20s and only one burst occurred in the reference period [-20s to 0s], (Fig.2. A2). As in

condition A1, in condition A2 the hemodynamic response started by a significant increase ($p<0.001$) in HbO, TOI, CBF, CMRO2 and a significant decrease ($p<0.001$) in HbR beginning at -10s, before the burst onset (Fig.2. A2). The amplitude of the hemodynamic response was significantly higher ($p<0.05$) than in condition A1 (Fig.2.A2 vs. Fig.2.A1). No significant changes in CBV were observed (Fig.2. A2.VII). In condition A3; the bursts were also separated by IBIs of less than 20s, but more than one burst occurred in the reference period [-20s to 0s], (Fig.2.A3). Compared to the previous conditions A1 and A2, the hemodynamic response was utterly inverted, consisting in a significant decrease ($p<0.001$) in HbO, TOI, CBF, CMRO2 and a simultaneous significant increase ($p<0.001$) in HbR beginning - 10 sec, before the burst onset. A slight nonsignificant decrease in CBV was observed in relation to the burst of activity (Fig.2.A3.VII). In condition B and C, the hemodynamic responses were strongly different and mainly characterized by changes in CBV. In condition B it consisted in a significant ($p<0.001$) simultaneous increase in both HbO and HbR (3s to 12s and -1s to 12.4s, respectively) and in CMRO2 (4.8s to 7.2s) with no significant changes in CBF and TOI (Fig.2.B). In contrast to the previous A conditions, the CBV increased significantly ($p<0.001$) between 5.1s to 10.5s after the burst of activity (Fig.2.B.VII). In condition C, the hemodynamic response was opposite to condition B, but still the CBV effect is dominant. The responses consisted in a significant ($p<0.001$) decreases in HbO (-2.1s to 20.4s), HbR (0.6s to 14.7s), TOI (-10s to 20.8s), CMRO2 (-10s to 17s), with no significant changes in CBF (Fig.2.C). This resulted in a significant ($p<0.001$) decreases in CBV from -4.6s to 14.2s around the burst of activity (Fig.2.C.VII). It must be noted that similar dynamics in HbO and HbR fluctuations were observed whatever a frequency-domain fNIRS or a continuous-wave fNIRS were used (Fig.2.II and 2.III) and whatever the distance between emitters and detectors. In addition, these burst of activity did not induce any systemic changes in arterial blood pressure (ABP) (Fig.2.VIII).

5.4.2 Linear and Nonlinear interactions between the neuronal and the hemodynamic changes

To identify linear relationship between EEG and NIRS data, changes in *rms* of hemodynamic signals were plotted as a function of *rms* of EEG. A significant linear correlation was found between the amplitude of the *rms* of the bursts and the amplitude of the *rms* of the hemodynamic responses (HbO, HbR, TOI, CBF and CMRO2) (Fig.S.3).

To identify a nonlinear and causal relationship between EEG and NIRS data, the transfer entropy analysis was used as it detects the relationship between the past of one signal and the present of another signal (Nourashemi et al., 2017). Figure S.4 shows the values of

directionality=($TE_{NIRS→EEG}$)-($TE_{EEG→NIRS}$) for the 31 neonates, resulting in a fluctuating directionality between EEG and NIRS (DCS) with a tendency toward a negative directionality in 23⁄31 (21/31) preterms and a positive directionality in the remaining 8 (10) preterms. The negative values of the directionality suggest that EEG was predominant over NIRS.

5.4.3 Wavelet real-time analysis of NVC in healthy and PDA premature

Significant in-phase coherence between the amplitude of the different hemodynamic parameter and the amplitude of the EEG burst were analysis by wavelet coherence. The Wavelet-based coherence was first calculated in a healthy premature neonate, in the wavelet scale of 25–30 minutes equivalent to a very-low-frequency (VLF) range of 0.003–0.125 Hz and then compared to PDA preemies. Wavelet-based hemodynamic responses (CBF-EEG, CMRO2-EEG, HbO-EEG, HbR-EEG, TOI-EEG) coherence showed decreased NVC for a premature neonate with PDA compared to healthy (Fig.3.A-B). Figure 3.A-B highlights a case example of high NVC in a healthy premature neonate and low NVC in a PDA preemie. According to the boxplot distribution Fig.3.C at the group level, the NVC coherence was lower in PDA prematures (not significant) compared to healthy. Significant differences were observed in CBF-EEG and CMRO2-EEG coherences between normal and IVH groups, (CBF-EEG: median IQR 20.3[17.2–22.8] vs 22.2[21.2–26.9], p = 0.03), (CMRO2-EEG: median IQR 18.8[17–24.3] vs 25[21.7–27.3], p = 0.02) (Fig.S.5). It should be underlined that in contrast to this wavelet analysis, the pattern of the hemodynamic responses to EEG bursts (different conditions) (Fig.S.6-7) in PDA and IVH patients was similar to those in healthy neonates. The boxplot distribution of maximum amplitude of the hemodynamic responses in (Fig.S.8-9) shows that there is no significant difference between PDA (IVH) new-borns compared to healthy.

5.4.4 The effect of age on wavelet real-time analysis

There is positive correlation between age and the percentage of significant coherence ($p<0.05$) between hemodynamic responses and EEG ($R2>0.5$ between the frequency range of 0.003–0.125 Hz) whatever the hemodynamic parameters studied (Fig.3.D). In contrast, no significant relationship between the maximum amplitude of the hemodynamic responses and the age was observed (Fig.S.10-11).

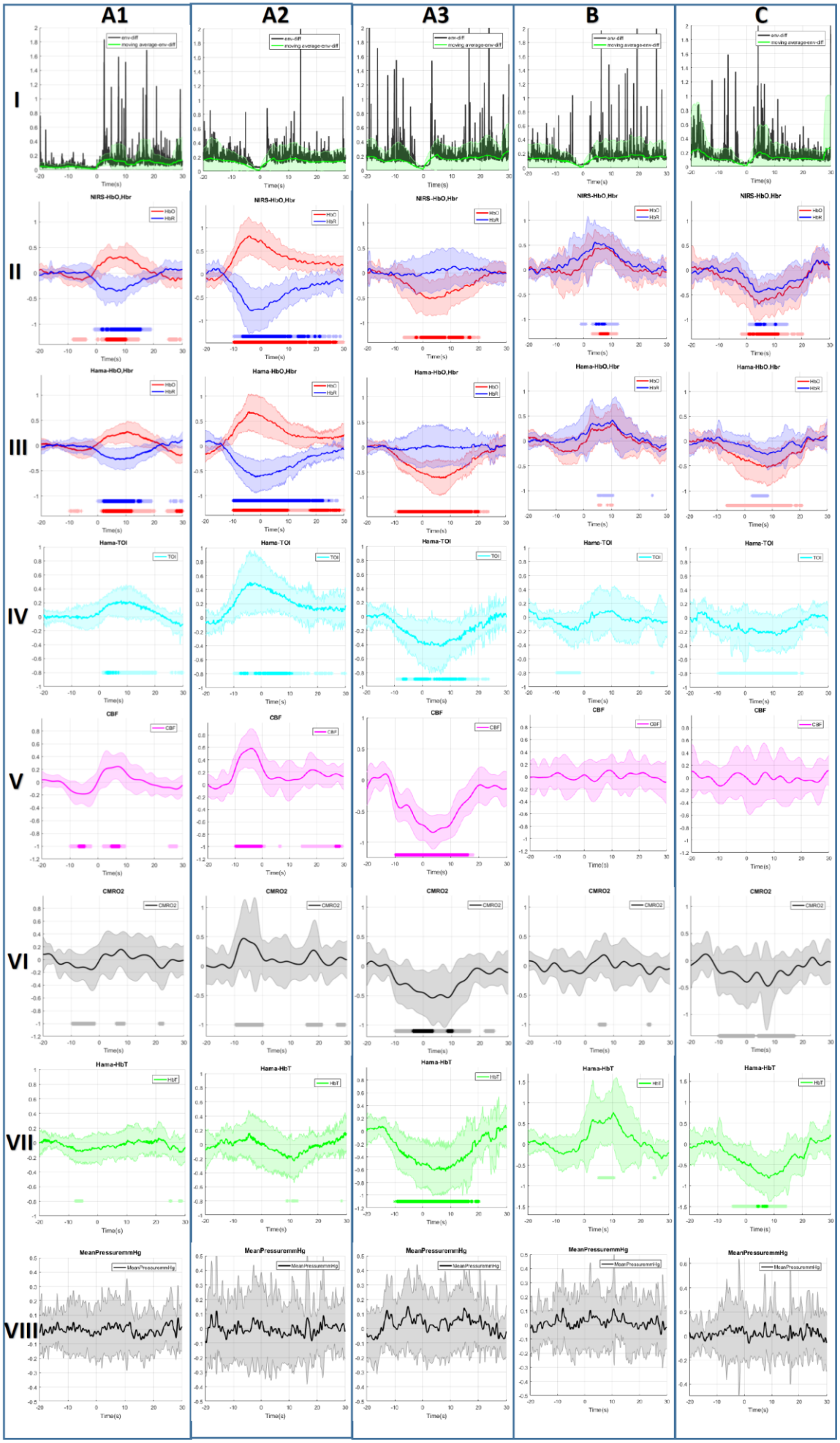
A1
A2
A3
B
C
I
II
III
IV
V
VI
VII
VIII
env-diff
moving average-env-diff
NIRS-HbO,Hbr
HbO
HbR
Hama-HbO,Hbr
Hama-TOI
TOI
CBF
CMRO2
Hama-HbT
HbT
MeanPressuremmHg
Time(s)

Figu.2 *The grand average of the regional hemodynamic responses of the onset of EEG bursts at 0s (the time duration was shown 20s before and 30s after the onset of EEG burst, the first 10s was defined as a baseline). The longitudinal panels indicates envelope-derivative of EEG and moving average of envelope-derivative over all EEG bursts in one subject (I), the grand average of changes in HbO_HbR measured by ISS (II), the grand average of changes in HbO_HbR measured by Hamamatsu (III), the grand average of changes in TOI (IV), CBF (V) and CMRO2 (VI). The vertical panels related to the classification of the burst of activities, with no EEG burst during previous 20s (A1), one EEG burst during the first 20s (A2), two EEG bursts during the first 20s (A3) and the vertical panels (B and C) related to the burst of activities that accompanying with increase in both HbO_HbR (B) and decrease in both HbO_HbR (C). The annotations below the signal highlighting the times duration of hemodynamic response were significantly different from the reference period (-20 to -10 s), light stars related to (t-test, p<0.001) and dark stars related to (t-test, p<1.1e-6). Shaded error bars indicate the standard deviations for the corresponding signals at each time-point.*

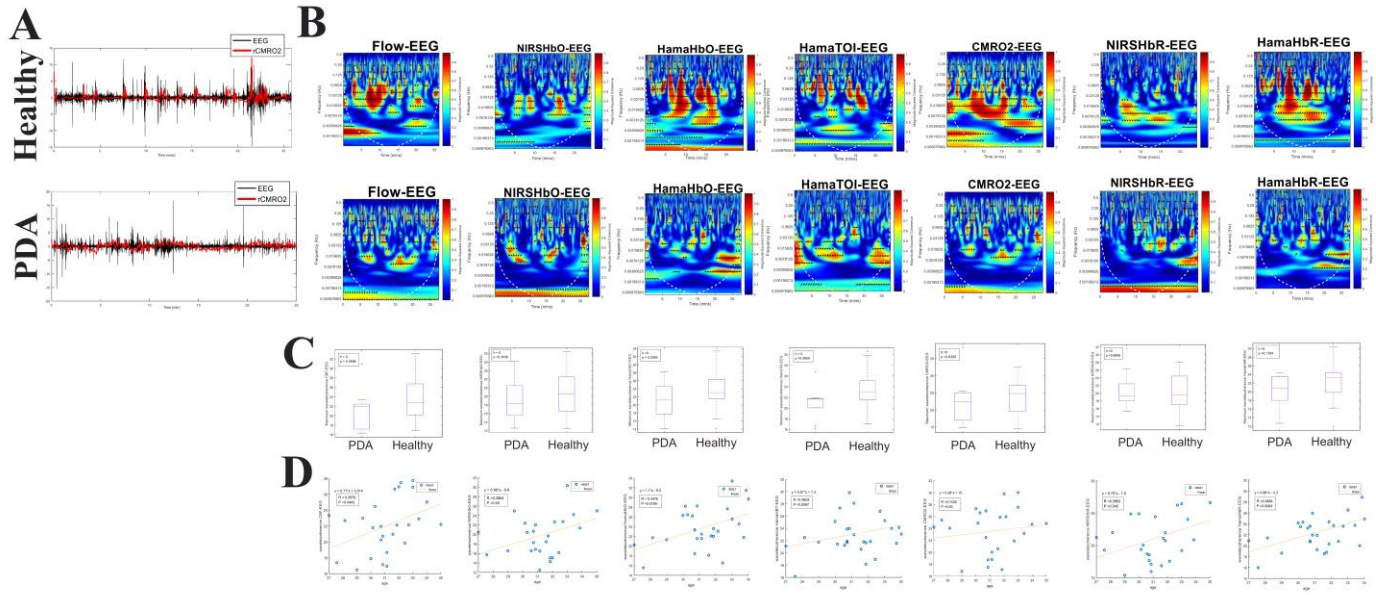

Fig.3 *(A) An enlarged segment of the real-time CMRO2 and EEG data of a sample healthy premature neonate #15 (UP); in a sample premature neonate with Patent ductus arteriosus #28 (Down). (B) Wavelet-based hemodynamic responses (CBF-EEG, CMRO2-EEG, HbO-EEG, HbR-EEG, TOI-EEG) coherence showing intact neurovascular coupling (NVC) in a healthy premature neonate #15. Squared wavelet coherence, R2hemodynamic responses →EEG, where the x-axis represents time in minute, the y-axis represents the range of frequencies, and the color scale represents the magnitude of R2. Significant coherence between the (CBF, CMRO2, HbO, HbR, TOI) and EEG is seen in a very low frequency (VLF) range of 0.0003–0.125 Hz (UP), in a sample premature neonate with Patent ductus arteriosus #28 (DOWN). (C) The boxplot distribution of percentage of area for significant NVC coherence per total considered area over the frequency range of 0.003–0.125Hz between two groups: with PDA(n = 9) and without PDA(n = 23). (D) The percentage of area with high NVC coherence per total considered area for each premature neonate as a function of age.*

5.5 Discussion

This study demonstrates that,

1. Spontaneous physiological neuronal burst of activity in premature infants (<35 wGA) in resting state is coupled with the different type of hemodynamic response such as

a) Positive NIRS responses (increases in HbO, decreases in HbR together with increases in CBF and CMRO2 with no changes in CBV),

b) Negative NIRS responses (increases in HbR, decreases in HbO together with decreases in CBF and CMRO2),

c) Increases and decreases in both HbO-HbR, CBV and CMRO2 together with no changes in CBF.

2. These different types of hemodynamic responses to EEG bursts occurred similarly in pathological and healthy patients, but the dynamic coherence between hemodynamic responses and EEG bursts to assess NVC is lower in newborns with PDA and IVH) than in healthy patients.

3. The wavelet measures of NVC in the neonatal brain are age-dependent, suggesting that the developmental trajectory of the hemodynamic responses in the postnatal brain reflects, at least in part, the gradual development of the neurovascular coupling.

5.5.1 Cerebral Hemodynamic patterns

Fine-tuning of neural wiring is subject to the inhibitory trajectories maturation (Crook et al., 1998). GABAergic interneurons establish at various stage after birth related to region-dependent critical periods (Le Magueresse and Monyer, 2013). In particular, there is a maturational shift from the excitatory to inhibitory of the developing brain. This maturational transition happens as a consequence of change of the neurotransmitter GABA from depolarizing to hyperpolarizing at almost day seven postpartum in mouse (Amin and Marinaro, 2017; Ben-Ari, 2014). This shift have the potential to impact the profile of the brain hemodynamics, since some studies hypothesize that interneurons perform a crucial contribution in neurovascular coupling (Cauli et al., 2004).

In addition, the weighting between arterial, venous and capillaries contributions in neurovascular coupling, are significantly different for excitatory and inhibitory task in human brain (Huber et al., 2014). The interplay of different vascular compartments in NVC, with their considerable prematurity (Miyawaki et al., 1998), suggest different hemodynamic patterns

consequence of different underlying hemodynamic mechanisms. The different patterns of hemodynamic response we observed might provide some explanations for the divergent hemodynamic responses previously reported in immature neurovascular networks. It further suggests that the strategy developed for the NVC in premature is much more complex than in adults.

5.5.1.1 Positive hemodynamic response

This response is the most frequent and confirm the ability of the vascular system to couple with neuronal activity in early premature. This response is in total agreement with our previous study (Roche-Labarbe et al., 2007b). The significant initial decrease in HbO (increase in HbR)12s prior to the onset of the EEG burst correspond to an increase in oxygen consumption likely to mimic an initial dip in which the oxygenation is preceded by a brief deoxygenation, related to oxygen consumption preceding a vasoactive response (Devor et al., 2003; Jasdzewski et al., 2003). The hemodynamic changes (measured with both frequency-domain fNIRS and continuous-wave fNIRS devices) preceded any visible neuronal activity (measured by EEG). These early hemodynamic changes have been related to a low number of synchronized activated neurons or activation of unsynchronized neurons within the first few seconds (Roche-Labarbe et al., 2007b). The origins of the burst recorded by EEG in premature are still unknown. They are likely to be related to intimate mechanisms between the subplate and the cortical plate under development with an interplay between ascending pyramidal neurons and subplate neurons (Routier et al., 2017). In such condition, an earlier endogenous activation of subplate neurons (Arichi et al., 2012) which electromagnetic field, not orientated perpendicular to the surface of the brain, is not reachable by EEG recordings but might be able to develop a NVC. Despite the possible implication of the subplate neurons, the *rms* of the neuronal EEG activity is correlated to the *rms* of the hemodynamic NIRS parameters. But in nonlinear investigation, the predominant driving influence of EEG on NIRS-DCS (or invers) in different preterm newborns were different. The cause for this phenomenon can be multifactorial and might be related to the regulation of brain hemodynamics.

The following increase in HbO (decrease in HbR) starting at the onset of the EEG burst is associated with an increase in cerebral blood flow (CBF) and CMRO2, bringing oxygenated hemoglobin into the brain. A decrease in CBF and CMRO2 before the onset of the burst, supporting the assumption of a recruitment of the capillaries accompanied by a changeover in low blood flow before the onset of the burst to a high blood flow during the burst (Kuschinsky and Paulson, 1992; Malonek et al., 1997a; Nourhashemi et al., 2017a). The decreased concentration of HbR during the

burst further suggests that oxygen delivery exceeds oxygen consumption during spontaneous bursts in premature.

The consequence of considering the hemodynamic response with an IBI of less than 20s (Condition A2) results in a second burst onset occurring during the hemodynamic response of the previous burst. This masks the initial decrease in HbO (increase in HBR) prior to the second burst which is replaced by an earlier onset of the neurovascular coupling in case of short IBI. Whatever these initial differences, the following pattern of hemodynamic changes is similar. Nevertheless, because in short IBIs, the hemodynamic response had a higher amplitude, it is likely that a cumulative effect occurs during the NVC.

The involvement of NVC in positive NIRS response, fitted well with the classical balloon model (Buxton and Frank, 1997; Buxton et al., 2004). In positive NIRS response, an increase in flow velocity without accompanying either vasodilatation or recruitment might account for the absence of an increase in HbT during activation, which resulted in increases in venous oxygenation.

5.5.1.2 Negative neurovascular coupling

The negative hemodynamic responses to EEG burst was regularly observed whatever the duration of the IBI. Such negative coupling has been described in many experimental setups not only in fNIRS following peripheral stimulation (Maggioni et al., 2015; Seiyama et al., 2004), but also in fMRI (visual (Born et al., 2000; Martin et al., 1999; Sie et al., 2001), (somatosensory (Erberich et al., 2006; Heep et al., 2009)). The literature on the negative hemodynamic response is still controversial (Colonnese et al., 2008; Zimmermann et al., 2012). These negative hemodynamic responses could be due to a “negative surround” often characterized as either “vascular steal” or an index of reduced or inhibitory neural activity (Boas et al., 2008; Devor et al., 2008). Nonetheless, this negative hemodynamic response may also be an independent neurovascular coupling potentially linked to cholinergic or noradrenergic-base vasoconstriction to regulate blood flow to activated regions (Bekar et al., 2012; Takata et al., 2013). However, this mechanism is not fully understood, whether this vasoconstriction vail to restrict the degree of functional hemodynamic responses, and its formation in developing brain before neurovascular maturation could provide to preserve frail neonatal vasculature, which is notably predisposed to hemorrhage in premature infants, from immoderate vasodilation and systemic hypertension (Volpe, 1997).

Alternatively, an inverted NVC related to a situation of anaerobic metabolism has been suggested to explain the hemodynamic response to epileptic spasms associated with metabolic

dysfunction treated by a ketogenic diet only (Bourel-Ponchel et al., 2017). The setting of such anaerobic metabolism (Booth et al., 1980; Rodríguez-Balderrama et al., 2016) fits well with the observed decrease in CBF and CMRO2.

In the positive NIRS, the fluctuation of HbO-HbR prior to the onset of EEG burst is concomitant with the decrease in CBF. Likewise, the negative NIRS seems to be driven by the decrease in CBF. A decrease in rCBF concomitant with a slight increase in HbR, might represent increasing the oxygen extraction, in consequence of the limitations in oxygen transport, the brain switch to anaerobic glucose consumption during activation. This could be explained by the neonatal and early infantile maturation which corresponds to the period of rapid formation of synapses (Bourgeois et al., 1989; Huttenlocher and Dabholkar, 1997).

5.5.1.3 Changes in volume

EEG bursts might also trigger another mechanism of NVC based on changes (increase or decrease) in CBV and in HbO and HbR without any changes in CBF or CMRO2. Considering the different models of NVC (Hoshi et al., 2001) increase, decrease in blood volume with no changes in CBF are more likely related to venous constriction or dilatation, respectively. The increases in both HbO and HbR with no significant change in CBF, support the hypothesis that O2-consumption was not fully compensated by the increase in HbO, thus an increase in oxygen supply insufficient to meet the oxygen demand. The similar type of pattern in hemodynamic response was also observed in the visual stimulation of neonates (Meek et al., 1995; Meek et al., 1998). The decreases in both HbO and HbR, support the hypothesis that a decrease in HbO during burst of activity linked to an insufficient increase in CBF, but a decrease in HbR reflecting a decrease in venous blood oxygenation and volume (Hoshi et al., 2001).

Following our results, in the positive NIRS (Fig.2.A1-A2), the degree of decreases in HbR during the burst of activity is likely attributed to venous hyperoxia due to overcompensation of the flow. In negative NIRS conditions (Fig.2.A3), the increase in HbR mainly reflects venous hypoxia, whereas in volume changes conditions (Fig.2.B-C), the changes in HbR mainly reflects changes in venous blood volume.

The increase or decrease in CBV could be related to the different contribution of vascular compartments in NVC. As Huber et al. demonstrated that the inhibitory stimuli are associated with decreases in CBV (in negative BOLD) due to constriction of surface arteries, while the excitatory

stimuli are accompanied with increases in CBV (in positive BOLD) in cortex and pial vasculature (Huber et al., 2014).

The different hemodynamic responses that have been observed using the two devices, scanning thus the same area, in the same premature, at different times reflect the complexity of the interactions between the neuronal and vascular networks in premature. We found a correlations between the amplitude or the *rms* of the bursts and the *rms* of the hemodynamic response, despite a possible implication of subplate neurons and other non-synchronized or non well-orientated pyramidal cells, which might participate in the elaboration of the type of neurovascular response triggered by the underlying neuronal activity (cortical plate or subplate). In addition, other metabolic nonoxidative mechanisms are like to participate, notably in pathological neonates (Bourel-Ponchel et al., 2017).

5.5.2 Assessment of neurovascular coupling dynamics by Wavelet coherence analysis

5.5.2.1 Influence of cerebral impairment on NVC

Although the pattern of the hemodynamic response is similar in the PDA and healthy premature, the dynamic of the response is decreased in PDA. In healthy neonates, the coupling in the very low-frequency range (0.003–0.125 Hz) between the neuronal activation and the hemodynamic response is higher in healthy than in PDA premature. This corresponds to a decrease in the dynamic of the neurovascular coupling as previously described in IVH premature in response to spontaneous bursts (Roche-Labarbe et al., 2007b) or syllable stimulations (Mahmoudzadeh et al., 2018). In PDA prematures, it reflects a defect of the vascular network in the functional neuro-vascular coupling (e.g., elasticity) (Perlman et al., 1983; Van Bel et al., 1987). The vascular network in PDA prematures may not be capable of rapid or large local changes in CBF in response to neuronal activation, due to their very low CBF and lack of autoregulation (Malamateniou et al., 2006). The present results show low NVC is statistically significant, particularly in CBF and CMRO2 (rather than the other hemodynamic responses; HbO, HbR, TOI) in IVH preterms relative to healthy group, which is in good agreement with many studies from different imaging modalities that described altered vascular function consisting in a decrease in CBF in IVH preterms at resting state (Meek et al., 1999; Osborn et al., 2003).

Our results suggest the presence of altered NVC in the group of preterm with PDA and IVH. The slow rhythms have also been shown in adults to synchronize large spatial domains affecting functions (Sirota et al., 2003), and the present study findings would suggest they are also probably to be impaired in the abnormal neonatal brain.

5.5.2.2 Variability of the NVC as a function of age (Evolution of the NVC with Increasing Age)

The coherence analysis of the hemodynamic responses-EEG activity increased as a function of age demonstrating that oscillatory coupling of the neuronal and the vascular networks mature progressively.

5.5.3 Assessment of the systemic impact as a potential confound

Because autoregulation is not fully mature in the newborn brain (Greisen, 2009), variations in systemic blood pressure might be more easily reflected in the hemodynamics of the neonatal brain. In fact, dynamics and direction of the cortical hemodynamic response might be affected by stimulus-evoked increases in systemic blood pressure (Kozberg et al., 2013). To evaluate the possible contribution from the blood pressure to the hemodynamic signal, an accurate non-invasive beat-to-beat blood pressure monitoring has been performed. The systemic blood pressure was not significantly correlated with the burst-evoked hemodynamic signal in the resting-state neonatal brain (Fig.2.VIII), suggesting that the complexity of the observed NVC in resting state was likely not related to the systemic changes.

5.6 Conclusion

Noninvasive functional hemodynamic imaging modalities (i.e., fMRI and fNIRS), serve to investigate brain activity, rely on assessment of hemodynamics as a proxy for neural activity. If naturally, there are stages of early brain maturation in which neurovascular coupling is variant than in adults, classical analysis and interpretation of functional hemodynamic data could be misleading. Contrarily, with reformed insight of how to comprehend functional neuroimaging data in these populations, functional hemodynamic imaging approaches could assert helpful for delineate the development of neurovascular coupling.

This study describes the different pattern of cerebral hemodynamic response to the spontaneous cerebral burst of activities in resting state in premature neonates. This might be related to the immaturity of the neuronal and vascular networks together with the cellular mechanisms of the neurovascular coupling. This study confirms and describes more precisely the abnormal NVC not only in IVH but also in PDA in resting state. The amplitude of the spontaneous NVC is described as being age-dependant on resting-state.

Immaturity of neurovascular coupling suggests that functional hemodynamic data obtained in preterm neonates, and probably term infants need to be interpreted differently from adult signals.

Such multimodal study are paving the way for further research which factors should be considered in the analysis of these data. We are confident that our results may improve knowledge about neurovascular development. This multiscale, multimodal non-invasive approach of the neurovascular coupling in spontaneous cerebral burst in premature allows investigating the NVC in the two neuronal and vascular dimension that constitutes the same neurovascular functional system.

Moreover, altered neurovascular development is an element in disorders of brain development given neurovascular development is an essential element of neonatal brain development, following alongside with neural development. A more complete understanding of the normal state of neurovascular coupling development could give influential advanced visions into the etiology of neurodevelopmental disorders and may provide novel biomarkers for track and analysis therapeutic objectives. Insights into variations in neurovascular coupling patterns in normal and abnormal will provide brain indicators that could be used for following effective therapies. In fact, such non-invasive approach might be interesting to test in a larger population of premature to evaluate its ability to discriminate between neuronal and vascular pathologies that could help to identify infants at risk of the abnormal outcome. In our view, these results represent an excellent initial step toward providing a unique approach to explore and assess this developmental course and provide new therapeutic biomarkers.

5.7 Supplementary Information

Thirty-two preterm neonates (12 females; mean gestational age (GA) at birth: 29.3 weeks GA [27-34wGA]) were tested in the supine position (recording age: 31.3 wGA, Table 1). This study is part of the French public hospital Clinical Research Project (PHRC National). The study was approved by the Amiens University Hospital local ethics committee according to the guidelines of the Declaration of Helsinki of 1975 (CPP Nord-Ouest II-France IDRCB-2008-A00704-51). Parents were informed about the study and provided their written informed consent.

Table.S1 *Clinical features of the tested infants*

Infant number	Gender	GA at birth (wk)	GA at test (wk)	Birth Weight (g)	Test Weight (g)	Apgar (1 min)	Apgar (5 min)	Multiple Birth	Delivery	Patent ductus arteriosus	Clinical conditions (Etiology)	Brain US	Drug use	EEG	Vascular resistance inde
1	M	31 1/7	32 1/7	1250	1285	7	8	No	caesarean	Closed ductus	HELLP syndrome preeclampsia	normal	_	normal	0.70
2	F	25 5/7	28 1/7	750	1110	7	8	No	vaginal	Closed ductus	Multiple pregnancy - second twin died - chorioamnionitis	bilateral IVH-II + Intraventricular cysts	ibuprofen	PRS	0.84
3	M	26 6/7	30 2/7	900	1350	9	9	Yes	caesarean	Closed ductus at 27 wk	chorioamnionitis-T-T syndrome multi gestation	expanding precerebral areas	_	normal	0.85

4	M	26 6/7	32	1200	NA	2	5	Yes	caesarean	Closed ductus at 27 1/7 wk	Chorioamniotitis-T-T syndrome multiple pregnancy	normal	_	normal	0.76
5	F	28 4/7	30 5/7	1600	NA	7	8	No	caesarean	Patent ductus	prolapsed cord	suprasystemic PAH	ibuprofen	PRS	0.79
6	F	29	33 3/7	1000	2180	8	10	Yes	caesarean	Closed ductus at 29 1/7 wk	maternal hypertension, preeclampsia, and twin pregnancy	minor cerebral edema	_	normal	0.77
7	F	29	34	1249	1690	8	10	Yes	caesarean	Closed ductus at 29 4/7 wk	maternal hypertension, preeclampsia and twin pregnancy	normal	_	normal	0.85
8	F	33 3/7	35	1300	1360	10	10	Yes	caesarean	Closed ductus	Birth spontaneous triple	minor cerebral edema_ cardiac congenital abnormalities CIV	_	normal	0.61
9	M	26 4/7	29 3/7	790	1150	2	7	No	caesarean	Closed ductus	Diabetes gravidis; uterine bleeding; Preterm labor	bilateral IVH-III + hydrocephalus	Dopamine - ibuprofen- lorazepam	normal	0.90
10	F	26 1/7	27	950	1150	7	9	No	vaginal	Patent ductus	metrorrhagia+ threat of premature delivery	bilateral IVH-II	ibuprofen	normal	0.69
11	F	32	32 2/7	1730	1615	7	10	No	caesarean	(Patent ductus) Closed ductus at 32 1/7 wk	preeclampsia	normal	_	normal	0.73
12	M	28 3/7	31 4/7	1505	1350	5	_	No	caesarean	Closed ductus at 29 2/7 wk	MAP sur pré eclampsie	normal	Dobutamn /noradrena line	normal	0.65
13	F	30	31 1/7	1255	1285	8	10	Yes	caesarean	Closed ductus	Respiratory distress secondary to hyaline membrane disease	normal	_	normal	0.69
14	M	30	31 1/7	1230	1210	9	9	Yes	caesarean	Closed ductus	Twin pregnancy	normal	_	normal	0.71
15	M	32 2/7	33 6/7	1950	1978	10	10	No	vaginal	Closed ductus at 32 4/7 wk	MAP	normal	_	normal	0.7
16	M	29	30 6/7	1370	1615	9	10	No	vaginal	Closed ductus at 29 3/7 wk	CPAP- MAP	bilateral IVH-I	cafeine	normal	0.75
17	M	30 4/7	31 6/7	1255	1335	10	10	1	caesarean	(Patent ductus) Closed ductus at 31 2/7 wk	MAP-RCIU triamniotique pregnancy	normal	_	normal	0.7
18	M	30 4/7	31 6/7	1680	1790	9	9	1	caesarean	Closed ductus at 29 wk (ibuprofen)	rupture de membrane sur MAP et défaut de progression	normal	ibuprofen	normal	0,75
19	M	31 6/7	32 5/7	1775	1760	10	10	0	caesarean	(Patent ductus) Closed ductus at 32 3/7 wk	Césarienne en urgence devant persistance metrorragie et ARCF	normal	cafeine	normal	0,6
20	M	28 3/7	30 6/7	1040	1030	8	8	1	vaginal	Closed ductus at 28 5/7 wk (ibuprofen)	grossesse gemellaire	IVH-I (in right) + bilateral HEPV	ibuprofen	normal	
21	M	30 4/7	32 3/7	805	900	10	10	1	caesarean	Closed ductus at 31 2/7 wk	MAP-RCIU grossesse triamniotique	bilateral IVH-I	_	normal	0.7
22	F	28 3/7	31 5/7	1195	1490	3	6	1	vaginal	Closed ductus at 28 5/7 wk (ibuprofen)	MAP- grossesse gemellaire- Detresse respiratoire secondaire sur maladie des membranes hyalines	Ventricle slightly enlarged	ibuprofen	normal	0.7
23	M	30	30 5/7	1060	1055	7	9	1	caesarean	canal artériel bidirectionnel at 30 wk	MAP-Birth spontaneous triple	normal	_	normal	0.65

24	M	27 2/7	30	950	965	2	4	0	vaginal	Closed ductus at 28 1/7 wk (significant)	rupture prématuré des membranes apres fissuration des membranes à 17SA secondaire à une amniocentèse	normale	_	normal	0,7
25	M	32	33	1800	1890	6	9	1	vaginal	Closed ductus	MAP-infection materno-fœtale confirmé- grossesses gemellaire	normale	_	normal	
26	F	32	33	1530	1685	1	6	1	vaginal	Closed ductus	MAP-infection materno-fœtale confirmé- grossesses gemellaire	confirmation agenesie du corps calleus à j4 (abnormal)	_	normal	0.75
27	F	31	33 5/7	1435	1820	10	10	0	vaginal	Closed ductus at 31 1/7 wk (no significant)	Suspicion d'infection materno-fœtale- grossesses gemellaire	normal	_	normal	0.75
28	M	27 2/7	29	1055	1115	5	7	0	caesarean	Patent ductus	MAP	bilateral IVH-II, corps calleux présent.	Dopamine	normal	
29	F	27 1/7	27 4/7	900	955	5	9	0	vaginal	Patent ductus	MAP spontanée	bilateral IVH-II (in left), IVH-III and IVH-IIII (in right)	Sufenta - Hypnovel	normal	0,79
30	M	29 3/7	30 1/7	1180	1060	8	10	1	caesarean	(Patent ductus) Closed ductus at 29 4/7 wk	GRossesse gemelaire - Présence ARCF	normal	_	normal	0.6
31	M	29	30 4/7	1050	1350	10	10	1	caesarean	Closed ductus at 29 2/7 wk (ibuprofen)	Grossesse gemelaire - MAP-métrorragie	normal	ibuprofen	normal	0.65
32	M	28 4/7	30 5/7	1100	1290	10	10	1	caesarean	Patent ductus	MAP-metrorragies	normal	_	normal	0,75

M: Male, **F**: Female, **GA**: Gestational Age, **Brain US:** Brain ultrasonography, **PAH:** pulmonary arterial hypertension, **PRS:** positive rolandic spikes.

5.7.1 **Hybrid EEG-NIRS-DCS**

DCS/NIRS/EEG devices were synchronized and all data were acquired simultaneously from the frontal area of premature neonate at the resting state. The overall measurement duration was between 30 and 40 minutes for each subject including discontinuous activity during quiet and active sleep as required by clinical purposes (du Plessis, 2009b).

Because EEG recordings were used for clinical needs, a standard 10-20 montage adapted for neonates were used. Measuring simultaneously the optical properties of the tissue by NIRS and DCS can provide useful information's about blood flow and tissue oxygenation. The optical devices are time-multiplexed (i.e. turn the sources were turned on/off so as the brain tissue is illuminated for either DCS or NIRS at any given time). Any marked events in DCS were also registered by the EEG and NIRS devices.

5.7.2 EEG recording (EEG)

To define the onset of the burst of spontaneous activity and quantify the neuronal activation, eight EEG channels were recorded at the bedside using Ag/AgCl surface electrodes and a Cz reference at a sampling rate of 1024 Hz, amplified by A.N.T® (Enschede, The Netherlands). Recordings were acquired with a band pass filter of 0.1–100 Hz, and an additional notch filter at 50 Hz. Electrodes impedance were kept below 5 kΩ.

5.7.3 Continous-Wave Spectroscopy (CW NIRS)

To calculate cerebral tissue oxygenation index (TOI), a CW near-infrared spectroscopy probe NIRO-200NX (Hamamatsu Photonics Corp., Tokyo, Japan) was placed on the infant's forehead. The NIRO 200 NX uses spatially resolved spectroscopy at three wavelengths (λ=735 nm, 810 nm, and 850 nm). It is based on the solution of the diffusion approximation equation for a highly scattering semi-infinite homogeneous medium. The effective light attenuation coefficient can be estimated by measuring the decrease in reflected light as a function of distance. By assuming wavelength dependence of the reduced scattering coefficient, the spectral shape of the absorption coefficient can then be calculated and cerebral tissue oxygen index can be estimated (Matcher et al., 1995a). The average output power of the lasers was less than 2 mW and the CW acquisition rate was fixed to 5 Hz (200 ms).

5.7.4 Frequency-Domain Spectroscopy (FD NIRS)

To acquire [HbO] and [HbR] concentration changes, a multichannel frequency-domain-based optical imaging system (Imagent, ISS Inc., Champaign, IL) was used. Imagent is a frequency-domain tissue spectrometer. We used 8 out of the 32 intensity-modulated laser diodes at two wavelengths (λ=690 nm and 830 nm) coupled to optical fibers, and 1 out of the 4 gain-modulated photomultiplier tube (PMT) detectors to collect the signal at both wavelengths separately. The modulation frequency of laser intensity was 110MHz, and the cross-correlation frequency for heterodyne detection was 5 kHz. Reflected light collected by the PMT was then demodulated. Its mean intensity (DC), modulation amplitude (AC), and phase were determined. The average output power of the lasers was about 0.5 mW and the optical acquisition rate was 9.7656 Hz (about one sample every 100 ms). Oxy (HbO) and deoxyhemoglobin (Hb) are chromophores that absorb light at different wavelengths. To convert signal intensities into relative changes in (de)oxy-hemoglobin concentration, the Modified Beer Lambert Law was applied to the two wavelengths (690 and 830 nm).

5.7.5 Diffuse Correlation Spectroscopy (DCS)

To noninvasively quantify CBF, a DCS device was used. DCS is an optical blood flow measurement modality that uses intensity fluctuations of near-infrared (NIR) light (Nourhashemi et al., 2016b). The light scattered by moving red blood cells causes temporal fluctuation of the detected light intensity. The time lag of these fluctuations was quantified by the intensity-time autocorrelation function of the detected light (Durduran et al., 2010a). The correlation diffusion equation is applied to fit the autocorrelation function in order to calculate a cerebral blood flow index (CBFi) (Durduran et al., 2010a). Neuro-Monitor-FloMo (Hemophotonics SL, Spain) consists of a narrowband CW laser (785 nm, Crystalaser Inc., NV) with a long coherence length (> 50 meters), four fast photon-counting avalanche photodiodes (APD) (SPCM-AQR-14-FC, Pacer Components Inc., UK), and a four-channel autocorrelator board (Flex03OEM-4CH, Correlator Inc., NJ). The system uses continuous-wave (CW) lasers in the NIR range (~785 nm) with an acquisition rate of 0.3921 Hz (one sample every 2.55 s). The light was delivered to the brain surface via multi-mode fibers and detected by 4 single-mode fibers away from the source (d_{DCS}=2 cm).

5.7.6 The Hybrid EEG-NIRS-DCS probe

The optical hybrid EEG-NIRS-DCS probe used for this study was designed specially to overcome the challenges of simultaneous NIRS-DCS/EEG recording. Recording sites on the subject's head and a diagram of the probes are shown in Figure 2(a). The infants were placed in the supine position on a comfortable pad in a dark and quiet incubator. The incubator was further protected against ambient light by dark sheets. The probe was smoothly secured to the infant's head with straps and foam padding. Figure 2(b) shows the diagram of the combined DCS-NIRS-EEG probe. The probe was based on a rectangular, 3 mm thick rubber plate attached to optodes. The probe consists of 90° bent fibers (DCS) and prism-coupled (NIRS) fibers that were placed into flexible, light-sealed pads attached to the head by straps.

The DCS part of the probe is made off one series of source (light emitting) fiber-optics (400 μm core diameter), and one fibre-optic (light collecting) detector bundle (3 mm diameter) placed at the end of the rows of emitters fibres, creating 4 measuring points (channels) over the frontal area.

The FD NIRS part of the probe is made off four emitters fibres (one row) that were connected to 690 nm and 830 nm lasers (see Figure 2.b). The emitting tips were 'clad' with plastic tubing and slid into holes in rubber block. The input tip of the detector bundle was fixed in place of well contact

with prisms. The probe was held in place by a headband to wrap the probe, to minimize any light interference. Special care was considered to ensure that the light from the source of one modality do not saturate the detectors of the other modality.

The CW-NIRS part of the probe is made off 2 detectors and 1 source. The emitter-detector distance was 3 cm. The NIRS source contained three wavelength emitters (735, 810 and 850 nm) (bottom right-hand corner). SO_2 (tissue oxygenation) was measured by using the Spatially Resolved Spectroscopy (SRS) method (Nourhashemi et al., 2017a). SRS is a method used to calculate concentrations by measuring the change of light attenuation (A) over distance (d), i.e. $\frac{\partial A}{\partial d}$, as shown in Figure 2(c).

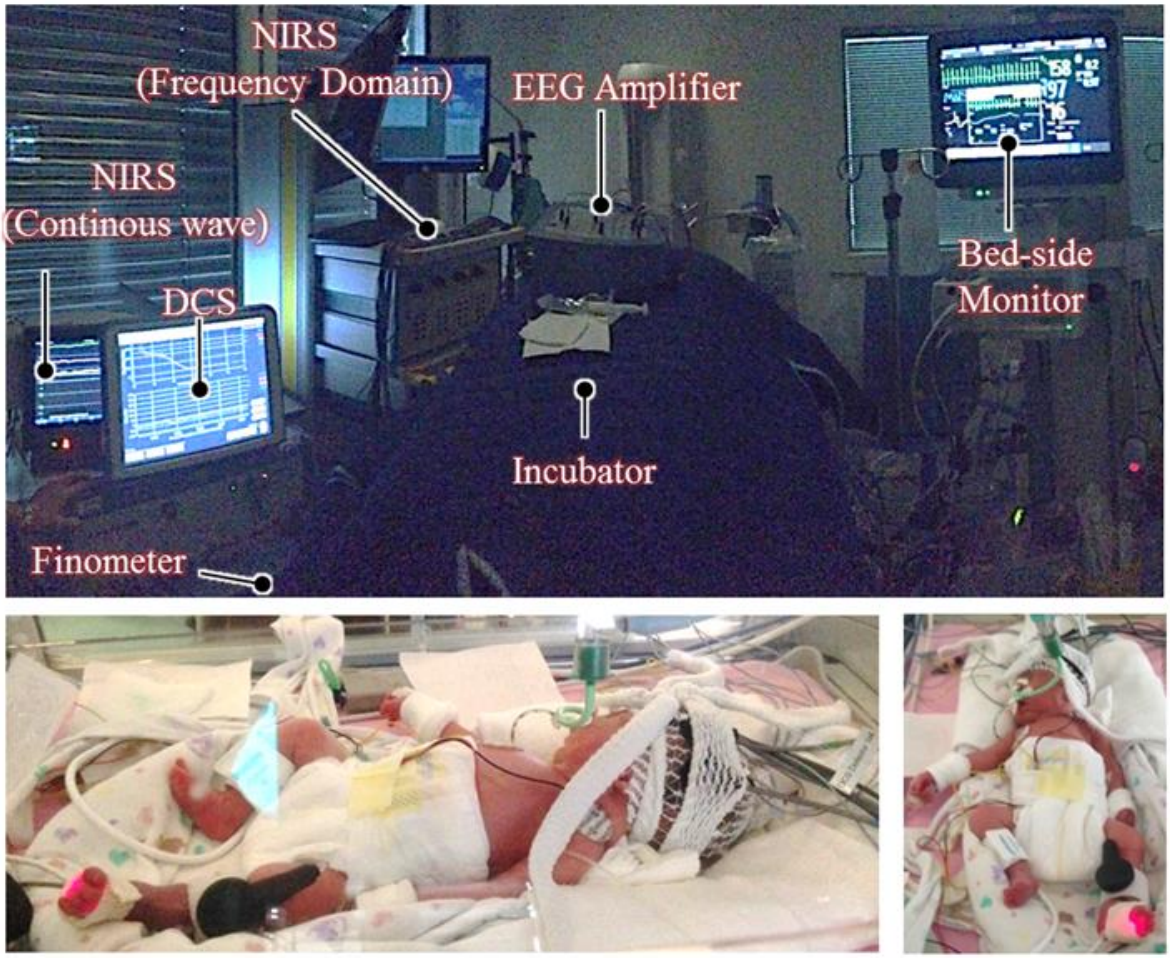

Fig.S1 *Picture of the hybrid portable set up. (Left) DCS and CW-NIRS device (center) ISS Imagent FD NIRS device.*

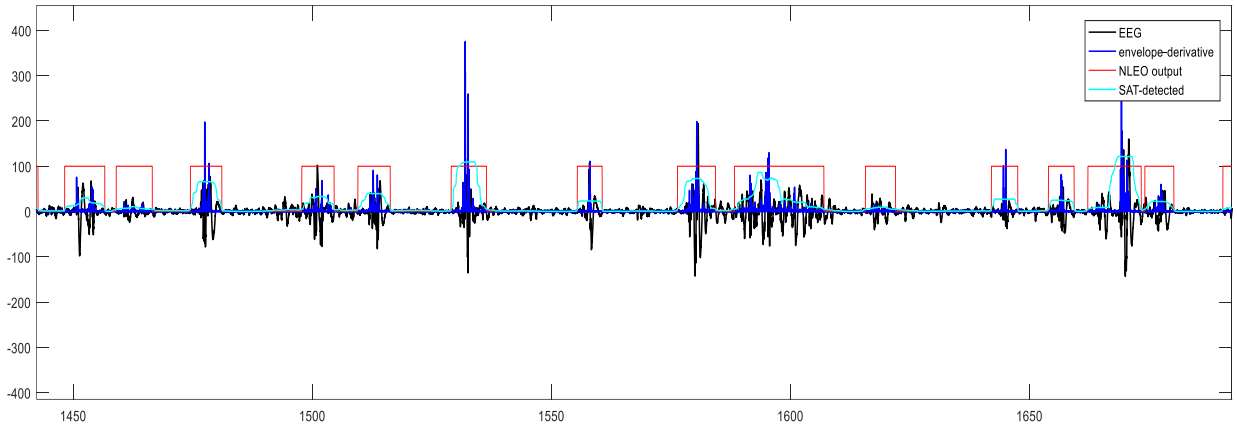

Fig.S2 *Example of the EEG bursts of activity (black), envelope-derivative of EEG depends on both amplitude and frequency of the signal (blue), baseline corrected average of envelope-derivative signal in a sliding window of length WIN, xNLEO (cyan), and the NLEO output: detected burst of activity requires xNLEO to be above defined threshold (red).*

Table.S2 *The percentages of the number of the classified hemodynamic responses to EEG bursts in each condition*

	Condition A1	***Condition A2***	***Condition A3***	***Condition B***	***Condition C***
Sub1	***44.1%***	***25%***	***30.8%***	***0%***	***0%***
Sub2 (IVH;II)	***60%***	***0%***	***2.2%***	***33.3%***	***4.4%***
Sub3	***53.7%***	***31.3%***	***14.9%***	***0%***	***0%***
Sub4	***34.7%***	***23.9%***	***41.3%***	***0%***	***0%***
Sub5 (PDA)	***100%***	***0%***	***0%***	***0%***	***0%***
Sub6	***41.4%***	***15.9%***	***19.7%***	***19.7%***	***3.1%***
Sub7	***43.9%***	***15.2%***	***18.4%***	***18.4%***	***3.8%***
Sub8	***19.4%***	***27.4%***	***33.1%***	***10.2%***	***9.7%***
Sub9 (IVH;III)	***47.1%***	***31.7%***	***21.1%***	***0%***	***0%***
Sub10 (PDA-IVH;II)	***68.4%***	***0%***	***31.5%***	***0%***	***0%***
Sub11 (PDA)	***62.1%***	***16.6%***	***21.2%***	***0%***	***0%***
Sub12	***72.7%***	***13.6%***	***13.6%***	***0%***	***0%***
Sub13	***52.1%***	***26%***	***21.8%***	***0%***	***0%***
Sub14	***44%***	***10%***	***23%***	***7%***	***16%***
Sub15	***21.1%***	***13.3%***	***38.8%***	***14.4%***	***12.2%***

Sub16 (IVH;I)	*51.5%*	*12.6%*	*9.4%*	*10.5%*	*15.7%*
Sub17 (PDA)	*34.5%*	*9.7%*	*28.3%*	*15.9%*	*11.5%*
Sub18	*22%*	*8%*	*33%*	*26%*	*11%*
Sub19 (PDA)	*26%*	*18.2%*	*30.4%*	*13.9%*	*11.3%*
Sub20 (IVH;I)	*29.5%*	*20%*	*24.3%*	*16.5%*	*9.5%*
Sub21 (IVH;I)	*30%*	*13.3%*	*28.3%*	*20%*	*8.3%*
Sub22	*37%*	*21.3%*	*20.3%*	*14.8%*	*6.4%*
Sub23	*26.4%*	*9.4%*	*33.3%*	*20.1%*	*10.6%*
Sub24	*24.2%*	*24.2%*	*24.2%*	*15.1%*	*12.1%*
Sub25	*25.8%*	*22.4%*	*25.8%*	*18.9%*	*6.9%*
Sub26	*27%*	*20%*	*32%*	*12%*	*9%*
Sub27	*32.2%*	*17.7%*	*24.4%*	*16.6%*	*8.8%*
Sub28 (PDA-IVH;II)	*23.8%*	*23%*	*30.1%*	*14.2%*	*8.7%*
Sub29 (PDA-IVH;III)	*70.7%*	*0%*	*29.2%*	*0%*	*0%*
Sub30 (PDA)	*30.2%*	*18.6%*	*18.6%*	*23.2%*	*9.3%*
Sub31	*33%*	*12.2%*	*22.6%*	*25.4%*	*6.6%*
Sub32 (PDA)	*27.6%*	*16.9%*	*28.5%*	*18.7%*	*8%*
Total PDA	*49.3%*	*11.4%*	*24.2%*	*9.5%*	*5.4%*
Total IVH (I,II,III,IV)	*47.7%*	*12.5%*	*22%*	*11.8%*	*5.8%*
Total IVH (III,IV)	*58.9%*	*15.8%*	*25.1%*	*0%*	*0%*
Total	*39.04%*	*17.18%*	*24.15%*	*12.92%*	*6.71%*

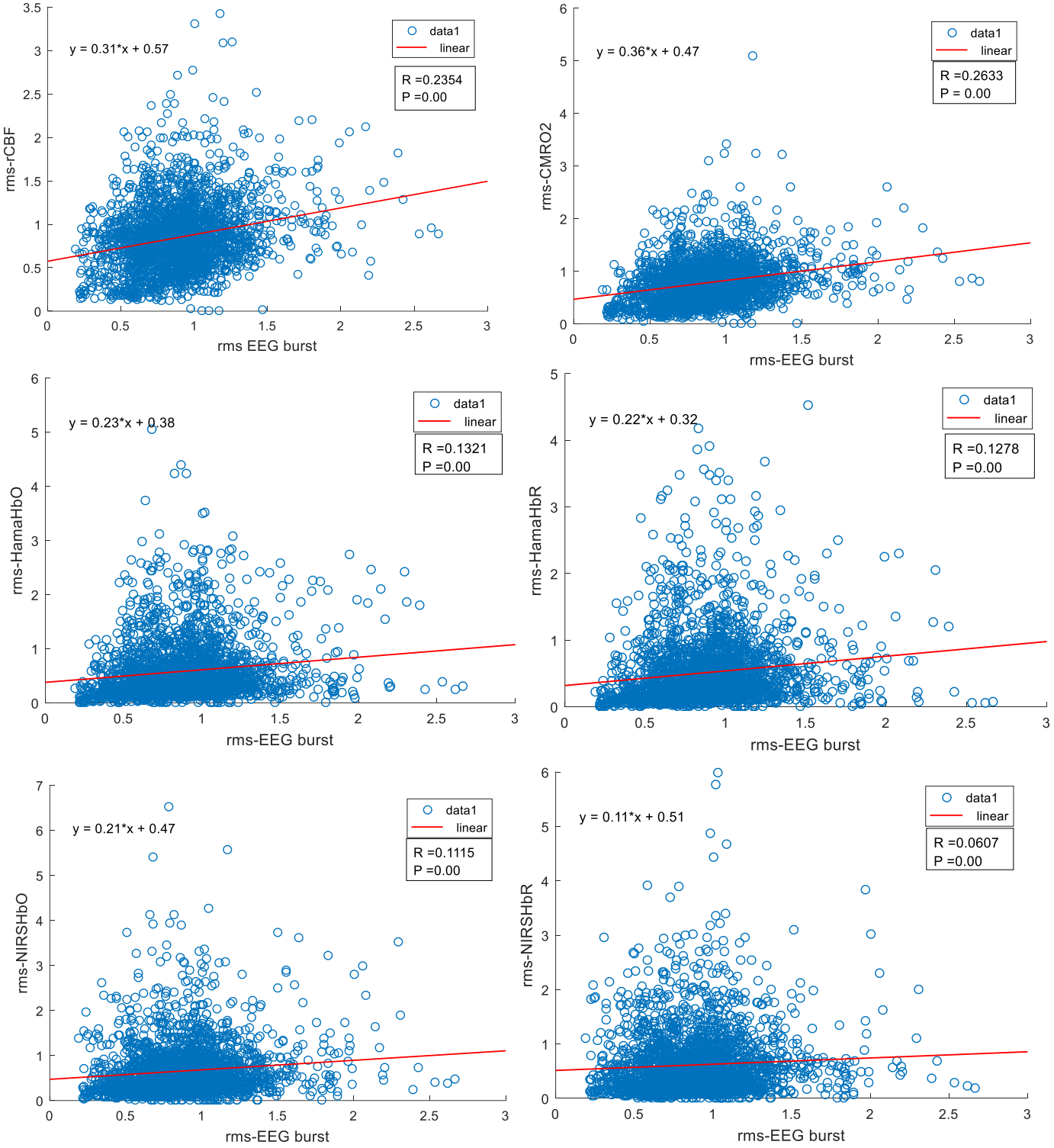

Fig.S3 *The correlation between rms of the hemodynamic responses and rms of envelope derivative of EEG bursts (IBIs of bursts are more than 20s).*

A

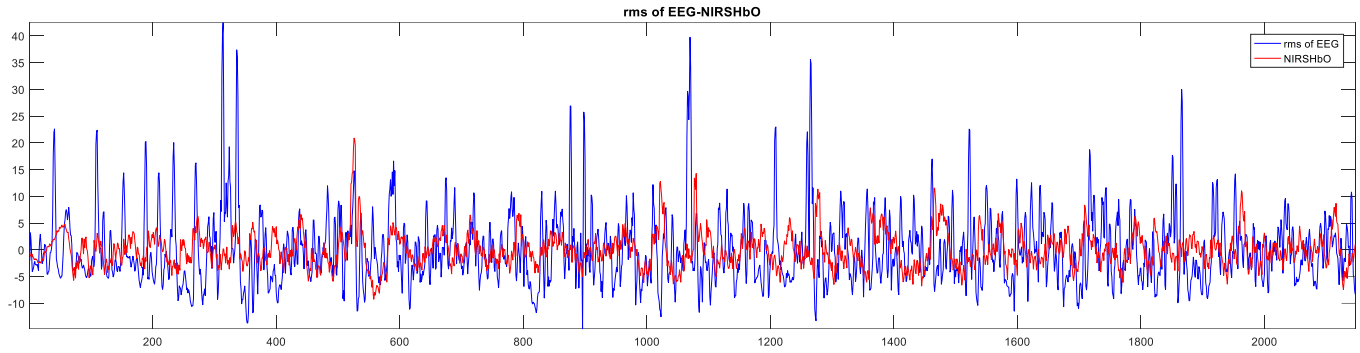
rms of EEG-NIRSHbO
rms of EEG
NIRSHbO

B

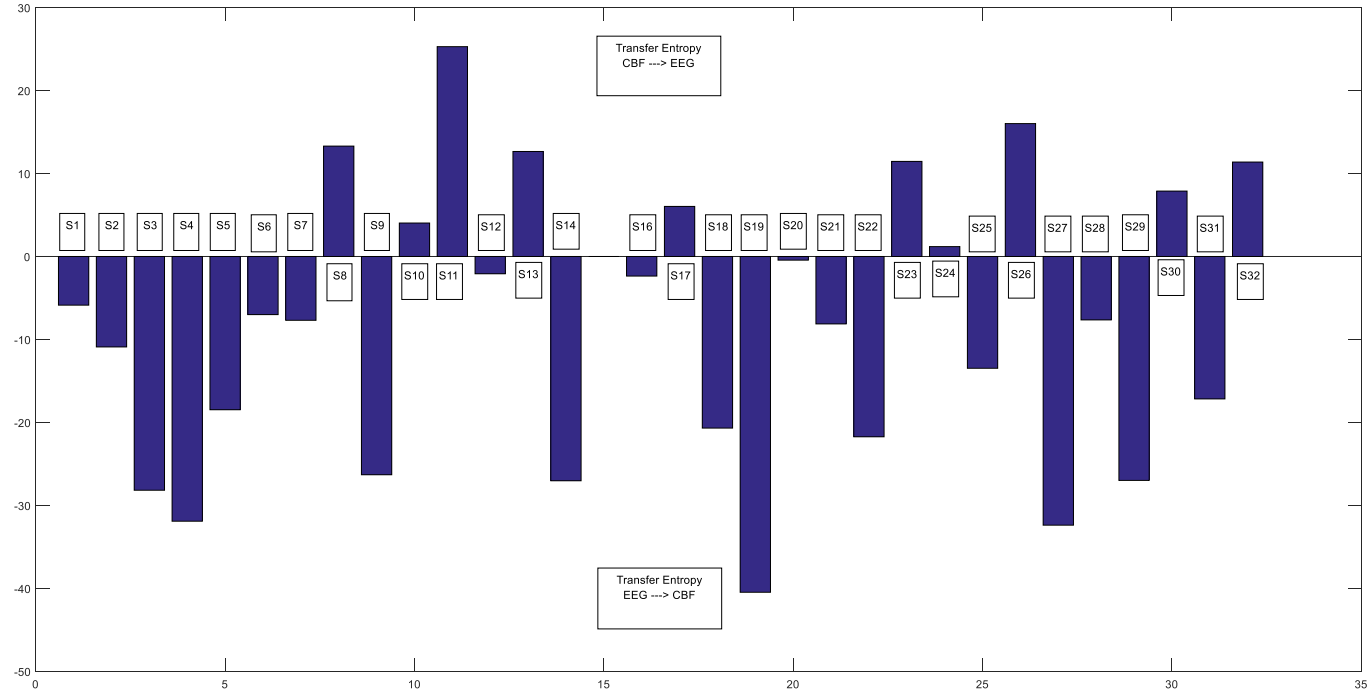
Transfer Entropy
CBF ---> EEG
Transfer Entropy
EEG ---> CBF

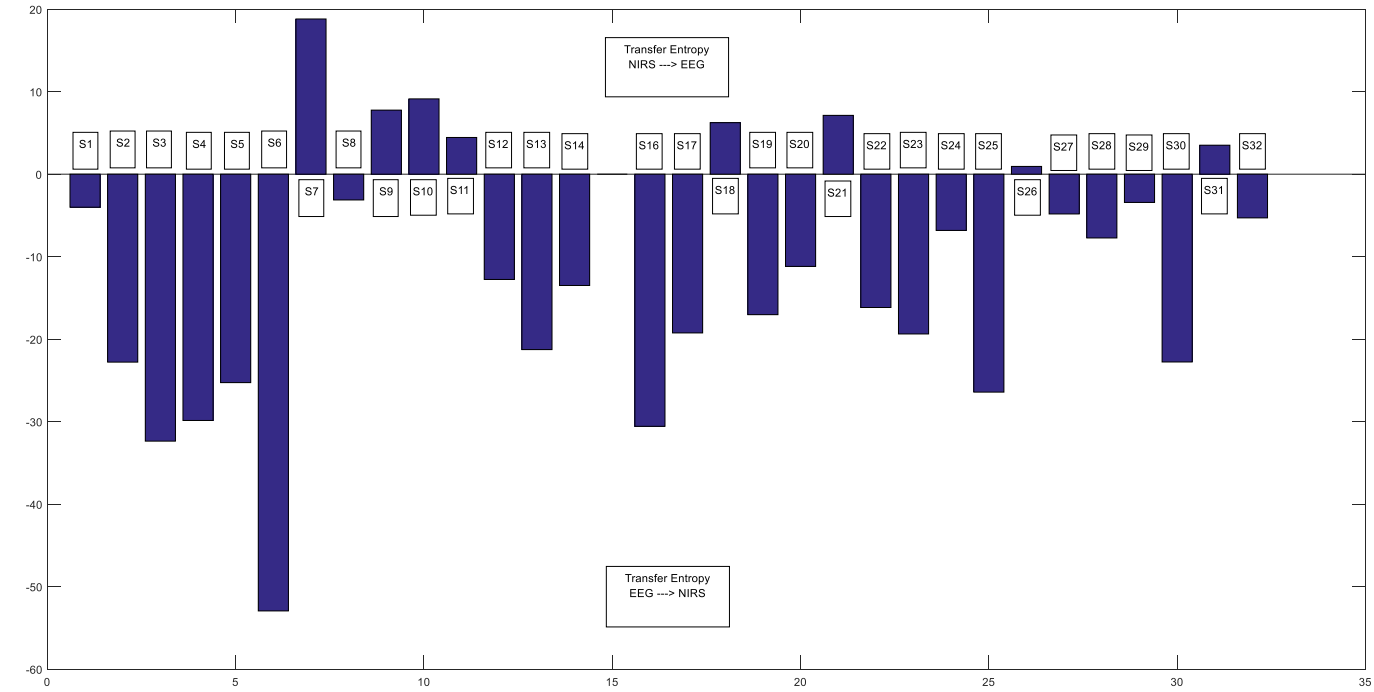
Transfer Entropy
NIRS ---> EEG
Transfer Entropy
EEG ---> NIRS

Fig.S4 *A) Row data of rms-EEG and NIRS, B) Rate of information (TE) exchanged from rms-EEG to CBF (rms-EEG to NIRS) and vice versa.*

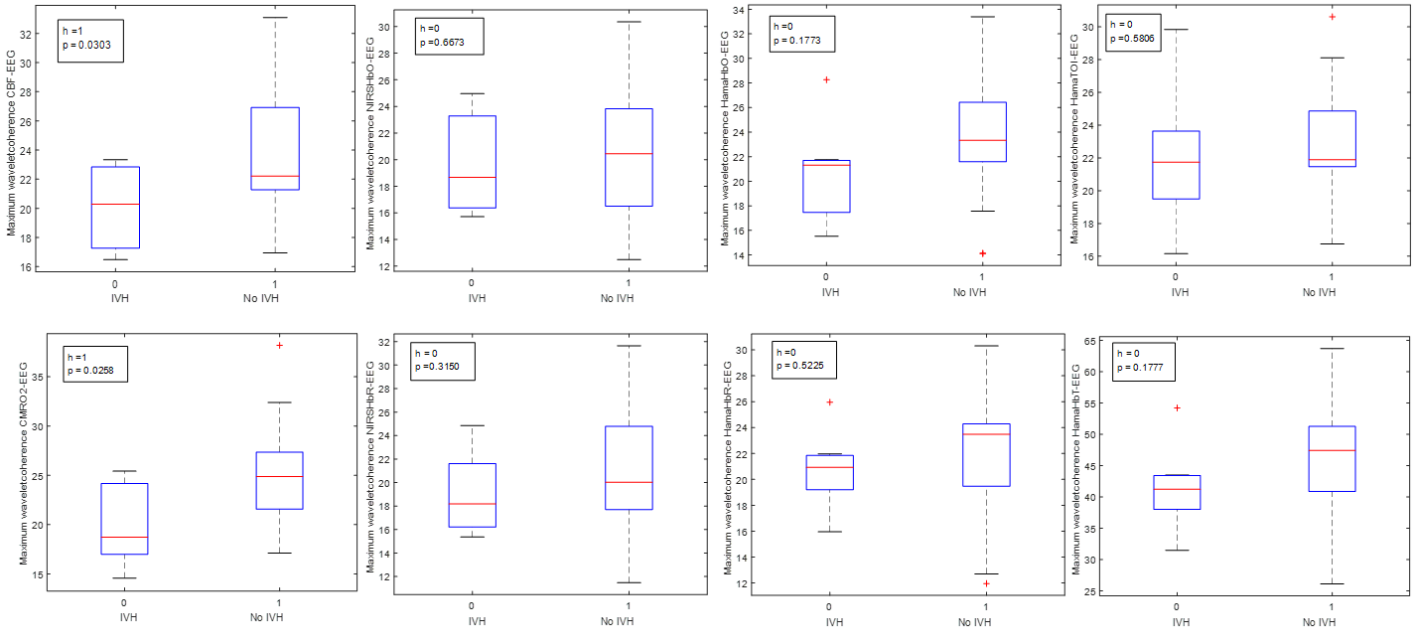

Fig.S5 *The boxplot distribution of percentage of area for significant NVC coherence per total considered area over the frequency range of 0.003–0.125Hz between two groups: with IVH and without IVH.*

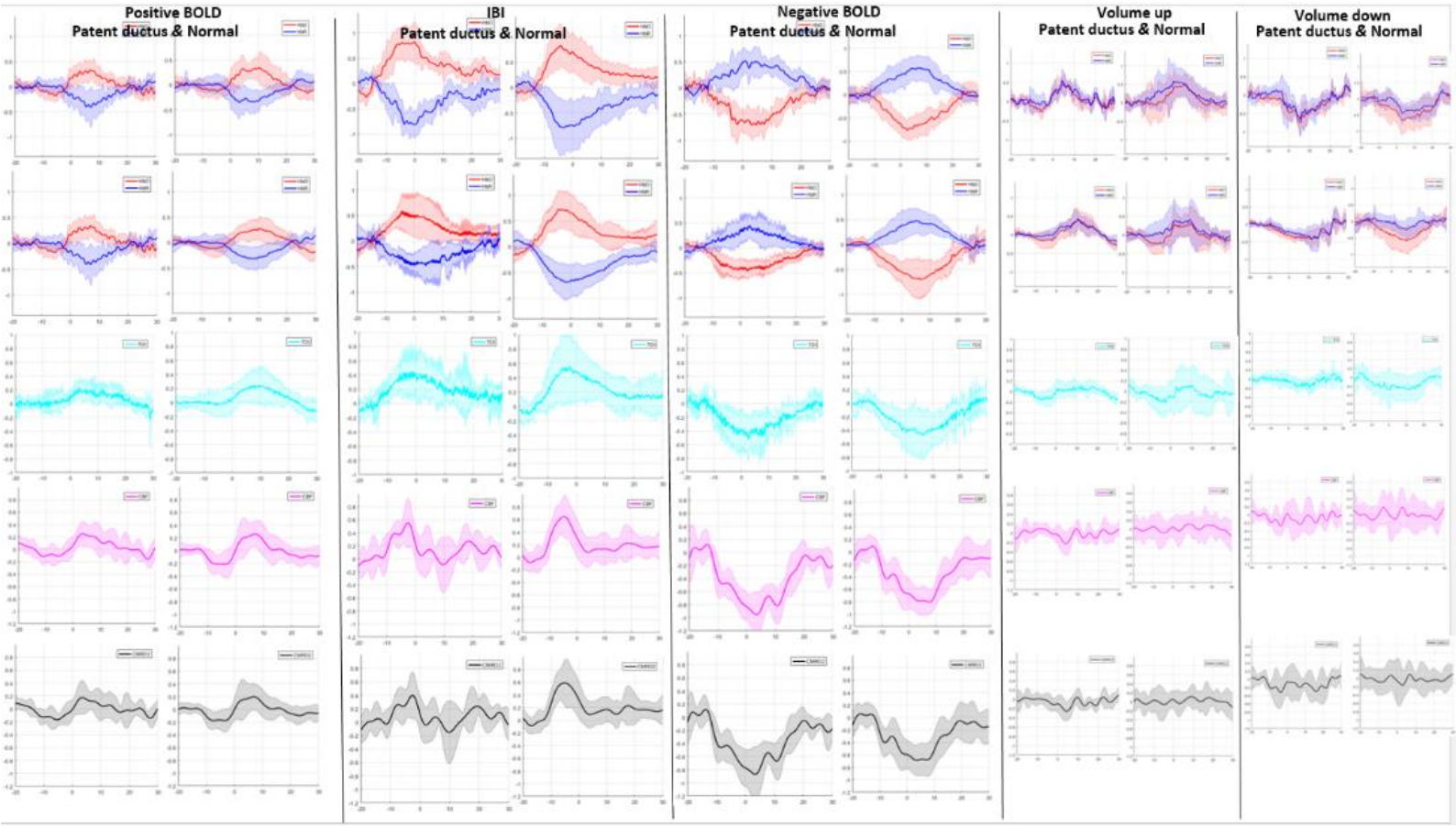

Fig. S6 *The grand average of the regional hemodynamic responses of the onset of EEG bursts (5 conditions), compared between two groups of normal and pathological premature neonates (with PDA).*

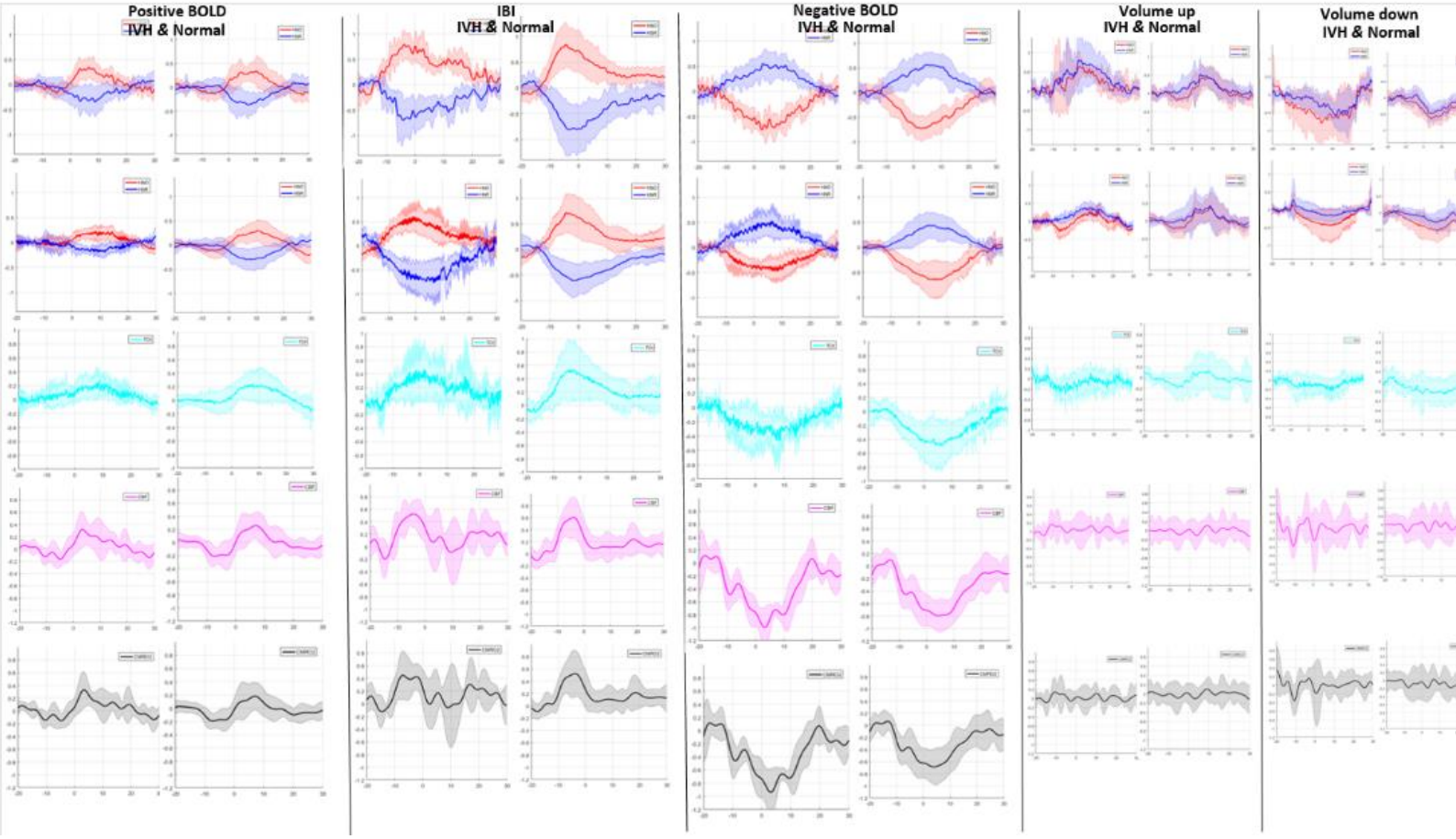

Fig.S7 *The grand average of the regional hemodynamic responses of the onset of EEG bursts (5 conditions), compared between two groups of normal and pathological premature neonates (with IVH).*

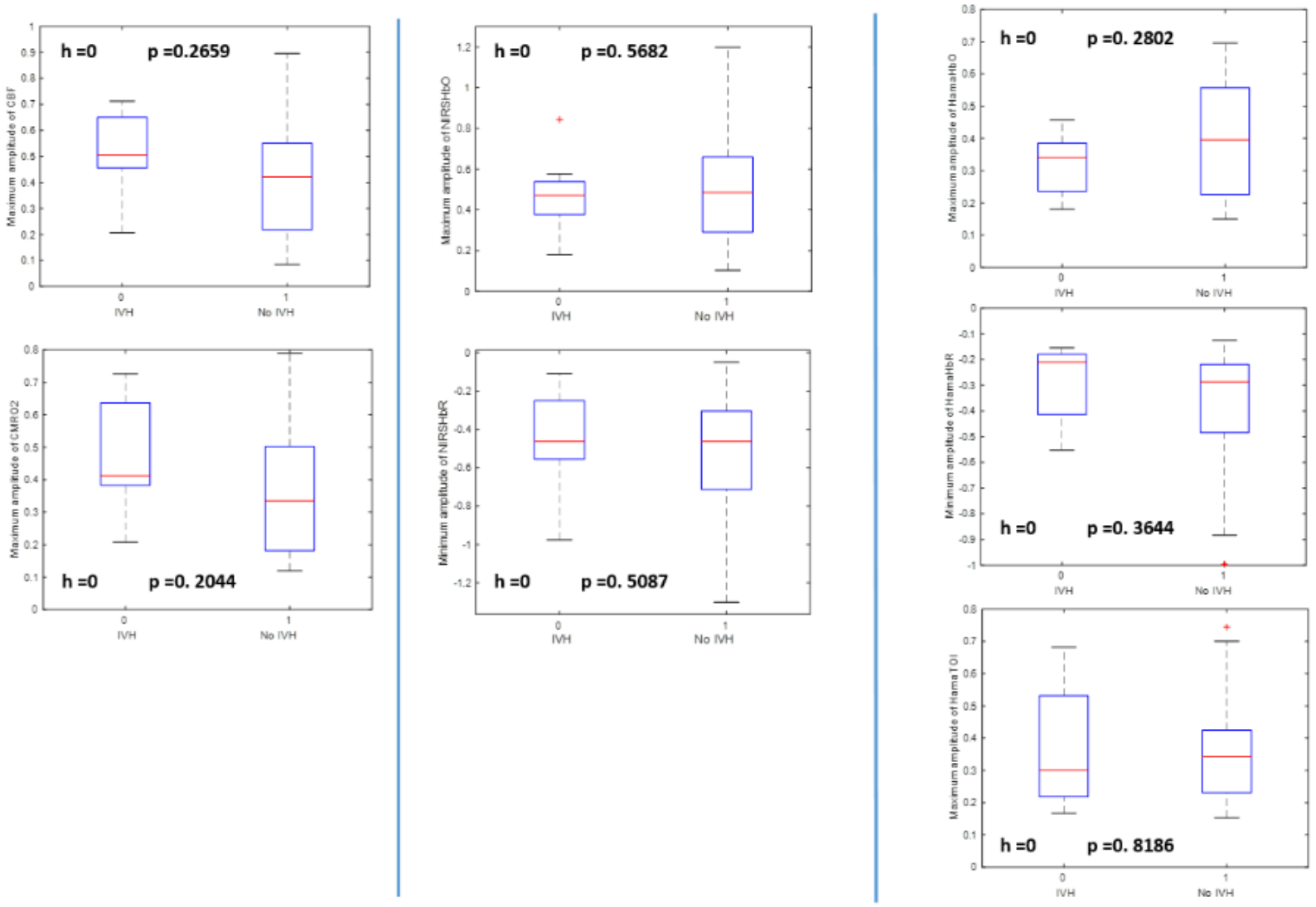

Fig.S8 *The boxplot distribution of maximum amplitude of the grand average of hemodynamic responses of EEG bursts for each premature neonate, compared between two groups of with and without IVH in premature neonates.*

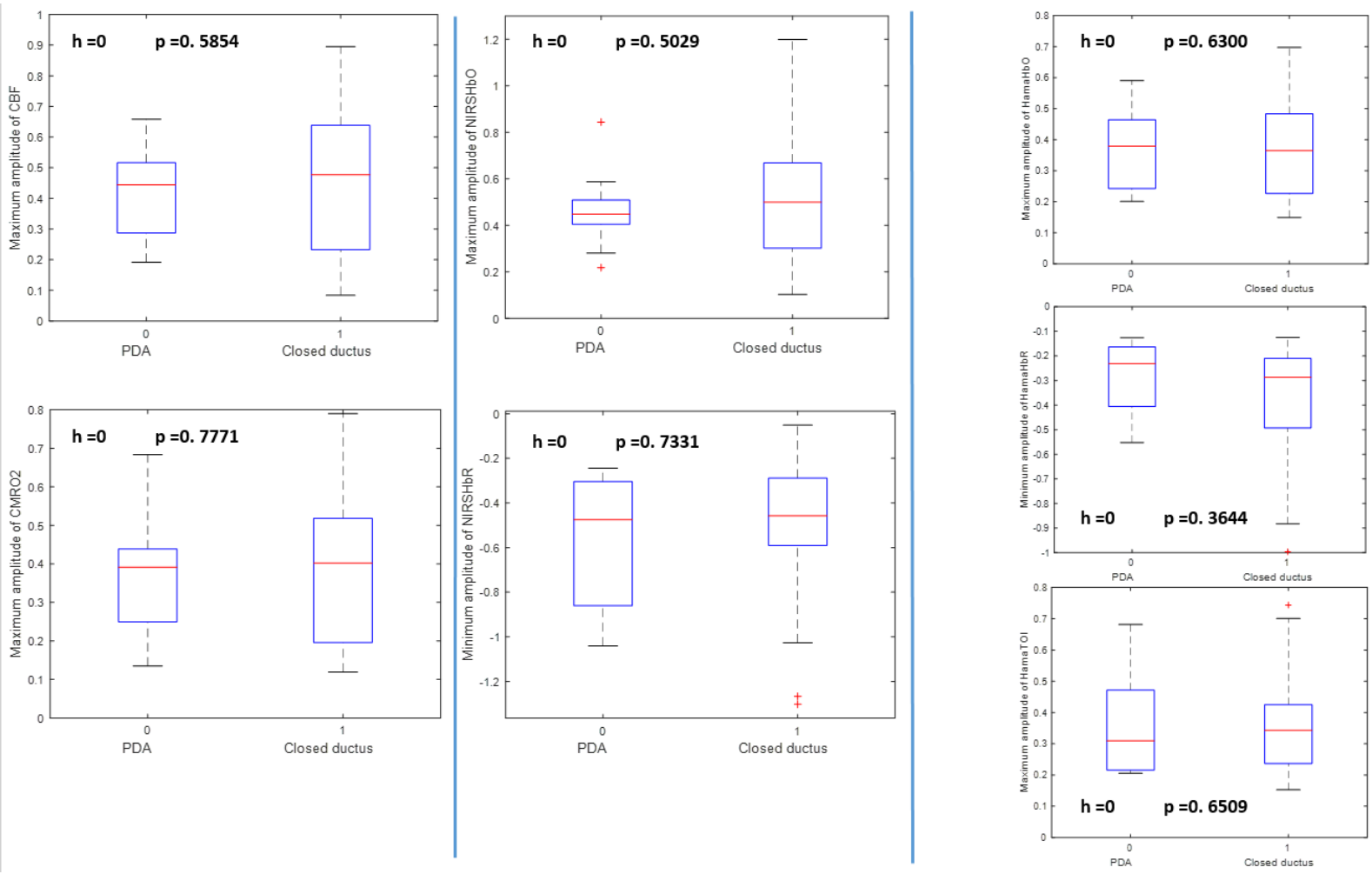

Fig.S9 *The boxplot distribution of maximum amplitude of the grand average of hemodynamic responses of EEG bursts for each premature neonate, compared between two groups of with and without PDA in premature neonates.*

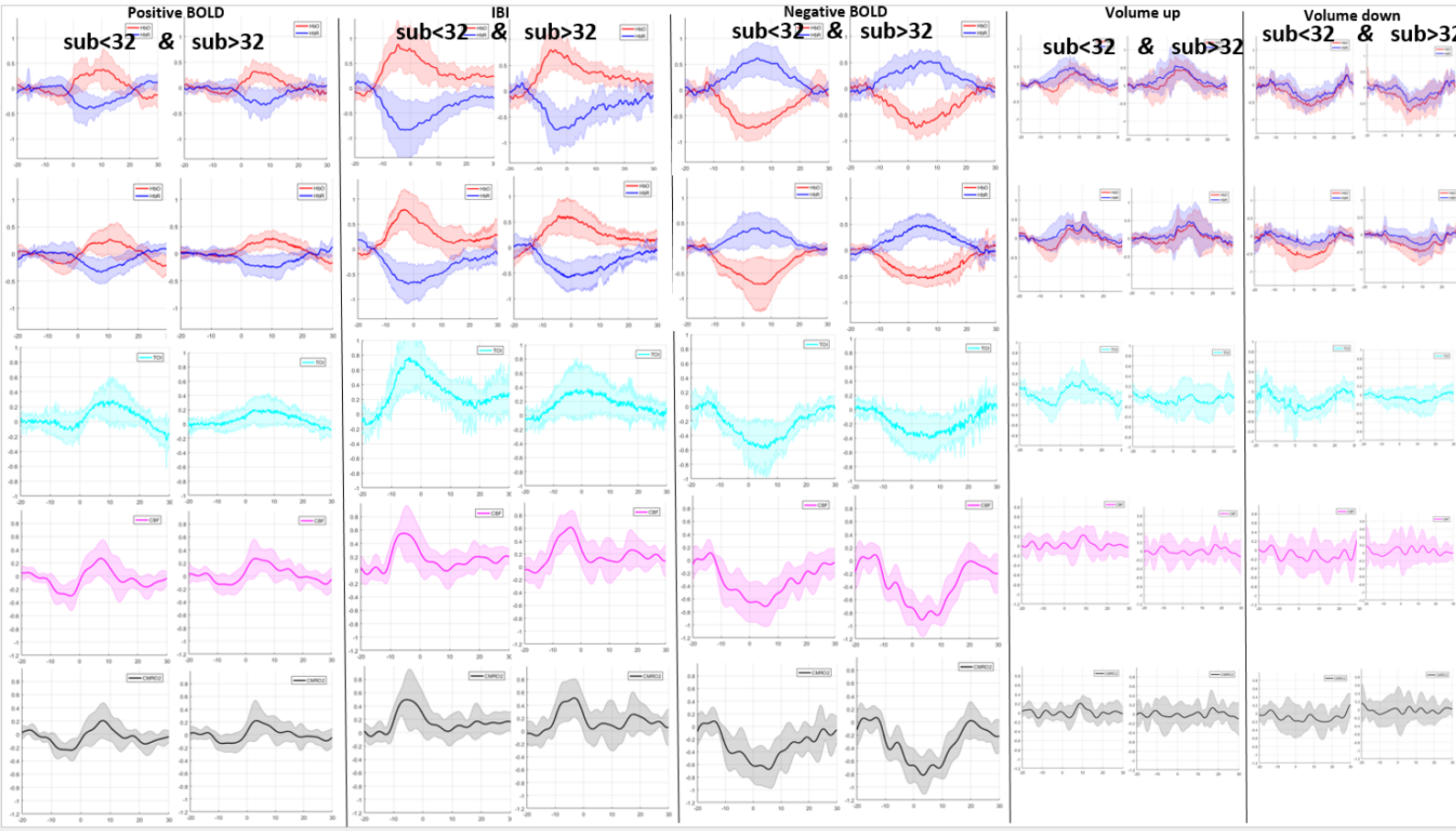

Fig. S10 *The grand average of the regional hemodynamic responses of the onset of EEG bursts (5 conditions), compared between two groups of <32GA(wk) and >32GA(wk) premature neonates.*

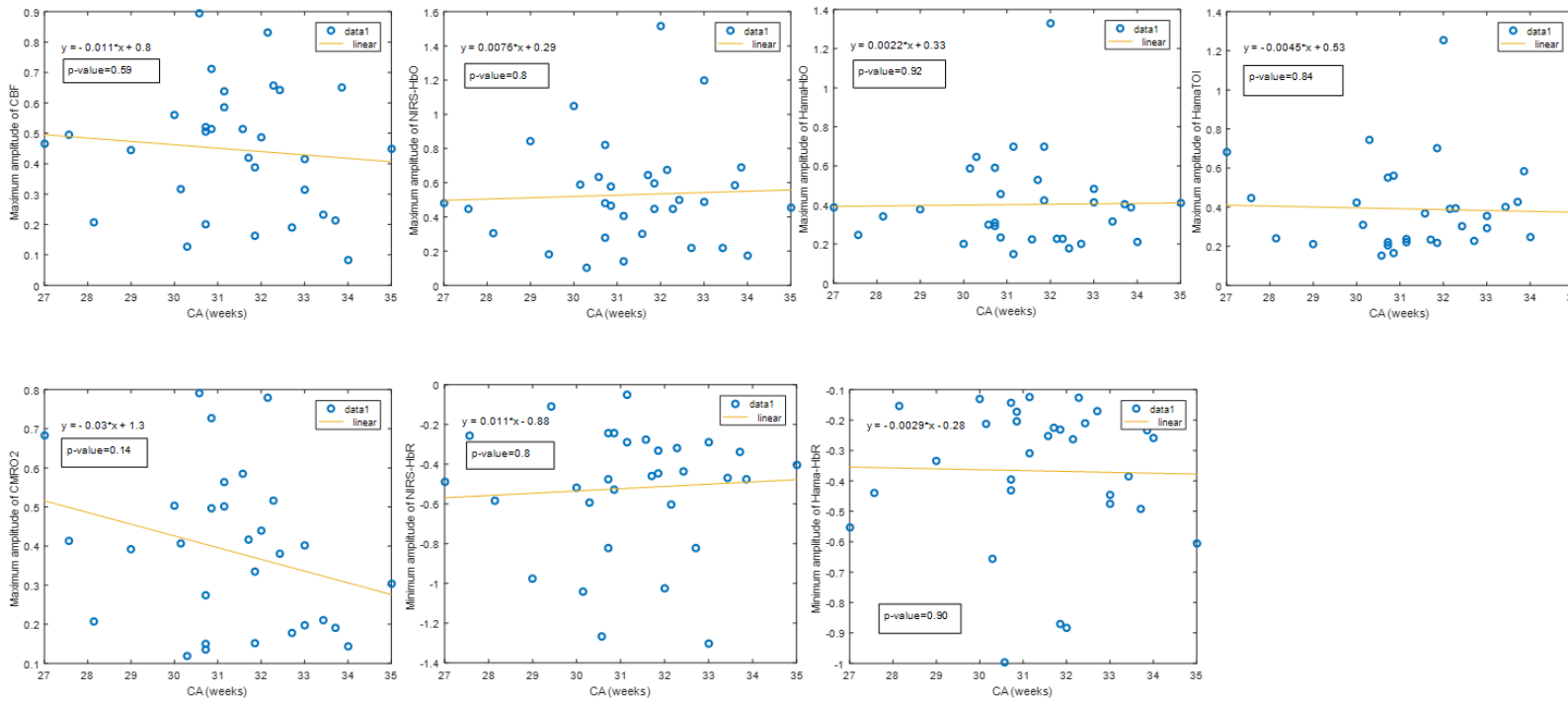

Fig.S11 *The maximum amplitude of the grand average of hemodynamic responses of EEG bursts for each premature neonate as a function of age.*

CHAPTER

Conclusion and Perspective 6

6.1 Introduction

Several progresses in neuroimaging technology have greatly developed the research in the neurovascular field. Neuroimaging, and notably "neurovascular imaging," is a combining method which can be considered at the intersection of different fields. Neurovascular coupling are essential to provide the energy demands of cerebral tissue during both normal physiological function and pathological conditions. Thus, advances in functional imaging techniques have improved our understanding of the relationship between cerebral activity and energy supply in developing brain. While in the beginning of brain imaging particular brain imaging method was exclusively used, currently more and more studies describe research in which different brain imaging methods are combined.

Each chapter in this thesis describes a combination of techniques applied to preterm neonates in either a healthy or an abnormal brain. It is valuable that most of these approaches can be adapted to a variety of situations to measure different aspects of neurovascular coupling in both normal and pathological brain states in animal as well as human.

This thesis thus presented a framework from which a group of additional studies could be performed as these approaches can be performed to a variety of other species and other areas of the cortex or pathological conditions. What is obvious, is the increasing importance and potency of optical approaches in neurovascular coupling investigation. Moreover, the

noninvasive nature of optical approaches renders them useful in the neonatal ICU for use in humans. In addition, multiple techniques are combined in order to measure signals from multiple sources, not just hemodynamic but also neuronal. The combination of multiple approaches allows us to draw conclusions on the coupling dynamics between these different sources of the signals. In our data, it is clear that neurovascular uncoupling may be specific to pathological brain states. This chapter reviews the objectives and contributions that are presented in this thesis. Finally I give an account of future perspectives of this thesis.

6.2 Conclusions

In this dissertation, multimodal hybrid EEG-NIRS-DCS and non-invasive blood pressure monitoring techniques were used to measure electro-hemodynamic activities of the premature neonatal brain under resting states (Fig.1). The differences in functional responses correspond to the immaturity of NVC, support the massive growth and neurogenesis at rest in neonatal brain. The complex process of NVC development continues to occur postnatally in normal development, prompting consideration of the role of this developing system in normal and abnormal trajectories of brain development. Disruptions or delays in NVC could lead to abnormalities in both neural and vascular development. It may have a profound impact on developing neural circuitry. So there is a need to understand the optimal metabolic state of the perinatal brain. At the resting state, data of immature brain can be more challenging to interpret than stimulus-evoked responses: our finding demonstrated the directionality of these slow fluctuations in neural and hemodynamic activity, and the presence of positive, negative, or absent NVC in premature neonatal brain. The main achievements of this thesis can be summarized as follow:

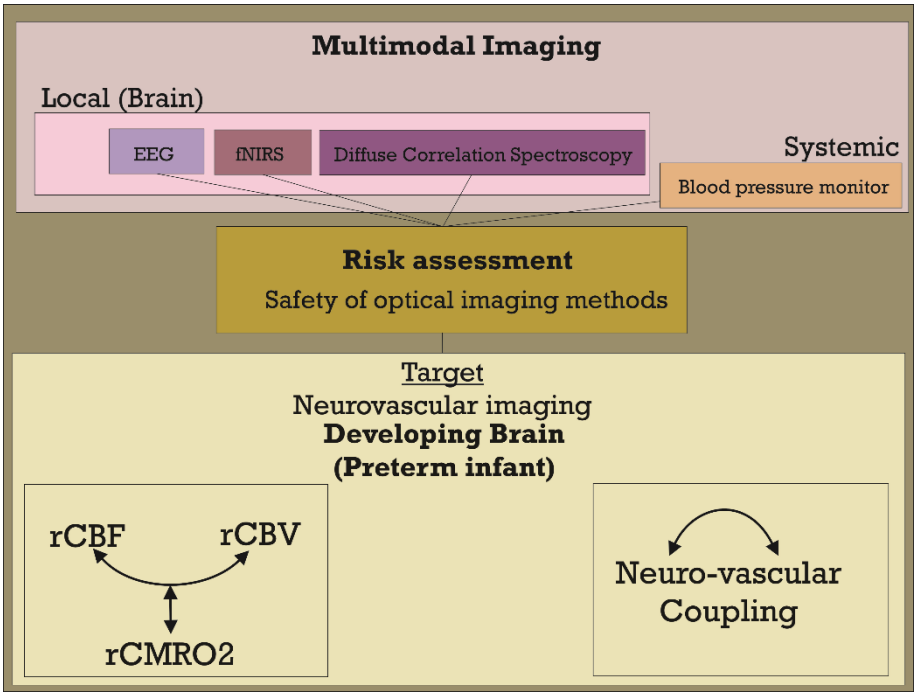

Fig. 1 *summery of thesis.*

1) **Safety issues of optical imaging:** There are currently not any major safety problems associated with functional optical imaging measurements. The only safety issue is a potential heating of the light source attached to the scalp. Thus, careful monitoring of the temperature and timely termination of the study will prevent any harmful effect. As there are no substantial medical or ethical constraints associated with functional optical imaging, it can easily be used to study brain processes of normal and healthy subjects. The photothermal interaction of NIR laser on human tissues (with different laser powers and various spot sizes) were modelled. The results demonstrated the maximum temperature increase was higher in the neonatal brain than in the adult brain, these results can be useful to optimize laser parameters for a variety of laser applications in the brain to avoid any possible tissue damage.

2) Transfer entropy robustly detected the relation between CBF_CBV, CBF_CMRO2, and neuronal-vascular system as a complex non-linear coupling in preterm infants recorded before 32 wGA. The findings of this study suggest that the mechanisms by which rCBV drives rCBF (rCMRO2 drives rCBF) are already functional at this early age of development regardless of whether or not these two variables are strictly correlated.

3) This thesis describes the different pattern of cerebral hemodynamic response to the spontaneous cerebral burst of activities in resting state in premature neonates. This may be a consequence of the immaturity of the neuronal and vascular networks together with the cellular mechanisms of the neurovascular coupling.

4) As wavelet coherence analysis presents the multi-frequency aspect of neurovascular coupling, the results of this study suggest that neurovascular development represents the establishment of neurovascular coupling system as a function of age. The age-dependent hemodynamic responses that we observed, could be explained by changes in the underlying neuronal behavior or by changes in the coupling between neural activity and hemodynamic responses.

5) The neurovascular coupling is affected by neonatal encephalopathy in pathological groups (i.e., PDA). Thus, the neurovascular coupling analyzing in the premature neonatal brain at rest, have clinical value as sensitive markers of diseases.

6.3 Perspective

This thesis provided an overview of a variety of techniques currently available to investigate neurovascular coupling in both health and disease neonates. Understanding normal neurovascular coupling during sensory and eventually higher order brain functions like memory and language will be essential in the development of novel neuroimaging techniques. Likewise, the propagation of these approaches to diagnose disease will require a complete understanding of how neurovascular coupling mechanisms fail in disease states to permit accurate interpretation of cortical hemodynamic signals as a proxy for neuronal activity.

A comprehensive understanding of the neurovascular coupling relationship needs the concurrent measurement of neuronal and vascular responses. The value of this approach, is the ability to measure hemodynamics through an intact skull, which provides translational techniques for noninvasive measurements in humans for clinical diagnostic purposes and a new insights into the etiology of developmental disorders. This section contains several suggestions for the future direction that might help in studying neurovascular coupling development in premature neonatal brain and infants.

6.3.1 Investigation of nonlinear NVC in deeper layers and different areas of neonatal brain

The results in Chapter 4, explored a causal relationship between the hemodynamic responses in the frontal area of the premature brain. As the penetration of light is limited in NIRS technique, it is not possible to investigate the nonlinear relation between hemodynamic responses in the deeper layer of the premature neonatal brain. Thus using more technique such as fMRI images can be helpful to investigate nonlinearity of hemodynamic parameters in the deeper layers and more areas of the neonatal brain.

6.3.2 Investigation of impaired cerebral autoregulation in preterm newborns

The immaturity of the cerebral vasculature coupled with unstable cerebral hemodynamic play an essential role in the aetiologies of the major forms of preterm brain injury (du Plessis, 2009a). Hemodynamically significant patent ductus arteriosus (hsPDA) in preterm infants lead to cerebral injury and cerebral autoregulation impairment because of lower cerebral oxygenation and reduced cerebral blood flow due to left-to-right shunting. The pressure of passive cerebral blood flow in distressed preterm infants has been widely accepted as an important aspect within the physiopathological considerations of the hemorrhagic/ischaemic cerebral injury in preterm neonates (Vutskits, 2014). These patients seem to be exceptionally prone to loss of autoregulation and risk of intraventricular hemorrhage (IVH) under blood pressure changing events like suctioning, pneumothorax, and rapid volume restoration. Roche et al. previously demonstrated that the neurovascular coupling was impaired by IVH grade III and IV (Roche-Labarbe et al., 2007a). In the present study, we evaluate whether PDA and IVH grade I and II, which are less dramatic situations but are likely to impair future neuronal abilities, might impact the neurovascular coupling in response to spontaneous bursts (chapter 5).

As the characteristics of cerebral autoregulation and the ideal range of systemic blood pressure in preterm infants remain unclear, and DCS, Finometer, and NIRS have established techniques for the assessment of cerebral blood flow, systemic blood pressure and cerebral oxygenation respectively. As a future work, the assessment of the correlation between dynamic indexes of cerebral autoregulation in preterm infants, with indices obtained in this study using DCS and Finometer/NIRS will be done. Initial results (in the following part) suggest that

DCS/NIRS derived cerebrovascular reactivity indices (CBF, CBV) correlate well with Pressure.

6.3.2.1 The linear relationship between CBF_CMRO$_2$ and MBP

To investigate how PDA affects cerebral autoregulation and brain injury, the degree of correlation between (MBP) and (CBF) by Finometer and DCS, determines cerebral pressure passivity and loss of autoregulation. Maximum concordance between signals (MBP, CBF), (MBP, CMRO2) were determined by maximum correlation. Greater concordance between signals (MBP, CBF), (MBP, CMRO2) is seen when cerebral autoregulation is impaired. Figure 2 display the relationship between (z-score-CBF, z-score-MBP) and (z-score-CMRO2, z-score-MBP) by linear regression line for the premature neonate #28, respectively.

A

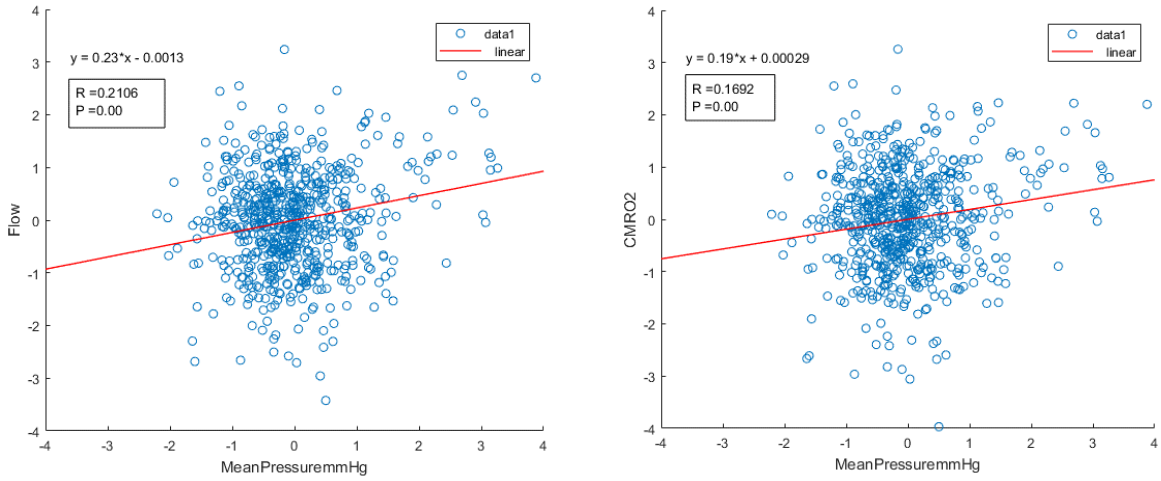

B

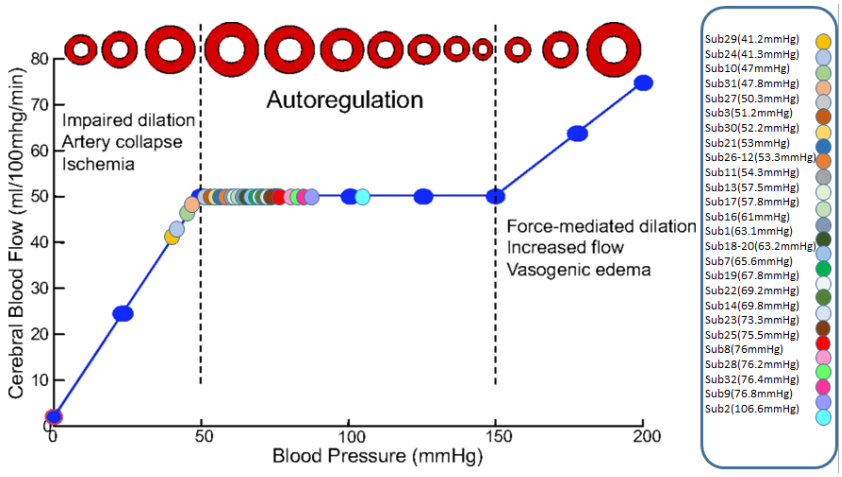

Fig. *1 (A) Scatterplots of z-score-CBF and z-score-MBP and (z-score-CMRO2, z-score-MBP) (with calculated R and p-value), (B) Autoregulation curve; cerebral blood flow in relation to artery lumen diameter. Dotted lines represent the lower and upper limits of cerebral blood flow autoregulation. The circles in colors represent the mean value of CBF and MBP for each individual premature neonates.*

6.3.3 Development of hemodynamic responses function (HRF) in preterm newborns

As the hemodynamic response to brain activity forms the basis for imaging modalities as a surrogate measure of neural activity, it is therefore critical to understand how the coupling between neuronal activity and hemodynamic response is mediated and if the model of Hemodynamic Response Function (HRF) can link hemodynamic and electrophysiological measures of brain activity in resting neonatal brain with varied ages and pathologies.

In the adult human brain, the morphology of the HRF has been well determined and found to be reproducible across different populations (Handwerker et al., 2004). Arichi et al. characterized the morphology of the HRF to neural stimulation during the term and preterm neonates, with hypothesized that the neonatal HRF differs from the canonical adult waveform and considering a systematic maturational trend (Arichi et al., 2012). As presented in chapter 5, because of the different appearances of hemodynamic response to the burst of activities during the preterm newborn period, the morphology of the HRF to burst of activities at rest will be more complex that need a more precise algorithm. Changes in the neonatal brain would complicate the determination of the HRF during development at different gestational age and also pathology cases. As a future work, HRF at different gestational age and pathology cases will be estimated. Initial results for HRF fitting by using Genetic algorithms will be presented in the figure 2.

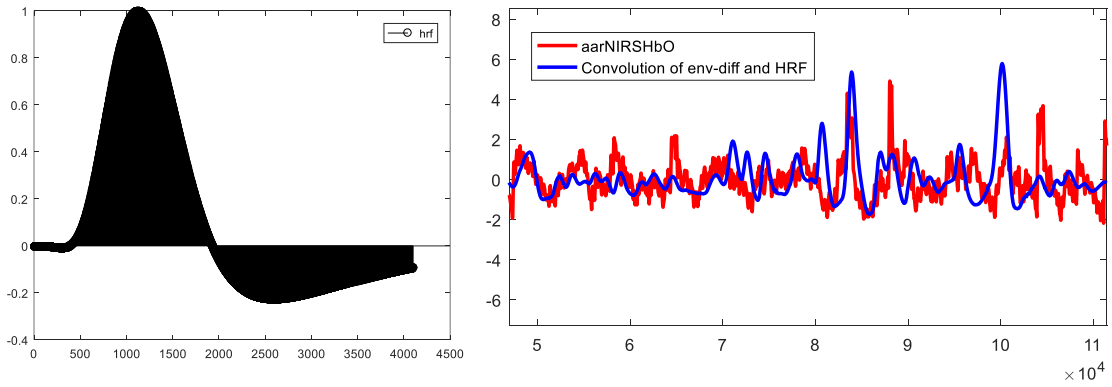

Fig. 2 *HRF, Convolution of envelope-derivative of EEG and estimated HRF is compared with the simultaneously recorded HbO, (sub1).*

6.3.4 Somatosensory evoked changes in hemodynamic responses on bald scalp

We combined multiple near-infrared spectroscopy techniques to measure hemodynamic responses in the somatosensory cortex of 6 bald scalp during passive tactile stimulation of the hand (Fig.3). This experiment was designed to provide a preliminary control condition to evaluate the functional hemodynamic response as a reliable marker of neuronal activity. As a future work, to independently evaluate our multimodal method for studying the pathophysiological cases such as epileptic patient (absence seizure), we obtained event-related optical signals such as HbO, HbR, CBF, and CMRO2 in response to exogenous stimulation of median nerve as a control experiment.

Fig. 3 *Stimulation somatosensory was applied on the hairless skin.*

6.3.5 Investigation of multimodal imaging during absence seizure in epileptic children

The present results of this thesis demonstrated the abnormalities of spontaneous neurovascular coupling in IVH premature neonates (chapter 5). In contrast, in infants without impairment of the vascular system (no IVH), the hemodynamic response is still present in response to neuronal “seizure-like” discharges (Wallois et al., 2009). Childhood absence epilepsy is an idiopathic, generalized non-convulsive epilepsy with a multifactorial genetic etiology. The complex pathophysiological mechanisms of absence seizure in epileptic children require a global approach of the interactions between neural synaptic and non-synaptic, vascular and metabolic systems. As a future work, we will focus on the interaction between synaptic and non-synaptic mechanisms through the simultaneous non-invasive multimodal

multiscale recordings of EEG and optical signal (NIRS, DCS), that evaluate the hemodynamic responses of absence seizure occurring in epileptic children.

To evaluate changes in hemodynamic responses in absence seizure area, six children with absence seizure were simultaneously recorded with EEG, NIRS and DCS. Figures 4 and 5 as initial results, illustrates how the seizure discharges with maximal amplitude in ictal areas induced a change in local hemodynamic parameters characterized by the first decrease in HbO, rCBF followed by an increase in HbO, rCBF and decrease in HbR.

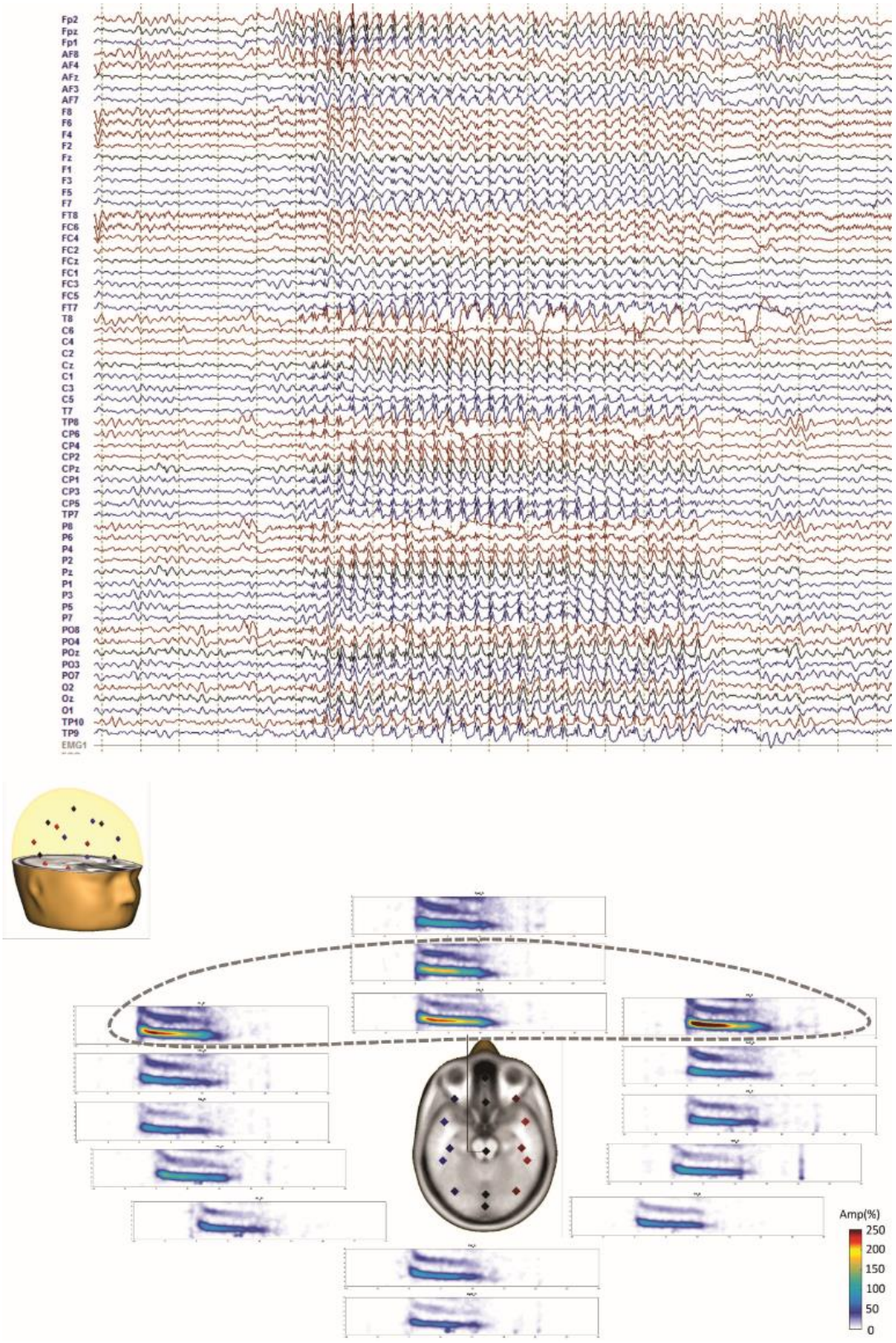

Fig. 4 *High-resolution EEG in a premature during the recording seizures.*

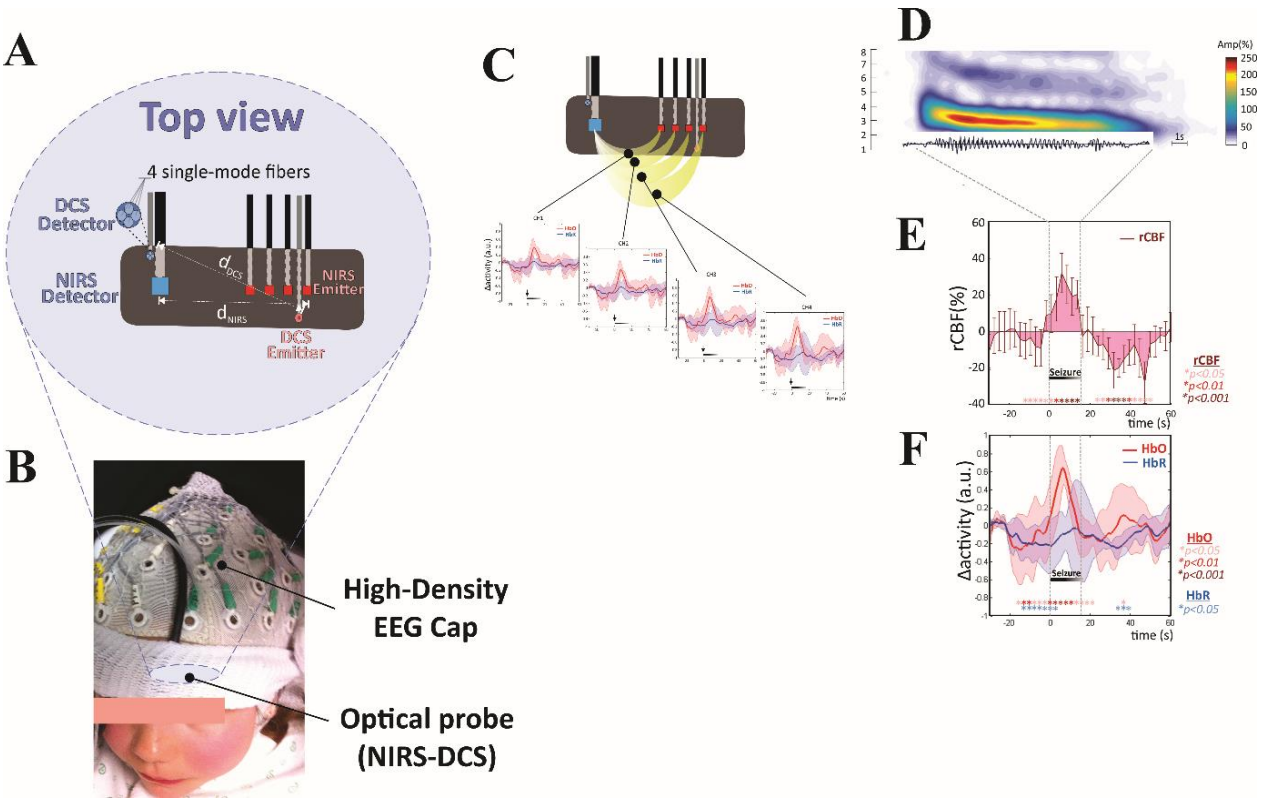

Fig. 5 *Optical probe (NIRS and DCS) (A), High-density EEG cap (B), four detectors of NIRS probe (C), Average changes in HbO, HbR, rCBF during seizures (D,E,F).*

CHAPTER

7 French Summary

7.1 Aperçu de la thèse

Le premier chapitre de cette thèse commence par une introduction générale. Je présente brièvement les différents chapitres de la thèse qui vise à évaluer le couplage neurovasculaire chez les nouveau-nés prématurés au repos grâce à une approche multimodale non-invasive qui combine l'évaluation de l'activité neuronale (EEG), de l'activité hémodynamique local (fNIRS-DCS) et de l'activité hémodynamique systémique (surveillance de la pression artérielle non invasive).

Chapitre 1: Introduction et contexte. Dans le chapitre 1, je précise les caractéristiques des composants neuronaux et vasculaires susceptibles d'être impliqués dans le couplage neurovasculaire et leur rôle dans la médiation des changements de flux sanguin. J'aborde les mécanismes de couplage neurovasculaire sous-jacent (aérobies et anaérobies). Puis je présente brièvement une revue du fonctionnement neuronale et vasculaire et cardiovasculaire fœtale. Enfin je décris certains aspects de la physiopathologie du canal artériel persistant er de l'hémorragie intraventriculaire, principales pathologies cérébrales néonatales.

Chapitre 2 : Matériel et méthodes. Au chapitre 2, je fournis une vue d'ensemble des systèmes d'imagerie multimodales qui ont été utilisés dans notre étude. Je décrits leurs principes sous-jacents. Ce chapitre contient une introduction méthodologique générale

concernant la spectroscopie proche infrarouge, la spectroscopie de corrélation de diffusion avec les bases mathématiques et physiques de la propagation des photons dans les tissus biologiques. Je présente les méthodes de calcul du taux de consommation cérébrale en oxygène (CMRO2), de la mesure et de l'estimation de la pression artérielle par le dispositif Finometer® (surveillance de la pression artérielle non invasive).

Chapitre 3: Impact thermique du laser dans le proche infrarouge dans l'imagerie cérébrale optique non invasive. Dans le chapitre 3, nous avons modélisé l'interaction photothermique du laser NIR d'imagerie optique sur les modèles de tête quasi réalistes néonataaux et adultes. Nous avons modélisé l'effet thermique de différentes puissances de laser avec différentes tailles de fibres et différentes caractéristiques de tissu de tête. Ceci a été réalisé par simulation numérique en développant une analyse par éléments finis. Les résultats du chapitre 3 peuvent permettre d'optimiser les paramètres des lasers pour une variété d'applications cliniques, notamment concernant les études menées sur le cerveau de l'adulte et du nouveau-né.

Chapitre 4 : Relation entre le débit sanguin cérébral relatif, le volume sanguin cérébral relatif et le taux de consommation cérébral d'oxygène (CMRO2) dans le cerveau néonatal prématuré. Dans le chapitre 4, la directivité et une relation causale ont été identifié par des mesures de transfert d'entropie concernant la relation entre la circulation sanguine cérébrale relative et le volume sanguin cérébral (rCBF-rCBV) ainsi qu'entre la circulation sanguine cérébrale relative et le taux *de consommation cérébral d'oxygène* (rCBF - rCMRO2) chez le prématuré à l'état de repos.. Ceci participe à une meilleure compréhension des principes de l'hémodynamique corticale au cours du développement.

Chapitre 5: Couplage neurovasculaire dans le cerveau néonatal en développement à l'état de repos. Le couplage entre l'activité physiologique neuronale spontanée et le profil hémodynamique chez les nourrissons prématurés à l'état de repos a été abordé en évaluant la désoxygénation, l'oxygénation, le débit sanguin cérébral, le volume sanguin cérébral et le métabolisme cérébral de l'oxygène. Ceci, permet de préciser les principes liant l'hémodynamique neuronale et l'activité électrique cérébrale corticale au cours du développement. L'aspect multifréquence du couplage neurovasculaire a été abordé par une analyse de cohérence par ondelettes, en comparant deux groupes normaux et pathologiques tout en s'attachant à préciser l'impact de l'âge gestationnel sur ces paramètres.

Chapitre 6: Conclusion et Perspective. Dans le dernier chapitre de cette thèse, le chapitre 6 résume les principales conclusions et envisage des perspectives pour de futures recherches.

7.2 Étude 1

Impact thermique du laser proche infrarouge dans l'imagerie cérébrale optique non invasive avancée

7.2.1 Objectif

Les systèmes d'imagerie optique conventionnels comprennent généralement certains composants de base tels que divers types de lasers et fibres optiques flexibles. Au cours des dernières décennies, des méthodes optiques ont été utilisées pour surveiller le fonctionnement du cerveau, le couplage neurovasculaire qui est corrélé avec l'activité cérébrale, l'hémodynamique cérébrale, le volume sanguin cérébral, et l'oxygénation. De telles modalités ont une large gamme d'applications pratiques d'imagerie chez les adultes et les nouveau-nés, en particulier chez les nouveau-nés prématurés, allant des changements d'oxygénation tissulaire (par spectroscopie proche infrarouge, NIRS) à la mesure du débit sanguin cérébral (DCS), aux changements dans la configuration de la membrane tels que le gonflement et le rétrécissement des neurones (Fast Optical Signal, FOS). L'impact photothermique des lasers est un paramètre critique qui doit être déterminé afin d'évaluer l'efficacité et la sécurité laser de ces systèmes, notamment avec une consommation d'énergie élevée. Le laser a des interactions photothermiques avec les tissus, provoquées par l'élévation de température due à l'irradiation laser, qui peut endommager les tissus, y compris en provoquant une dénaturation des protéines, une augmentation de la perméabilité de la membrane mitochondriale et finalement la vaporisation. Les augmentations de température peuvent également conduire à des changements dans le métabolisme cellulaire, la capacité de la membrane électrique et, à long terme, peuvent conduire à une nécrose. Cependant, les mécanismes responsables des dommages tissulaires causés par l'exposition à la chaleur sont complexes et encore mal compris.

Par conséquent, la propagation de l'énergie de la lumière laser à travers les tissus est donc une question importante en imagerie optique. L’imagerie optique fonctionnelle efficace est possible en adaptant les paramètres laser à des caractéristiques optiques du tissu cible (capacité thermique, conductivité thermique, coefficient d’absorption, coefficient de diffusion). Les paramètres du laser (ie énergie radiante, fréquence, taille du faisceaux, durée de l'impulsion) doivent être prudemment choisis afin d’optimiser l’efficacité de l’imagerie tout en minimisant

les dommages tissulaires indésirables. L'énergie délivrée aux tissus doit donc être déterminée afin d'assurer des normes de sécurité en imagerie optique. Les limites spécifiques de la puissance laser qui déterminent les effets néfastes de la chaleur sur le tissu néonatal sont mal élucidées. En raison de la spécificité des tissus de la tête néonatale, tels que la peau fine et le crâne, les coefficients d'absorption tissulaire peuvent être différents de ceux observés chez les adultes. Il est donc essentiel de tester la sécurité des lasers d'imagerie optiques dans cette population spécifique et sensible.

Le but de cette étude était de modéliser l'interaction photothermique du laser NIR sur les tissus humains. Nous avons étudié l'influence du taux de chaleur et la fluence de diverses puissances rayonnantes laser sur deux modèles (tête adulte vs. nouveau-né).

7.2.2 Matériel et Méthodes

Nous avons modélisé l'effet thermique de différentes puissances laser avec différentes tailles de faisceaux et différentes caractéristiques de tissu de tête sur des modèles de tête quasi-réalistes néonatals et adultes. L'effet photothermique de NIR-laser (800nm) a été étudié par simulation numérique en utilisant l'analyse par éléments finis. Deux modèles de têtes quasi-réalistes à six couches dans une coordonnée cartésienne (x, y, z) en 3D ont été simulés pour résoudre les équations de propagation de la lumière dans les tissus de tête néonatale et adulte, comme le montre la figure 1.

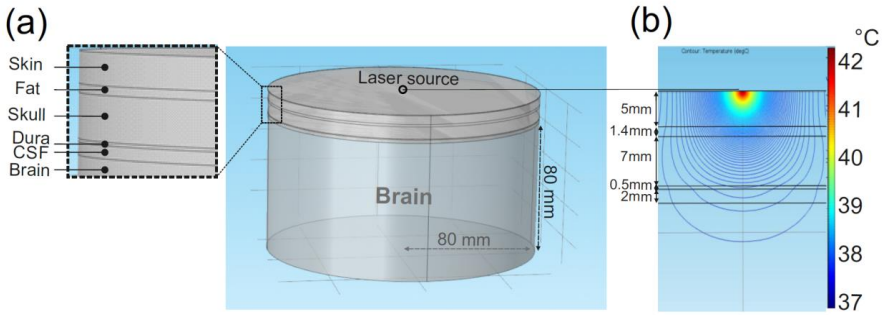

Fig. 1 *(a) Structure géométrique de la 3D-CAD composée de six couches (peau, graisse, crâne, dure-mère, LCR et cerveau) (l'encart montre une région zoomée). L'origine était située immédiatement sous la source. (b) Les distributions de la vitesse de photon-fluence dans la tête calculée dans le modèle de tête.*

La distribution de la température à l'intérieur du tissu a été modélisée en utilisant des simulations FEM et l'équation de transfert de chaleur biologique pour déterminer la fonction de température transitoire requise pour calculer l'interaction photothermique. Une gamme de différentes puissances laser (1mW-100mW) avec différentes tailles de faisceaux, les différents

coefficients d'absorption de la peau et du cerveau, les profils de distribution de la température chez les adultes par rapport aux nouveau-nés et l'influence de la perfusion sanguine ont été étudiés en utilisant le modèle simulé. L'irradiation laser a été simulée en utilisant la théorie de la diffusion et a été validée par comparaison avec la méthode de Monte-Carlo.

7.2.3 Résultats et conclusion

Nos résultats démontrent que l'augmentation de température maximale sur le cerveau, pour une irradiance laser entre 0.127W / cm ² (1mW) et 12.73W / cm ² (100mW) à une taille de faisceau de 1mm, variait de 0.0025 à 0.26°C et de 0.03 à 2,85°C à des profondeurs de 15,9 mm et 4,9 mm dans le cerveau adulte et néonatal, respectivement. En raison de la distance plus courte des couches de tissus de la tête par rapport à la surface, l'augmentation de la température maximale était plus élevée dans le cerveau néonatal que dans le cerveau adulte. Nos résultats montrent également que, à puissance constante, les changements de taille des faisceaux ont un effet moindre sur les tissus profonds.

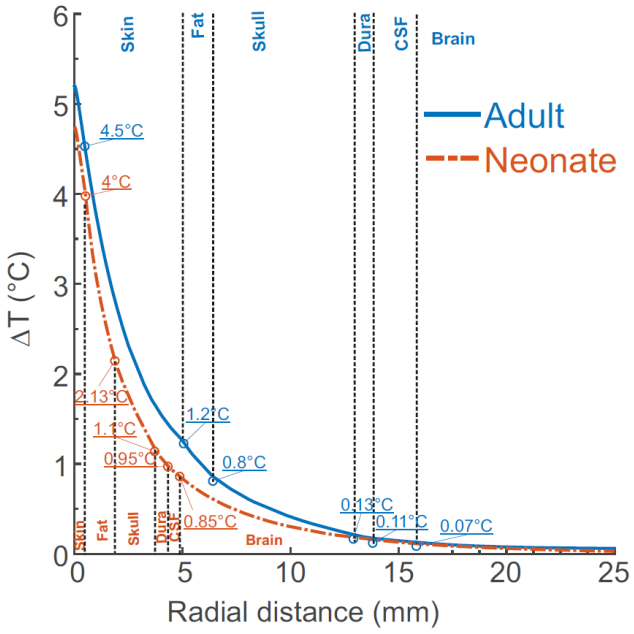

Fig. 2 *Variations de température en fonction de la distance radiale de la source laser (I = 3,81 W / cm 2) pour six couches de tête adulte et néonatale (peau, graisse, crâne, dure-mère, LCR et cerveau) obtenues à partir de simulations numériques.*

D'après notre étude bibliographique, ces résultats constituent la première étude à utiliser deux modèles quasi-réalistes (nouveau-né à six couches vs. Modèles de tête adulte) pour quantifier la distribution de température par modélisation de la diffusion bio-heat. En outre, malgré l'utilisation de modèles animaux, cette étude est la première à utiliser une approche FEA pour étudier l'influence de la chaleur et du taux de fluence de divers pouvoirs radiants laser sur les modèles humains (adulte et néonatal) tout en considérant la perfusion sanguine. Un modèle d'interaction laser-tissu a été développé pour prédire les changements dynamiques spatiaux dans l'augmentation de la température au cours de l'exposition au laser des tissus de la tête humaine. Nous décrivons les bases nécessaires pour calculer les effets des changements de température provoqués par l'absorption de l'énergie lumineuse dans les tissus, en utilisant l'équation de bio-heat et en incluant les effets de refroidissement du sang dans le tissu afin de modéliser l'interaction photothermique du laser NIR sur les tissus humains.

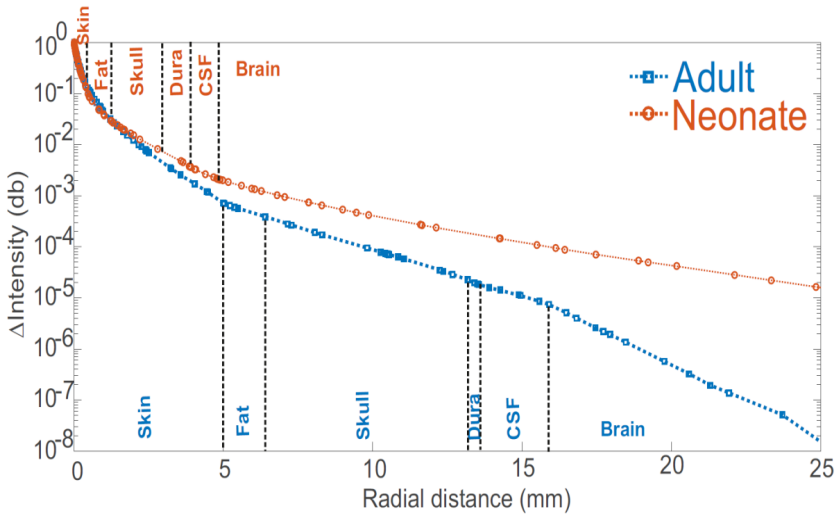

Fig. 3 *Distributions comparatives de l'intensité normalisée des photons (I / I 0) en fonction de la distance radiale de la source laser (I = 3,81 W / cm2) pour six couches de tête adulte (schéma inférieur) et néonatal (peau, graisse, crâne) , dura, CSF et cerveau) obtenus à partir de simulations numériques.*

Les variations de température de la zone impliquée calculées à partir de notre simulation et des expériences in vitro a présenté un petit écart. Deux des principales raisons de cet écart sont (i) le manque de valeurs précises des propriétés optiques des tissus et (ii) la théorie de l'approximation de la diffusion dans les surfaces superficielles. D'autres études dans différentes conditions sont nécessaires pour obtenir un accord complet avec les données in vivo et, si nécessaire, définir des facteurs de correction d'erreur à ajouter à l'ensemble des équations. Cependant, ceci n'élimine pas le besoin de valeurs précises pour caractériser les propriétés optiques et thermiques des différents tissus. Notre modèle introduit une étape dans l'utilisation

de tissus de tête simulés comme base pour des expériences d'interaction photothermique laser beaucoup plus détaillées. Les résultats présentés dans ce travail devraient être utiles pour optimiser la taille et la puissance des lasers pour diverses applications en imagerie laser fonctionnelle (ie. Spectroscopie à corrélation diffuse (DCS) nécessitant une lumière proche infrarouge (NIR) avec une puissance laser relativement élevée). Une combinaison de simulation et d'expériences in vitro adéquates pourrait aider à développer une imagerie optique plus efficace tout en s'affranchissant de toute lésion tissulaire.

7.3 Étude 2

Relation entre le débit sanguin cérébral relatif, le volume sanguin cérébral relatif et le taux métabolique cérébral relatif de l'oxygène dans le cerveau néonatal prématuré

7.3.1 Objectif

Le couplage entre débit sanguin cérébral (CBF), volume sanguin cérébral (CBV) et métabolisme cérébral de l'oxygène (CMRO2) est une fonction primaire importante de la microcirculation, car le cerveau a besoin d'un apport continu de glucose et d'oxygène (O2) par le CBF pour maintenir une teneur en oxygène du sang afin de répondre aux besoins en oxygène cellulaire. L'identification d'une relation causale entre le volume sanguin cérébral relatif (rCBV) et le débit sanguin cérébral relatif (rCBF) d'une part et d'autre part entre que le métabolisme cérébral relatif de l'oxygène (rCMRO2) et le débit sanguin cérébral relatif (rCBF) dans des conditions physiologiques au repos dans le cerveau néonatal pourrait concourir à élucider les principes de la fonction hémodynamique corticale au cours du développement.

Un couplage élevé entre les changements de CBF et de CBV a été démontré à la fois à l'état de repos et lors d'activations induites par un stimulus. Roy et Sherrington ont proposé l'hypothèse d'une augmentation du CBF induite par le stimulus, liée à une demande métabolique locale augmentée. Un couplage marqué entre CBF et CMRO2 est observée au cours de la stimulation neuronale chez l'adulte, mais un décalage dans le couplage CBF-métabolisme a été rapporté par Fox et al., qui ont décrit que, lors de l'activation neuronale, le débit sanguin cérébral régional (CBF) a augmenté de 50%, tandis que le CMRO2 n'augmentait que de seulement 5%. En fait, le CBF peut augmenter en l'absence de variations significatives de CMRO2, et inversement, le CMRO2 peut augmenter sans augmentation significative du CBF. La présence ou non d'un couplage précis entre CBF et CMRO2 au cours de la stimulation

neurale a fait l'objet de nombreuses études tant chez les adultes que chez les prématurés. Alors que la relation linéaire entre les changements de CBF et de CMRO2 à l'état de repos a été démontrée chez les adultes, elle reste un sujet de débat chez les prématurés. Cette étude a été conçue pour déterminer si les variations de rCBV conduisent à une modification de rCBF chez les prématurés ou *vice – versa*. Cette vise aussi à fournir des informations sur la directionnalité et la causalité entre les changements mesurés de rCBV et rCBF ainsi qu'entre rCMRO2 estimé et rCBF.

7.3.2 Matériel et méthodes

Nous avons simultanément enregistré rCBF et rCBV et rCMRO2 estimé par deux systèmes d'acquisition indépendants : la spectroscopie de corrélation diffuse (DCS) et la spectroscopie proche infrarouge (NIRS), respectivement, chez 10 prématurés âgés de 28 à 35 semaines d'âge gestationnel. Le calcul du transfert d'entropie a été utilisé afin de déterminer la directionnalité entre rCBF-rCBV et rCBF-rCMRO2. La méthode de substitution a été appliquée pour déterminer la signification statistique.

Nous avons utilisé la méthode de transfert d'entropie (TE) basée sur la théorie de l'information pour évaluer les interactions non linéaires entre rCBV-rCBF et rCBF-rCMRO2 chez les nourrissons prématurés au repos. Le transfert d'entropie détermine l'intensité et la direction de la relation de même que la dominance entre deux variables aléatoires discrètes (rCBF et rCMRO2). Basé sur le concept de causalité, nous avons étudié une éventuelle interaction causale entre rCBF et rCBV par analyse prédictive des séries temporelles de mesures de rCBF (ou rCBV) en incorporant des données d'une autre série chronologique de rCBV (ou rCBF).

La spectroscopie proche infrarouge (NIRS) et la spectroscopie de corrélation de diffusion (DCS) sont des techniques d'imagerie optique qui mesurent de manière non invasive, les paramètres vasculaires cérébraux au chevet des prématurés. Le dispositif NIRS permet de mesurer les changements relatifs ([HBT] ([HbO] + [Hb]) qui équivaut à des changements relatifs de CBV. Les variations relatives du CBF sont proportionnelles aux variations relatives du flux sanguin tissulaire liées au mouvement de globules rouges qui peuvent être mesurée par le dispositif de DCS.

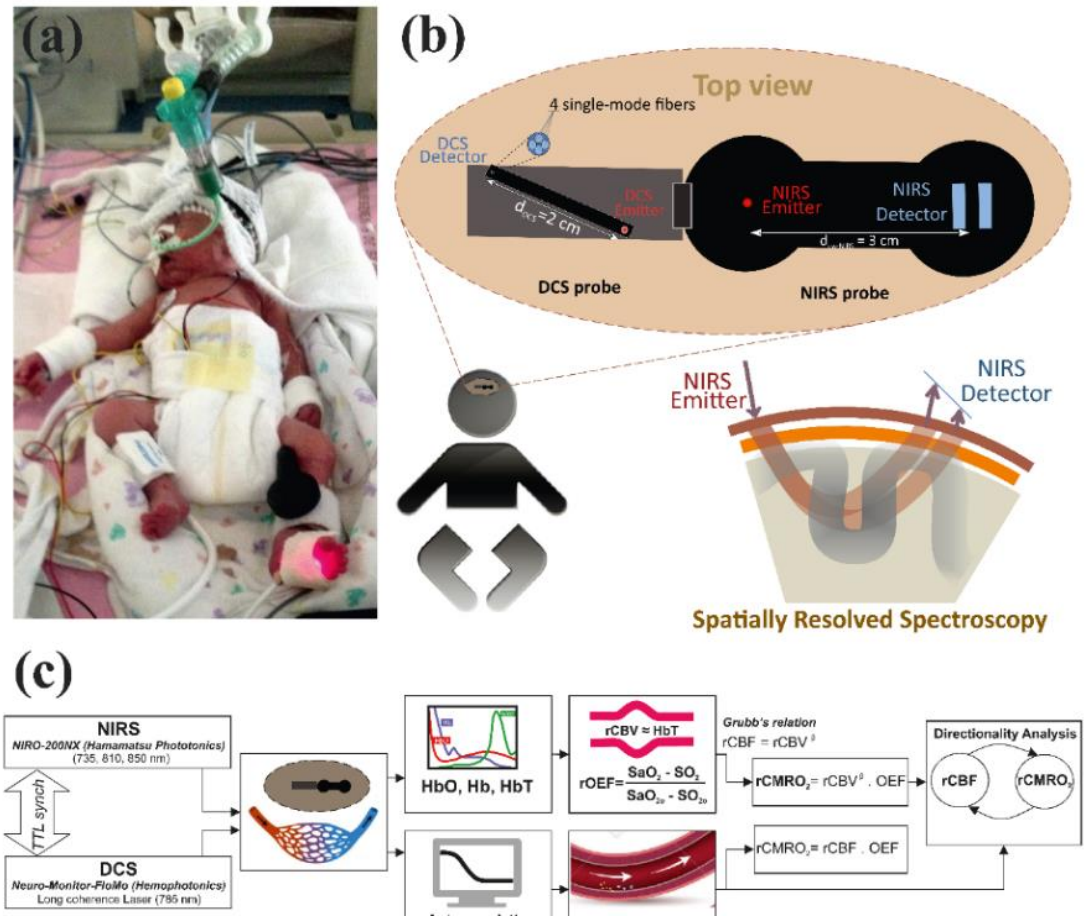

Fig. 4 *(a) Les nourrissons ont été testés avec les systèmes DCS et CW-NIRS, (b) D iagramme de la sonde DCS-NIRS combinée, (c) Diagramme du calcul de rCMRO 2 par les données NIRS et rCBF par les données DCS.*

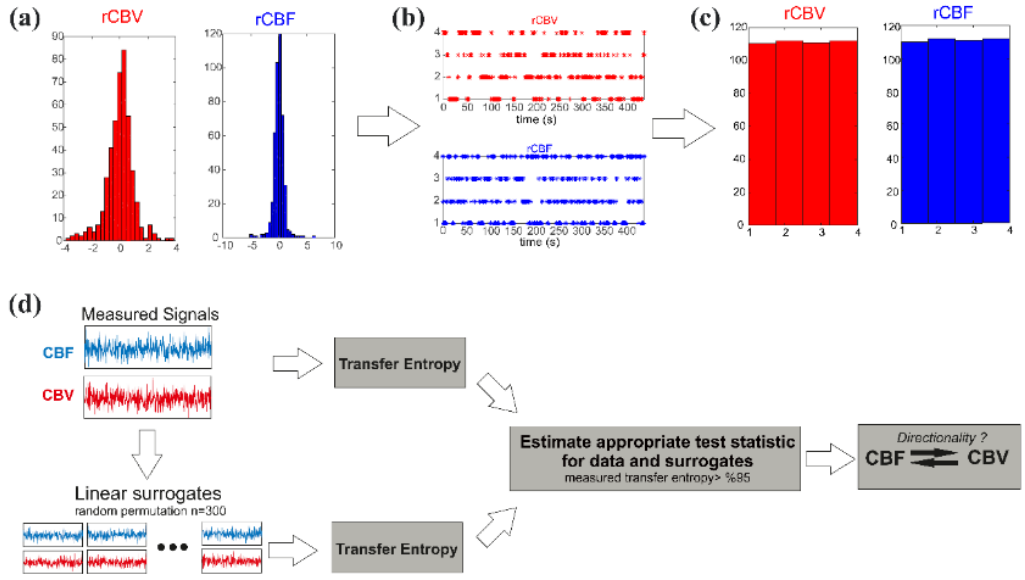

Fig. 5 *(a) Histogramme de distribution de rCBV et de rCBF , (b) les séries temporelles de rCBV et de rCBF exprimées en valeurs quantifiées pour produire des séries chronologiques avec des variables de probabilité identiques , c) Distribution à plat de rCBV et de rCBF , (ré) Diagramme de l'approche des données de substitution de l' hypothèse de couplage rCBF- rCBV .*

Le calcul du transfert d'entropie a été utilisé pour définir la force de la causalité et le couplage entre rCBV-rCBF et rCBF-rCMRO2. Le concept d'entropie est lié au degré d'incertitude associé à une variable de signal aléatoire (rCBF). En d'autres termes, il fournit une mesure de l'incertitude moyenne dans une variable aléatoire.

7.3.3 Résultats et conclusion

Les résultats montrent que rCBV et rCMRO2 ont une influence prédominante sur le rCBF à l'état de repos dans le cerveau néonatal du prématuré. L'analyse statistique a détecté de manière robuste la directivité correcte de rCBV sur rCBF et de rCMRO2 sur rCBF. Cette étude aide à clarifier l'organisation précoce de l'interrelation rCBV-rCBF et rCBF-rCMRO2 dans le cortex immature.

Cette relation peut être résumée par l'indice de directionalité (DI) entre rCBF et rCBV. Les valeurs négatives de l'indice de directionnalité (DI <0) suggèrent que le rCBV était prédominant par rapport au rCBF. L'analyse statistique avec une limite de confiance statistique

correspondant au 95ème percentile des 300 essais a été effectuée selon la méthode de substitution. Comme l'indice de directivité (DI) mesuré chez chacun des 10 sujets était plus élevé que le 95ème percentile, l'analyse statistique a détecté la direction correcte de rCBV sur rCBF. En appliquant la même analyse à la relation entre le rCBF et le rCMRO2, les valeurs négatives de DI <0 suggèrent que le rCMRO2 estimé serait prédominant par rapport au rCBF mesuré (Fig . 6).

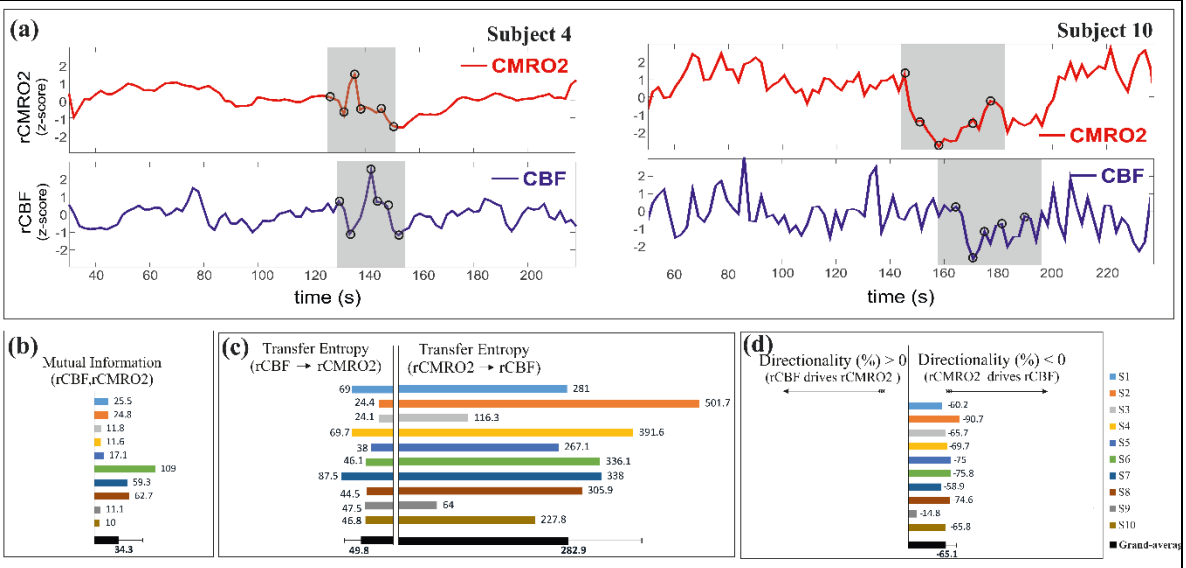

Fig. 6 *(a) Une partie sélectionnée de rCMRO 2 et rCBF (sujets # 4, # 10), illustrant l'évaluation de TE de rCMRO2 à rCBF, (b) Informations mutuelles partagées entre rCBF_rCMRO2 , (c) Taux d'information (TE) échangé de rCBF à rCMRO 2 et vice versa , (d) Indice de directionnalité (D). (* toutes les valeurs sont multipliées par 10 [3]).*

Les résultats actuels démontrent que, chez les nouveau-nés très prématurés (<32 SAG), le rCBV est prédominant par rapport au rCBF et que les interactions neurovasculaires semblent être suffisamment efficaces pour que le rCMRO2 soit déjà capable de conduire le rCBF au repos.

Cette étude a porté sur la relation non linéaire entre rCBF et rCBV (rCBF et rCMRO2) chez les nourrissons prématurés enregistrés avant 32 SAG . Les mécanismes par lesquels rCBV pilote rCBF (rCMRO2 pilote rCBF) sont déjà fonctionnels à cet âge précoce du développement, indépendamment de si oui ou non ces deux variables sont strictement corrélées. Comme la directionnalité a été observée chez tous les nourrissons prématurés indépendamment du type d'anesthésie, il serait intéressant de tester l'application de cette

technique dans la pratique clinique courante comme un indice potentiel de couplage neurovasculaire dans une plus grande population de prématurés à risque de lésion neuronale ou vasculaire cérébrale.

7.4 Étude 3

Couplage neurovasculaire dans le cerveau néonatal en développement au repos

7.4.1 Objectif

Les réseaux neuronaux et vasculaires constituent les deux moitiés de la même unité fonctionnelle reposant sur l'unité neurovasculaire qui couple étroitement le débit sanguin régional en réponse aux demandes métaboliques locales connues sous le nom de couplage neurovasculaire (NVC) bien caractérisé chez les adultes par une augmentation du flux sanguin dans réponse à l'activation neuronale. L'équilibre entre la consommation locale et l'apport artériel lié à l'activation neuronale est beaucoup plus délicat dans le cerveau en développement et comment ce NVC est affecté par des troubles métaboliques et vasculaires particuliers dans le cerveau immature est cliniquement pertinent par rapport aux conséquences neurodéveloppementales de son dysfonctionnement.

Structurellement, au cours du dernier trimestre de la gestation humaine, le système neuronal et le système vasculaire subissent encore des développements drastiques. Les processus de migration neuronale, synaptogenèse, courte et longue-connectivité, la mort cellulaire, la différenciation dendritique des neurones, la maturation neurochimique et la myélinisation construisent progressivement les réseaux de neurones, fournissant au prématurée une double innervation des cellules pyramidales par la sous-plaque et les axones thalamiques. En parallèle, le système vasculaire est également immature et fragile. La question de savoir si ce réseau immature est capable de répondre aux demandes métaboliques par une augmentation du débit sanguin chez les nouveau-nés prématurés au repos n'est pas complètement élucidée.

Fonctionnellement, la maturation du réseau neuronal néonatal est associée à des caractéristiques transitoires dépendant de l'âge, des activités mixtes de haute amplitude et des patterns discontinus reflétant l'interaction entre générateurs transitoires endogènes de la sous-plaque et de la plaque corticale, générateurs endogènes et exogènes liés au monde extérieur. Les bouffées d'activités EEG spontanées, le tracé discontinu constituent des événements discernables et offrent l'opportunité de monitorer de manière non invasive et passive, les réponses hémodynamiques à l'activation corticale endogène chez les nouveau-nés prématurés, en évitant une stimulation exogène.

L'adaptation du réseau vasculaire immature à l'activation neuronale est encore un sujet de discussion. Des études fNIRS et IRMf chez des animaux ont suggéré qu'il se développe après la naissance. En revanche, chez les nouveau-nés prématurés, nous avons observé un couplage neurovasculaire à partir de 28 SAG, en réponse à des bouffés endogènes spontanées ou à des stimulations exogènes de phonèmes ou de voix. Chez les adultes, la réponse du réseau vasculaire est bien établie comme un couplage neurovasculaire positif. Chez les populations immatures, prématurés par exemple, une augmentation-diminution du débit sanguin ou du volume sanguin a été décrite en réponse à une stimulation exogène chez les nouveau-nés ou les animaux prématurés soulignant une variabilité inter-étude, inter-sujets, et même une variabilité régionale intra-sujet dans le développement précoce du couplage neurovasculaire.

7.4.2 Matériel et Méthodes

Afin de mieux caractériser la dynamique du réseau vasculaire au repos par rapport à l'activité neuronale spontanée, deux approches sont considéré. La première approche est classique et considère le NVC en réponse à une activation neuronale. Pour cela, nous avons saisi l'opportunité des bouffées spontanés dans l'activité corticale discontinue de la prématurité pour déclencher l'analyse de la réponse hémodynamique. Pour mieux explorer les différents types de réponses hémodynamiques (direction des changements de [HbO] et [HbR], circulation sanguine cérébrale et oxygénation cérébrale) , une approche multimodale, multi-échelles simultanée, combinant

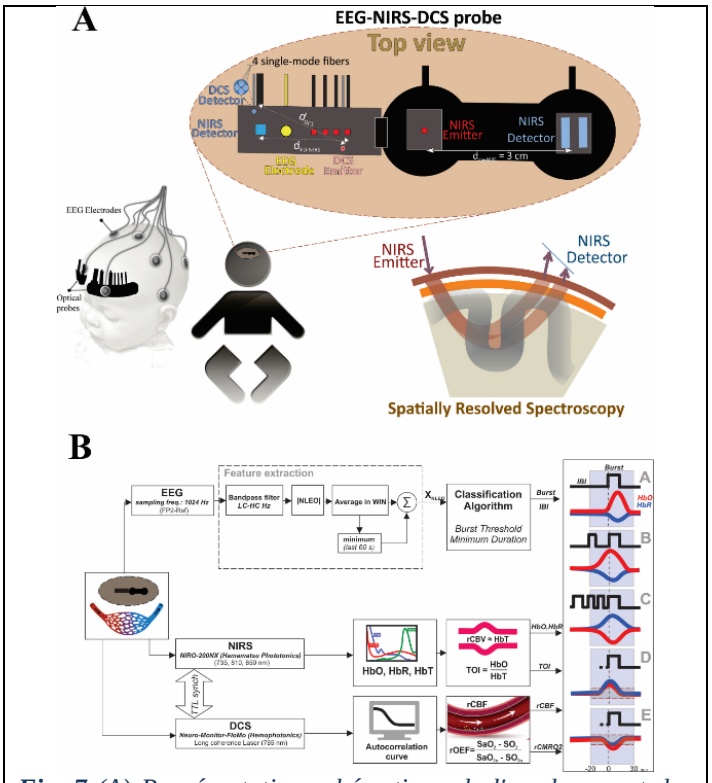

Fig. 7 *(A) Représentation schématique de l'emplacement des sondes EEG et optiques sur la tête d'un nourrisson. (UP) (B). Diagramme des réponses hémodynamiques (HbO , HbR, calculé HbT et TOI par les données NIRS, rCBF par les données DCS et le calcul de rCMRO2 par des données NIRS) et présentation schématique de l'algorithme. | NLEO | appliqué sur le signal EEG, la classification des réponses hémodynamiques aux salves EEG.*

l'électroencéphalographie (EEG) avec la spectroscopie de corrélation de diffusion (DCS) et la spectroscopie proche infrarouge fonctionnelle à ondes continues et dans le domaine fréquentiel (CW et FD) (fNIRS) et associant un monitoring de la pression sanguine artérielle au chevet du patient a été développé. Une autre approche, consiste a examiner les interactions entre les oscillations spontanées de l'activité neuronale et les dynamiques du compartiment vasculaire dans le domaine fréquentiel. Cette approche a été appliquée à nos données multi-échelles multimodales en utilisant la méthode d'analyse par ondelettes qui s'était avérée adéquate chez les nouveau-nés pour fournir des arguments concourant à discerner les nouveau-nés sains des nouveau-nés avec encéphalopathie anoxique. La méthode a également été appliquée à un sous-groupe de patients présentant un canal artériel persistant pour tester la validité de la méthode dans les situations où l'autorégulation est considérée comme altérée.

7.4.3 **Résultats et conclusion**

Réponses hémodynamiques aux bouffées d'activités cérébrales chez les nouveau-nés prématurés :

4 types de réponses ont été observés. Elels consistaient soit en une réponse de type CBF avec un changement positif / négatif de CBF (Conditions A1, A2, et A3) ou une réponse de type CBV avec un changement positif / négatif de CBV (Conditions B et C). Les réponses les plus fréquentes ont été observées dans l'état A au cours de laquelle la réponse hémodynamique CBF consistait en des changements opposés de HbO et HbR. Les états A1 et A2 étaient également plus fréquents avec un couplage neurovasculaire positif et une augmentation du CBF.

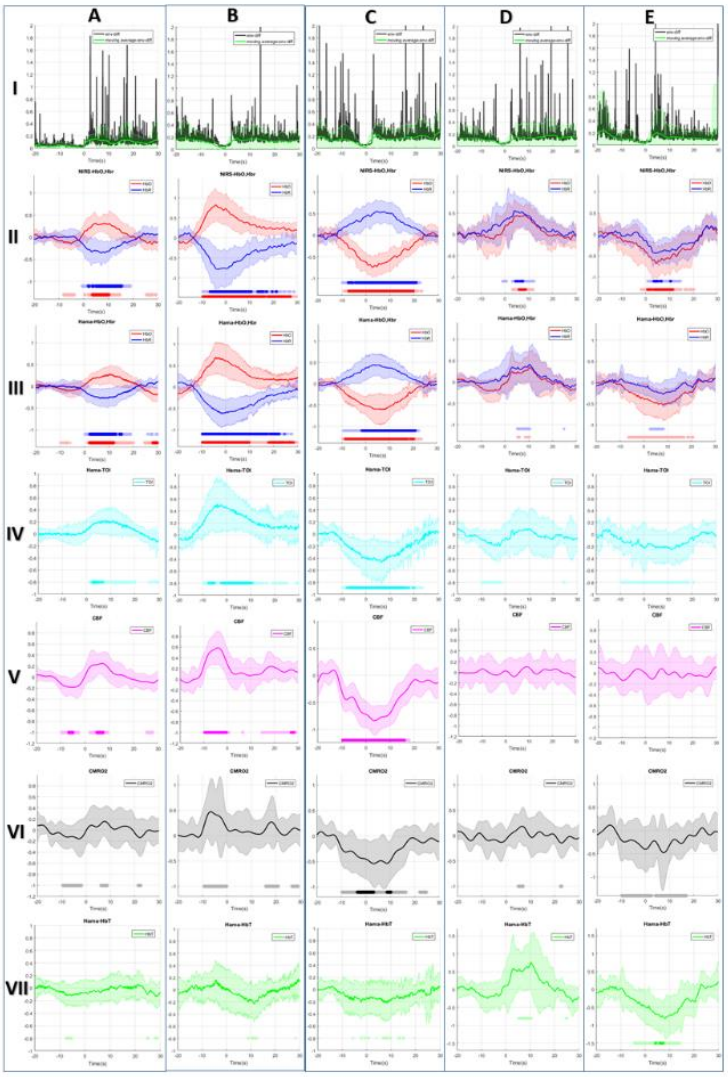

Fig. 8 *La grande moyenne des réponses hémodynamiques régionales de l'apparition des éclats d'EEG à 0s (la durée a été montrée 20s avant et 30s après le début de l'éclatement de l'EEG, les 10 premiers ont été définis comme ligne de base). Les panneaux longitudinaux indiquent la dérivée de l'EEG et la moyenne mobile des sursauts EEG globaux dérivés de l'enveloppe chez un sujet (I), la moyenne des changements de HbO_HbR mesurée par ISS (II), la moyenne des changements de HbO_HbR mesurés par Hamamatsu (III), la moyenne générale des changements dans TOI (IV), CBF (V) et CMRO2 (VI). Les panneaux verticaux liés à la classification de la rafale d'activités, sans éclats EEG au cours des années 20 précédentes* ***(A)****, une rafale EEG pendant les 20 premières* ***(B)****, deux éclats EEG pendant les 20 premiers* ***(C)*** *et les panneaux verticaux (D et E) liés à l'explosion des activités qui accompagnent avec une augmentation de HbO_HbR* ***(D)*** *et une diminution des deux HbO_HbR* ***(E)****. Les annotations ci - dessous le signal mettant en évidence les temps de réponse hémodynamique durée étaient significativement différents de la période de référence (- 20 à -10s), étoiles légères liées à (test t, p <0,001) et les étoiles sombres liées à (test t, p <1,1e-6). Les barres d'erreur ombrées indiquent les écarts-types pour les signaux correspondants à chaque point de temps.*

La cohérence significative de phase entre l'amplitude du paramètre hémodynamique et l'amplitude de la salve EEG a été réalisée par une analyse de cohérence par ondelettes. L'analyse de cohérence basée sur les ondelettes a d'abord été calculée chez un nouveau - né prématuré sains, sur une période de 25-30 minutes équivalente à une très-basse fréquence (VLF) (0,003 à 0,125 Hz) puis ensuite comparé aux résultats obtenus chez le prématuré avec un canal artériel persistant (Fig. 9).

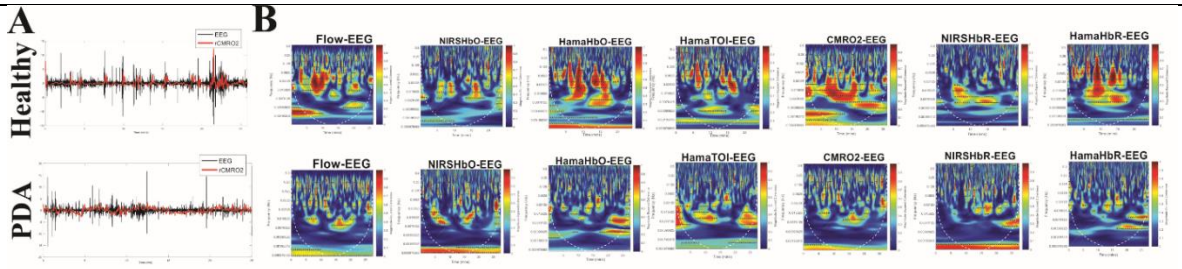

Fig. 9 *(A) Un segment agrandi des données CMRO2 et EEG en temps réel d'un échantillon de nouveau-né prématuré sain # 15 (UP); dans un échantillon de nouveau-nés prématurés avec le brevet ductus arteriosus # 28 (Down). (B) les réponses hémodynamiques à base d'ondelettes cohérence (CBF-EEG, CMRO2-EEG, HbO -EEG, HBr-EEG, TOI-EEG) montre un couplage neurovasculaire intact (NVC)*

Cette étude démontre que,

(1) L'ctivité des bouffées neuronales physiologiques spontanées de nouveau-nés prématurés (<35 SAG) au repos est couplée à différents types de réponses hémodynamiques :

a. Réponses NIRS positives (augmentation de HbO, diminution de HbR avec augmentation de CBF et CMRO2),

b. Réponses NIRS négatives (augmentation de HbR, diminution de HbO avec diminution de CBF et CMRO2),

c. Augmentation et diminution à la fois de HbO-HbR et de CMRO2, sans modification du CBF.

(2) Ces différents types de réponses hémodynamiques aux bouffées EEG se sont produits de manière similaire chez les patients pathologiques et sains, mais la cohérence dynamique entre les réponses hémodynamiques et les bouffées EEG pour évaluer le NVC est plus faible chez les nouveau-nés avec PDA et HIV que chez les sujets sains.

(3) Les mesures en ondelettes de NVC dans le cerveau néonatal dépendent de l'âge, ce qui suggère que la trajectoire développementale des réponses hémodynamiques dans le cerveau postnatal reflète, au moins en partie, le développement progressif du couplage neurovasculaire.

Cette étude décrit les différentes formes de réponse hémodynamique cérébrale aux bouffées d'activités cérébrales spontanées au repos chez les nouveau-nés prématurés. Cela pourrait être lié à l'immaturité des réseaux neuronaux et vasculaires ainsi qu'à l'immaturité des mécanismes cellulaires du couplage neurovasculaire. Cette étude confirme et décrit plus précisément le NVC anormale non seulement dans les HIV mais aussi dans les PDA au repos. L'amplitude du NVC spontanée est décrite comme étant dépendante de l'âge au repos.

Cette approche multi-échelle, non-invasive multimodale du couplage neurovasculaire en réponse aux bouffées d'activités cérébrales spontanées chez le prématurée permet d'étudier le NVC dans les deux dimensions neuronale et vasculaire qui constituent en fait le même système fonctionnel neurovasculaire. Cette approche non invasive pourrait être permettre de tester sur une plus grande population de prématuré sa capacité à distinguer les pathologies vasculaires et neuronales et donc facilité l'identification des enfants à risque.

7.5 Conclusions générales et perspectives

Plusieurs progrès dans la technologie de neuroimagerie ont largement développé la recherche dans le domaine de la compréhension du couplage neurovasculaire. La neuroimagerie, et notamment «l'imagerie neurovasculaire», peut être considéré comme à l'intersection de différents domaines. Le couplage neurovasculaire est essentiel pour fournir les besoins en énergie du tissu cérébral pendant la fonction physiologique normale et dans les conditions pathologiques. Ainsi, les progrès dans les techniques d'imagerie fonctionnelle ont amélioré notre compréhension de la relation entre l'activité cérébrale et l'apport d'énergie dans le cerveau en développement. Alors qu'au début de l'imagerie cérébrale, chaque méthode d'imagerie cérébrale était utilisée séparément, de plus en plus d'études en recherche comme en clinique soulignent l'intérêt de combiner ces différentes techniques d'imagerie.

Chaque chapitre de cette thèse décrit une combinaison de techniques appliquées aux nouveau-nés prématurés dans un cerveau sain ou pathologique. Il est utile que la plupart de ces approches puissent être adaptées à une variété de situations pour mesurer différents aspects du couplage neurovasculaire dans les états cérébraux normaux et pathologiques.

Cette thèse a donc présenté un cadre à partir duquel un groupe d'études complémentaires pourrait être réalisé car les approches misent en place dans cette thèse peuvent s'appliquer à d'autres espèces d'autres zones du cortex ou d'autres conditions pathologiques. Ce qu'il faut souigner, c'est l'importance croissante et la puissance des approches optiques dans l'investigation du couplage neurovasculaire. De plus, la nature non invasive des approches optiques les rend adéquates dans les unités de soins intensifs néonatales. Dans cette thèse, plusieurs techniques ont été combinées afin de mesurer les signaux provenant de sources multiples, non seulement hémodynamiques mais aussi neuronales. La combinaison de plusieurs approches de manière simultanée nous permet de tirer des conclusions sur la dynamique du couplage entre ces différentes sources de signaux. Dans nos données, il est clair

que le découplage neurovasculaire peut être spécifique aux états cérébraux pathologiques. Ce chapitre passe en revue les objectifs et les contributions présentés dans cette thèse. Enfin, je rends compte des perspectives futures de cette thèse.

Dans cette thèse, une approche multimodale hybride EEG-NIRS-DCS a été utilisée pour mesurer les activités electro-hémodynamique du cerveau néonatal chez le prématuré au repos (Fig.10). Les différences de réponses fonctionnelles correspondent à l'immaturité du NVC, Le processus complexe de développement du NVC continue de se produire au cours de développement, ce qui incite à considérer le rôle de ce système en développement dans les pathologies neurodéveloppementales. Des perturbations ou des retards du NVC pourraient ainsi conduire à des anomalies dans le développement neuronal et vasculaire. Ceci pourrait avoir un impact profond sur le développement des circuits neuronaux. Il est donc nécessaire de mieux comprendre l'état métabolique optimal du cerveau périnatal. Les données sur l'état de repos du cerveau immature sont plus difficiles à interpréter que les réponses évoquées par un stimulus. Notre travail de thèse démontre la directionnalité de ces fluctuations lentes dans l'activité neuronale et hémodynamique. LeNVC peut être positif, négatif ou absent dans le cerveau du prématuré en réponse à une bouffée d'activité spontanée. Les principales réalisations de cette thèse ont été résumées sur la Fig. 10.

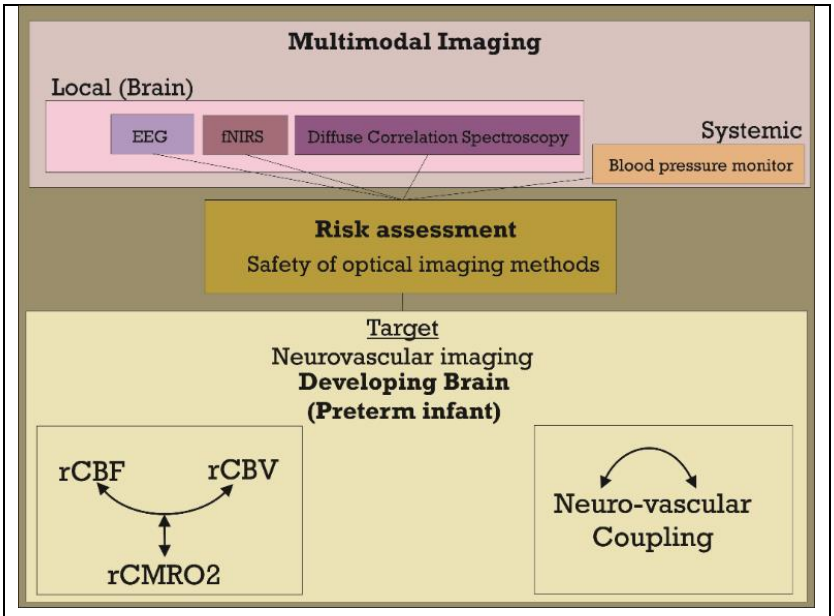

Fig. 10 *aperçu de la thèse.*

7.6 La perspective

Cette thèse fournit un aperçu d'une variété de techniques actuellement disponibles pour étudier le couplage neurovasculaire chez les nouveau-nés sains et pathologiques. La compréhension du couplage neurovasculaire normale en relation avec les fonctions sensorielles et les fonctions d'ordre supérieur comme la mémoire et le langage sera essentielle dans le

développement des techniques de neuroimagerie. De même, le développement de ces approches pour participer au diagnostic de certaines maladies exigera une complète compréhension des mécanismes de couplage neurovasculaire pour permettre l'interprétation précise des signaux hémodynamiques corticaux comme indicateur de l'activité neuronale.

Une compréhension globale de la relation de couplage neurovasculaire nécessite la mesure simultanée des réponses neuronales et vasculaires. La valeur de cette approche est la capacité de mesurer l'hémodynamique à travers un crâne intact, qui fournit des mesures non invasives chez l'homme à des fins de diagnostic et clinique et qui ouvre de nouvelles perspectives sur l'étiologie des troubles du neurodéveloppement.

References

2006. COMSOL Multiphysics 3.2b User's Guide. FEMLAB Tutorial.

A. G. Yodh, D.A.B., 2003. Biomedical Photonics chapter Functional Imaging with Diffusing Light.

A. Yodh, B.C., 1995. Spectroscopy and imaging with diffusing light., 34–40

Aaslid, R., Lindegaard, K.F., Sorteberg, W., Nornes, H., 1989. Cerebral autoregulation dynamics in humans. Stroke 20, 45-52.

Ackerman RH, L.M., Mackay BC, 1989. PET studies in acute stroke: Findings and relevance to therapy. . Cereb Blood Flow Metab.

Ackman, J.B., Burbridge, T.J., Crair, M.C., 2012. Retinal waves coordinate patterned activity throughout the developing visual system. Nature 490, 219-225.

Alawadhi, E., 2010. Finite element simulation using ANSYS. London: CRC Press Taylor & Francis Group. (page 186, different types of boundary conditions).

Albers, C.A., Grieve, A.J., 2007. Test Review: Bayley, N. (2006). Bayley Scales of Infant and Toddler Development– Third Edition. San Antonio, TX: Harcourt Assessment. Journal of Psychoeducational Assessment 25, 180-190.

Alderliesten, T., Lemmers, P.M., Smarius, J.J., van de Vosse, R.E., Baerts, W., van Bel, F., 2013. Cerebral oxygenation, extraction, and autoregulation in very preterm infants who develop peri-intraventricular hemorrhage. J Pediatr 162, 698-704 e692.

Allen, C.L., Bayraktutan, U., 2009. Oxidative stress and its role in the pathogenesis of ischaemic stroke. Int J Stroke 4, 461-470.

Allievi, A.G., Arichi, T., Tusor, N., Kimpton, J., Arulkumaran, S., Counsell, S.J., Edwards, A.D., Burdet, E., 2016. Maturation of Sensori-Motor Functional Responses in the Preterm Brain. Cereb Cortex 26, 402-413.

Altman, D.I., Powers, W.J., Perlman, J.M., Herscovitch, P., Volpe, S.L., Volpe, J.J., 1988. Cerebral blood flow requirement for brain viability in newborn infants is lower than in adults. Ann Neurol 24, 218-226.

Amin, H., Marinaro, F., 2017. Developmental excitatory-to-inhibitory GABA-polarity switch is disrupted in 22q11.2 deletion syndrome: a potential target for clinical therapeutics. 7, 15752.

Anderson, A.W., Marois, R., Colson, E.R., Peterson, B.S., Duncan, C.C., Ehrenkranz, R.A., Schneider, K.C., Gore, J.C., Ment, L.R., 2001. Neonatal auditory activation detected by functional magnetic resonance imaging. Magn Reson Imaging 19, 1-5.

ANSI, 2014. The American National Standards Institute

Arichi, T., Fagiolo, G., Varela, M., Melendez-Calderon, A., Allievi, A., Merchant, N., Tusor, N., Counsell, S.J., Burdet, E., Beckmann, C.F., Edwards, A.D., 2012. Development of BOLD signal hemodynamic responses in the human brain. Neuroimage 63, 663-673.

Arichi, T., Moraux, A., Melendez, A., Doria, V., Groppo, M., Merchant, N., Combs, S., Burdet, E., Larkman, D.J., Counsell, S.J., Beckmann, C.F., Edwards, A.D., 2010. Somatosensory cortical activation identified by functional MRI in preterm and term infants. Neuroimage 49, 2063-2071.

Arkin, H., Xu, L.X., Holmes, K.R., 1994. Recent developments in modeling heat transfer in blood perfused tissues. IEEE Trans Biomed Eng 41, 97-107.

Armulik, A., Abramsson, A., Betsholtz, C., 2005. Endothelial/pericyte interactions. Circ Res 97, 512-523.

Attwell, D., Buchan, A.M., Charpak, S., Lauritzen, M., Macvicar, B.A., Newman, E.A., 2010. Glial and neuronal control of brain blood flow. Nature 468, 232-243.

Attwell, D., Iadecola, C., 2002. The neural basis of functional brain imaging signals. Trends Neurosci 25, 621-625.

Attwell, D., Laughlin, S.B., 2001. An energy budget for signaling in the grey matter of the brain. J Cereb Blood Flow Metab 21, 1133-1145.

Azevedo, F.A., Carvalho, L.R., Grinberg, L.T., Farfel, J.M., Ferretti, R.E., Leite, R.E., Jacob Filho, W., Lent, R., Herculano-Houzel, S., 2009. Equal numbers of neuronal and nonneuronal cells make the human brain an isometrically scaled-up primate brain. J Comp Neurol 513, 532-541.

Bamett, A.H., Culver, J.P., Sorensen, A.G., Dale, A., Boas, D.A., 2003. Robust inference of baseline optical properties of the human head with three-dimensional segmentation from magnetic resonance imaging. Appl Opt 42, 3095-3108.

Baron JC, S.Y., Pantano P, 1987. Inter relationships of local CBF, OEF and CMRO2 in ischemic areas with variable outcome: further PET studies in humans. Cereb Blood Flow Metab.

Basar, E., Basar-Eroglu, C., Karakas, S., Schurmann, M., 2001. Gamma, alpha, delta, and theta oscillations govern cognitive processes. Int J Psychophysiol 39, 241-248.

Baumgartner, R.W., 2006. Handbook on Neurovascular Ultrasound. Karger.

Baylen, B.G., Ogata, H., Ikegami, M., Jacobs, H.C., Jobe, A.H., Emmanouilides, G.C., 1983. Left ventricular performance and regional blood flows before and after ductus arteriosus occlusion in premature lambs treated with surfactant. Circulation 67, 837-843.

Bekar, L.K., Wei, H.S., Nedergaard, M., 2012. The locus coeruleus-norepinephrine network optimizes coupling of cerebral blood volume with oxygen demand. J Cereb Blood Flow Metab 32, 2135-2145.

Ben-Ari, Y., 2014. The GABA excitatory/inhibitory developmental sequence: a personal journey. Neuroscience 279, 187-219.

Bernardi, P., Cavagnaro, M., Pisa, S., Piuzzi, E., 2000. Specific absorption rate and temperature increases in the head of a cellular-phone user. Microwave Theory and Techniques, IEEE Transactions on 48, 1118-1126.

Biagioni, E., Frisone, M.F., Laroche, S., Rutherford, M., Counsell, S., Cioni, G., Azzopardi, D., Mercuri, E., Cowan, F., 2000. Occipital sawtooth: a physiological EEG pattern in very premature infants. Clin Neurophysiol 111, 2145-2149.

Bianco, M., Nardini, Tamburrino, 2008. A Numerical Model for Transient Heat Conduction in Semi-Infinite Solids Irradiated by a Moving Heat Source. Excerpt from the Proceedings of the COMSOL Conference Hannover.

Binmoller, F.J., Muller, C.M., 1992. Postnatal development of dye-coupling among astrocytes in rat visual cortex. Glia 6, 127-137.

Biswal, B., Yetkin, F.Z., Haughton, V.M., Hyde, J.S., 1995. Functional connectivity in the motor cortex of resting human brain using echo-planar MRI. Magn Reson Med 34, 537-541.

Boas, D.A., Campbell, L.E., Yodh, A.G., 1995a. Scattering and Imaging with Diffusing Temporal Field Correlations. Phys Rev Lett 75, 1855-1858.

Boas, D.A., Campbell, L.E., Yodh, A.G., 1995b. Scattering and Imaging with Diffusing Temporal Field Correlations. Phys Rev Lett 75, 1855-1858.

Boas, D.A., Jones, S.R., Devor, A., Huppert, T.J., Dale, A.M., 2008. A vascular anatomical network model of the spatio-temporal response to brain activation. Neuroimage 40, 1116-1129.

Boas, D.A., Payne, S.J., 2009. Comment on 'Estimating a modified Grubb's exponent in healthy human brains with near infrared spectroscopy and transcranial Doppler'. Physiol Meas 30, L9-L11; author reply L13-L14.

Boas, D.A., Yodh, A.G., 1997. Spatially varying dynamical properties of turbid media probed with diffusing temporal light correlation. Journal of the Optical Society of America A 14, 192-215.

Booth, R.F., Patel, T.B., Clark, J.B., 1980. The development of enzymes of energy metabolism in the brain of a precocial (guinea pig) and non-precocial (rat) species. J Neurochem 34, 17-25.

Born, A.P., Miranda, M.J., Rostrup, E., Toft, P.B., Peitersen, B., Larsson, H.B., Lou, H.C., 2000. Functional magnetic resonance imaging of the normal and abnormal visual system in early life. Neuropediatrics 31, 24-32.

Bouissou, A., Rakza, T., Klosowski, S., Tourneux, P., Vanderborght, M., Storme, L., 2008. Hypotension in preterm infants with significant patent ductus arteriosus: effects of dopamine. J Pediatr 153, 790-794.

Bourel-Ponchel, E., Mahmoudzadeh, M., Delignières, A., Berquin, P., Wallois, F., 2017. Non-invasive, multimodal analysis of cortical activity, blood volume and neurovascular coupling in infantile spasms using EEG-fNIRS monitoring. NeuroImage : Clinical 15, 359-366.

Bourgeois, J.P., Jastreboff, P.J., Rakic, P., 1989. Synaptogenesis in visual cortex of normal and preterm monkeys: evidence for intrinsic regulation of synaptic overproduction. Proc Natl Acad Sci U S A 86, 4297-4301.

Bozkurt, A., Onaral, B., 2004. Safety assessment of near infrared light emitting diodes for diffuse optical measurements. Biomed Eng Online 3, 9.

Buxton, R.B., Frank, L.R., 1997. A model for the coupling between cerebral blood flow and oxygen metabolism during neural stimulation. J Cereb Blood Flow Metab 17, 64-72.

Buxton, R.B., Uludag, K., Dubowitz, D.J., Liu, T.T., 2004. Modeling the hemodynamic response to brain activation. Neuroimage 23 Suppl 1, S220-233.

Buxton, R.B., Wong, E.C., Frank, L.R., 1998. Dynamics of blood flow and oxygenation changes during brain activation: the balloon model. Magn Reson Med 39, 855-864.

Buzsaki, G., Anastassiou, C.A., Koch, C., 2012. The origin of extracellular fields and currents--EEG, ECoG, LFP and spikes. Nat Rev Neurosci 13, 407-420.

Cauli, B., Hamel, E., 2010. Revisiting the role of neurons in neurovascular coupling. Front Neuroenergetics 2, 9.

Cauli, B., Tong, X.K., Rancillac, A., Serluca, N., Lambolez, B., Rossier, J., Hamel, E., 2004. Cortical GABA interneurons in neurovascular coupling: relays for subcortical vasoactive pathways. J Neurosci 24, 8940-8949.

Chang, C., Glover, G.H., 2010. Time-frequency dynamics of resting-state brain connectivity measured with fMRI. Neuroimage 50, 81-98.

Charkoudian, N., 2010. Mechanisms and modifiers of reflex induced cutaneous vasodilation and vasoconstriction in humans. J Appl Physiol (1985) 109, 1221-1228.

Chorobski, J., Penfield, W., 1932. Cerebral vasodilator nerves and their pathway from the medulla oblongata: With observations on the pial and intracerebral vascular plexus. Archives of Neurology & Psychiatry 28, 1257-1289.

Clyman, R., Noori, S., 2012. Chapter 13 - The Very Low Birth Weight Neonate with Hemodynamically Significant Ductus Arteriosus During the First Postnatal Week A2 - Kleinman, Charles S. In: Seri, I. (Ed.), Hemodynamics and Cardiology: Neonatology Questions and Controversies (Second Edition). W.B. Saunders, Philadelphia, pp. 269-291.

Cohen, B.M., Yurgelun-Todd, D., English, C.D., Renshaw, P.F., 1995. Abnormalities of regional distribution of cerebral vasculature in schizophrenia detected by dynamic susceptibility contrast MRI. Am J Psychiatry 152, 1801-1803.

Colonnese, M.T., Kaminska, A., Minlebaev, M., Milh, M., Bloem, B., Lescure, S., Moriette, G., Chiron, C., Ben-Ari, Y., Khazipov, R., 2010. A conserved switch in sensory processing prepares developing neocortex for vision. Neuron 67, 480-498.

Colonnese, M.T., Phillips, M.A., Constantine-Paton, M., Kaila, K., Jasanoff, A., 2007. Development of hemodynamic responses and functional connectivity in rat somatosensory cortex. Nat Neurosci 11, 72.

Colonnese, M.T., Phillips, M.A., Constantine-Paton, M., Kaila, K., Jasanoff, A., 2008. Development of hemodynamic responses and functional connectivity in rat somatosensory cortex. Nat Neurosci 11, 72-79.

Cope, M., Delpy, D.T., 1988. System for long-term measurement of cerebral blood and tissue oxygenation on newborn infants by near infra-red transillumination. Med Biol Eng Comput 26, 289-294.

Cordes, D., Haughton, V.M., Arfanakis, K., Wendt, G.J., Turski, P.A., Moritz, C.H., Quigley, M.A., Meyerand, M.E., 2000. Mapping functionally related regions of brain with functional connectivity MR imaging. AJNR Am J Neuroradiol 21, 1636-1644.

Crone, C., 1963. THE PERMEABILITY OF CAPILLARIES IN VARIOUS ORGANS AS DETERMINED BY USE OF THE 'INDICATOR DIFFUSION' METHOD. Acta Physiol Scand 58, 292-305.

Crook, J.M., Kisvarday, Z.F., Eysel, U.T., 1998. Evidence for a contribution of lateral inhibition to orientation tuning and direction selectivity in cat visual cortex: reversible inactivation of functionally characterized sites combined with neuroanatomical tracing techniques. Eur J Neurosci 10, 2056-2075.

Culver, J.P., Durduran, T., Furuya, D., Cheung, C., Greenberg, J.H., Yodh, A.G., 2003. Diffuse optical tomography of cerebral blood flow, oxygenation, and metabolism in rat during focal ischemia. J Cereb Blood Flow Metab 23, 911-924.

Davis, T.L., Kwong, K.K., Weisskoff, R.M., Rosen, B.R., 1998. Calibrated functional MRI: mapping the dynamics of oxidative metabolism. Proc Natl Acad Sci U S A 95, 1834-1839.

de Alarcón, P.A., Werner, E.J., 2005. Neonatal Hematology. Cambridge University Press.

de Graaf-Peters, V.B., Hadders-Algra, M., 2006. Ontogeny of the human central nervous system: what is happening when? Early Hum Dev 82, 257-266.

Dehaes, M., Aggarwal, A., Lin, P.Y., Rosa Fortuno, C., Fenoglio, A., Roche-Labarbe, N., Soul, J.S., Franceschini, M.A., Grant, P.E., 2014. Cerebral oxygen metabolism in neonatal hypoxic ischemic encephalopathy during and after therapeutic hypothermia. J Cereb Blood Flow Metab 34, 87-94.

DeMarco, S.C., Lazzi, G., Wentai, L., Weiland, J.D., Humayun, M.S., 2003. Computed SAR and thermal elevation in a 0.25-mm 2-D model of the human eye and head in response to an implanted retinal stimulator - part I: models and methods. Antennas and Propagation, IEEE Transactions on 51, 2274-2285.

Denda, M., Tsutsumi, M., Denda, S., 2010. Topical application of TRPM8 agonists accelerates skin permeability barrier recovery and reduces epidermal proliferation induced by barrier insult: role of cold-sensitive TRP receptors in epidermal permeability barrier homoeostasis. Exp Dermatol 19, 791-795.

Devor, A., Dunn, A.K., Andermann, M.L., Ulbert, I., Boas, D.A., Dale, A.M., 2003. Coupling of total hemoglobin concentration, oxygenation, and neural activity in rat somatosensory cortex. Neuron 39, 353-359.

Devor, A., Hillman, E.M., Tian, P., Waeber, C., Teng, I.C., Ruvinskaya, L., Shalinsky, M.H., Zhu, H., Haslinger, R.H., Narayanan, S.N., Ulbert, I., Dunn, A.K., Lo, E.H., Rosen, B.R., Dale, A.M., Kleinfeld, D., Boas, D.A., 2008. Stimulus-induced changes in blood flow and 2-deoxyglucose uptake dissociate in ipsilateral somatosensory cortex. J Neurosci 28, 14347-14357.

Dewey, W.C., Hopwood, L.E., Sapareto, S.A., Gerweck, L.E., 1977. Cellular responses to combinations of hyperthermia and radiation. Radiology 123, 463-474.

Diaz-Flores, L., Gutierrez, R., Varela, H., Rancel, N., Valladares, F., 1991. Microvascular pericytes: a review of their morphological and functional characteristics. Histol Histopathol 6, 269-286.

du Plessis, A.J., 2009a. The Role of Systemic Hemodynamic Disturbances in Prematurity-Related Brain Injury. Journal of child neurology 24, 1127-1140.

du Plessis, A.J., 2009b. The role of systemic hemodynamic disturbances in prematurity-related brain injury. J Child Neurol 24, 1127-1140.

Dua, R., Chakraborty, S., 2005. A novel modeling and simulation technique of photo--thermal interactions between lasers and living biological tissues undergoing multiple changes in phase. Comput Biol Med 35, 447-462.

Duarte, F.J., 2008. Tunable Laser Applications, Second Edition. CRC Press, pp. pp. 245-280.

Duarte, F.J., Hillman, L.W., Liao, P.F., Kelley, P., 2012. Dye Laser Principles: With Applications. Elsevier Science.

Duck, F.A., 2013. Physical Properties of Tissues: A Comprehensive Reference Book. Elsevier Science.

Durduran, T., Choe, R., Baker, W.B., Yodh, A.G., 2010a. Diffuse Optics for Tissue Monitoring and Tomography. Rep Prog Phys 73.

Durduran, T., Choe, R., Baker, W.B., Yodh, A.G., 2010b. Diffuse Optics for Tissue Monitoring and Tomography. Reports on progress in physics. Physical Society (Great Britain) 73, 076701.

Durduran, T., Choe, R., Baker, W.B., Yodh, A.G., 2010c. Diffuse optics for tissue monitoring and tomography. Reports on Progress in Physics 73, 076701.

Durduran, T., Yodh, A.G., 2014. Diffuse correlation spectroscopy for non-invasive, micro-vascular cerebral blood flow measurement. Neuroimage 85, 51-63.

Durduran, T., Zhou, C., Buckley, E.M., Kim, M.N., Yu, G., Choe, R., Gaynor, J.W., Spray, T.L., Durning, S.M., Mason, S.E., Montenegro, L.M., Nicolson, S.C., Zimmerman, R.A., Putt, M.E., Wang, J., Greenberg, J.H., Detre, J.A., Yodh, A.G., Licht, D.J., 2010d. Optical measurement of cerebral hemodynamics and oxygen metabolism in neonates with congenital heart defects. J Biomed Opt 15, 037004.

Duvernoy, H.M., Delon, S., Vannson, J.L., 1981. Cortical blood vessels of the human brain. Brain Res Bull 7, 519-579.

Edwards, A.D., Wyatt, J.S., Richardson, C., Delpy, D.T., Cope, M., Reynolds, E.O., 1988. Cotside measurement of cerebral blood flow in ill newborn infants by near infrared spectroscopy. Lancet 2, 770-771.

Ehrenfeld, J.M., Cannesson, M., 2013. Monitoring Technologies in Acute Care Environments: A Comprehensive Guide to Patient Monitoring Technology. Springer New York.

Elwell, C.E., Henty, J.R., Leung, T.S., Austin, T., Meek, J.H., Delpy, D.T., Wyatt, J.S., 2005. Measurement of CMRO2 in neonates undergoing intensive care using near infrared spectroscopy. Adv Exp Med Biol 566, 263-268.

Erberich, S.G., Panigrahy, A., Friedlich, P., Seri, I., Nelson, M.D., Gilles, F., 2006. Somatosensory lateralization in the newborn brain. Neuroimage 29, 155-161.

F. E. W. Schmit, M.E.F., E. M. C. Hillman, J. C. Hebden, and D. T. Delpy, 1998. A 32-channel time-resolved instrument for medical optical tomography.

Fantini, S., Sassaroli, A., Tgavalekos, K.T., Kornbluth, J., 2016. Cerebral blood flow and autoregulation: current measurement techniques and prospects for noninvasive optical methods. Neurophotonics 3, 031411.

Farkas, E., Luiten, P.G., 2001. Cerebral microvascular pathology in aging and Alzheimer's disease. Prog Neurobiol 64, 575-611.

Farrell, T.J., Patterson, M.S., 2001. Experimental verification of the effect of refractive index mismatch on the light fluence in a turbid medium. J Biomed Opt 6, 468-473.

Feller, M.B., 1999. Spontaneous correlated activity in developing neural circuits. Neuron 22, 653-656.

Fernandez-Klett, F., Offenhauser, N., Dirnagl, U., Priller, J., Lindauer, U., 2010. Pericytes in capillaries are contractile in vivo, but arterioles mediate functional hyperemia in the mouse brain. Proc Natl Acad Sci U S A 107, 22290-22295.

Ferrari, M., Quaresima, V., 2012. A brief review on the history of human functional near-infrared spectroscopy (fNIRS) development and fields of application. Neuroimage 63, 921-935.

Ferry, P.C., 1987. Neurological assessment during the first year of life. American Journal of Diseases of Children 141, 689-689.

Filosa, J.A., Bonev, A.D., Straub, S.V., Meredith, A.L., Wilkerson, M.K., Aldrich, R.W., Nelson, M.T., 2006. Local potassium signaling couples neuronal activity to vasodilation in the brain. Nat Neurosci 9, 1397-1403.

Flynn, P.A., da Graca, R.L., Auld, P.A., Nesin, M., Kleinman, C.S., 2005. The use of a bedside assay for plasma B-type natriuretic peptide as a biomarker in the management of patent ductus arteriosus in premature neonates. J Pediatr 147, 38-42.

Fox, M.D., Raichle, M.E., 2007. Spontaneous fluctuations in brain activity observed with functional magnetic resonance imaging. Nat Rev Neurosci 8, 700-711.

Fox, P.T., Raichle, M.E., 1986. Focal physiological uncoupling of cerebral blood flow and oxidative metabolism during somatosensory stimulation in human subjects. Proc Natl Acad Sci U S A 83, 1140-1144.

Franceschini, M.A., Thaker, S., Themelis, G., Krishnamoorthy, K.K., Bortfeld, H., Diamond, S.G., Boas, D.A., Arvin, K., Grant, P.E., 2007. Assessment of infant brain development with frequency-domain near-infrared spectroscopy. Pediatr Res 61, 546-551.

Fujii, T., Ibata, Y., 1982. Effects of heating on electrical activities of guinea pig olfactory cortical slices. Pflugers Arch 392, 257-260.

Fujimoto, K., 1995. Pericyte-endothelial gap junctions in developing rat cerebral capillaries: a fine structural study. Anat Rec 242, 562-565.

Fujita, H., Kuwabara, H., Reutens, D.C., Gjedde, A., 1999. Oxygen consumption of cerebral cortex fails to increase during continued vibrotactile stimulation. J Cereb Blood Flow Metab 19, 266-271.

Ganguly, M., 2012. Analyzing Thermal and Mechanical Effects of Pulsed Laser Irradiation on Tissues. Biomedical Department. Florida Institute of Technology.

Gelfand, M.V., Hong, S., Gu, C., 2009. Guidance from above: common cues direct distinct signaling outcomes in vascular and neural patterning. Trends Cell Biol 19, 99-110.

Genina, É.A., Bashkatov, A.N., Kochubey, V.I., Tuchin, V.V., 2005. Optical clearing of human dura mater. Optics and Spectroscopy 98, 470-476.

Glickman, R.D., 2002. Phototoxicity to the retina: mechanisms of damage. Int J Toxicol 21, 473-490.

Gobin, L., Blanchot, L., Saint-Jalmes, H., 1999. Integrating the digitized backscattered image to measure absorption and reduced-scattering coefficients in vivo. Appl Opt 38, 4217-4227.

Goldman-Rakic, P.S., Brown, R.M., 1982. Postnatal development of monoamine content and synthesis in the cerebral cortex of rhesus monkeys. Brain Res 256, 339-349.

Goldman, L., 1990. Dye laser principles: with applications. In: Duarte, F.J., Hillman, L.W. (Eds.), Dye laser principles. Academic Press, New York.

Gordon, G.R., Choi, H.B., Rungta, R.L., Ellis-Davies, G.C., MacVicar, B.A., 2008. Brain metabolism dictates the polarity of astrocyte control over arterioles. Nature 456, 745-749.

Gordon, R.G., Roemer, R.B., Horvath, S.M., 1976. A mathematical model of the human temperature regulatory system--transient cold exposure response. IEEE Trans Biomed Eng 23, 434-444.

Gourevitch, B., Eggermont, J.J., 2007. Evaluating information transfer between auditory cortical neurons. J Neurophysiol 97, 2533-2543.

Greisen, G., 1986. Cerebral blood flow in preterm infants during the first week of life. Acta Paediatr Scand 75, 43-51.

Greisen, G., 2009. To autoregulate or not to autoregulate--that is no longer the question. Semin Pediatr Neurol 16, 207-215.

Greisen, G., 2012. Chapter 2 - Autoregulation of Vital and Nonvital Organ Blood Flow in the Preterm and Term Neonate A2 - Kleinman, Charles S. In: Seri, I. (Ed.), Hemodynamics and Cardiology: Neonatology Questions and Controversies (Second Edition). W.B. Saunders, Philadelphia, pp. 29-47.

Greisen, G., Trojaborg, W., 1987. Cerebral blood flow, PaCO2 changes, and visual evoked potentials in mechanically ventilated, preterm infants. Acta Paediatr Scand 76, 394-400.

Grinsted, A., Moore, J. C. Jevrejeva, S., 2004. Application of the cross wavelet transform and wavelet coherence to geophysical time series. Nonlinear Proc Geoph, 561–566.

GRUBB, R.L., RAICHLE, M.E., EICHLING, J.O., TER-POGOSSIAN, M.M., 1974a. The Effects of Changes in PaCO₂ Cerebral Blood Volume, Blood Flow, and Vascular Mean Transit Time . Stroke 5, 630-639.

GRUBB, R.L., RAICHLE, M.E., EICHLING, J.O., TER-POGOSSIAN, M.M., 1974b. The Effects of Changes in PaCO₂ Cerebral Blood Volume, Blood Flow, and Vascular Mean Transit Time. Stroke 5, 630-639.

H. Khodabakhshi, A.C., 2010. Irradiation of a Six-Layered Spherical Model of Human Head in the Near Field of a Half-Wave Dipole Antenna. Microwave Theory and Techniques, IEEE Transactions 58, 680-690

Hahn, J.S., 2012. Chapter 4 - Neonatal and Pediatric Electroencephalography A2 - Aminoff, Michael J. Aminoff's Electrodiagnosis in Clinical Neurology (Sixth Edition). W.B. Saunders, London, pp. 85-128.

Hall, C.N., Reynell, C., Gesslein, B., Hamilton, N.B., Mishra, A., Sutherland, B.A., O'Farrell, F.M., Buchan, A.M., Lauritzen, M., Attwell, D., 2014. Capillary pericytes regulate cerebral blood flow in health and disease. Nature 508, 55-60.

Hampson, M., Peterson, B.S., Skudlarski, P., Gatenby, J.C., Gore, J.C., 2002. Detection of functional connectivity using temporal correlations in MR images. Hum Brain Mapp 15, 247-262.

Handwerker, D.A., Ollinger, J.M., D'Esposito, M., 2004. Variation of BOLD hemodynamic responses across subjects and brain regions and their effects on statistical analyses. Neuroimage 21, 1639-1651.

Harder, D.R., Narayanan, J., Gebremedhin, D., 2011. Pressure-induced myogenic tone and role of 20-HETE in mediating autoregulation of cerebral blood flow. Am J Physiol Heart Circ Physiol 300, H1557-1565.

Harris, J.J., Reynell, C., Attwell, D., 2011. The physiology of developmental changes in BOLD functional imaging signals. Dev Cogn Neurosci 1, 199-216.

Hayakawa, M., Okumura, A., Hayakawa, F., Watanabe, K., Ohshiro, M., Kato, Y., Takahashi, R., Tauchi, N., 2001. Background electroencephalographic (EEG) activities of very preterm infants born at less than 27 weeks gestation: a study on the degree of continuity. Arch Dis Child Fetal Neonatal Ed 84, F163-167.

Heep, A., Scheef, L., Jankowski, J., Born, M., Zimmermann, N., Sival, D., Bos, A., Gieseke, J., Bartmann, P., Schild, H., Boecker, H., 2009. Functional magnetic resonance imaging of the sensorimotor system in preterm infants. Pediatrics 123, 294-300.

Henderson, R., Schulmeister, K., 2003. Laser Safety. Taylor & Francis.

Herculano-Houzel, S., 2009. The human brain in numbers: a linearly scaled-up primate brain. Frontiers in Human Neuroscience 3.

Herken, R., Gotz, W., Wattjes, K.H., 1989. Initial development of capillaries in the neuroepithelium of the mouse. J Anat 164, 85-92.

Herkenham, M., 1980. Laminar organization of thalamic projections to the rat neocortex. Science 207, 532-535.

Hill, A.V., 1913. The Combinations of Haemoglobin with Oxygen and with Carbon Monoxide. I. Biochem J 7, 471-480.

Hoge, R.D., Franceschini, M.A., Covolan, R.J., Huppert, T., Mandeville, J.B., Boas, D.A., 2005. Simultaneous recording of task-induced changes in blood oxygenation, volume, and flow using diffuse optical imaging and arterial spin-labeling MRI. Neuroimage 25, 701-707.

Hoshi, Y., Kobayashi, N., Tamura, M., 2001. Interpretation of near-infrared spectroscopy signals: a study with a newly developed perfused rat brain model. J Appl Physiol (1985) 90, 1657-1662.

Hoshi, Y., Kosaka, S., Xie, Y., Kohri, S., Tamura, M., 1998. Relationship between fluctuations in the cerebral hemoglobin oxygenation state and neuronal activity under resting conditions in man. Neurosci Lett 245, 147-150.

Hoshi, Y., Tamura, M., 1993. Dynamic multichannel near-infrared optical imaging of human brain activity. J Appl Physiol (1985) 75, 1842-1846.

Huber, L., Goense, J., Kennerley, A.J., Ivanov, D., Krieger, S.N., Lepsien, J., Trampel, R., Turner, R., Moller, H.E., 2014. Investigation of the neurovascular coupling in positive and negative BOLD responses in human brain at 7 T. Neuroimage 97, 349-362.

Hughson, R.L., Edwards, M.R., O'Leary, D.D., Shoemaker, J.K., 2001. Critical analysis of cerebrovascular autoregulation during repeated head-up tilt. Stroke 32, 2403-2408.

Hutchinson, E.B., Stefanovic, B., Koretsky, A.P., Silva, A.C., 2006. Spatial flow-volume dissociation of the cerebral microcirculatory response to mild hypercapnia. Neuroimage 32, 520-530.

Huttenlocher, P.R., Dabholkar, A.S., 1997. Regional differences in synaptogenesis in human cerebral cortex. J Comp Neurol 387, 167-178.

Huttenlocher, P.R., de Courten, C., Garey, L.J., Van der Loos, H., 1982. Synaptogenesis in human visual cortex--evidence for synapse elimination during normal development. Neurosci Lett 33, 247-252.

Iadecola, C., Li, J., Xu, S., Yang, G., 1996. Neural mechanisms of blood flow regulation during synaptic activity in cerebellar cortex. J Neurophysiol 75, 940-950.

ICNIRP, 2013. International Commission on Non-Ionizing Radiation Protection. ICNIRP Guidelines on limits of exposure to laser radiation of wavelengths between 180nm and 1000mm. Health Phys 105:271–295. (page -288).

Ignarro, L.J., Cirino, G., Casini, A., Napoli, C., 1999. Nitric oxide as a signaling molecule in the vascular system: an overview. J Cardiovasc Pharmacol 34, 879-886.

Institute, A.N.S., 2014. American National Standard for Safe Use of Lasers ANSI Z136.1. Orlando, FL: Laser Institute of America.

Ito, H., Kanno, I., Ibaraki, M., Hatazawa, J., Miura, S., 2003. Changes in human cerebral blood flow and cerebral blood volume during hypercapnia and hypocapnia measured by positron emission tomography. J Cereb Blood Flow Metab 23, 665-670.

Ito, Y., Kennan, R.P., Watanabe, E., Koizumi, H., 2000. Assessment of heating effects in skin during continuous wave near infrared spectroscopy. J Biomed Opt 5, 383-390.

Iwata, S., Tachtsidis, I., Takashima, S., Matsuishi, T., Robertson, N.J., Iwata, O., 2014. Dual role of cerebral blood flow in regional brain temperature control in the healthy newborn infant. Int J Dev Neurosci 37, 1-7.

Izzetoglu, K., Bunce, S., Izzetoglu, M., Onaral, B., Pourrezaei, K., 2004. Functional near-infrared neuroimaging. Conf Proc IEEE Eng Med Biol Soc 7, 5333-5336.

Jacques, S.L., 2013. Optical properties of biological tissues: a review. Phys Med Biol 58, R37-61.

Jain, V., Buckley, E.M., Licht, D.J., Lynch, J.M., Schwab, P.J., Naim, M.Y., Lavin, N.A., Nicolson, S.C., Montenegro, L.M., Yodh, A.G., Wehrli, F.W., 2014. Cerebral oxygen metabolism in neonates with congenital heart disease quantified by MRI and optics. J Cereb Blood Flow Metab 34, 380-388.

Jasdzewski, G., Strangman, G., Wagner, J., Kwong, K.K., Poldrack, R.A., Boas, D.A., 2003. Differences in the hemodynamic response to event-related motor and visual paradigms as measured by near-infrared spectroscopy. Neuroimage 20, 479-488.

Jeong, S.w., Liu, H., Chen, W.R., 2003a. Temperature control in deep tumor treatment. Saratov Fall Meeting 2002 Laser Physics and Photonics, Spectroscopy, and Molecular Modeling III; Coherent Optics of Ordered and Random Media III. SPIE, p. 7.

Jeong, S.w., Liu, H., Chen, W.R., 2003b. Temperature control in deep tumor treatment. pp. 210-216.

Jim, W.T., Chiu, N.C., Chen, M.R., Hung, H.Y., Kao, H.A., Hsu, C.H., Chang, J.H., 2005. Cerebral hemodynamic change and intraventricular hemorrhage in very low birth weight infants with patent ductus arteriosus. Ultrasound Med Biol 31, 197-202.

Jobsis, F.F., 1977. Noninvasive, infrared monitoring of cerebral and myocardial oxygen sufficiency and circulatory parameters. Science 198, 1264-1267.

Johnson, A., 2000. Cerebral palsies: epidemiology and causal pathways. Arch Dis Child 83, 279-279.

Jones, M., Berwick, J., Johnston, D., Mayhew, J., 2001. Concurrent optical imaging spectroscopy and laser-Doppler flowmetry: the relationship between blood flow, oxygenation, and volume in rodent barrel cortex. Neuroimage 13, 1002-1015.

Jones, M., Berwick, J., Mayhew, J., 2002. Changes in blood flow, oxygenation, and volume following extended stimulation of rodent barrel cortex. Neuroimage 15, 474-487.

K.H. Wesseling, B.d.W., G.M.A. van der Hoeven, J. van Goudoever, J.J. Settels 1995. Physiocal, calibrating finger vascular physiology for finapres Homeostasis in health and disease : international journal devoted to integrative brain functions and homeostatic systems, 36, 67-82

Kanold, P.O., Luhmann, H.J., 2010. The subplate and early cortical circuits. Annu Rev Neurosci 33, 23-48.

Kato, T., Kamei, A., Takashima, S., Ozaki, T., 1993. Human visual cortical function during photic stimulation monitoring by means of near-infrared spectroscopy. J Cereb Blood Flow Metab 13, 516-520.

Kauppinen, R.A., Vidyasagar, R., Childs, C., Balanos, G.M., Hiltunen, Y., 2008. Assessment of human brain temperature by 1H MRS during visual stimulation and hypercapnia. NMR Biomed 21, 388-395.

Keijzer, M., Jacques, S.L., Prahl, S.A., Welch, A.J., 1989. Light distributions in artery tissue: Monte Carlo simulations for finite-diameter laser beams. Lasers Surg Med 9, 148-154.

Kellaway, 2003. Orderly approach to visual analysis: Elements of the normal eeg, and their characteristics in children and adults. In: Ebersole JS, Pedley TA, editors. Current Practice of Clinical Electroencephalography. Philadelphia: Lippincott Williams & Wilkins. . 100-159.

Kenshalo, D.R., Scott, H.A., Jr., 1966. Temporal course of thermal adaptation. Science 151, 1095-1096.

Khodabakhshi, H., Cheldavi, A., 2010. Irradiation of a Six-Layered Spherical Model of Human Head in the Near Field of a Half-Wave Dipole Antenna. Microwave Theory and Techniques, IEEE Transactions on 58, 680-690.

Kida, I., Rothman, D.L., Hyder, F., 2007. Dynamics of changes in blood flow, volume, and oxygenation: implications for dynamic functional magnetic resonance imaging calibration. J Cereb Blood Flow Metab 27, 690-696.

Kiguchi, M., Ichikawa, N., Atsumori, H., Kawaguchi, F., Sato, H., Maki, A., Koizumi, H., 2007. Comparison of light intensity on the brain surface due to laser exposure during optical topography and solar irradiation. J Biomed Opt 12, 062108.

Kim, J.H., Hahn, E.W., Antich, P.P., 1982. Radiofrequency hyperthermia for clinical cancer therapy. Natl Cancer Inst Monogr 61, 339-342.

Kim, S., Jeong, S., 2014. Effects of temperature-dependent optical properties on the fluence rate and temperature of biological tissue during low-level laser therapy. Lasers Med Sci 29, 637-644.

Kim, S., Tathireddy, P., Normann, R.A., Solzbacher, F., 2007. Thermal impact of an active 3-D microelectrode array implanted in the brain. IEEE Trans Neural Syst Rehabil Eng 15, 493-501.

Kim, T., Kim, S.G., 2011. Temporal dynamics and spatial specificity of arterial and venous blood volume changes during visual stimulation: implication for BOLD quantification. J Cereb Blood Flow Metab 31, 1211-1222.

Kleinman, C.S., Seri, I., 2012. Hemodynamics and Cardiology: Neonatology Questions and Controversies. Elsevier Health Sciences.

Kleinschmidt, A., Obrig, H., Requardt, M., Merboldt, K.D., Dirnagl, U., Villringer, A., Frahm, J., 1996. Simultaneous recording of cerebral blood oxygenation changes during human brain activation by magnetic resonance imaging and near-infrared spectroscopy. J Cereb Blood Flow Metab 16, 817-826.

Kluckow, M., Evans, N., 1995. Early echocardiographic prediction of symptomatic patent ductus arteriosus in preterm infants undergoing mechanical ventilation. J Pediatr 127, 774-779.

Kocharyan, A., Fernandes, P., Tong, X.K., Vaucher, E., Hamel, E., 2008. Specific subtypes of cortical GABA interneurons contribute to the neurovascular coupling response to basal forebrain stimulation. J Cereb Blood Flow Metab 28, 221-231.

Kostovic, I., Judas, M., 2010. The development of the subplate and thalamocortical connections in the human foetal brain. Acta Paediatr 99, 1119-1127.

Kozberg, M., Hillman, E., 2016. Neurovascular coupling and energy metabolism in the developing brain. Prog Brain Res 225, 213-242.

Kozberg, M.G., Chen, B.R., DeLeo, S.E., Bouchard, M.B., Hillman, E.M., 2013. Resolving the transition from negative to positive blood oxygen level-dependent responses in the developing brain. Proc Natl Acad Sci U S A 110, 4380-4385.

Kratzer, I., Chip, S., Vexler, Z.S., 2014. Barrier mechanisms in neonatal stroke. Front Neurosci 8, 359.

Kroth, J., Weidlich, K., Hiedl, S., Nussbaum, C., Christ, F., Genzel-boroviczeny, O., 2008. Functional vessel density in the first month of life in preterm neonates. Pediatr Res 64, 567-571.

Kuroda, Y., Murakami, M., Tsuruta, J., Murakawa, T., Sakabe, T., 1997. Blood flow velocity of middle cerebral artery during prolonged anesthesia with halothane, isoflurane, and sevoflurane in humans. Anesthesiology 87, 527-532.

Kusaka, T., Okubo, K., Nagano, K., Isobe, K., Itoh, S., 2005. Cerebral distribution of cardiac output in newborn infants. Arch Dis Child Fetal Neonatal Ed 90, F77-78.

Kuschinsky, W., 1991. Coupling of function, metabolism, and blood flow in the brain. Neurosurgical Review 14, 163-168.

Kuschinsky, W., Paulson, O.B., 1992. Capillary circulation in the brain. Cerebrovasc Brain Metab Rev 4, 261-286.

Kuschinsky, W.P., O. B., 1992. Cerebrovasc. Brain Metab. 261–286.

Lacroix, A., Toussay, X., Anenberg, E., Lecrux, C., Ferreiros, N., Karagiannis, A., Plaisier, F., Chausson, P., Jarlier, F., Burgess, S.A., Hillman, E.M., Tegeder, I., Murphy, T.H., Hamel, E., Cauli, B., 2015. COX-2-Derived Prostaglandin E2 Produced by Pyramidal Neurons Contributes to Neurovascular Coupling in the Rodent Cerebral Cortex. J Neurosci 35, 11791-11810.

Lam, A.M., Matta, B.F., Mayberg, T.S., Strebel, S., 1995. Change in cerebral blood flow velocity with onset of EEG silence during inhalation anesthesia in humans: evidence of flow-metabolism coupling? J Cereb Blood Flow Metab 15, 714-717.

LaManna, J.C., McCracken, K.A., Patil, M., Prohaska, O.J., 1989. Stimulus-activated changes in brain tissue temperature in the anesthetized rat. Metab Brain Dis 4, 225-237.

Lamblin, M.D., Andre, M., Challamel, M.J., Curzi-Dascalova, L., d'Allest, A.M., De Giovanni, E., Moussalli-Salefranque, F., Navelet, Y., Plouin, P., Radvanyi-Bouvet, M.F., Samson-Dollfus, D., Vecchierini-Blineau, M.F., 1999. [Electroencephalography of the premature and term newborn. Maturational aspects and glossary]. Neurophysiol Clin 29, 123-219.

Landry, D.W., Oliver, J.A., 2001. The pathogenesis of vasodilatory shock. N Engl J Med 345, 588-595.

Lassen, N.A., 1959. Cerebral blood flow and oxygen consumption in man. Physiol Rev 39, 183-238.

Lassen, N.A., 1985. Normal average value of cerebral blood flow in younger adults is 50 ml/100 g/min. J Cereb Blood Flow Metab 5, 347-349.

Lassen, N.A., Ingvar, D.H., Skinhoj, E., 1978. Brain function and blood flow. Sci Am 239, 62-71.

Le Bé, J.-V., Markram, H., 2006. Spontaneous and evoked synaptic rewiring in the neonatal neocortex. Proceedings of the National Academy of Sciences 103, 13214-13219.

Le Magueresse, C., Monyer, H., 2013. GABAergic interneurons shape the functional maturation of the cortex. Neuron 77, 388-405.

Lee, S.H., Dan, Y., 2012. Neuromodulation of brain states. Neuron 76, 209-222.

Lemmers, P.M., Toet, M.C., van Bel, F., 2008. Impact of patent ductus arteriosus and subsequent therapy with indomethacin on cerebral oxygenation in preterm infants. Pediatrics 121, 142-147.

Leung, T.S., Tachtsidis, I., Tisdall, M.M., Pritchard, C., Smith, M., Elwell, C.E., 2009. Estimating a modified Grubb's exponent in healthy human brains with near infrared spectroscopy and transcranial Doppler. Physiol Meas 30, 1-12.

Lewis, T.L., Jr., Courchet, J., Polleux, F., 2013. Cell biology in neuroscience: Cellular and molecular mechanisms underlying axon formation, growth, and branching. J Cell Biol 202, 837-848.

Lin, P.Y., Roche-Labarbe, N., Dehaes, M., Carp, S., Fenoglio, A., Barbieri, B., Hagan, K., Grant, P.E., Franceschini, M.A., 2013a. Non-invasive optical measurement of cerebral metabolism and hemodynamics in infants. J Vis Exp, e4379.

Lin, P.Y., Roche-Labarbe, N., Dehaes, M., Fenoglio, A., Grant, P.E., Franceschini, M.A., 2013b. Regional and hemispheric asymmetries of cerebral hemodynamic and oxygen metabolism in newborns. Cereb Cortex 23, 339-348.

Liu, X., Li, C., Falck, J.R., Harder, D.R., Koehler, R.C., 2012. Relative contribution of cyclooxygenases, epoxyeicosatrienoic acids, and pH to the cerebral blood flow response to vibrissal stimulation. Am J Physiol Heart Circ Physiol 302, H1075-1085.

Lowe, M.J., Mock, B.J., Sorenson, J.A., 1998. Functional connectivity in single and multislice echoplanar imaging using resting-state fluctuations. Neuroimage 7, 119-132.

M. Kozberg, E.H., 2016. Progress in Brain Research. In: Mark Bear, H.E., Hajime Hirase, Freda Miller, Shane O'Mara, Susan Rossell, Nathalie Rouach, Barbara Sahakian, Bettina Studer, Xiao-Jing Wang (Ed.).

Madsen, P.L., Schmidt, J.F., Wildschiodtz, G., Friberg, L., Holm, S., Vorstrup, S., Lassen, N.A., 1991. Cerebral O2 metabolism and cerebral blood flow in humans during deep and rapid-eye-movement sleep. J Appl Physiol (1985) 70, 2597-2601.

Madsen, S.J., 2012. Optical Methods and Instrumentation in Brain Imaging and Therapy. Springer New York.

Maggioni, E., Molteni, E., Zucca, C., Reni, G., Cerutti, S., Triulzi, F.M., Arrigoni, F., Bianchi, A.M., 2015. Investigation of negative BOLD responses in human brain through NIRS technique. A visual stimulation study. Neuroimage 108, 410-422.

Mahdi Mahmoudzadeh, G.D.-L., Guy, Kongolo, M.F., Sabrina Goudjil, Fabrice Wallois, 2016. Consequence of intraventricular hemorrhage on neurovascular

coupling evoked by speech syllables in preterm neonates.

Mahdi Mahmoudzadeh, G.D.-L., Guy Kongolo, Marc Fournier, Sabrina Goudjil, fabrice wallois, 2017. Consequence of intraventricular hemorrhage on neurovascular coupling evoked by speech syllables in preterm neonates. in revision.

Mahmoudzadeh, M., Dehaene-Lambertz, G., Fournier, M., Kongolo, G., Goudjil, S., Dubois, J., Grebe, R., Wallois, F., 2013a. Syllabic discrimination in premature human infants prior to complete formation of cortical layers. Proceedings of the National Academy of Sciences 110, 4846-4851.

Mahmoudzadeh, M., Dehaene-Lambertz, G., Fournier, M., Kongolo, G., Goudjil, S., Dubois, J., Grebe, R., Wallois, F., 2013b. Syllabic discrimination in premature human infants prior to complete formation of cortical layers. Proc Natl Acad Sci U S A 110, 4846-4851.

Mahmoudzadeh, M., Dehaene-Lambertz, G., Kongolo, G., Fournier, M., Goudjil, S., Wallois, F., 2018. Consequence of intraventricular hemorrhage on neurovascular coupling evoked by speech syllables in preterm neonates. Dev Cogn Neurosci 30, 60-69.

Mahmoudzadeh, M., Dehaene-Lambertz, G., Wallois, F., 2017a. Electrophysiological and hemodynamic mismatch responses in rats listening to human speech syllables. PLoS One 12, e0173801.

Mahmoudzadeh, M., Wallois, F., Kongolo, G., Goudjil, S., Dehaene-Lambertz, G., 2017b. Functional Maps at the Onset of Auditory Inputs in Very Early Preterm Human Neonates. Cereb Cortex 27, 2500-2512.

Mahmoudzadeh M, W.F., Kongolo G, Goudjil S, Dehaene Lambertz G Functional maps at the onset of auditory inputs in very early preterm human neonates. Cerebral Cortex (in press).

Malamateniou, C., Counsell, S.J., Allsop, J.M., Fitzpatrick, J.A., Srinivasan, L., Cowan, F.M., Hajnal, J.V., Rutherford, M.A., 2006. The effect of preterm birth on neonatal cerebral vasculature studied with magnetic resonance angiography at 3 Tesla. Neuroimage 32, 1050-1059.

Malonek, D., Dirnagl, U., Lindauer, U., Yamada, K., Kanno, I., Grinvald, A., 1997a. Vascular imprints of neuronal activity: relationships between the dynamics of cortical blood flow, oxygenation, and volume changes following sensory stimulation. Proc Natl Acad Sci U S A 94, 14826-14831.

Malonek, D., Dirnagl, U., Lindauer, U., Yamada, K., Kanno, I., Grinvald, A., 1997b. Vascular imprints of neuronal activity: Relationships between the dynamics of cortical blood flow, oxygenation, and volume changes following sensory stimulation. Proceedings of the National Academy of Sciences 94, 14826-14831.

Mancini, D.M., Bolinger, L., Li, H., Kendrick, K., Chance, B., Wilson, J.R., 1994. Validation of near-infrared spectroscopy in humans. J Appl Physiol (1985) 77, 2740-2747.

Mandeville, J.B., Marota, J.J., Ayata, C., Zaharchuk, G., Moskowitz, M.A., Rosen, B.R., Weisskoff, R.M., 1999. Evidence of a cerebrovascular postarteriole windkessel with delayed compliance. J Cereb Blood Flow Metab 19, 679-689.

Manoochehri, M., Mahmoudzadeh, M., Osharina, V., Wallois, F., submitted. Light on: Neural shrinking and swelling, in vivo, around epileptic changes.

Marin-Padilla, M., 1983. Structural organization of the human cerebral cortex prior to the appearance of the cortical plate. Anat Embryol (Berl) 168, 21-40.

Martin, E., Joeri, P., Loenneker, T., Ekatodramis, D., Vitacco, D., Hennig, J., Marcar, V.L., 1999. Visual processing in infants and children studied using functional MRI. Pediatr Res 46, 135-140.

Matcher, S.J., Elwell, C.E., Cooper, C.E., Cope, M., Delpy, D.T., 1995a. Performance comparison of several published tissue near-infrared spectroscopy algorithms. Anal Biochem 227, 54-68.

Matcher, S.J., Kirkpatrick, P.J., Nahid, K., Cope, M., Delpy, D.T., 1995b. Absolute quantification methods in tissue near-infrared spectroscopy. 2389, 486-495.

McAdams, R.M., Juul, S.E., 2012. The role of cytokines and inflammatory cells in perinatal brain injury. Neurol Res Int 2012, 561494.

McCaslin, A.F., Chen, B.R., Radosevich, A.J., Cauli, B., Hillman, E.M., 2011. In vivo 3D morphology of astrocyte-vasculature interactions in the somatosensory cortex: implications for neurovascular coupling. J Cereb Blood Flow Metab 31, 795-806.

Meek, J., Tyszczuk, L., Elwell, C., Wyatt, J., 1999. Low cerebral blood flow is a risk factor for severe intraventricular haemorrhage. Arch Dis Child Fetal Neonatal Ed 81, F15-F18.

Meek, J.H., Elwell, C.E., Khan, M.J., Romaya, J., Wyatt, J.S., Delpy, D.T., Zeki, S., 1995. Regional changes in cerebral haemodynamics as a result of a visual stimulus measured by near infrared spectroscopy. Proc Biol Sci 261, 351-356.

Meek, J.H., Firbank, M., Elwell, C.E., Atkinson, J., Braddick, O., Wyatt, J.S., 1998. Regional hemodynamic responses to visual stimulation in awake infants. Pediatr Res 43, 840-843.

Mesquita, R.C., Schenkel, S.S., Minkoff, D.L., Lu, X., Favilla, C.G., Vora, P.M., Busch, D.R., Chandra, M., Greenberg, J.H., Detre, J.A., Yodh, A.G., 2013. Influence of probe pressure on the diffuse correlation spectroscopy blood flow signal: extra-cerebral contributions. Biomed Opt Express 4, 978-994.

Metea, M.R., Newman, E.A., 2006. Glial cells dilate and constrict blood vessels: a mechanism of neurovascular coupling. J Neurosci 26, 2862-2870.

Mielke, G., Benda, N., 2001. Cardiac output and central distribution of blood flow in the human fetus. Circulation 103, 1662-1668.

Milej, D.F., Janusek, D., Wojtkiewicz, S., Treszczanowicz, J., Weigl, W., Liebert, A., 2014. Assessment of ICG inflow to the brain by time-resolved measurements of diffuse reflectance at 16 source-detector separations. Biomedical Optics 2014. Optical Society of America, Miami, Florida, p. BM3A.23.

Milligan, D.W., 1980. Failure of autoregulation and intraventricular haemorrhage in preterm infants. Lancet 1, 896-898.

Mintun, M.A., Lundstrom, B.N., Snyder, A.Z., Vlassenko, A.G., Shulman, G.L., Raichle, M.E., 2001. Blood flow and oxygen delivery to human brain during functional activity: theoretical modeling and experimental data. Proc Natl Acad Sci U S A 98, 6859-6864.

Miyawaki, T., Matsui, K., Takashima, S., 1998. Developmental characteristics of vessel density in the human fetal and infant brains. Early Hum Dev 53, 65-72.

Moore, A.R., Zhou, W.L., Jakovcevski, I., Zecevic, N., Antic, S.D., 2011. Spontaneous electrical activity in the human fetal cortex in vitro. J Neurosci 31, 2391-2398.

Moretti, R., Pansiot, J., Bettati, D., Strazielle, N., Ghersi-Egea, J.F., Damante, G., Fleiss, B., Titomanlio, L., Gressens, P., 2015. Blood-brain barrier dysfunction in disorders of the developing brain. Front Neurosci 9, 40.

Mosca, F., Bray, M., Lattanzio, M., Fumagalli, M., Tosetto, C., 1997. Comparative evaluation of the effects of indomethacin and ibuprofen on cerebral perfusion and oxygenation in preterm infants with patent ductus arteriosus. J Pediatr 131, 549-554.

Motamedi, M., Rastegar, S., Lecarpentier, G., Welch, A.J., 1989. Light and temperature distribution in laser irradiated tissue: the influence of anisotropic scattering and refractive index. Appl Opt 28, 2230-2237.

Mountcastle, V.B., 1997. The columnar organization of the neocortex. Brain 120 (Pt 4), 701-722.

Munro, M.J., Walker, A.M., Barfield, C.P., 2004. Hypotensive extremely low birth weight infants have reduced cerebral blood flow. Pediatrics 114, 1591-1596.

Munro, P.R.T., 2013. Principles of Diffuse Light Propagation: Light Propagation in Tissues with Applications in Biology and Medicine, by Jorge Ripoll Lorenzo. Contemporary Physics 54, 139-140.

Murkin, J.M., Arango, M., 2009. Near-infrared spectroscopy as an index of brain and tissue oxygenation. Br J Anaesth 103 Suppl 1, i3-13.

Niemz, M.H., 2004. Laser-Tissue Interactions: Fundamentals and Applications. Springer Berlin Heidelberg.

Noori, S., Stavroudis, T.A., Seri, I., 2012a. Chapter 1 - Principles of Developmental Cardiovascular Physiology and Pathophysiology. Hemodynamics and Cardiology: Neonatology Questions and Controversies (Second Edition). W.B. Saunders, Philadelphia, pp. 3-27.

Noori, S., Wlodaver, A., Gottipati, V., McCoy, M., Schultz, D., Escobedo, M., 2012b. Transitional changes in cardiac and cerebral hemodynamics in term neonates at birth. J Pediatr 160, 943-948.

Nourhashemi, M., Kongolo, G., Mahmoudzadeh, M., Goudjil, S., Wallois, F., 2017a. Relationship between relative cerebral blood flow, relative cerebral blood volume, and relative cerebral metabolic rate of oxygen in the preterm neonatal brain. Neurophotonics 4, 021104.

Nourhashemi, M., Kongolo, G., Mahmoudzadeh, M., Goudjil, S., Wallois, F., 2017b. Relationship between relative cerebral blood flow, relative cerebral blood volume, and relative cerebral metabolic rate of oxygen in the preterm neonatal brain. SPIE, p. 13.

Nourhashemi, M., Mahmoudzadeh, M., Wallois, F., 2016a. Thermal impact of near-infrared laser in advanced noninvasive optical brain imaging. Neurophotonics 3, 015001-015001.

Nourhashemi, M., Mahmoudzadeh, M., Wallois, F., 2016b. Thermal impact of near-infrared laser in advanced noninvasive optical brain imaging. Neurophotonics 3, 015001.

Nourhashemi, M., Mahmoudzadeh, M., Wallois, F., 2016c. Thermal impact of near-infrared laser in advanced noninvasive optical brain imaging. SPIE, p. 13.

Obrig, H., 2014. NIRS in clinical neurology - a 'promising' tool? Neuroimage 85 Pt 1, 535-546.

Ogoh, G., 2010. Stefan's Problem: Validation of a One-Dimensional Solid-Liquid Phase Change Heat Transfer Process. Excerpt from the Proceedings of the COMSOL Conference 2010 Boston

Okada, E., Delpy, D.T., 2003. Near-infrared light propagation in an adult head model. I. Modeling of low-level scattering in the cerebrospinal fluid layer. Appl Opt 42, 2906-2914.

Okazawa, H., Vafaee, M., 2001. Effect of vascular radioactivity on regional values of cerebral blood flow: evaluation of methods for H(2)(15)O PET to distinguish cerebral perfusion from blood volume. J Nucl Med 42, 1032-1039.

Osborn, D.A., Evans, N., Kluckow, M., 2003. Hemodynamic and antecedent risk factors of early and late periventricular/intraventricular hemorrhage in premature infants. Pediatrics 112, 33-39.

Palmu, K., Stevenson, N., Wikstrom, S., Hellstrom-Westas, L., Vanhatalo, S., Palva, J.M., 2010. Optimization of an NLEO-based algorithm for automated detection of spontaneous activity transients in early preterm EEG. Physiol Meas 31, N85-93.

Park, L., Anrather, J., Girouard, H., Zhou, P., Iadecola, C., 2007. Nox2-derived reactive oxygen species mediate neurovascular dysregulation in the aging mouse brain. J Cereb Blood Flow Metab 27, 1908-1918.

Patel, J., Marks, K., Roberts, I., Azzopardi, D., Edwards, A.D., 1998. Measurement of cerebral blood flow in newborn infants using near infrared spectroscopy with indocyanine green. Pediatr Res 43, 34-39.

Paulson, O.B., Hasselbalch, S.G., Rostrup, E., Knudsen, G.M., Pelligrino, D., 2010. Cerebral blood flow response to functional activation. Journal of Cerebral Blood Flow and Metabolism: Official Journal of the International Society of Cerebral Blood Flow and Metabolism 30, 2-14.

Paulson, O.B., Strandgaard, S., Edvinsson, L., 1990. Cerebral autoregulation. Cerebrovasc Brain Metab Rev 2, 161-192.

Pennes, H.H., 1948. Analysis of tissue and arterial blood temperatures in the resting human forearm. J Appl Physiol 1, 93-122.

Peppiatt, C.M., Howarth, C., Mobbs, P., Attwell, D., 2006. Bidirectional control of CNS capillary diameter by pericytes. Nature 443, 700-704.

Perlman, J.M., Hill, A., Volpe, J.J., 1981. The effect of patent ductus arteriosus on flow velocity in the anterior cerebral arteries: ductal steal in the premature newborn infant. J Pediatr 99, 767-771.

Perlman, J.M., Nelson, J.S., McAlister, W.H., Volpe, J.J., 1983. Intracerebellar hemorrhage in a premature newborn: diagnosis by real-time ultrasound and correlation with autopsy findings. Pediatrics 71, 159-162.

Peterson, B.S., Anderson, A.W., Ehrenkranz, R., Staib, L.H., Tageldin, M., Colson, E., Gore, J.C., Duncan, C.C., Makuch, R., Ment, L.R., 2003. Regional brain volumes and their later neurodevelopmental correlates in term and preterm infants. Pediatrics 111, 939-948.

Petzold, G.C., Murthy, V.N., 2011. Role of astrocytes in neurovascular coupling. Neuron 71, 782-797.

Pine, D.J., Weitz, D.A., Chaikin, P.M., Herbolzheimer, E., 1988. Diffusing wave spectroscopy. Phys Rev Lett 60, 1134-1137.

Power, J.D., Schlaggar, B.L., Petersen, S.E., 2014. Studying brain organization via spontaneous fMRI signal. Neuron 84, 681-696.

Powers, W.J., Grubb, R.L., Jr., Darriet, D., Raichle, M.E., 1985. Cerebral blood flow and cerebral metabolic rate of oxygen requirements for cerebral function and viability in humans. J Cereb Blood Flow Metab 5, 600-608.

Powers, W.J., Hirsch, I.B., Cryer, P.E., 1996. Effect of stepped hypoglycemia on regional cerebral blood flow response to physiological brain activation. Am J Physiol 270, H554-559.

Protection, I.C.O.N.I.R., ICNIRP Guidelines On Limits Of Exposure To Laser Radiation Of Wavelengths Between 180 nm And 1,000 μm,. Health Physics 105(3):271-295; 201.

Pryds, O., Greisen, G., Johansen, K.H., 1988. Indomethacin and cerebral blood flow in premature infants treated for patent ductus arteriosus. Eur J Pediatr 147, 315-316.

Pryds, O., Greisen, G., Lou, H., Friis-Hansen, B., 1989. Heterogeneity of cerebral vasoreactivity in preterm infants supported by mechanical ventilation. J Pediatr 115, 638-645.

Rahmat-Samii, Y., Kim, K.W., 1998. Antennas and human in personal communications: applications of modern EM computational techniques. Microwaves and Radar, 1998. MIKON '98., 12th International Conference on, pp. 36-55 vol.34.

Raichle, M.E., 1998. Behind the scenes of functional brain imaging: a historical and physiological perspective. Proc Natl Acad Sci U S A 95, 765-772.

Rasmussen, P., Dawson, E.A., Nybo, L., van Lieshout, J.J., Secher, N.H., Gjedde, A., 2007. Capillary-oxygenation-level-dependent near-infrared spectrometry in frontal lobe of humans. J Cereb Blood Flow Metab 27, 1082-1093.

Reina-De La Torre, F., Rodriguez-Baeza, A., Sahuquillo-Barris, J., 1998. Morphological characteristics and distribution pattern of the arterial vessels in human cerebral cortex: a scanning electron microscope study. Anat Rec 251, 87-96.

Risser, L., Plouraboue, F., Cloetens, P., Fonta, C., 2009. A 3D-investigation shows that angiogenesis in primate cerebral cortex mainly occurs at capillary level. Int J Dev Neurosci 27, 185-196.

Roche-Labarbe, N., Carp, S.A., Surova, A., Patel, M., Boas, D.A., Grant, P.E., Franceschini, M.A., 2010. Noninvasive optical measures of CBV, StO2, CBF index, and rCMRO2 in human premature neonates' brains in the first six weeks of life. Human Brain Mapping 31, 341-352.

Roche-Labarbe, N., Fenoglio, A., Aggarwal, A., Dehaes, M., Carp, S.A., Franceschini, M.A., Grant, P.E., 2012. Near-infrared spectroscopy assessment of cerebral oxygen metabolism in the developing premature brain. J Cereb Blood Flow Metab 32, 481-488.

Roche-Labarbe, N., Fenoglio, A., Radhakrishnan, H., Kocienski-Filip, M., Carp, S.A., Dubb, J., Boas, D.A., Grant, P.E., Franceschini, M.A., 2014. Somatosensory evoked changes in cerebral oxygen consumption measured non-invasively in premature neonates. Neuroimage 85 Pt 1, 279-286.

Roche-Labarbe, N., Wallois, F., Ponchel, E., Kongolo, G., Grebe, R., 2007a. Coupled oxygenation oscillation measured by NIRS and intermittent cerebral activation on EEG in premature infants. Neuroimage 36, 718-727.

Roche-Labarbe, N., Wallois, F., Ponchel, E., Kongolo, G., Grebe, R., 2007b. Coupled oxygenation oscillation measured by NIRS and intermittent cerebral activation on EEG in premature infants. Neuroimage 36, 718-727.

Rodríguez-Balderrama, I., Ostia-Garza, P.J., Villarreal-Parra, R.D., Tijerina-Guajardo, M., 2016. Risk factors and the relation of lactic acid to neonatal mortality in the first week of life. Medicina Universitaria 18, 3-9.

Ronghou, Y., Weiqin, 2014. Study on Generalized Thermoelastic Problem of Semi-infinite Plate Heated Locally by the Pulse Laser. IJEPR.

Routier, L., Mahmoudzadeh, M., Panzani, M., Azizollahi, H., Goudjil, S., Kongolo, G., Wallois, F., 2017. Plasticity of neonatal neuronal networks in very premature infants: Source localization of temporal theta activity, the first endogenous neural biomarker, in temporoparietal areas. Hum Brain Mapp 38, 2345-2358.

Rowell, L.B., 1993. Human Cardiovascular Control.

Rowland, M., Tozer, T.N., 1995. Clinical Pharmacokinetics: Concepts and Applications. Williams & Wilkins.

Roy, C.S., Sherrington, C.S., 1890. On the Regulation of the Blood-supply of the Brain. J Physiol 11, 85-158 117.

Saidi, I.S., 1992a. Transcutaneous optical measurement of hyperbilirubinemia in neonates. Rice University.

Saidi, I.S., 1992b. Transcutaneous Optical Measurement of Hyperbilirubinemia in Neonates. Rice, University.

Sajjadian, N., Shajari, H., Saalehi, Z., Esphahani, F., Alizadeh Taheri, P., 2012. Transcutaneous bilirubin measurement in preterm neonates. Acta Med Iran 50, 765-770.

Sakatani, K., Chen, S., Lichty, W., Zuo, H., Wang, Y.P., 1999. Cerebral blood oxygenation changes induced by auditory stimulation in newborn infants measured by near infrared spectroscopy. Early Hum Dev 55, 229-236.

Saliba, E., 2003. Hémodynamique cérébrale postnatale (débits sanguins cérébraux et autorégulation cérébrale). in Neurologie périnatale.

Saouli, A., Mansour, K., 2013. Modelling of the near infra-red radiation pulse propagation in biological tissues for medical imaging application. journal of intense pulsed lasers and applications in advanced physics 3, pp. 41-45.

Sarnat, H.B., Flores-Sarnat, L., 2002. Cajal-Retzius and subplate neurons: their role in cortical development. Eur J Paediatr Neurol 6, 91-97.

Scheinberg, P., Blackburn, L.I., Rich, M., Saslaw, M., 1954. Effects of vigorous physical exercise on cerebral circulation and metabolism. Am J Med 16, 549-554.

Schmidt, B., Davis, P., Moddemann, D., Ohlsson, A., Roberts, R.S., Saigal, S., Solimano, A., Vincer, M., Wright, L.L., Trial of Indomethacin Prophylaxis in Preterms, I., 2001. Long-term effects of indomethacin prophylaxis in extremely-low-birth-weight infants. N Engl J Med 344, 1966-1972.

Scholkmann, F., Kleiser, S., Metz, A.J., Zimmermann, R., Mata Pavia, J., Wolf, U., Wolf, M., 2014. A review on continuous wave functional near-infrared spectroscopy and imaging instrumentation and methodology. Neuroimage 85 Pt 1, 6-27.

Schreiber, T., 2000. Measuring Information Transfer. Phys Rev Lett 85, 461-464.

Schröder, K., 2000. Handbook on Industrial Laser Safety. Technical University of Vienna.

Schulmeister, R.H.a.K., (Taylor & Francis, 2004). Laser Safety

Schweiger, 1994. Application of the finite element method in infrared image reconstruction of scattering media.

Seese, T.M., Harasaki, H., Saidel, G.M., Davies, C.R., 1998. Characterization of tissue morphology, angiogenesis, and temperature in the adaptive response of muscle tissue to chronic heating. Lab Invest 78, 1553-1562.

Seiyama, A., Seki, J., Tanabe, H.C., Sase, I., Takatsuki, A., Miyauchi, S., Eda, H., Hayashi, S., Imaruoka, T., Iwakura, T., Yanagida, T., 2004. Circulatory basis of fMRI signals: relationship between changes in the hemodynamic parameters and BOLD signal intensity. Neuroimage 21, 1204-1214.

Selton, D., Andre, M., Hascoet, J.M., 2000. Normal EEG in very premature infants: reference criteria. Clin Neurophysiol 111, 2116-2124.

Seregi, A., Keller, M., Hertting, G., 1987. Are cerebral prostanoids of astroglial origin? Studies on the prostanoid forming system in developing rat brain and primary cultures of rat astrocytes. Brain Res 404, 113-120.

Sette, G., Baron, J.C., Mazoyer, B., Levasseur, M., Pappata, S., Crouzel, C., 1989. Local brain haemodynamics and oxygen metabolism in cerebrovascular disease. Positron emission tomography. Brain 112 (Pt 4), 931-951.

Shafirstein, G., Baumler, W., Lapidoth, M., Ferguson, S., North, P.E., Waner, M., 2003. Laser tissue interaction modeling for treatment planning of port-wine stain. The 16th Annual Meeting of the IEEE Lasers and Electro-Optics Society, 2003. LEOS 2003., pp. 313-315 vol.311.

Shannon, C.E., 1948. A Mathematical Theory of Communication. Bell System Technical Journal 27, 379-423.

Shargel, L., Wu-Pong, S., Yu, A., 2004. Applied Biopharmaceutics & Pharmacokinetics, Fifth Edition. McGraw-Hill Education.

Shargel, L., Yu, A.B.C., 1999. Applied Biopharmaceutics and Pharmacokinetics. McGraw-Hill Professional Publishing.

Sheth, S.A., Nemoto, M., Guiou, M., Walker, M., Pouratian, N., Toga, A.W., 2004. Linear and nonlinear relationships between neuronal activity, oxygen metabolism, and hemodynamic responses. Neuron 42, 347-355.

Sheth, S.A., Nemoto, M., Guiou, M.W., Walker, M.A., Toga, A.W., 2005. Spatiotemporal evolution of functional hemodynamic changes and their relationship to neuronal activity. J Cereb Blood Flow Metab 25, 830-841.

Shimada, S., Kasai, T., Konishi, M., Fujiwara, T., 1994. Effects of patent ductus arteriosus on left ventricular output and organ blood flows in preterm infants with respiratory distress syndrome treated with surfactant. J Pediatr 125, 270-277.

Shortland, D.B., Gibson, N.A., Levene, M.I., Archer, L.N., Evans, D.H., Shaw, D.E., 1990. Patent ductus arteriosus and cerebral circulation in preterm infants. Dev Med Child Neurol 32, 386-393.

Sie, L.T.L., Rombouts, S.A., Valk, I.J., Hart, A.A., Scheltens, P., van der Knaap, M.S., 2001. Functional MRI of visual cortex in sedated 18 month-old infants with or without periventricular leukomalacia. Dev Med Child Neurol 43, 486-490.

Siegel, A., Marota, J.J., Boas, D., 1999. Design and evaluation of a continuous-wave diffuse optical tomography system. Opt Express 4, 287-298.

Siesjo, B.K., 1978. Brain energy metabolism and catecholaminergic activity in hypoxia, hypercapnia and ischemia. J Neural Transm Suppl, 17-22.

Sirota, A., Csicsvari, J., Buhl, D., Buzsaki, G., 2003. Communication between neocortex and hippocampus during sleep in rodents. Proc Natl Acad Sci U S A 100, 2065-2069.

Skov, L., Pryds, O., Greisen, G., Lou, H., 1993. Estimation of cerebral venous saturation in newborn infants by near infrared spectroscopy. Pediatr Res 33, 52-55.

Sokoloff, L., Reivich, M., Kennedy, C., Des Rosiers, M.H., Patlak, C.S., Pettigrew, K.D., Sakurada, O., Shinohara, M., 1977. The [14C]deoxyglucose method for the measurement of local cerebral glucose utilization: theory, procedure, and normal values in the conscious and anesthetized albino rat. J Neurochem 28, 897-916.

Steen, W.M., 2003. Laser Material Processing. Springer.

Stein, T., Moritz, C., Quigley, M., Cordes, D., Haughton, V., Meyerand, E., 2000. Functional connectivity in the thalamus and hippocampus studied with functional MR imaging. AJNR Am J Neuroradiol 21, 1397-1401.

Sukstanskii, A.L., Yablonskiy, D.A., 2006. Theoretical model of temperature regulation in the brain during changes in functional activity. Proc Natl Acad Sci U S A 103, 12144-12149.

Takano, T., Tian, G.F., Peng, W., Lou, N., Libionka, W., Han, X., Nedergaard, M., 2006. Astrocyte-mediated control of cerebral blood flow. Nat Neurosci 9, 260-267.

Takata, N., Nagai, T., Ozawa, K., Oe, Y., Mikoshiba, K., Hirase, H., 2013. Cerebral blood flow modulation by Basal forebrain or whisker stimulation can occur independently of large cytosolic Ca2+ signaling in astrocytes. PLoS One 8, e66525.

Tau, G.Z., Peterson, B.S., 2010. Normal development of brain circuits. Neuropsychopharmacology 35, 147-168.

Thompson, A.C., Wade, S.A., Brown, W.G., Stoddart, P.R., 2012. Modeling of light absorption in tissue during infrared neural stimulation. J Biomed Opt 17, 075002.

Tian, F., Tarumi, T., Liu, H., Zhang, R., Chalak, L., 2016. Wavelet coherence analysis of dynamic cerebral autoregulation in neonatal hypoxic–ischemic encephalopathy. NeuroImage : Clinical 11, 124-132.

Tokumaru, A.M., Barkovich, A.J., O'Uchi, T., Matsuo, T., Kusano, S., 1999. The evolution of cerebral blood flow in the developing brain: evaluation with iodine-123 iodoamphetamine SPECT and correlation with MR imaging. AJNR Am J Neuroradiol 20, 845-852.

Torrence, C., Webster, P.J., 1999. Interdecadal Changes in the ENSO–Monsoon System. Journal of Climate 12, 2679-2690.

Tuchin, V., 2000. Tissue Optics: Light Scattering Methods and Instruments for Medical Diagnosis. SPIE Optical Engineering Press.

Tuchin, V.V., Engineers, S.o.P.-o.I., 2007. Tissue Optics: Light Scattering Methods and Instruments for Medical Diagnosis. SPIE/International Society for Optical Engineering.

Uchino, H., Ushijima, K., Ikeda, Y., Williams, J., Barroga, E.F., 2015. Neuroanesthesia and Cerebrospinal Protection. Springer Japan.

Ueda, M., Bures, J., Fischer, J., 1977. Spreading depression elicited by thermal effects of ultrasonic irradiation of cerebral cortex in rats. J Neurobiol 8, 381-393.

Vafaee MS, G.A., 2001. CMRO2−CBF changes by finger motion: evidence of no flow-metabolism coupling. Int Soc Cereb Blood Flow Metab, 21:122.

van Beek, A.H., Claassen, J.A., Rikkert, M.G., Jansen, R.W., 2008. Cerebral autoregulation: an overview of current concepts and methodology with special focus on the elderly. J Cereb Blood Flow Metab 28, 1071-1085.

Van Bel, F., Van de Bor, M., Stijnen, T., Baan, J., Ruys, J.H., 1987. Aetiological role of cerebral blood-flow alterations in development and extension of peri-intraventricular haemorrhage. Dev Med Child Neurol 29, 601-614.

van der Zee, P., Essenpreis, M., Delpy, D.T., 1993. Optical properties of brain tissue. pp. 454-465.

Vander, A.J., Sherman, J.H., Luciano, D.S., 2001. Human Physiology: The Mechanisms of Body Function. McGraw-Hill.

Vanhatalo, S., Palva, J.M., Andersson, S., Rivera, C., Voipio, J., Kaila, K., 2005. Slow endogenous activity transients and developmental expression of K+-Cl- cotransporter 2 in the immature human cortex. Eur J Neurosci 22, 2799-2804.

Vanzetta, I., Grinvald, A., 2008. Coupling between neuronal activity and microcirculation: implications for functional brain imaging. HFSP J 2, 79-98.

Vanzetta, I., Hildesheim, R., Grinvald, A., 2005. Compartment-resolved imaging of activity-dependent dynamics of cortical blood volume and oximetry. J Neurosci 25, 2233-2244.

Victor, S., Marson, A.G., Appleton, R.E., Beirne, M., Weindling, A.M., 2006. Relationship between blood pressure, cerebral electrical activity, cerebral fractional oxygen extraction, and peripheral blood flow in very low birth weight newborn infants. Pediatr Res 59, 314-319.

Victor, S., Weindling, M., 2012. Chapter 7 - Near-Infrared Spectroscopy and Its Use for the Assessment of Tissue Perfusion in the Neonate A2 - Kleinman, Charles S. In: Seri, I. (Ed.), Hemodynamics and Cardiology: Neonatology Questions and Controversies (Second Edition). W.B. Saunders, Philadelphia, pp. 151-172.

Villringer, A.D., U. , 1995. Cerebrovasc. Brain Metab. 240–276.

Vo-Dinh, T., 2014. Biomedical Photonics Handbook, Second Edition: Fundamentals, Devices, and Techniques. Taylor & Francis.

Volpe, J.J., 1997. Brain injury in the premature infant – from pathogenesis to prevention. Brain and Development 19, 519-534.

Vutskits, L., 2014. Cerebral blood flow in the neonate. Pediatric Anesthesia 24, 22-29.

Wallois, F., 2010. Synopsis of maturation of specific features in EEG of premature neonates. Neurophysiol Clin 40, 125-126.

Wallois, F., Patil, A., Kongolo, G., Goudjil, S., Grebe, R., 2009. Haemodynamic changes during seizure-like activity in a neonate: a simultaneous AC EEG-SPIR and high-resolution DC EEG recording. Neurophysiol Clin 39, 217-227.

Wang, D.B., Blocher, N.C., Spence, M.E., Rovainen, C.M., Woolsey, T.A., 1992. Development and remodeling of cerebral blood vessels and their flow in postnatal mice observed with in vivo videomicroscopy. J Cereb Blood Flow Metab 12, 935-946.

Wang, L.V., Wu, H., 2007. Biomedical Optics: Principles and Imaging. Wiley.

Watzman, H.M., Kurth, C.D., Montenegro, L.M., Rome, J., Steven, J.M., Nicolson, S.C., 2000. Arterial and venous contributions to near-infrared cerebral oximetry. Anesthesiology 93, 947-953.

Weber, B., Keller, A.L., Reichold, J., Logothetis, N.K., 2008. The microvascular system of the striate and extrastriate visual cortex of the macaque. Cereb Cortex 18, 2318-2330.

Welch, A.J., van Gemert, M.J.C., 1995. Optical- Response of Laser-Irradiated Tissue. Springer US.

Welch, A.J., van Gemert, M.J.C., 2011. Optical-Thermal Response of Laser-Irradiated Tissue. Springer Netherlands.

White, R.P., Vallance, P., Markus, H.S., 2000. Effect of inhibition of nitric oxide synthase on dynamic cerebral autoregulation in humans. Clin Sci (Lond) 99, 555-560.

Widmaier, E.P., Raff, H., Strang, K.T., 2004. Vander, Sherman, & Luciano's Human Physiology: The Mechanisms of Body Function. McGraw-Hill Higher Education.

Wiener, N., 1956. The theory of prediction. In: Beckenbach, E. (Ed.), Modern Mathematics for Engineers., McGraw-Hill, New York.

Williams, L.R., Leggett, R.W., 1989. Reference values for resting blood flow to organs of man. Clin Phys Physiol Meas 10, 187-217.

Winkler, E.A., Bell, R.D., Zlokovic, B.V., 2011. Central nervous system pericytes in health and disease. Nat Neurosci 14, 1398-1405.

Wolf, M., Greisen, G., 2009. Advances in near-infrared spectroscopy to study the brain of the preterm and term neonate. Clin Perinatol 36, 807-834, vi.

Wolff, J.A., Goodfellow, A.M., 1955. Hematopoiesis in premature infants with special consideration of the effect of iron and of animal-protein factor. Pediatrics 16, 753-762.

Wong, F.Y., Barfield, C.P., Horne, R.S., Walker, A.M., 2009. Dopamine therapy promotes cerebral flow-metabolism coupling in preterm infants. Intensive Care Med 35, 1777-1782.

Wong, F.Y., Leung, T.S., Austin, T., Wilkinson, M., Meek, J.H., Wyatt, J.S., Walker, A.M., 2008. Impaired autoregulation in preterm infants identified by using spatially resolved spectroscopy. Pediatrics 121, e604-611.

Wray, S., Cope, M., Delpy, D.T., Wyatt, J.S., Reynolds, E.O., 1988. Characterization of the near infrared absorption spectra of cytochrome aa3 and haemoglobin for the non-invasive monitoring of cerebral oxygenation. Biochim Biophys Acta 933, 184-192.

X. Ronghou, G.Y., L. Weiqin,X. Ronghou, G. Yanfeng, L. Weiqin, 2014. Study on Generalized Thermoelastic Problem of Semi-infinite Plate Heated Locally by the Pulse Laser. IJEPR.

Xiong, J., Parsons, L.M., Gao, J.H., Fox, P.T., 1999. Interregional connectivity to primary motor cortex revealed using MRI resting state images. Hum Brain Mapp 8, 151-156.

Yang, Y., Liu, H., Li, X., Chance, B., 1997. Low-cost frequency-domain photon migration instrument for tissue spectroscopy, oximetry, and imaging. SPIE, p. 8.

Yoxall, C.W., Weindling, A.M., 1998. Measurement of cerebral oxygen consumption in the human neonate using near infrared spectroscopy: cerebral oxygen consumption increases with advancing gestational age. Pediatr Res 44, 283-290.

Yu, G., Durduran, T., Zhou, C., Wang, H.W., Putt, M.E., Saunders, H.M., Sehgal, C.M., Glatstein, E., Yodh, A.G., Busch, T.M., 2005. Noninvasive monitoring of murine tumor blood flow during and after photodynamic therapy provides early assessment of therapeutic efficacy. Clin Cancer Res 11, 3543-3552.

Zaramella, P., Freato, F., Amigoni, A., Salvadori, S., Marangoni, P., Suppiej, A., Schiavo, B., Chiandetti, L., 2001. Brain auditory activation measured by near-infrared spectroscopy (NIRS) in neonates. Pediatr Res 49, 213-219.

Zhang, J., Penny, D.J., Kim, N.S., Yu, V.Y., Smolich, J.J., 1999. Mechanisms of blood pressure increase induced by dopamine in hypotensive preterm neonates. Arch Dis Child Fetal Neonatal Ed 81, F99-F104.

Zimmermann, B.B., Roche-Labarbe, N., Surova, A., Boas, D.A., Wolf, M., Grant, P.E., Franceschini, M.A., 2012. The confounding effect of systemic physiology on the hemodynamic response in newborns. Adv Exp Med Biol 737, 103-109.

mots clés

niveau d'oxygénation du sang
flux sanguin cérébral
volume sanguin cérébral
liquide cérébro-spinal
Onde continue
Pression de perfusion cérébrale
Spectroscopie à corrélation diffuse
facteur de longueur de trajet différentiel
électroencéphalogramme
imagerie par résonance magnétique fonctionnelle
spectroscopie fonctionnelle proche infrarouge
désoxyhémoglobine
hémoglobine
oxyhémoglobine
Pression intracrânienne
Hémorragie intra-ventriculaire
loi de Beer-Lambert modifiée
pression artérielle moyenne
proche infrarouge
débit sanguin cérébral relatif
Volume de sang cérébral relatif
Taux métabolique cérébral relatif d'oxygène
rapport signal sur bruit
tomographie par émission de photons uniques
Transfert d'entropie
hémoglobine totale
indice d'oxygénation des tissus
saturation en oxygène de l'hémoglobine tissulaire
modification de la concentration en désoxyhémoglobine
changements dans la concentration d'oxyhémoglobine